NMR LOGGING

PRINCIPLES & APPLICATIONS

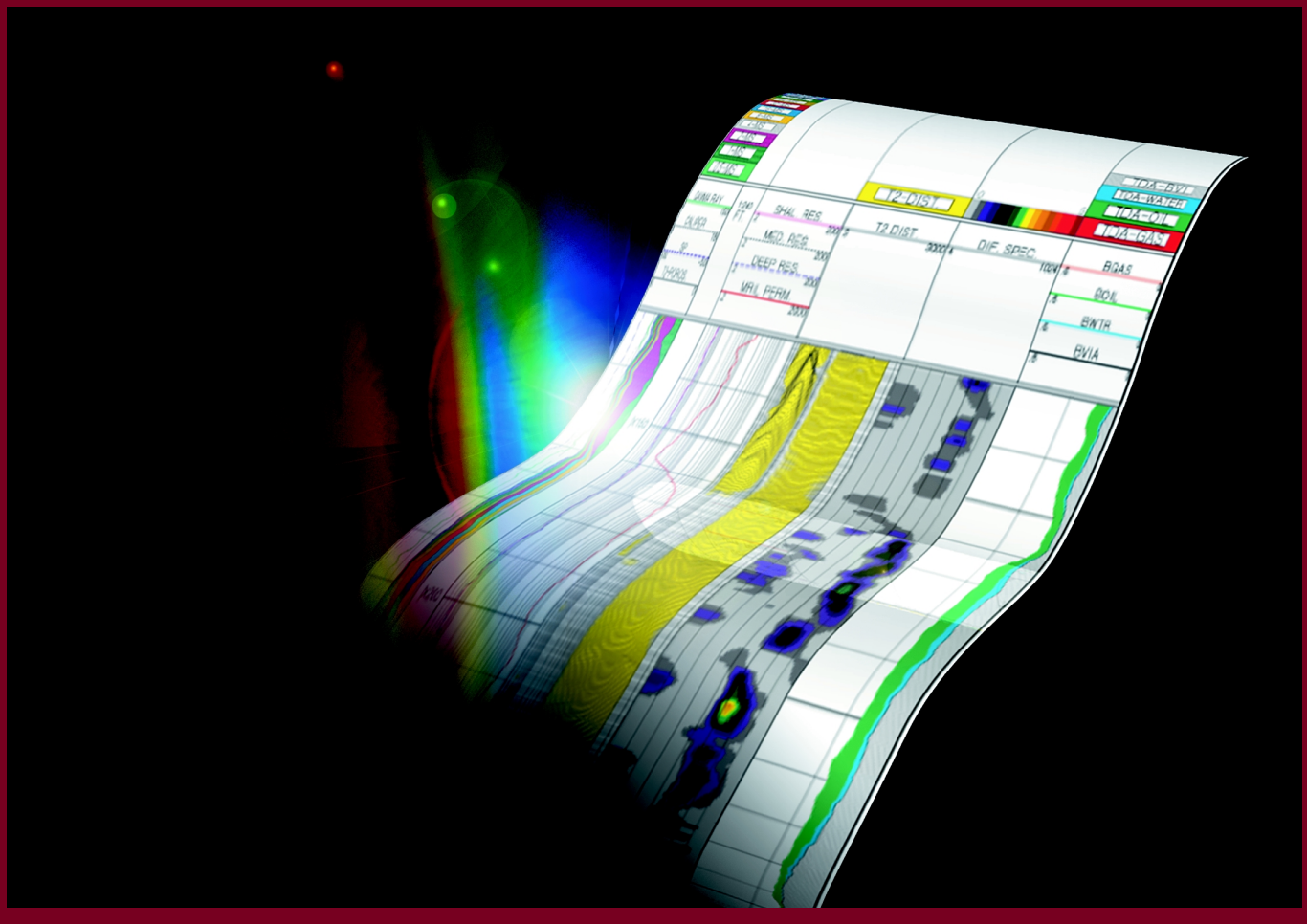

George R. Coates, Lizhi Xiao, and Manfred G. Prammer

NMR Logging
Principles and Applications

NMR Logging
Principles and Applications

George R. Coates, Lizhi Xiao, and Manfred G. Prammer

Halliburton Energy Services
Houston

Printed in the United States of America

Halliburton Energy Services Publication H02308

Contents

Foreword

Halliburton Energy Services is pleased to contribute this important technical volume on Nuclear Magnetic Resonance Logging to the petroleum industry. The NMR logging represents a new revolution in formation evaluation with wireline logging, and this book gives a comprehensive treatment of this new technology. Since its acquisition of NUMAR in 1997, Halliburton has focused on advancing NMR techniques, and on integrating conventional log data with the NMR interpretation methodology to further enhance the NMR applications. To this end, a new NMR tool has been introduced, new data processing techniques have been developed, and new data interpretation packages (such as our real-time NMR answer product) have been made available to the industry. Besides explaining basic NMR principles and applications, this book provides an understanding of these latest achievements in NMR logging.

This book was developed by three of our finest NMR experts in Halliburton and was reviewed by many recognized experts from our organization, from clients' organizations, and from other institutions. I am particularly grateful for the dedication of the authors, Mr. George R. Coates, Director of Reservoir Applications at the Halliburton Houston Technology Center, Dr. Lizhi Xiao, Senior Research Scientist and Project Manager for this book, Dr. Manfred G. Prammer, President of NUMAR, and to the editors, Dr. Richard F. Sigal and Mr. Stephen J. Bollich.

As the largest oilfield service company in the world, Halliburton is committed to providing services of the highest quality and best value, not only through field delivery but also through an understanding of underlying technology. This book is an example of this commitment, and I trust that you will find it useful in learning how NMR services can be of benefit in your applications.

Dick Cheney
CEO of Halliburton Company

Preface

Well logging, the economic method of choice for evaluating drilled formations, has progressively improved its determination of porosity and fractional fluid saturation, but could not provide a systematic estimate of permeability. This shortcoming was why Nuclear Magnetic Resonance captured the interest of the petroleum industry when researchers published results showing a good permeability correlation in the 1960's.

Unfortunately this industry interest was left waiting for nearly 30 years on a reliable downhole measurement of NMR relaxation. In 1992, when NUMAR introduced its MRIL logging service this wait was over; and it was soon demonstrated that the long hoped for permeability determination could be systematically provided, especially in shaly sand formations.

However, permeability was not the only petrophysical benefit provided by this new pulse-echo NMR log. Many other petrophysical parameters — mineral-independent total porosity; water, gas, and oil saturation independent of other logs; oil viscosity — all have been found achievable. Several other parameters appear within reach, thus ensuring that this new uniform gradient NMR logging measurement will prove to be the richest single source of formation petrophysics yet devised by the well logging industry.

This book has been prepared as a means of sharing these very exciting developments and to support those of you who are interested in formation evaluation technology.

George R. Coates
Director Reservoir Applications, Halliburton Energy Services

Editors

Richard F. Sigal and Stephen J. Bollich

Editorial Review Board

Internal Members

Prabhakar Aadireddy	Ron Cherry	Gary J. Frisch	Stefan Menger
Ronnel C. Balliet	Peter I. Day	James E. Galford	Daniel L. Miller
Ron J. M. Bonnie	Bob Engelman	John S. Gardner	Moustafa E. Oraby
James Buchanan	Maged Fam	Dave Marschall	Nick Wheeler

External Members

Ridvan Akkurt	J. Justin Freeman	George J. Hirasaki	James D. Klein
Robert J. S. Brown	David C. Herrick	Jasper A. Jackson	

Acknowledgments

In addition to our appreciation for the contributions of the editors and editorial review board, we wish to acknowledge and thank those who have helped so much with this book:

Jennifer Wood reprocessed most of the MRIL data for the examples in the book. Karen J. Campbell prepared many of the plots and figures. Sandra Moynihan and Communication Services coordinated the final product process. Jorge Velasco, Ramsin Y. Eyvazzadeh, Fernando Salazar, Greg Strasser, and Jim Witkowsky provided most of the NMR logging data and support. Charley Siess, MRIL Product Manager, provided encouragement and support. Peter O'Shea, Tim Epresi, and Halliburton Resevoir Applications colleagues, provided help and support.

Many thanks to the oil companies for release of their data for this publication. Finally, thanks to Metamor Documentation Solutions, Duncan, Oklahoma, for their role in preparing the book for publication.

The Authors
Houston, Texas
September 18, 1999

Chapter 1

Summary of NMR Logging Applications and Benefits

Since its discovery in 1946, nuclear magnetic resonance has become a valuable tool in physics, chemistry, biology, and medicine. With the invention of NMR logging tools that use permanent magnets and pulsed radio frequencies, the application of sophisticated laboratory techniques to determine formation properties in situ is now possible. This capability opens a new era in formation evaluation and core analysis just as the introduction of NMR has revolutionized the other scientific areas just mentioned. This chapter summarizes the applications and benefits of NMR logging to formation evaluation.

Medical MRI

Magnetic resonance imaging (MRI) is one of the most valuable clinical diagnostic tools in health care today. With a patient placed in the whole-body compartment of an MRI system, magnetic resonance signals from hydrogen nuclei at specific locations in the body can be detected and used to construct an image of the interior structure of the body. These images may reveal physical abnormalities and thereby aid in the diagnosis of injury and disease.

The MRI of the human head in **Fig. 1.1** demonstrates two important MRI characteristics. First, the signals used to create each image come from a well-defined location, typically a thin slice or cross section of the target. Because of the physical principles underlying NMR technology, each image is sharp, containing only information from the imaged cross section, with material in front or behind being essentially invisible. Second, only fluids (such as in blood vessels, body cavities, and soft tissues) are visible, while solids (such as bone) produce a signal that typically decays too fast to be recorded. By taking advantage of these two characteristics, physicians have been able to make valuable diagnostic use of MRI without needing to understand complex NMR principles.

These same NMR principles, used to diagnose anomalies in the human body can be used to analyze the fluids held in the pore spaces of reservoir rocks. And, just as physicians do not need to be NMR experts to use MRI technology for effective medical diagnosis, neither do geologists, geophysicists, petroleum engineers, nor reservoir engineers need to be NMR experts to use MRI logging technology for reliable formation evaluation.

MRI Logging

Magnetic Resonance Imaging Logging (MRIL®), introduced by NUMAR in 1991,[1] takes the medical MRI or laboratory NMR equipment and turns it inside-out. So, rather than placing the subject at the center of the instrument, the instrument itself is placed, in a wellbore, at the center of the formation to be analyzed.

At the center of an MRIL tool, a permanent magnet produces a magnetic field that magnetizes formation materials. An antenna surrounding this magnet transmits into the formation precisely timed bursts of radio-frequency energy in the form of an oscillating magnetic field. Between these pulses, the antenna is used to listen for the decaying "echo" signal from those hydrogen protons that are in resonance with the field from the permanent magnet.

Because a linear relationship exists between the proton resonance frequency and the strength of the permanent magnetic field, the frequency of the transmitted and received energy can be tuned to investigate cylindrical regions at different diameters around an MRIL tool. This tuning of an MRI probe to be sensitive to a specific frequency allows MRI instruments to image narrow slices of either a hospital patient or a rock formation.

Fig. 1.2 illustrates the "cylinders of investigation" for the MRIL-Prime tool,[2] which was introduced in 1998. The diameter and thickness of each thin cylindrical region are selected by simply specifying the central frequency and bandwidth to which the MRIL transmitter and receiver are tuned. The diameter of the cylinder is temperature-dependent, but typically is approximately 14 to 16 in.

Comparison of the MRIL Tool to Other Logging Tools

Because only fluids are visible to MRI,[3] the porosity measured by an MRIL tool contains no contribution from the matrix materials and does not need to be calibrated to formation lithology. This response characteristic makes an MRIL tool fundamentally different from conventional logging tools. The conventional neutron, bulk-density, and acoustic-travel-time porosity-logging tools are influenced by all components of a reservoir rock.[4, 5] Because

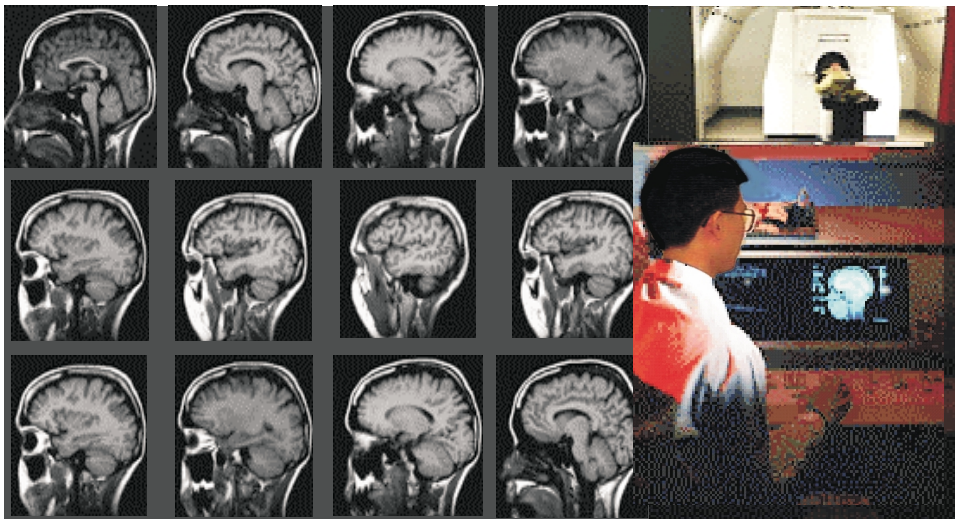

om000814

Figure 1.1—This "multi-slice," or multi-cross-sectional image of a human head demonstrates how a medical MRI scan can be used. In this example, the light areas represent tissues that have high fluid content (for example, brain matter) while the dark areas represent tissues that have low fluid content (for example, bone). Typically, the thickness of material that is used in imaging each cross section is many times greater than the size of features that can be imaged on any individual cross section.

reservoir rocks typically have more rock framework than fluid-filled space, these conventional tools tend to be much more sensitive to the matrix materials than to the pore fluids. The conventional resistivity-logging tools, while being extremely sensitive to the fluid-filled space and traditionally being used to estimate the amount of water present in reservoir rocks, cannot be regarded as true fluid-logging devices. These tools are strongly influenced by the presence of conductive minerals and, for the responses of these tools to be properly interpreted, a detailed knowledge of the properties of both the formation and the water in the pore space is required.

MRIL tools can provide three types of information, each of which make these tools unique among logging devices:

- information about the quantities of the fluids in the rock
- information about the properties of these fluids
- information about the sizes of the pores that contain these fluids

Fluid Quantity

An MRIL tool can directly measure the density of hydrogen nuclei in reservoir fluids.[6] Because the density of hydrogen nuclei present in water is known, data from an MRIL tool can be directly converted to an apparent water-filled porosity. This conversion can be done without any knowledge of the minerals that make up the solid fraction of the rock, and without any concern about trace elements in the fluids (such as boron) that can perturb neutron porosity measurements.

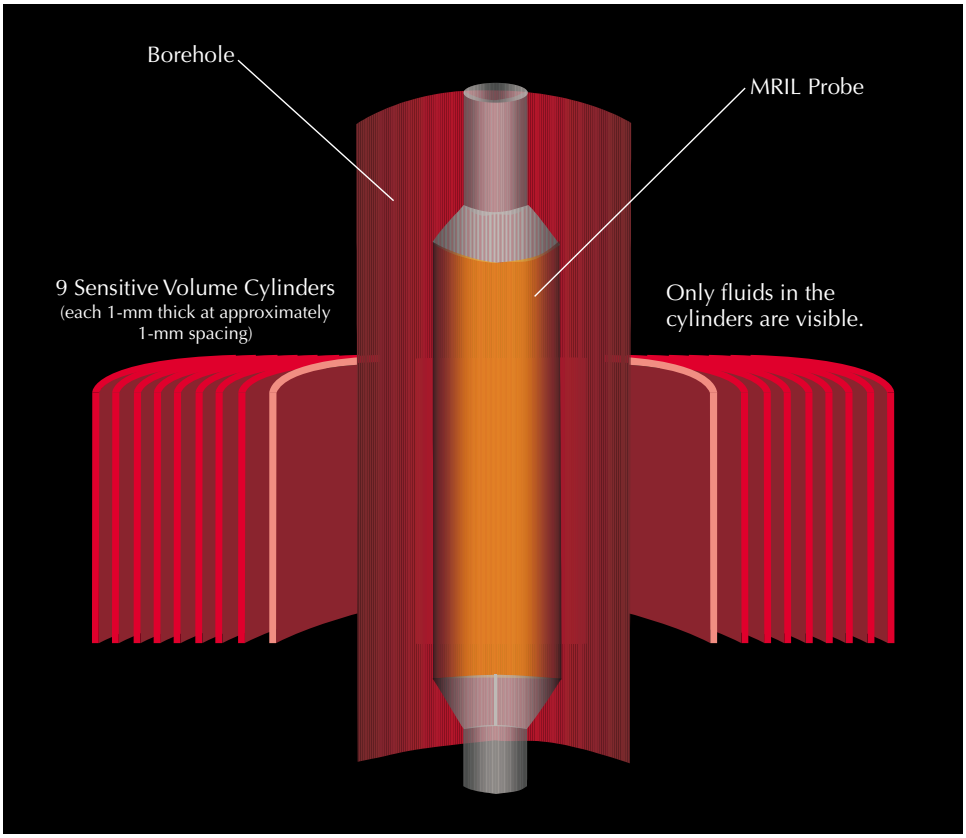

Figure 1.2—The MRIL-Prime tool can be operated at nine separate frequencies. The use of multiple frequencies allows independent information to be obtained from multiple concentric cylinders, thereby improving the signal-to-noise ratio, enabling faster logging speeds, and permitting different pulse-timing sequences for complex data acquisition.

Fluid Properties

Medical MRI relies on the ability to link specific medical conditions or organs in the body to different NMR behavior. A similar approach can be used with MRIL tools to study fluids in a thin zone a few inches from the borehole wall. MRIL tools can determine the presence and quantities of different fluids (water, oil, and gas),[7–11] as well as some of the specific properties of the fluids (for example, viscosity[12]). Both medical-MRI devices and MRIL tools can be run with specific pulse-sequence settings, or "activations," that enhance their ability to detect particular fluid conditions.

Pore Size and Porosity

The NMR behavior of a fluid in the pore space of a reservoir rock is different from the NMR behavior of the fluid in bulk form. For example, as the size of pores containing water decreases, the differences between the apparent NMR properties of the water in the pores and the water in bulk form increases.[13] Simple methods can be used to extract enough pore-size information from MRIL data to greatly improve the estimation of such key petrophysical properties as permeability and the volume of capillary-bound water.[14, 15]

Micro-porosity associated with clays and with some other minerals typically contains water that, from an NMR perspective, appears almost like a solid. Water in such micro-pores has a very rapid "relaxation time." Because of this rapid relaxation, this water is more difficult to see than, for example, producible water associated with larger pores. Earlier generations of NMR logging tools were unable to see water in these micro-pores, and because this water was associated most often with clays, the porosity measured by these earlier tools was often characterized as being an "effective porosity." Modern MRIL logging tools can see essentially all the fluids in the pore space, and the porosity measurement made by these tools is thus characterized as being a "total-porosity" measurement. Pore-size information supplied by the modern tools is used to calculate an effective porosity that mimics the porosity measured by the older NMR tools.[16]

In addition, one of the key features of the MRIL design philosophy is that the NMR measurements of the formation made when the MRIL tool is in the wellbore can be duplicated in the laboratory by NMR measurements made on rock cores recovered from the formation. This ability to make repeatable measurements under very different conditions is what makes it possible for researchers to calibrate the NMR measurements to the petrophysical properties of interest (such as pore size) to the end user of MRIL data.[17–19]

Fig. 1.3 compares MRIL responses with those of conventional logging tools.[20] The common volumetric model used in the comparison consists of a matrix component and a pore-fluid component. The matrix component is composed of clay minerals and non-clay minerals, and the pore-fluid component is composed of water and hydrocarbons. Conceptually, the pore fluids can be more finely divided into clay-bound water, capillary-bound water, movable water, gas, light oil, medium-viscosity oil, and heavy oil.

Although conventional porosity tools, such as neutron, density, and sonic, exhibit a bulk response to all components of the volumetric model, they are more sensitive to matrix materials than to pore fluids. Furthermore, the responses of these tools are highly affected by the borehole and mudcake, and the sensitive volumes of these tools are not as well defined as that of the MRIL tool.

Resistivity tools, such as induction and laterolog, respond to conductive fluids such as clay-bound water, capillary-bound water, and movable water. Based on the conductivity contrast between (1) clay-bound water and (2) capillary-bound and movable water, the dual-water and

Waxman-Smits models were developed for better estimation of water saturation. Even with these models, recognition of pay zones is still difficult because no conductivity contrast exists between capillary-bound water and movable water. As with the conventional porosity tools, resistivity tools are very sensitive to the borehole and mudcake, and their sensitive volumes are poorly defined.

Conventional log interpretation uses environmentally corrected porosity and resistivity logs to determine formation porosity and water saturation. Assessing the accuracy of tool responses, selecting reliable values for model parameters, and matching the vertical resolutions and depths of investigation of the various measurements all add to the challenge of successfully estimating porosity and water saturation. Additionally, with conventional logs, distinguishing light oil, medium-viscosity oil, and heavy oil is impossible.

As indicated in Fig. 1.3, MRIL porosity is essentially matrix-independent—that is, MRIL tools are sensitive only to pore fluids. The difference in various NMR properties—such as relaxation times (T_1 and T_2) and diffusivity (D)—among various fluids makes it possible to distinguish (in the zone of investigation) among bound water, movable water, gas, light oil, medium-viscosity oil, and heavy oil. The sensitive volumes of MRIL tools are very well defined; thus, if the borehole and mudcake are not in the sensitive volumes, then they will not affect MRIL measurements.

The volumetric model of Fig. 1.3 does not include other parameters that can be estimated from NMR measurements: pore-size; formation permeability; the presence of clay, vugs, and fractures; hydrocarbon properties such as viscosity; and grain-size. These factors affect MRIL measurements, and their effects can be extracted to provide very important information for reservoir description and evaluation. Conventional logging measurements are insensitive to these factors.

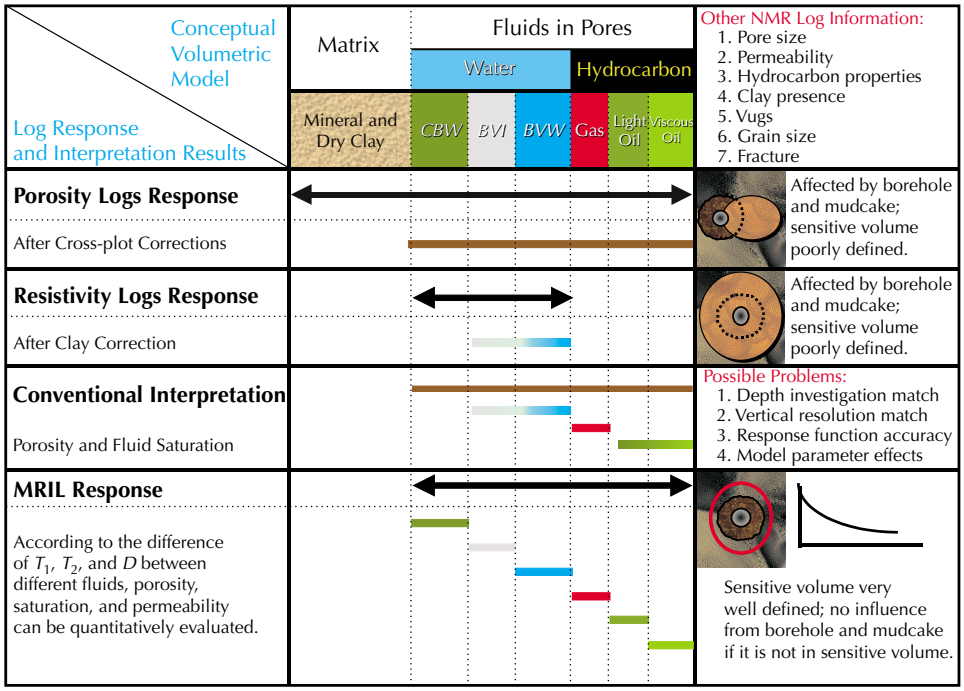

Figure 1.3—MRIL tool responses are unique among logging tools. MRIL porosity is independent of matrix minerals, and the total response is very sensitive to fluid properties. Because of differences in relaxation times and/or diffusivity among fluids, MRIL data can be used to differentiate clay-bound water, capillary-bound water, movable water, gas, light oil, and viscous oils. Other information, such as pore size, permeability, hydrocarbon properties, vugs, fractures, and grain size, often can be extracted. In addition, because the volumes to which MRIL tools are sensitive are very well defined, borehole fluids and rugosity minimally affect MRIL measurements.

NMR-Logging Raw Data

Before a formation is logged with an NMR tool, the protons in the formation fluids are randomly oriented. When the tool passes through the formation, the tool generates magnetic fields that activate those protons. First, the tool's permanent magnetic field aligns, or polarizes, the spin axes of the protons in a particular direction. Then the tool's oscillating field is applied to tip these protons away from their new equilibrium position. When the oscillating field is subsequently removed, the protons begin tipping back, or relaxing, toward the original direction in which the static magnetic field aligned them.[21] Specified pulse sequences are used to generate a series of so-called spin echoes, which are measured by the NMR logging tool and are displayed on logs as spin-echo trains. These spin-echo trains constitute the raw NMR data.

To generate a spin-echo train such as the one of **Fig. 1.4**, an NMR tool measures the amplitude of the spin echoes as a function of time. Because the spin echoes are measured over a short time, an NMR tool travels no more than a few inches in the well while recording the spin-echo train. The recorded spin-echo trains can be displayed on a log as a function of depth.

The initial amplitude of the spin-echo train is proportional to the number of hydrogen nuclei associated with the fluids in the pores within the sensitive volume. Thus, this amplitude can be calibrated to give a porosity. The observed echo train can be linked both to data acquisition parameters and to properties of the pore fluids located in the measurement volumes. Data acquisition parameters include inter-echo spacing (*TE*) and polarization time (*TW*). *TE* is the time between the individual echoes in an echo train. *TW* is the time between the cessation of measurement of one echo train and the beginning of measurement of the next echo train. Both *TE* and *TW* can be adjusted to change the information content of the acquired data.

Properties of the pore fluids that affect the echo trains are the hydrogen index (*HI*), longitudinal relaxation time (T_1), transverse relaxation time (T_2), and diffusivity (*D*). *HI* is a measure of the density of hydrogen atoms in the fluid. T_1 is an indication of how fast the tipped

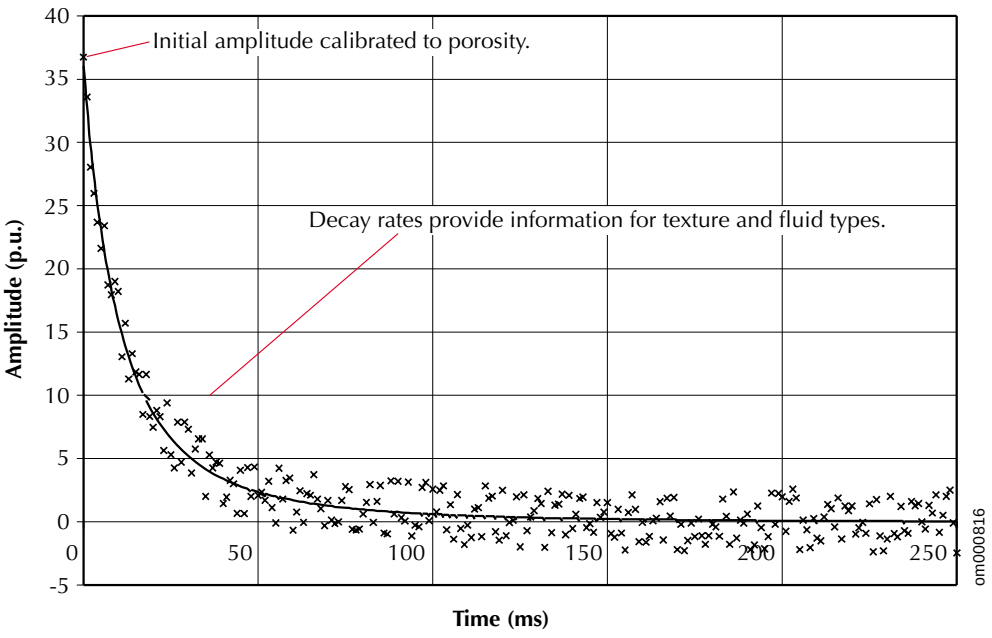

Figure 1.4—The decay of a spin-echo train, which is a function of the amount and distribution of hydrogen present in fluids, is measured by recording the decrease in amplitude of the spin echoes over time. Petrophysicists can use decay-rate information to establish pore-fluid types and pore-size distributions. In this example, the spin echoes are recorded at 1-ms inter-echo spacing. The discrete points in this figure represent the raw data, and the solid curve is a fit to that data.

protons in the fluids relax longitudinally (relative to the axis of the static magnetic field), while T_2 is an indication of how fast the tipped protons in the fluids relax transversely (again relative to the axis of the static magnetic field). *D* is a measure of the extent to which molecules move at random in the fluid.

NMR Porosity

The initial amplitude of the raw decay curve is directly proportional to the number of polarized hydrogen nuclei in the pore fluid. The raw reported porosity is provided by the ratio of this amplitude to the tool response in a water tank (which is a medium with 100% porosity). This porosity is independent of the lithology of the rock matrix and can be validated by comparing laboratory NMR measurements on cores with conventional laboratory porosity measurements.

The accuracy of the raw reported porosity depends primarily on three factors:[17]

- a sufficiently long *TW* to achieve complete polarization of the hydrogen nuclei in the fluids
- a sufficiently short *TE* to record the decays for fluids associated with clay pores and other pores of similar size
- the number of hydrogen nuclei in the fluid being equal to the number in an equivalent volume of water, that is, *HI* = 1

Provided the preceding conditions are satisfied, the NMR porosity is the most accurate available in the logging industry.

The first and third factors are only an issue for gas or light hydrocarbons. In these cases, special activations can be run to provide information to correct the porosity. The second factor was a problem in earlier generations of tools. They could not, in general, see most of the fluids associated with clay minerals. Because in shaly sand analysis the non-clay porosity is referred to as effective porosity, the historical MRIL porosity (*MPHI*) was also called effective porosity. Current MRIL tools now capture a total porosity (*MSIG*) by using both a short *TE* (0.6 ms) with partial polarization and a long *TE* (1.2 ms) with full polarization. The difference between *MSIG* and *MPHI* is taken as the clay-bound water (*MCBW*). This division of porosity is useful in analysis and often corresponds to other measures of effective porosity and clay-bound water. The division of porosity into clay-bound porosity and effective porosity depends to some extent on the method used; thus, other partitions can differ from that obtained from the MRIL porosity.

NMR measurements on rock cores are routinely made in the laboratory. The porosity can be measured with sufficiently short *TE* and sufficiently long *TW* to capture all the NMR-visible porosity. Thousands of laboratory measurements on cores verify that agreement between the NMR porosity and a Helium Boyles Law porosity is better than 1 p.u. **Fig 1.5** illustrates such an agreement.

NMR T_2 Distribution

The amplitude of the spin-echo-train decay can be fit very well by a sum of decaying exponentials, each with a different decay constant. The set of all the decay constants forms the decay spectrum or transverse-relaxation-time (T_2) distribution. In water-saturated rocks, it

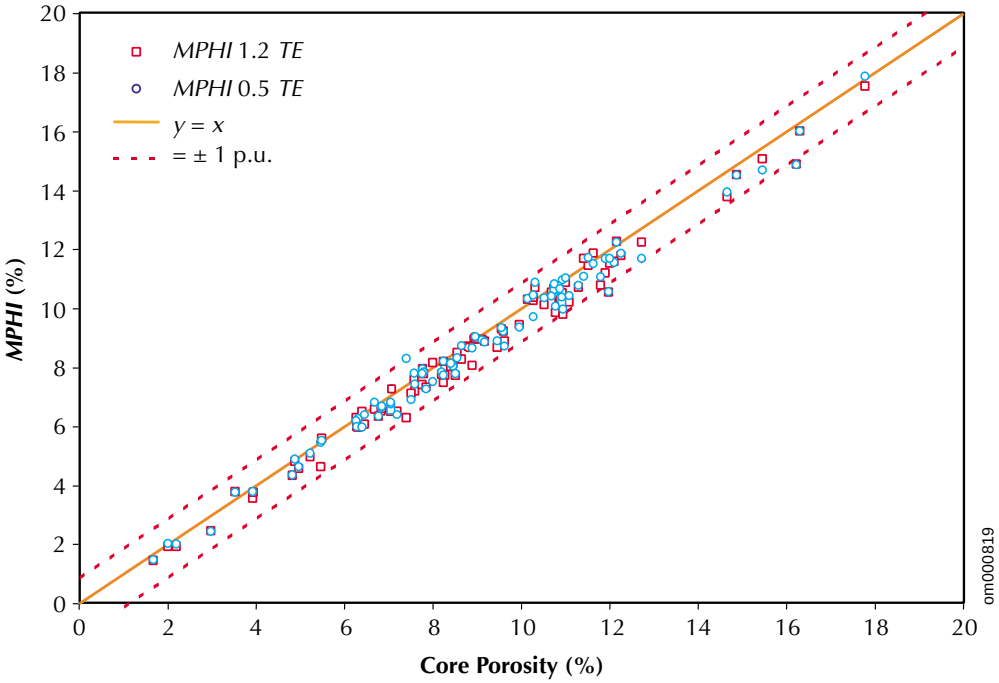

Figure 1.5—As exemplified here for a set of clean sandstones, good agreement is typically observed between porosity derived from laboratory NMR measurements and porosity derived from conventional core analysis. NMR-porosity values typically fall within ±1 p.u. of the measured core-porosity values. The figure shows NMR laboratory data measured at two different *TE* values, namely, 0.5 and 1.2 ms. Comparing the core data to the NMR data indicates whether micro-porosity is present. (Fluid in micro-pores exhibits a fast T_2 that can be observed when *TE* = 0.5 ms, but not when *TE* = 1.2 ms.) In this case, because no evidence exists for micro-porosity, the NMR "effective porosity" (*MPHI*) and total porosity (*MSIG*) would be the same.

can be proven mathematically that the decay curve associated with a single pore will be a single exponential with a decay constant proportional to pore size; that is, small pores have small T_2 values and large pores have large T_2 values.[13, 22] At any depth in the wellbore, the rock samples probed by the MRIL tool will have a distribution of pore sizes. Hence, the multi-exponential decay represents the distribution of pore sizes at that depth, with each T_2 value corresponding to a different pore size. **Fig. 1.6** shows the T_2 distribution that was derived from the spin-echo train in Fig. 1.4.

Properly defined, the area under the T_2-distribution curve is equal to the initial amplitude of the spin-echo train. Hence, the T_2 distribution can be directly calibrated in terms of porosity. In essence, a key function of the NMR tool and its associated data-acquisition software is to provide an accurate description of the T_2 distribution at every depth in the wellbore. In terms of the T_2 distribution, *MPHI* is the area under the part of the curve for which $T_2 \oplus 4$ ms, *MCBW* is the area for which $T_2 < 4$ ms, and *MSIG* is the total area.

The NMR T_2 distribution can be displayed in three ways: waveform presentation, image format, and bin-distribution plot. Each represents the distribution of the porosity over T_2 values and, hence, over the pore sizes. The three displays reflect different visualizations of the same set of data. **Fig 1.7** shows an example of these displays.

NMR Free-Fluid Index and Bulk Volume Irreducible

The porosity and pore-size information from NMR measurements can be used to estimate both the permeability and the potentially producible porosity (that is, the movable fluids).

The NMR estimate of producible porosity is called the free-fluid index (*MFFI* and also *FFI*). The estimate of *MFFI* is based on the assumption that the producible fluids reside in large pores, whereas the bound fluids reside in small pores. Because T_2 values can be related to pore sizes, a T_2 value can be selected below which the corresponding fluids are expected to reside in small pores

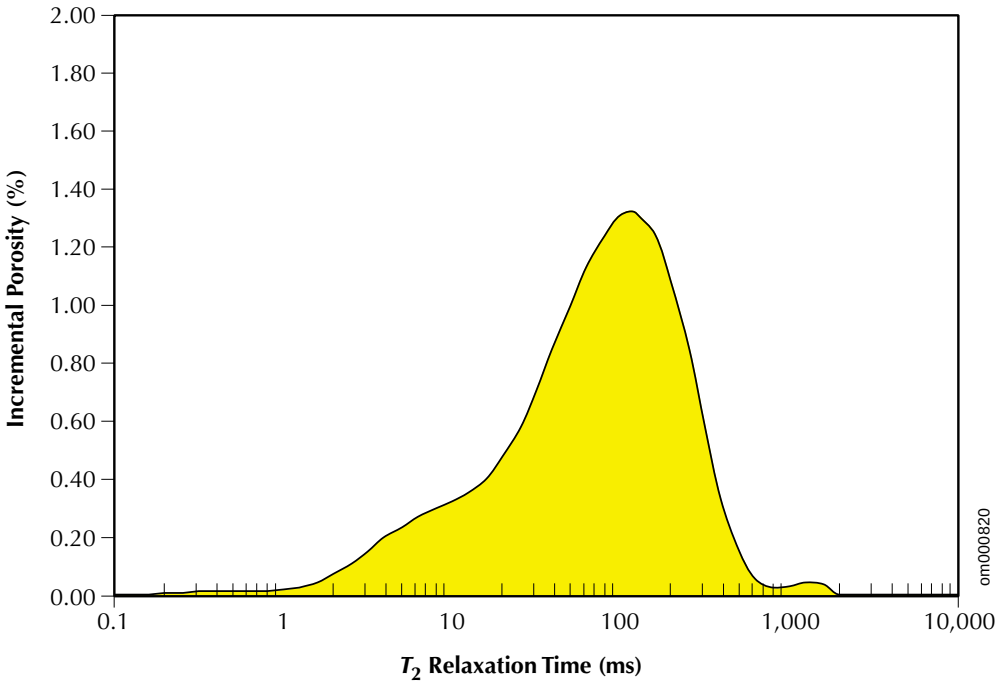

Figure 1.6—Through the mathematical process of inversion, the spin-echo decay data can be converted to a T_2 distribution. This distribution is the "most likely" distribution of T_2 values that produce the echo train. (The T_2 distribution shown here corresponds to the spin-echo train of Fig. 1.4.) With proper calibration, the area under the T_2-distribution curve is equal to the porosity. This distribution will correlate with a pore-size distribution when the rock is 100% water-saturated. However, if hydrocarbons are present, the T_2 distribution will be altered depending on the hydrocarbon type, viscosity, and saturation.

and above which the corresponding fluids are expected to reside in larger pores. This T_2 value is called the T_2 cutoff ($T_{2cutoff}$).[23, 24]

Through the partitioning of the T_2 distribution, $T_{2cutoff}$ divides *MPHI* into free-fluid index (*MFFI*) and bound-fluid porosity, or bulk volume irreducible (*BVI*), as shown in **Figs. 1.8** and **1.9**.

The $T_{2cutoff}$ can be determined with NMR measurements on water-saturated core samples. Specifically, a comparison is made between the T_2 distribution of a sample in a fully water-saturated state, and the same sample in a partially saturated state, the latter typically being attained by centrifuging the core at a specified air-brine capillary pressure.[23] Although capillary pressure, lithology, and pore characteristics all affect $T_{2cutoff}$ values, common practice establishes local field values for $T_{2cutoff}$. For example, in the Gulf of Mexico, $T_{2cutoff}$ values of 33 and 92 ms are generally appropriate for sandstones and carbonates, respectively.[23] Generally though, more accurate values are obtained by performing measurements on core samples from the actual interval logged by an MRIL tool.

NMR Permeability

NMR relaxation properties of rock samples are dependent on porosity, pore size, pore-fluid properties and mineralogy. The NMR estimate of permeability is based on theoretical models that show that permeability increases with both increasing porosity and increasing pore size.[24–29] Two related kinds of permeability models have been developed. The free-fluid or Coates model can be applied in formations containing water and/or hydrocarbons. The average-T_2 model can be applied to pore systems containing only water.[30] Measurements on core samples are necessary to refine these models and produce a model customized for local use. **Fig. 1.10** shows that the decay of an echo train contains information related to formation permeability. **Fig. 1.11** shows how the Coates model can be calibrated with laboratory core data. **Fig. 1.12** demonstrates MRIL permeability derived from a customized Coates model.

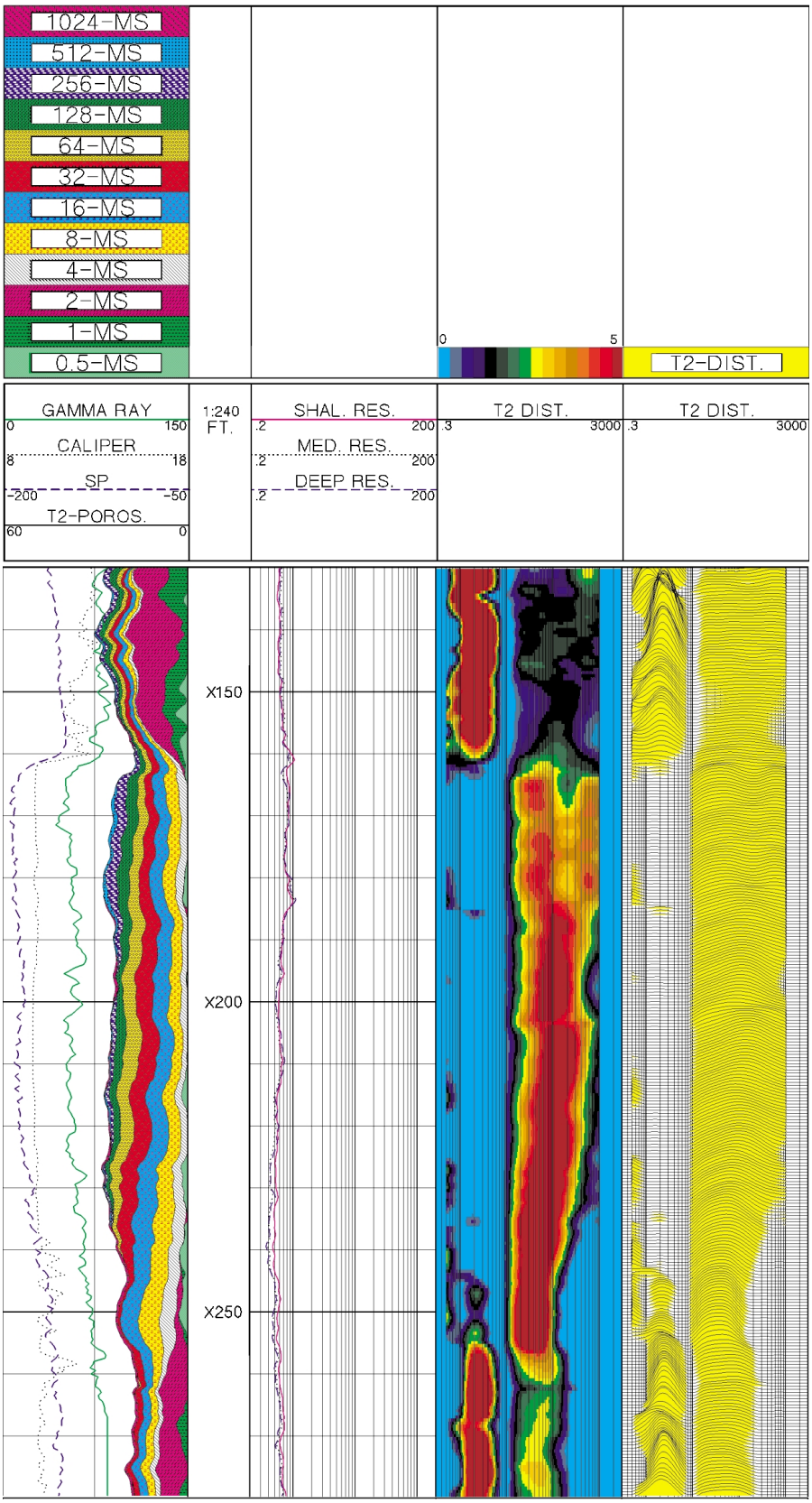

Figure 1.7— T_2 distributions are displayed in three ways on this log: A plot of the cumulative amplitudes from the binned T_2-distribution in Track 1, a color image of the binned T_2-distribution in Track 3, and a waveform presentation of the same information in Track 4. The T_2-distribution typically displayed for MRIL data corresponds to binned amplitudes for exponential decays at 0.5, 1, 2, 4, 8, 16, 32, 64, 128, 256, 512, and 1024 ms when *MSIG* is shown and from 4 ms to 1024 ms when *MPHI* is shown. The 8-ms bin, for example, corresponds to measurements made between 6 and 12 ms. Because logging data are much noisier than laboratory data, only a comparatively coarse T_2-distribution can be created from MRIL log data.

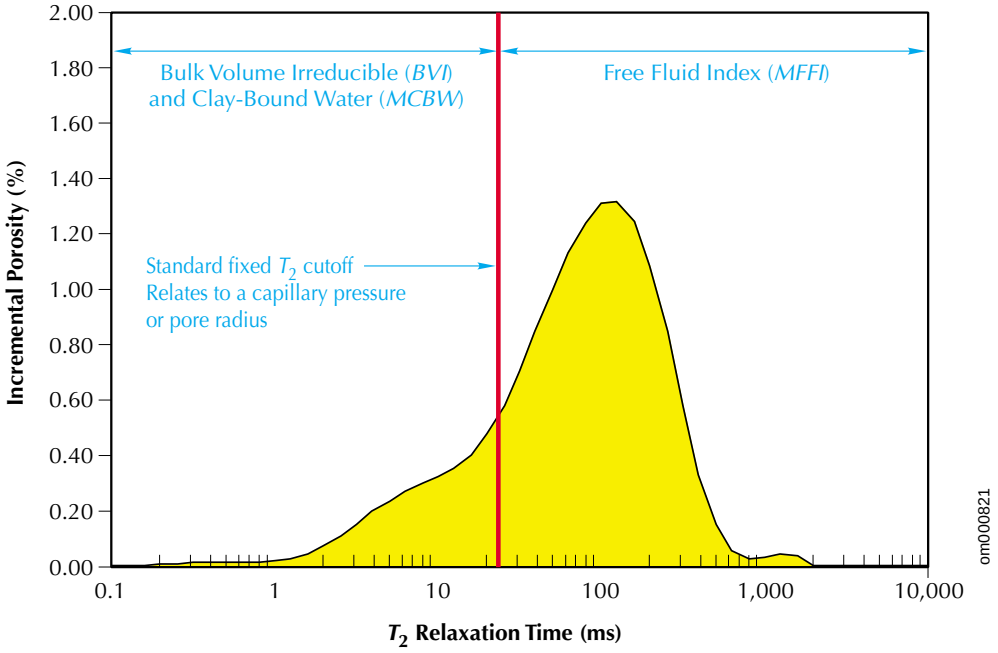

Figure 1.8—The T_2 distribution is composed of movable (*MFFI*) and immovable (*BVI* and *MCBW*) components. Because pore size is the primary controlling factor in establishing the amount of fluid that can potentially move, and because the T_2 spectrum is often related to pore-size distribution, a fixed T_2 value should directly relate to a pore size at and below which fluids will not move. This information is used to decompose *MPHI* into *MFFI* and *BVI*.

NMR Properties of Reservoir Fluids

Clay-bound water, capillary-bound water, and movable water occupy different pore sizes and locations. Hydrocarbon fluids differ from brine in their locations in the pore space, usually occupying the larger pores. They also differ from each other and brine in viscosity and diffusivity. NMR logging uses these differences to characterize the fluids in the pore space. **Fig. 1.13** qualitatively indicates the NMR properties of different fluids found in rock pores.[31–34] In general, bound fluids have very short T_1 and T_2 times, along with slow diffusion (small D) that is due to the restriction of molecular movement in small pores. Free water commonly exhibits medium T_1, T_2, and D values. Hydrocarbons, such as natural gas, light oil, medium-viscosity oil, and heavy oil, also have very different NMR characteristics. Natural gas exhibits very long T_1 times but short T_2 times and a single-exponential type of relaxation decay. NMR characteristics of oils are quite variable and are largely dependent on oil viscosities. Lighter oils are highly diffusive, have long T_1 and T_2 times, and often exhibit a single-exponential decay. As viscosity increases and the hydrocarbon mix becomes more complex, diffusion decreases, as do the T_1 and T_2 times, and events are accompanied by increasingly complex multi-exponential decays. Based on the unique NMR characteristics of the signals from the pore fluids, applications have been developed to identify and, in some cases, quantify the type of hydrocarbon present.

NMR Hydrocarbon Typing

Despite the variability in the NMR properties of fluids, the locations of signals from different types of fluids in the T_2 distribution can often be predicted or, if measured data are available, identified. This capability provides important information for NMR data interpretation and makes many applications practical.

Fig. 1.14 shows two methods for differentiating fluids. In one method, different *TW* values are used with a T_1-weighted mechanism to differentiate light hydrocarbons (light oil or gas, or both) from water. In the second method, different *TE* values are used with a diffusivity-

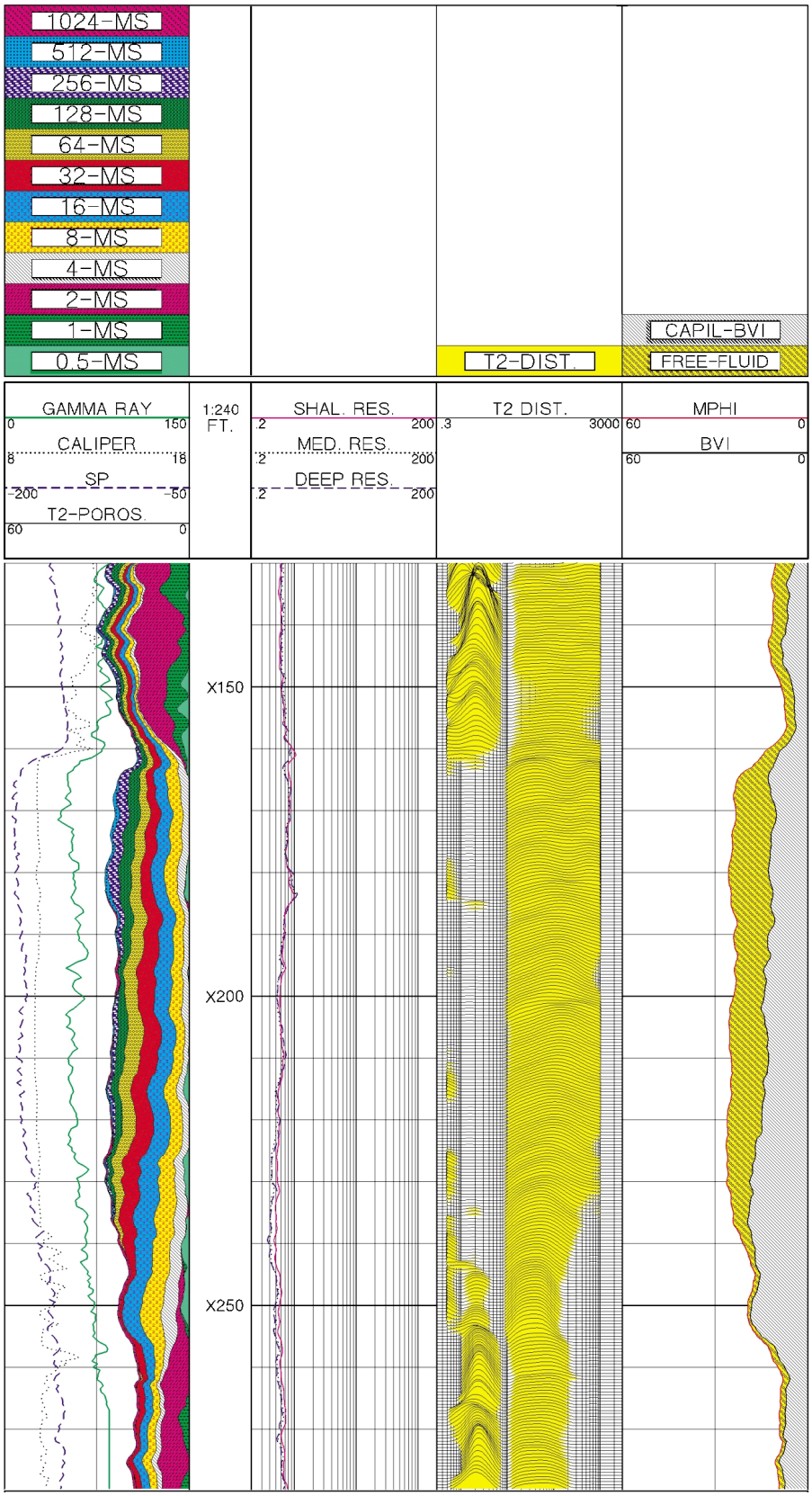

Figure 1.9—This Gulf of Mexico silty-sand formation illustrates the variability of *BVI* (Track 4). A coarsening-upward sequence from X160 to X255 is apparent based upon the increase of *BVI* and gamma ray with depth. If the free fluid were predominantly hydrocarbon, then the increased irreducible water deeper in the interval would account for the observed reduction in the logged resistivity. What appears at first sight to be a transition zone from X190 to X255 could actually be just a variation of grain size with depth.

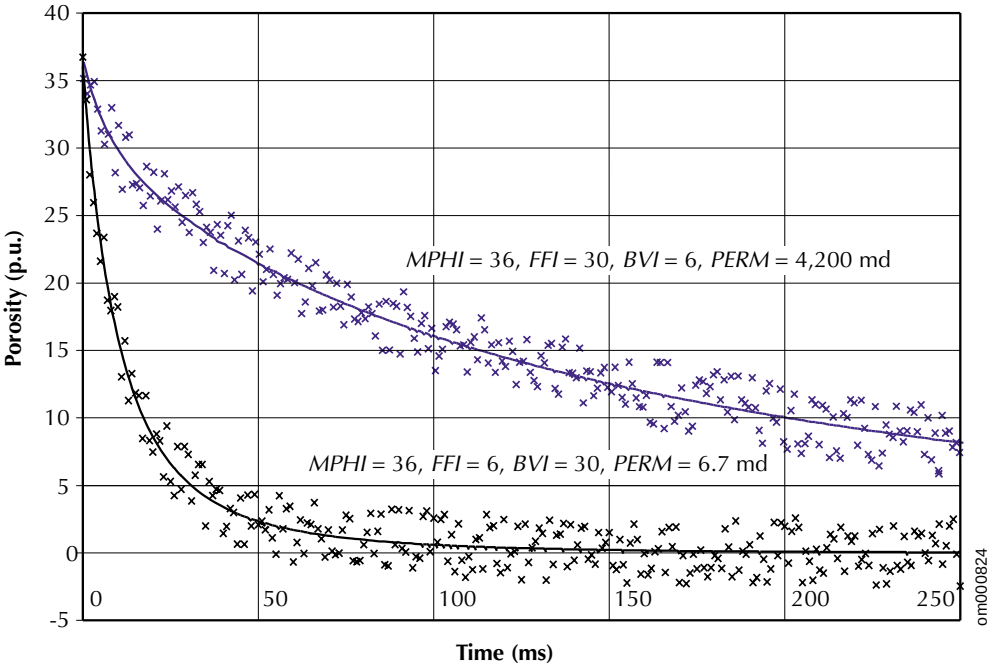

Figure 1.10—Two echo trains were obtained from formations with different permeability. Both formations have the same porosity but different pore sizes. This difference leads to shifted T_2 distributions, and therefore to different values of the ratio of *MFFI* to *BVI*. The permeabilities computed from the Coates model $\{k = [(MPHI/C)^2(MFFI/BVI)]^2$, where k is formation permeability and C is a constant that depends on the formation} also are indicated in the figure.

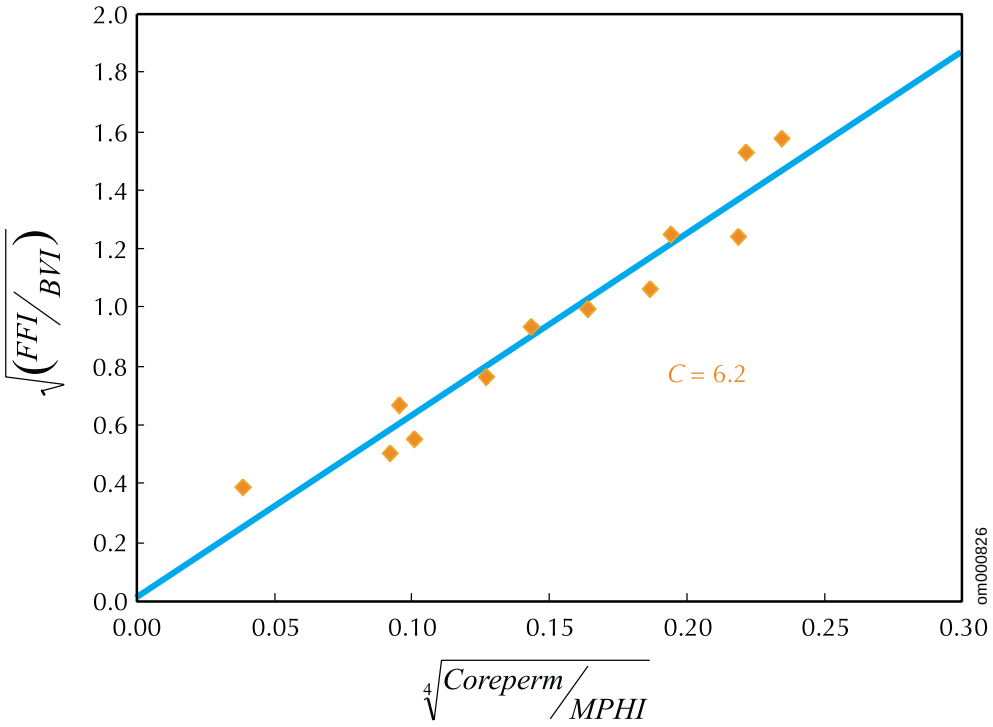

Figure 1.11—A crossplot that utilizes core data can be used to determine the constant C in the Coates permeability model.

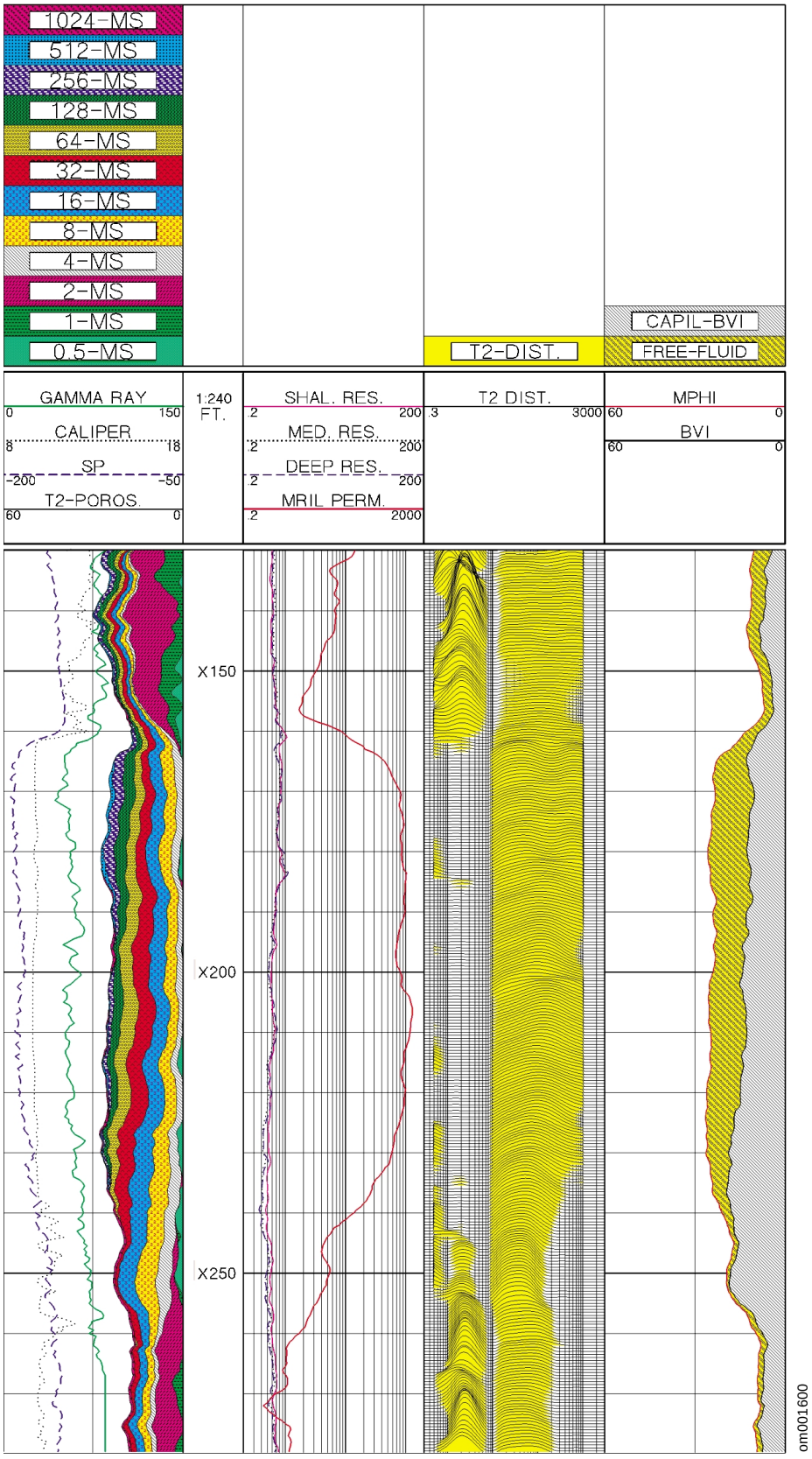

Figure 1.12—Track 2 of this log shows the MRIL permeability derived from a customized Coates model.

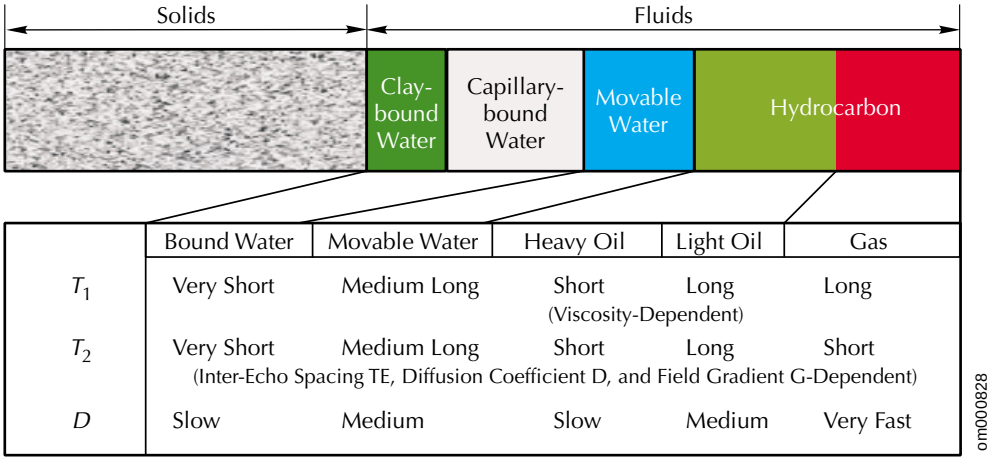

Figure 1.13—The typical qualitative values of T_1, T_2, and D for different fluid types and rock pore sizes demonstrate the variability and complexity of the T_1 and T_2 relaxation measurements.

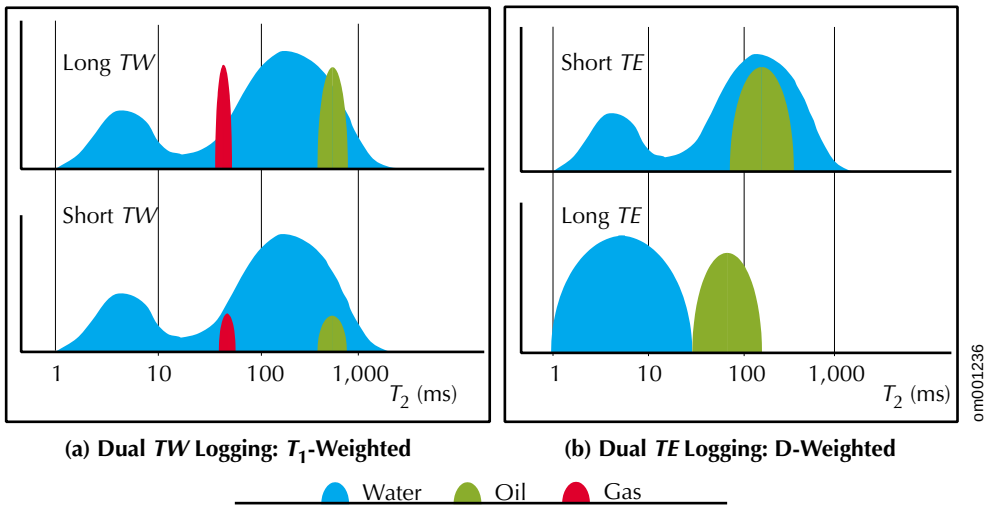

Figure 1.14—(a) Different T_2 distributions can arise from different TW values. In this case a T_1-weighted mechanism is used to differentiate hydrocarbons from water. **(b)** Different T_2 distributions also can arise from different TE values. In this case, a diffusivity-weighted mechanism is used to differentiate viscous oil from water, or to differentiate gas from liquids.

weighted mechanism in a well-defined gradient magnetic field to differentiate viscous oil from water, or to differentiate gas from liquid.

The Differential Spectrum Method (DSM) is an example of a T_1-weighted mechanism in which two echo trains are gathered over the same interval using two different polarization times. The echo train recorded after the short TW contains almost all of the water signals but only some of the light-hydrocarbon signals. However, the echo train recorded after the long TW contains all of the signals from both the water and the light hydrocarbons that are present. A differential spectrum that contains only light-hydrocarbon components can be created by taking the difference between the T_2 distributions computed separately from the echo trains acquired at the two different polarization times.[7–9]

The two echo trains used to compute a differential spectrum can also be subtracted from one another and the resulting echo train examined through a process referred to as Time-Domain Analysis (TDA™).[35] TDA starts by resolving the exponential decays associated with light

hydrocarbons (oil and/or gas), thereby confirming the presence of these fluids, and then provides estimates of the fluid volumes. TDA is a more robust process than DSM.

The log in **Fig. 1.15** provides an example combining both DSM and TDA results. Because NMR analysis does not rely on formation water salinity to obtain water saturation, it has an advantage over conventional resistivity analysis in mixed or unknown salinity conditions. This feature can be extremely useful in waterflood projects to evaluate residual oil saturation (*ROS*) after the waterflood or to look for bypassed oil.

NMR Enhanced Water Saturation with Resistivity Data

Because resistivity tools have a large depth of investigation, a resistivity-based water-saturation model is preferred for determining water saturation in the virgin zone of a formation. However, resistivity measurements cannot distinguish between capillary-bound water and movable water. This lack of contrast makes it difficult to recognize hydrocarbon-productive low-resistivity and/or low-contrast pay zones from data provided by traditional logging suites.

The unique information, such as *BVI* and *MCBW*, provided by NMR logging can significantly enhance the estimation of resistivity-based water saturation and can greatly assist in the recognition of pay zones that will produce water-free.

Through an MRI analysis process referred to as "MRIAN™",[36] the NMR data and the deep-resistivity data are integrated to determine whether producible water is in the virgin zone, or whether an interval with high water saturation may actually produce water-free hydrocarbons. The log shown in **Fig. 1.16** includes MRIAN results.

MRIL Application Examples

MRIL Porosity and Permeability

Fig. 1.17 presents data from a shaly sand formation in Egypt. Track 1 contains MRIL permeability (green curve) and core permeability (red asterisks). Track 2 contains MRIL porosity (blue curve) and core porosity (black asterisks). In this reservoir, the highly variable grain sizes lead to a considerable variation in rock permeability. Capillary-pressure measurements on rock samples yielded a good correlation between the pore bodies and the pore throat structures. This correlation indicates that the NMR T_2 distribution is a good representation of the pore throat size distribution when the pores are 100% water-saturated.

Fig. 1.18 shows an MRIL log through a massive low-porosity (approximately 10 p.u.), low-permeability (approximately 1 to 100 md) sandstone reservoir in Australia's Cooper basin.[23] Track 1 contains gamma ray and caliper logs. Track 2 contains deep- and shallow-reading resistivity logs. Track 3 presents the MRIL calculated permeability and core permeability. Track 4 shows the MRIL porosity response, neutron and density porosity readings (based on a sandstone matrix), and core porosity. This well was drilled with a potassium chloride (KCl) polymer mud [48-kppm sodium chloride (NaCl) equivalent] and an 8.5-in. bit. MRIL data were acquired with TW = 12 s and TE = 1.2 ms.

Over the interval depicted, the log shows a clean sandstone formation at the top, a shaly sandstone at the bottom, and an intervening shale between the two sandstones. Agreement between *MPHI* and the core porosity is good. The slight underestimation of *MPHI* relative to

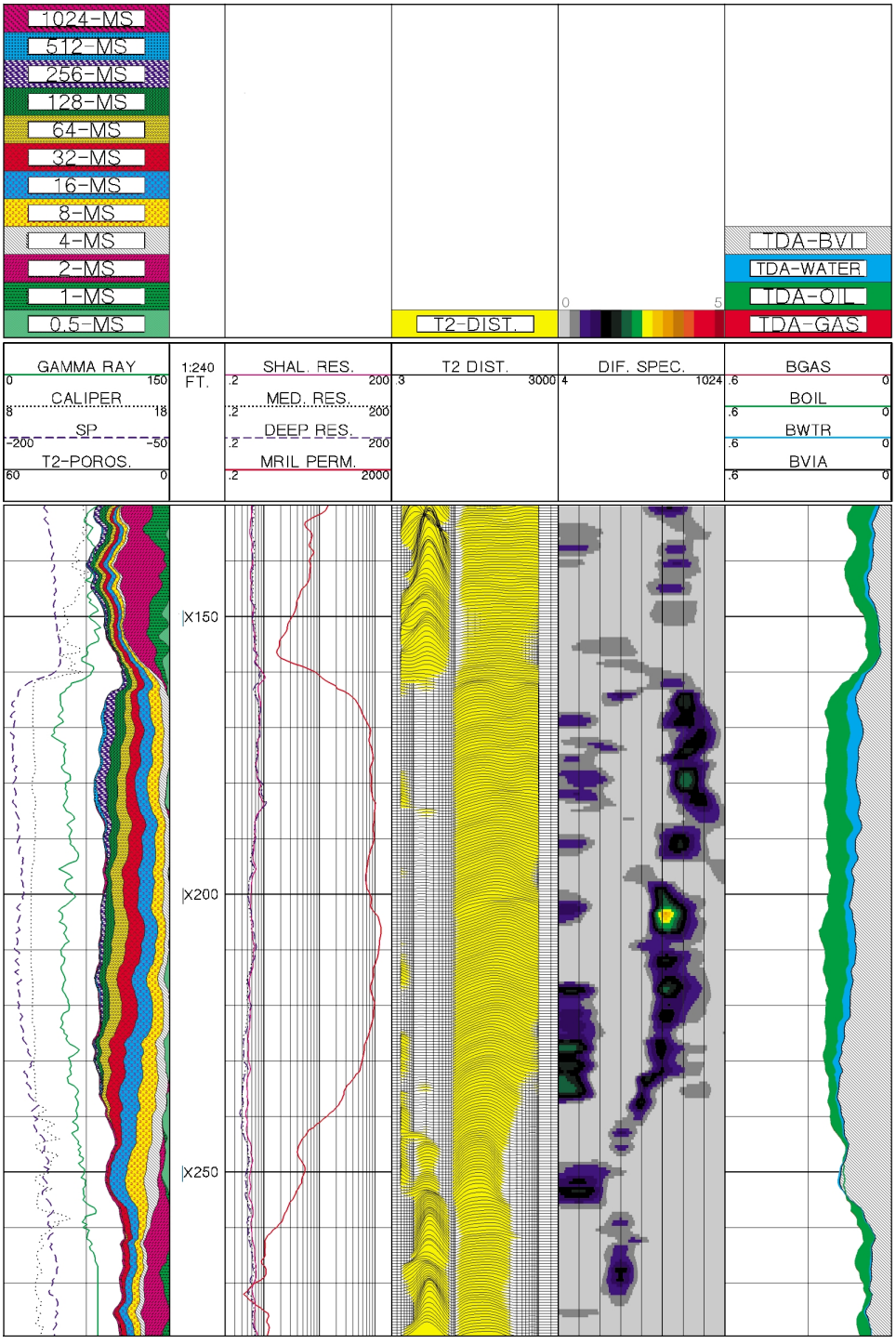

Figure 1.15—Through the subtraction of echo trains obtained at two polarization times, light hydrocarbons can be identified. Track 5 displays the differential spectrum obtained from the subtraction of the two separate T_2-distributions derived from echo trains acquired with short and long polarization times, TW_S = 1 s and TW_L = 8 s. The water signals completely cancel while hydrocarbon signals only partially cancel and remain when the two T_2 distributions are subtracted from one another. Track 6 displays the TDA results. Performed in time domain (as opposed to T_2 domain), TDA can quantify up to three phases (gas, light oil, and water; gas and water; or light oil and water). Mud filtrate that flushed the oil constitutes the movable water shown in Track 6.

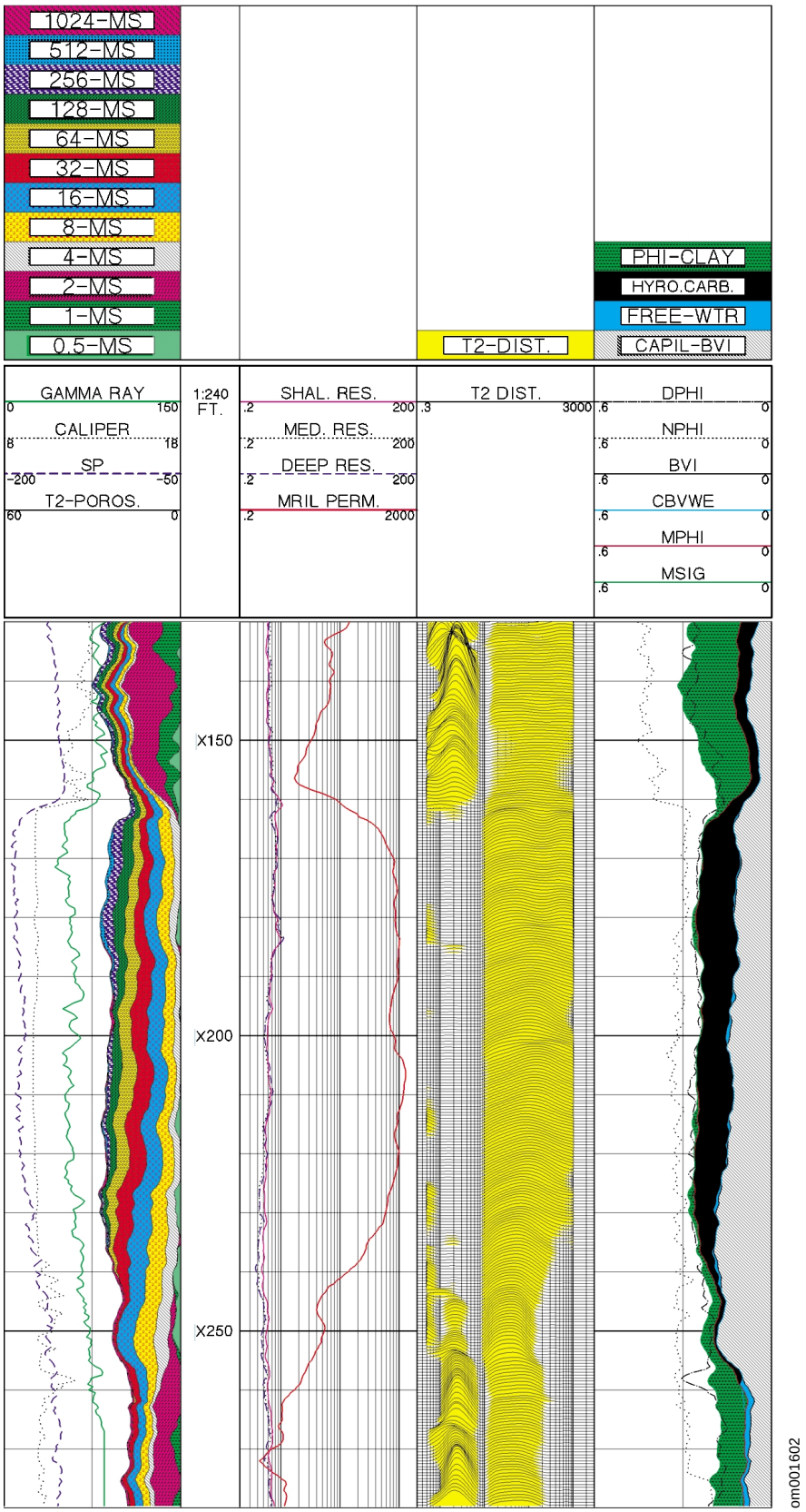

Figure 1.16—The combination of conventional deep-resistivity data with NMR-derived *MCBW*, *BVI*, *MFFI*, and *MPHI* can greatly enhance petrophysical estimations of effective pore volume, water cut, and permeability. The MRIAN analysis results displayed in Track 5 show that the whole interval from X160 to X255 has a *BVI* almost identical to the water saturation interpreted from the resistivity log. This zone will likely produce water-free because of this high *BVI*.

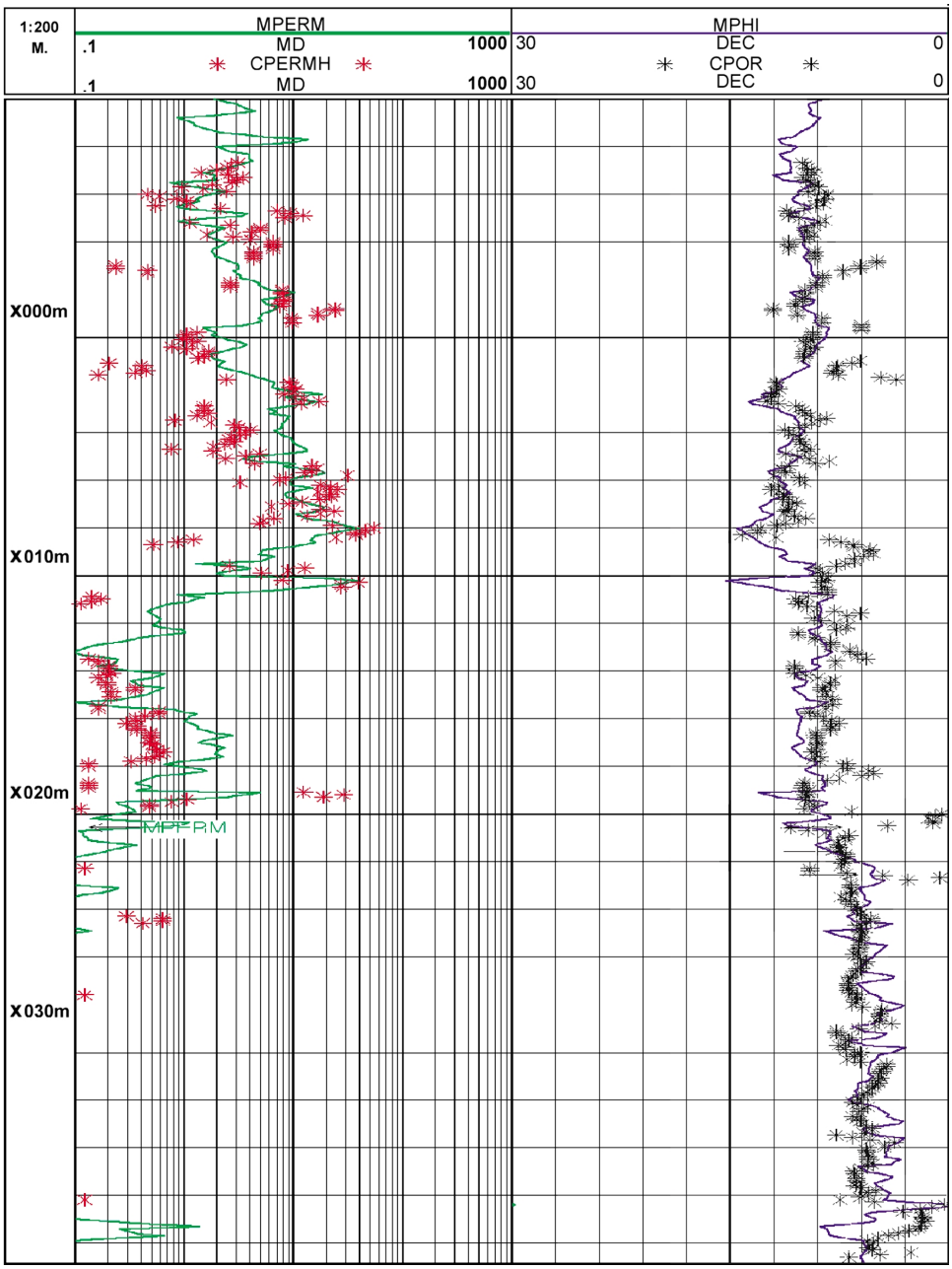

Figure 1.17—These data from a shaly sand formation in Egypt show the good agreement between core data and MRIL porosity and permeability.

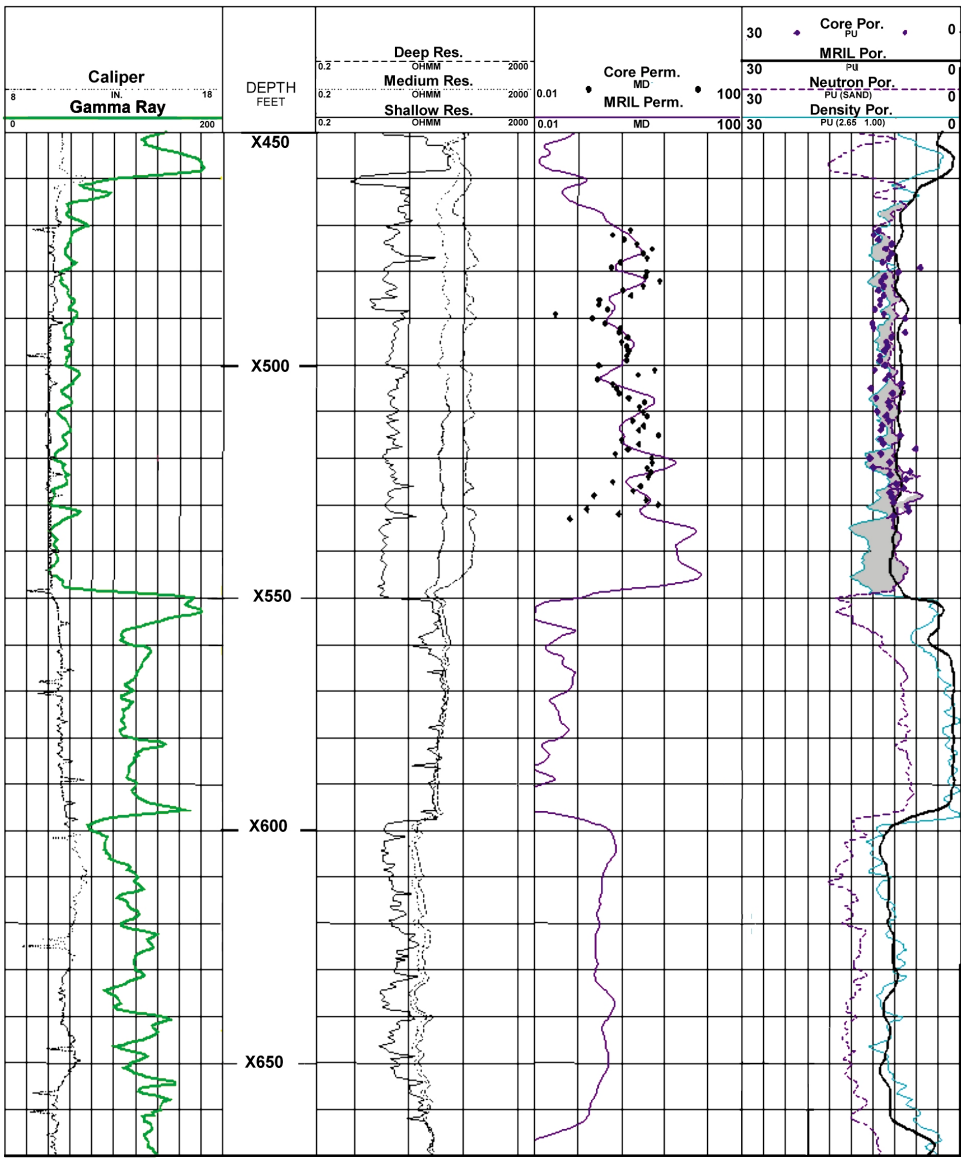

Figure 1.18—This low-porosity, low-permeability example from South Australia shows good agreement between core data and MRIL porosity and permeability.

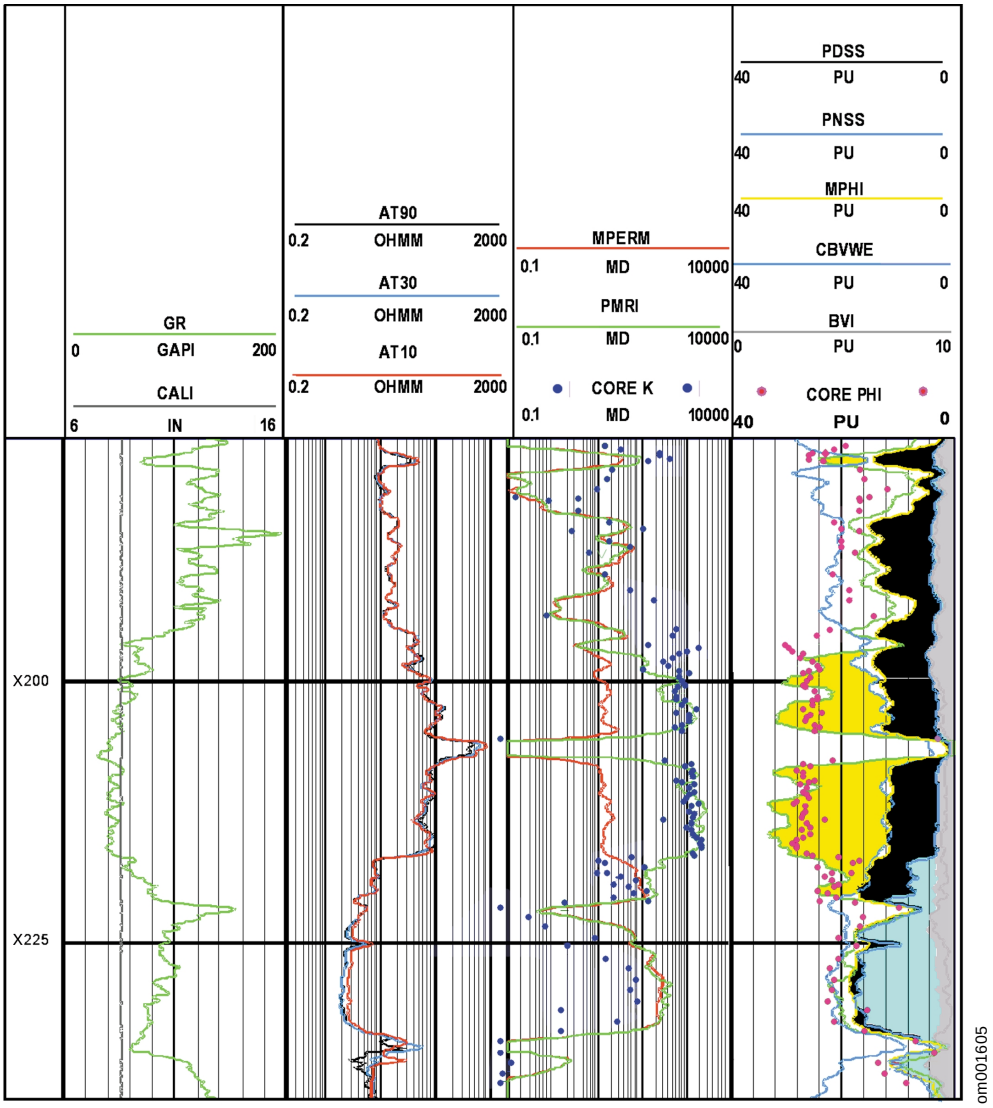

Figure 1.19—In this gas reservoir, MRIL porosity is affected by the hydrogen index of the pore fluids. A corrected porosity, either from another source such as nuclear logs or from *MPHI* after *HI* correction, should be used for permeability calculation.

core porosity is attributed to residual gas in the flushed zone. The MRIL permeability curve was computed using a model customized to this area. The agreement between MRIL permeability and core permeability is very good.

Fig. 1.19 compares core data with MRIL porosity and permeability recorded in a gas reservoir.[23] Track 1 contains gamma ray and caliper logs. Track 2 contains deep- and shallow-reading resistivity logs. Track 3 presents the MRIL-derived permeability and core permeability. Track 4 presents the core porosity, MRIL porosity *MPHI*, neutron and density porosity (based on a sandstone matrix), *BVI* from a model customized to this reservoir, and a bulk volume water (*CBVWE*) from resistivity logs. The MRIL log in this example was acquired with a TW = 10 s, TE = 1.2 ms, and NE = 500, where NE is the number of echoes per echo train.

A gas/water contact at X220 is easily identified on the resistivity logs. Immediately above the contact, a large gas crossover (yellow) is observed between the neutron and density logs. A decrease in MRIL porosity occurs here because of the hydrogen-index effect of the unflushed gas. Accurate data for *BVI* and *MFFI* are important for permeability calculations with the Coates model. The *MPERM* curve in Track 3 was calculated from the Coates model: *MPHI* was used for porosity, and the difference between *MPHI* and *BVI* was used for *MFFI*. Used in this way, the Coates model will give good estimates of permeability when the MRIL porosity is unaffected by gas. In zones where the MRIL porosity is affected by gas, *MPERM* is pessimistic because the difference between *MPHI*, and *BVI* underestimates *MFFI*. In this situation, the difference between *BVI* and the porosity obtained from the nuclear logs gives a better estimate of *MFFI* for calculating permeability The *PMRI* curve was computed in this manner. It is a more reasonable representation of permeability in the gas zones and in this example, matched very well with the core permeability. Below the gas/water contact, MRIL porosity and permeability match core data quite well.

Low-Resistivity Reservoir Evaluation

An interval from a Gulf of Mexico well has been used several times throughout this chapter to illustrate various MRIL measurements (Figs. 1.7, 1.9, 1.12, 1.15, and 1.16). The same well is now discussed in the context of a specific case study.

The reservoir penetrated by the well consists of a massive medium- to fine-grained sandstone formation, which developed from marine shelf sediments. Intense bioturbation is observed within the formation. Air permeability typically ranges between 1 and 200 md, with core porosity varying between 20 and 30 p.u. The upper portion of the reservoir (Zone A) has higher resistivity (approximately 1 ohm-m) than that of the lower reservoir (Zone B, approximately 0.5 ohm-m). The produced hydrocarbons are light oil with viscosity from 1 to 2 cp. The well was drilled with water-based mud. Conventional logs are shown in **Fig. 1.20**. MRIL results from both TDA and MRIAN are illustrated in **Fig. 1.21**.

The operator was concerned about the decrease in resistivity in the lower portion of the reservoir. The question was whether the decrease was due to textural changes (smaller grain sizes, in which case the well might produce free of water) or to an increase in the volume of movable water. The ability to reliably answer this question could have significant implications on reserve calculations, well-completion options, and future field-development decisions. An additional piece of key information for this type of reservoir is that the actual cumulative production often far exceeds the initial calculated recoverable reserves based on a water-saturation cutoff of 60%. If the entire zone in question were actually at irreducible water saturation, then the total net productive interval could be increased from 25 to 70 ft. The resulting increase in net hydrocarbon pore volume would be more than 200%, and expected recoverable reserves would increase significantly.

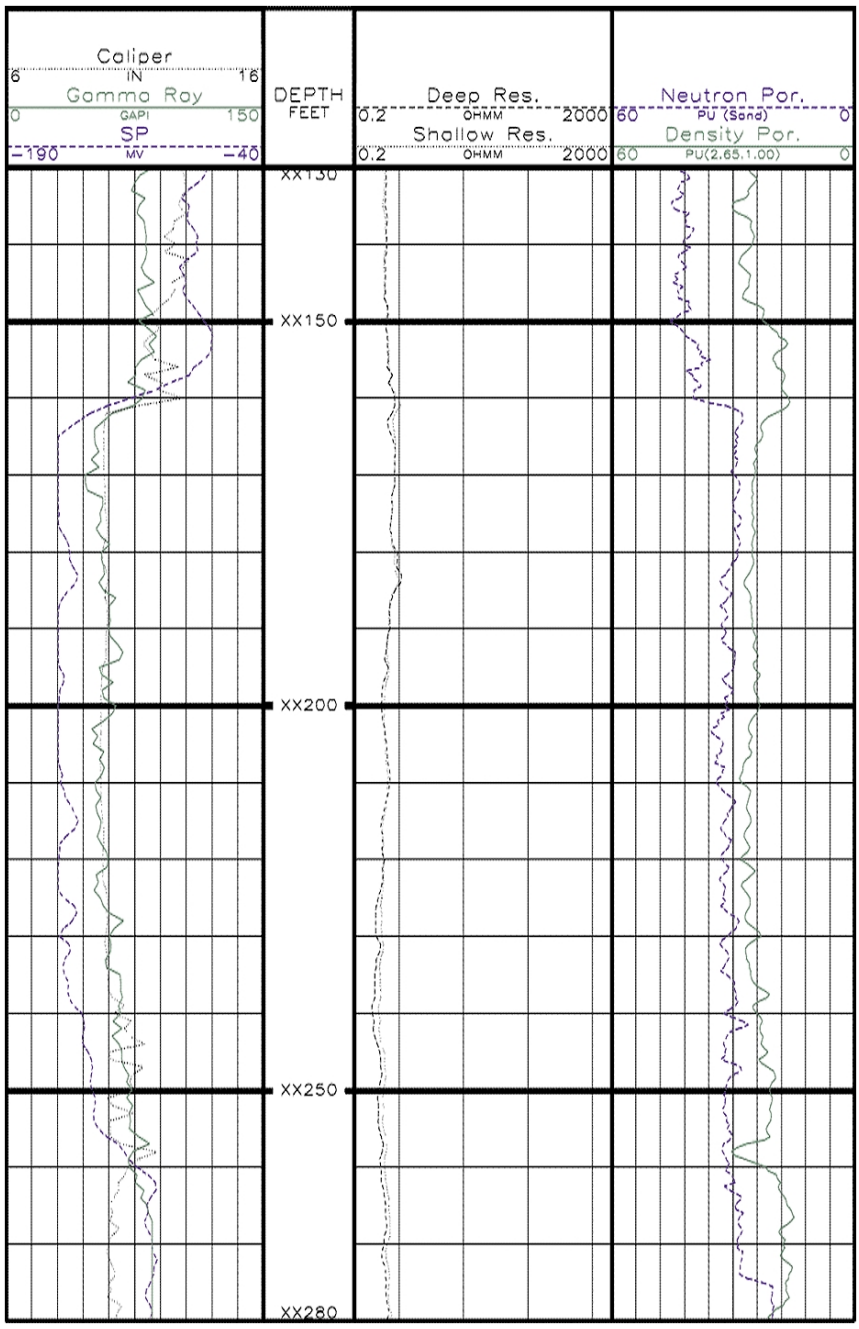

Figure 1.20—Conventional logs (SP, resistivity, and neutron/density) suggested that the upper part of the sand (XX160 to XX185) would possibly produce with high water cut, but that the lower part of the sand (XX185 to XX257) is probably wet.

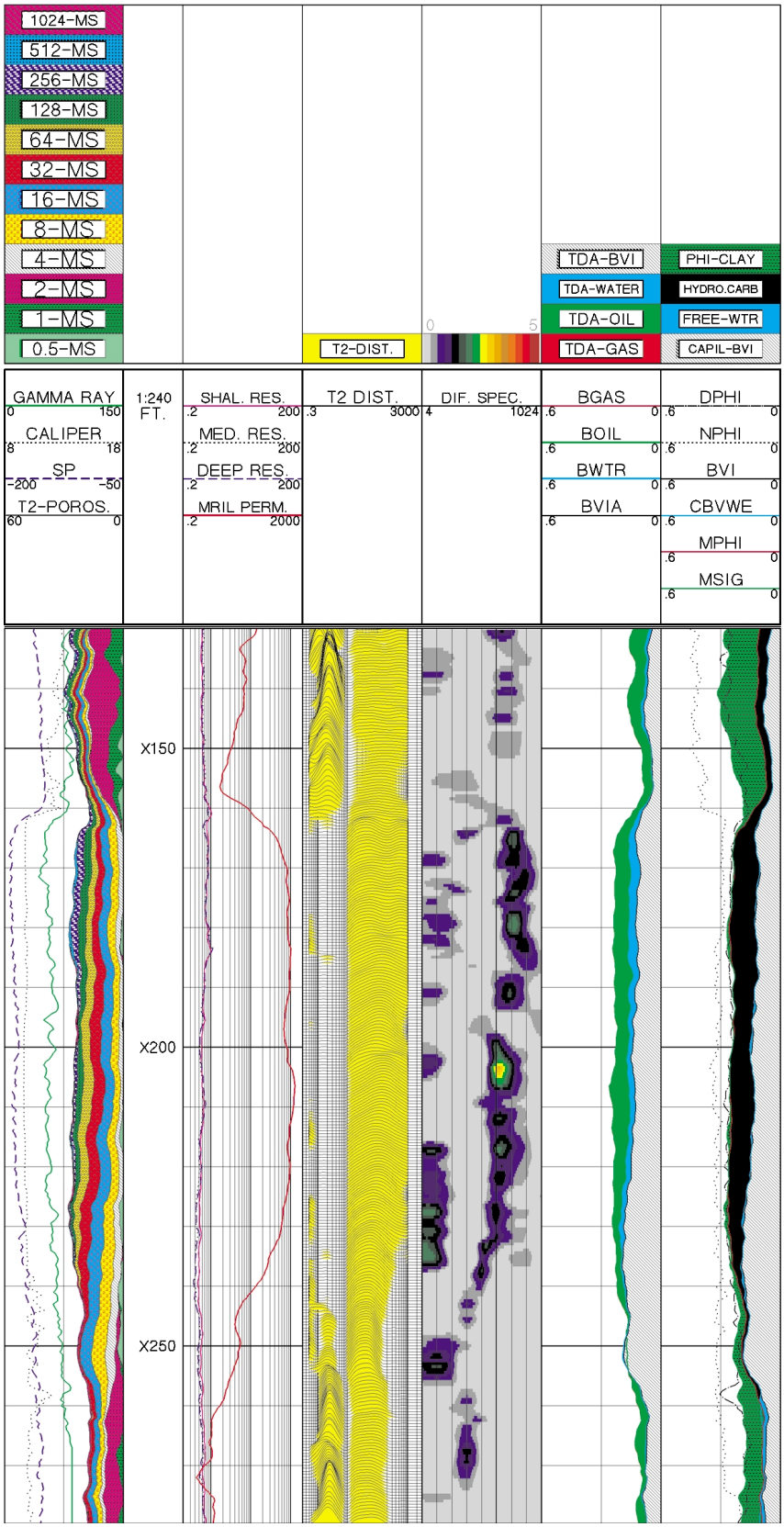

Figure 1.21—MRIL data were acquired in the well of Fig. 1.20 and were used in DSM, TDA, and MRIAN analyses. The MRIAN results (Track 7) indicate that both the upper and lower intervals have high water saturation, but that the formation water is at irreducible conditions. Thus, the zone should not produce any formation water. The entire zone has permeability in excess of 100 md (Track 2). The TDA analysis (Track 6) determined oil saturation in the flushed zone to be in the 35 to 45% range. With this information, the operator perforated the entire interval and recorded an initial production rate of 2,000 BOPD with no water influx.

MRIL logs were incorporated into the logging suite for two principal reasons:

1. To distinguish zones of likely hydrocarbon production from zones of likely water production by establishing the bulk volume of irreducible water (*BVI*) and the volume of free fluids (*MFFI*).
2. To improve the estimation of recoverable reserves by defining the producible interval

The MRIL data acquired in this well were to include total porosity to determine clay-bound water, capillary-bound water, and free fluids. Dual-*TW* logging was to be used to distinguish and quantify hydrocarbons.

The MRIL data in Fig. 1.21 helped determine that the resistivity reduction was due to a change in grain size and not to the presence of movable water. The two potential types of irreducible water that can cause a reduction in measured resistivity are clay-bound water (whose volume is designated by *MCBW*) and capillary-bound water (whose volume is indicated by *BVI*). The MRIL clay-bound-water measurement (Track 3) indicates that the entire reservoir has very low *MCBW*. The MRIL *BVI* curve (Track 7) indicates a coarsening-upward sequence (*BVI* increases with depth). The increase in *BVI* and the corresponding reduction in resistivity are thus attributed to the textural change. Results of the TDA (Track 6) and TDA/MRIAN (Track 7) combination analysis imply that the entire reservoir contains no significant amount of movable water and is at irreducible condition.

Based on these results, the operator perforated the interval from XX163 to XX234. The initial production of 2,000 BOPD was water-free and thus confirmed the MRIL analysis.

A difference can be found between the TDA and TDA/MRIAN results in Fig. 1.21. The TDA shows that the free fluids include both light oil and water, whereas the TDA/MRIAN results show that all of the free fluids are hydrocarbons. This apparent discrepancy is simply due to the different depth of investigation of different logging measurements. TDA saturation reflects the flushed zone as seen by MRIL measurement. The TDA/MRIAN combination saturation reflects the virgin zone as seen by deep-resistivity measurements. Because water-based mud was used in this well, some of the movable hydrocarbons are displaced in the invaded zone by the filtrate from the water-based mud.

MRIL Acquisition Data Sets

The unique capacity of the MRIL logging tool to measure multiple quantities needed for prospect evaluation and reservoir modeling depends on making multiple NMR measurements on the “same” rock volume using different activations. These different activations can usually be used during the same logging run with a multiple-frequency tool such as the MRIL Prime.[2] Three general categories of activation sets are in common use: total porosity, dual *TW*, and dual *TE*.

A total-porosity activation set acquires two echo trains to obtain the total porosity *MSIG*. To acquire one of the echo trains, the tool uses *TE* = 0.9 or 1.2 ms and a long *TW* to achieve complete polarization. This echo train provides the “effective porosity” *MPHI*. To acquire the second echo train, the tool uses *TE* = 0.6 ms and a short *TW* that is only long enough to achieve complete polarization of the fluids in the small pores. The second echo train is designed to provide the porosity *MCBW* contributed by pores of the same size as clay pores.[16]

A dual-*TW* activation is primarily used to identify light hydrocarbons (gas and light oil). Typically, measurements are made with *TW* = 1 and 8 s, and *TE* = 0.9 or 1.2 ms. The water signal is contained in both activations, but light hydrocarbons (which have long T_1 values)

have a greatly suppressed signal in the activation with TW = 1 s. The presence of a signal in the difference of the measurements is a very robust indicator of gas or light oils.[37]

A dual-TE activation is primarily used to identify the presence of viscous oil, which has a small diffusion constant relative to water. This type of activation set has a long TW and has TE values of 0.9 or 1.2 ms and 3.6 or 4.8 ms. For this set, the fluid with the larger diffusion constant (water) has a spectrum shifted more to earlier times than the fluid with the smaller diffusion constant (viscous oil). The presence in the spectra of a minimally shifted portion identifies high-viscosity oil in the formation.[38, 39]

MRIL Response in Rugose Holes

As shown in **Fig. 1.22**, an MRIL tool responds to the materials in a series of cylindrical shells, each approximately 1 mm thick. Borehole or formation materials outside these shells have no influence on the measurements, a situation similar to medical MRI. Hence, if the MRIL tool is centralized in the wellbore, and the diameter of any washout is less than the diameter of the inner sensitive shell, then the MRIL tool will respond solely to the NMR properties of formation. In other words, borehole rugosity and moderate washouts will not affect MRIL measurements. **Fig. 1.23** provides an example of an MRIL log run in a rugose borehole.

The diameters of the response shells for an MRIL tool are dependent on operating frequency and tool temperature. For an MRIL tool, the highest frequency of operation is 750 kHz, which corresponds to a diameter of investigation of approximately 16 in. at 100°F. At the lowest operating frequency of 600 kHz, the diameter of investigation is about 18 in. at 100°F. Charts that illustrate the dependence of the depth of investigation on operating frequency and tool temperature have been published.[40, 41]

NMR Logging Applications Summary

Case studies and theory have shown that MRIL tools furnish powerful data for

- distinguishing low-resistivity/low-contrast pay zones
- evaluating complex-lithology oil and/or gas reservoirs
- identifying medium-viscosity and heavy oils
- studying low-porosity/low-permeability formations
- determining residual oil saturation
- enhancing stimulation design

In particular, NMR data provide the following valuable information:

- mineralogy-independent porosity
- porosity distribution, complete with a pore-size distribution in water-saturated formations
- bulk volume irreducible and free fluid when a reliable $T_{2cutoff}$ value is available

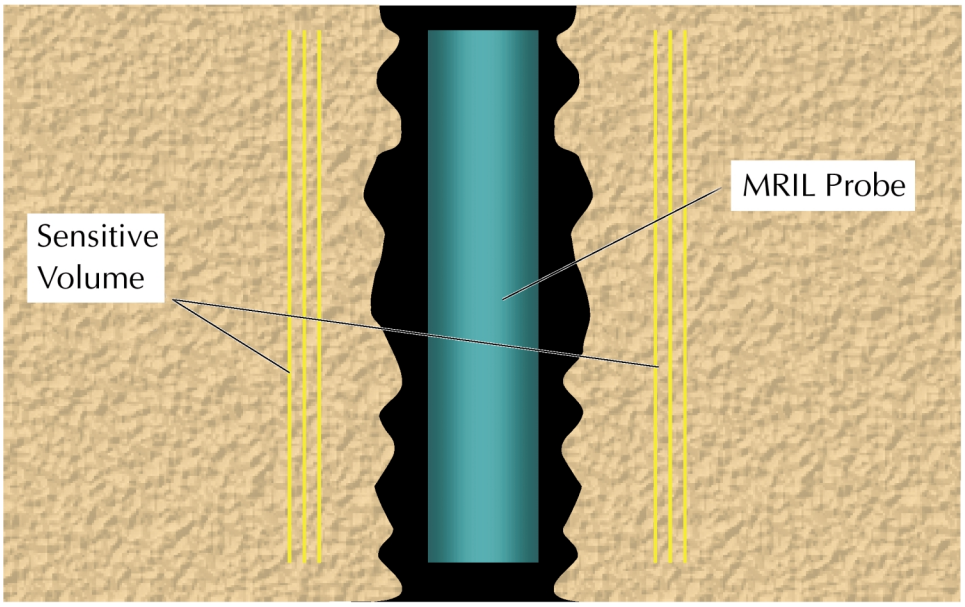

om000834

Figure 1.22—The depth of investigation of an MRIL tool is about 18 in. when operating at low frequency and about 16 in. at high frequency. Thus, in a 12-in. borehole, rugosity with an amplitude smaller than 2 in. will not affect the MRIL signal.

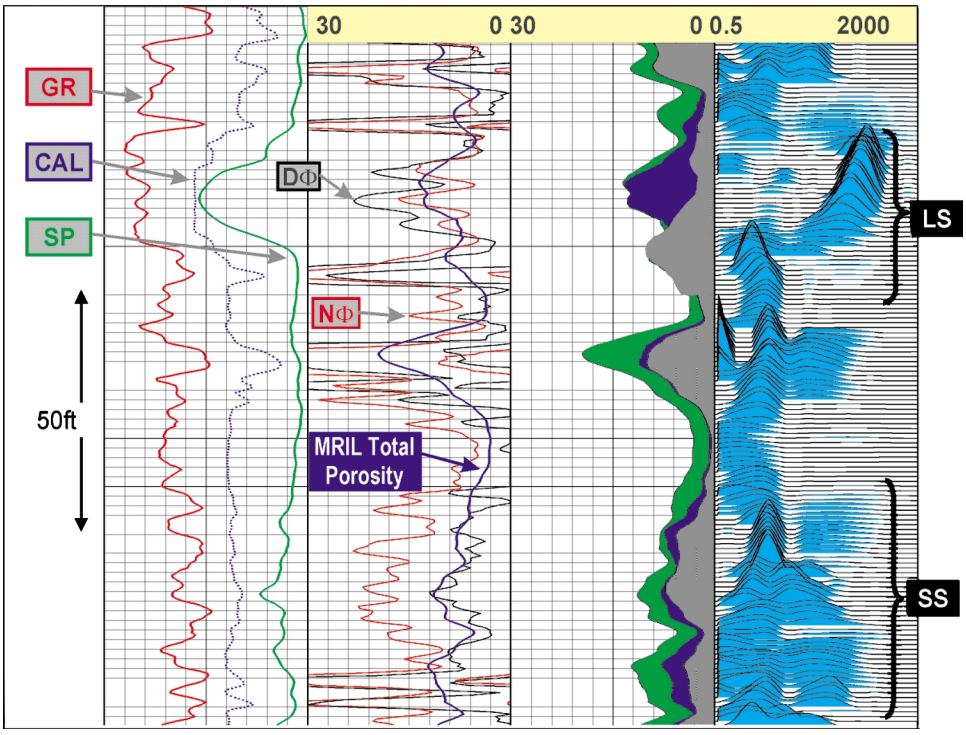

om001608

Figure 1.23—An MRIL tool can often provide reliable data in highly rugose holes where traditional porosity logs cannot. In this example, both neutron and density measurements are very sensitive to rugosity, and only the MRIL tool provides the correct porosity. Additionally, because MRIL porosity is lithology-independent, the change from limestone in an upper zone on the displayed log to sandstone in a lower zone has no effect on the accuracy of the MRIL porosity values. An MRIL-Prime tool was run at a logging speed of 24 ft/min to acquire these data.

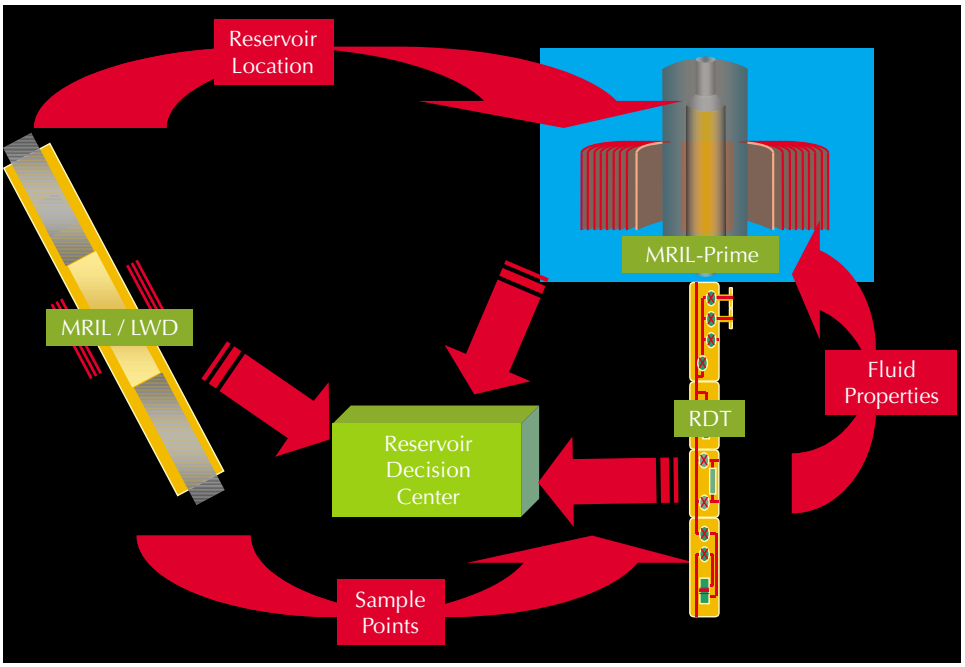

Figure 1.24—The LWD NMR device provides information for locating the reservoir while drilling. The MRIL-Prime furnishes information for producibility analysis after invasion has occurred. The RDT NMR device yields information for determining fluid NMR properties at reservoir conditions.

- permeability, determined from the free-fluid index and the bulk volume irreducible or average T_2
- hydrocarbon typing through the use of (1) T_1-weighted contrasts for water, gas, and/or light oil, (2) diffusivity-weighted contrasts for water and viscous oil, and (3) NMR enhanced water saturation calculations for the virgin zone

Although this monograph primarily addresses NMR wireline logging, NMR tools are also used in other parts of the prospecting and reservoir-characterization process. These tools include a logging-while-drilling (LWD) NMR tool for early reservoir identification and properties estimation, and an NMR device built into a reservoir description tool (RDT™), advanced formation testing and fluid-sampling device. The LWD tool uses the same principles as the MRIL tool, but provides information earlier and on uninvaded rocks. The RDT device provides fluid-property information at downhole reservoir conditions. All of the information from the LWD NMR tool, the MRIL tool, and the RDT NMR device can then be integrated at a reservoir decision center to give a more complete analysis. **Fig. 1.24** provides a schematic of this process.

References

1. Coates, G.R., et al., 1991, The MRIL in Conoco 33-1—an investigation of a new magnetic resonance imaging log, paper DD, *32nd Annual SPWLA Logging Symposium Transactions*, 24 p.
2. Prammer, M.G., et al., 1998, A new multiband generation of NMR logging tools, SPE 49011, *1998 SPE Annual Technical Conference and Exhibition Proceedings*, p. 237–243.

3. Vinegar, H.J., 1986, X-ray CT and NMR imaging of rocks, SPE 15277, *Journal of Petroleum Technology*, v. 38, no. 3, p. 257–259. Later reprinted in 1994 in *Petrophysics*, SPE Reprint Series No. 39, p. 115–117.

4. Hearst, J.R., and Nelson, P.H., 1985, *Well Logging for Physical Properties*, McGraw-Hill Book Company, New York.

5. Bassiouni, Z., 1994, *Theory, Measurement, and Interpretation of Well Logs*, SPE Textbook Series, v. 4.

6. Miller, M.N., et al., 1990, Spin-echo magnetic-resonance logging—porosity and free-fluid index, SPE 20561, *1990 SPE Annual Technical Conference and Exhibition Proceedings*, v. Ω (Formation evaluation and reservoir geology), p. 321–334.

7. Akkurt, R., et al., 1995, NMR logging of natural gas reservoirs, paper N, *36th Annual SPWLA Logging Symposium Transactions*, 12 p. Also published in 1996 in *The Log Analyst*, v. 37, no. 5, p. 33–42.

8. Prammer, M.G., et al., 1995, Lithology-independent gas detection by gradient-NMR logging, SPE 30562, *1995 SPE Annual Technical Conference and Exhibition Proceedings*, v. Ω (Formation evaluation and reservoir geology), p. 325–336.

9. Moore, M.A., and Akkurt, R., 1996, Nuclear magnetic resonance applied to gas detection in a highly laminated Gulf of Mexico turbidite invaded with synthetic oil filtrate, SPE 36521, *1996 SPE Annual Technical Conference and Exhibition Proceedings*, v. Ω (Formation evaluation and reservoir geology), p. 305–310.

10. Mardon, D., et al., 1996, Characterization of light hydrocarbon-bearing reservoirs by gradient NMR well logging—a Gulf of Mexico case study, SPE 36520, *1996 SPE Annual Technical Conference and Exhibition Proceedings*, v. Ω (Formation evaluation and reservoir geology), p. 295–304. Also published in 1996 in condensed form in *Journal of Petroleum Technology*, v. 48, no. 11, p. 1035–1036.

11. Looyestijn, W., 1996, Determination of oil saturation from diffusion NMR logs, paper SS, *37th Annual SPWLA Logging Symposium Transactions*, 14 p.

12. Morriss, C.E., et al., 1994, Hydrocarbon saturation and viscosity estimation from NMR logging in the Belridge diatomite, paper C, *35th Annual SPWLA Logging Symposium Transactions*, 24 p. Later published in 1997 in *The Log Analyst*, v. 38, no. 2, p. 44–59.

13. Brownstein, K.R., and Tarr, C.E., 1979, Importance of classical diffusion in NMR studies of water in biological cells, *Physical Review*, Series A, v. 19, p. 2446–2453.

14. Prammer, M.G., 1994, NMR pore size distributions and permeability at the well site, SPE 28368, *1994 SPE Annual Technical Conference and Exhibition Proceedings*, v. Ω (Formation evaluation and reservoir geology), p. 55–64.

15. Sandor, R.K.J., and Looyestijn, W.J., 1995, NMR logging—the new measurement, Shell International Petroleum Maatschappij, The Hague, The Netherlands, 8 p.

16. Prammer, M.G., et al., 1996, Measurements of clay-bound water and total porosity by magnetic resonance logging, SPE 36522, *1996 SPE Annual Technical Conference and Exhibition Proceedings*, v. Ω (Formation evaluation and reservoir geology), p. 111–118. Also published in 1996 in *The Log Analyst*, v. 37, no. 5, p. 61–69.

17. Murphy, D.P., 1995, NMR logging and core analysis—simplified, *World Oil*, v. 216, no. 4, p. 65–70.

18. Cherry, R., 1997, Magnetic resonance technology and its applications in the oil and gas industry, part 1, *Petroleum Engineer International*, v. 70, no. 3, p. 29–35.

19. Marschall, D., 1997, Magnetic resonance technology and its applications in the oil and gas industry, part 2, *Petroleum Engineer International*, v. 70, no. 4, p. 65–70.

20. Xiao, L.Z., 1998, *NMR Imaging Logging Principles and Applications* (in Chinese), Science Press, Beijing.

21. Fukushima, E., and Roeder, S.B.W., 1981, *Experimental Pulse NMR: A Nuts and Bolts Approach*, Addison-Wesley Publishing Company, Advanced Book Program, Reading, Massachusetts, U.S.A.

22. Kenyon, W.E., 1992, Nuclear magnetic resonance as a petrophysical measurement, *Nuclear Geophysics*, v. 6, no. 2, p. 153-171. Later revised and published in 1997 under the title, Petrophysical principles of applications of NMR logging, in *The Log Analyst*, v. 38, no. 2, p. 21–43.

23. Coates, G., et al., 1997, A new characterization of bulk-volume irreducible using magnetic resonance, paper QQ, *38th Annual SPWLA Logging Symposium Transactions*, 14 p. Also published in 1997 in *DiaLog* (London Petrophysical Society), v. 5, no. 6, p. 9–16. Later revised and published in *The Log Analyst*, v. 39, no. 1, p. 51–63.

24. Timur, A., 1967, Pulsed nuclear magnetic resonance studies of porosity, movable fluid and permeability of sandstones, SPE 2045, 42nd Annual Meeting preprint, SPE. Later published in 1969 in *Journal of Petroleum Technology*, v. 21, no. 6, p. 775–786.

25. Timur, A., 1968, An investigation of permeability, porosity, and residual water saturation relationships for sandstone reservoirs, paper J, *9th Annual SPWLA Logging Symposium Transactions*, 18 p. Later published in 1968 in *The Log Analyst*, v. 9, no. 4, July-August, p. 8–17. Later reprinted in 1994 in *Petrophysics*, SPE Reprint Series No. 39, p. 128-137.

26. Timur, A., 1968, Effective porosity and permeability of sandstones investigated through nuclear magnetic principles, paper K, *9th Annual SPWLA Logging Symposium Transactions*, 18 p. Later published in 1969 in *The Log Analyst*, v. 10, no. 1, January-February, p. 3–11.

27. Ahmed, U., Crary, S.F., and Coates, G.R., 1989, Permeability estimation; the various sources and their interrelationship, SPE 19604, *1989 SPE Annual Technical Conference and Exhibition Proceedings*, v. Ω (Formation evaluation and reservoir geology), p. 649–662. Later published in 1990 under the title, The interrelationship between various permeability measurements, paper I, *1990 International Well Logging Symposium Transactions*, SPWLA, Beijing Chapter, 21 p. Later published in 1991 in *Journal of Petroleum Technology*, v. 43, no. 5, p. 578–587. Later reprinted in 1994 in *Petrophysics*, SPE Reprint Series No. 39, p. 118–127.

28. Allen, D., et al., 1988, Probing for permeability—An introduction of measurements, *The Technical Review*, v. 36, no. 1, p. 6–20.

29. Thompson, A., Katz, A.J., and Krohn, C.E., 1987, The microgeometry and transport properties of sedimentary rock, *Advances in Physics*, Vol. 36.

30. Marschall, D., Gardner, J., and Curby, F.M., 1997, MR laboratory measurements—requirements to assure successful measurements that will enhance MRI log interpretation, paper SCA 9704, *1997 International Symposium Proceedings*, SPWLA, Society of Core Analysts Chapter-at-Large, 12 p.

31. Morriss, C.E., et al., 1994, Hydrocarbon saturation and viscosity estimation from NMR logging in the Belridge diatomite, paper C, *35th Annual SPWLA Logging Symposium Transactions*, 24 p. Later published in 1997 in *The Log Analyst*, v. 38, no. 2, p. 44–59.

32. Kleinberg, R.L., and Vinegar, H.J., 1996, NMR properties of reservoir fluids, *The Log Analyst*, v. 37, no. 6, p. 20–32.

33. Gerritsma, C.J., Oosting, P.H., and Trappeniers, N.J., 1971, Proton spin-lattice relaxation and self-diffusion in methane, part 2—Experiemental results for proton spin-lattice relaxation times, *Physica*, v. 51, p. 381–394.

34. Gerritsma, C.J., and Trappeniers, N.J., 1971, Proton spin-lattice relaxation and self-diffusion in methanes, part 1, Spin-echo spectrometer and preparation of the methane samples, *Physica*, v. 51, p. 365–380.

35. Akkurt, R., Moore, A., and Freeman, J., 1997, Impact of NMR in the development of a deepwater turbidite field, paper SS, *38th Annual SPWLA Logging Symposium Transactions*, 14 p.

36. Coates, G.R., Gardner, J.S., and Miller, D.L., 1994, Applying pulse-echo NMR to shaly sand formation evaluation, paper B, *35th Annual SPWLA Logging Symposium Transactions*, 22 p.

37. Akkurt, R., Prammer, M., and Moore, A., 1996, Selection of optimal acquisition parameters for MRIL logs, paper TT, *37th Annual SPWLA Logging Symposium Transactions*, 13 p. Later published in 1996 in *The Log Analyst*, v. 37, no. 6, p. 43–52.

38. Akkurt, R., et al., 1998, Enhanced diffusion: expanding the range of NMR direct hydrocarbon-typing applications, paper GG, *39th Annual SPWLA Logging Symposium Transactions*, 14 p.

39. Akkurt, R., et al., 1998, Determination of residual oil saturation using enhanced diffusion, SPE 49014, *1998 SPE Annual Technical Conference and Exhibition Proceedings*, v. Ω (Formation evaluation and reservoir geology), 11 p.

40. Chandler, R.N., et al., 1994, Improved log quality with a dual-frequency pulsed NMR tool, SPE 28365, *1994 SPE Annual Technical Conference and Exhibition Proceedings*, v. Ω (Formation evaluation and reservoir geology), p. 23–35.

41. *MRIL Operation Manual*, Halliburton, 1998.

Chapter 2

NMR Physics

The physical principles on which NMR logging is based are complex. However, NMR logging measurements and NMR log interpretation can be understood with a knowledge of a few basic NMR concepts. These concepts include nuclear magnetism, polarization, T_1 relaxation time, pulse tipping, free induction decay, spin echoes, T_2 relaxation time, and CPMG pulse sequences. This chapter is devoted to a discussion of these concepts. More complete and advanced discussions of the basics of NMR physics are found in the textbooks referenced at the end of the chapter.

Nuclear Magnetism

Nuclear magnetic resonance (NMR) refers to the response of atomic nuclei to magnetic fields. Many nuclei have a net magnetic moment and angular momentum or spin. In the presence of an external magnetic field, an atomic nucleus precesses around the direction of the external field in much the same way a gyroscope precesses around the earth's gravitational field. When these spinning magnetic nuclei interact with the external magnetic fields, measurable signals can be produced.

NMR measurements can be made on any nucleus that has an odd number of protons or neutrons or both, such as the nucleus of hydrogen (^{1}H), carbon (^{13}C), and sodium (^{23}Na). For most of the nuclei found in earth formations, the nuclear magnetic signal induced by external magnetic fields is too small to be detected with a borehole NMR logging tool. However, hydrogen, which has only one proton and no neutrons, is abundant in both water and hydrocarbons, has a relatively large magnetic moment, and produces a strong signal. To date, almost all NMR logging and NMR rock studies are based on responses of the nucleus of the hydrogen atom. For this reason, sometimes the word "nuclear" is dropped from "nuclear magnetic resonance," and instead "magnetic resonance" (MR) logging or "magnetic resonance imaging" (MRI) logging is used. This text will concentrate on proton (i.e., hydrogen) NMR.

The nucleus of the hydrogen atom is a proton, which is a small, positively charged particle with an associated angular momentum or spin. The spinning proton represents a current loop that generates a magnetic field (or magnetic moment) with two poles (north and south) aligned with the spin axis. Therefore, the hydrogen nucleus can be

considered as a bar magnet whose magnetic axis is aligned with the spin axis of the nucleus, as illustrated in **Fig. 2.1** (left). When many hydrogen atoms are present and no external magnetic field exists, the hydrogen nuclear spin axes are randomly aligned, as seen in Fig. 2.1 (right).

Polarization

The first step in making an NMR measurement is to align magnetic nuclei with a static magnetic field, $\mathbf{B}_0$. When $\mathbf{B}_0$ is applied to a magnetic nucleus, $\mathbf{B}_0$ exerts a torque on the nucleus that acts to align the nuclear spin axis with $\mathbf{B}_0$.

When a torque is applied to a spinning object, the axis of the object moves perpendicular to the torque in a motion called precession, as illustrated in **Fig. 2.2** (left). Thus, when $\mathbf{B}_0$ is applied to a magnetic nucleus, the nucleus will precess around $\mathbf{B}_0$. The precessional frequency (f), called the Larmor frequency, is given by

$$f = \frac{\gamma B_0}{2\pi} \tag{2.1}$$

where γ is the gyromagnetic ratio, which is a measure of the strength of the nuclear magnetism. For hydrogen, $\gamma/2\pi$ = 42.58 MHz/tesla. Other nuclei have other γ values.[1]

Equation 2.1 shows that the Larmor frequency of a given nucleus is proportional to the magnitude of the static magnetic field and to the gyromagnetic ratio of the given nucleus. For a given magnetic field, different nuclear species have different Larmor frequencies (because of their different gyromagnetic ratios); therefore, the various species can be differentiated on the basis of these frequencies.

Alternatively, for a given nuclear species, such as hydrogen, the gyromagnetic ratio has a fixed value, and according to Eq. 2.1, the Larmor frequency is a function of the strength of the static magnetic field. If the strength of the magnetic field is position-dependent, then the

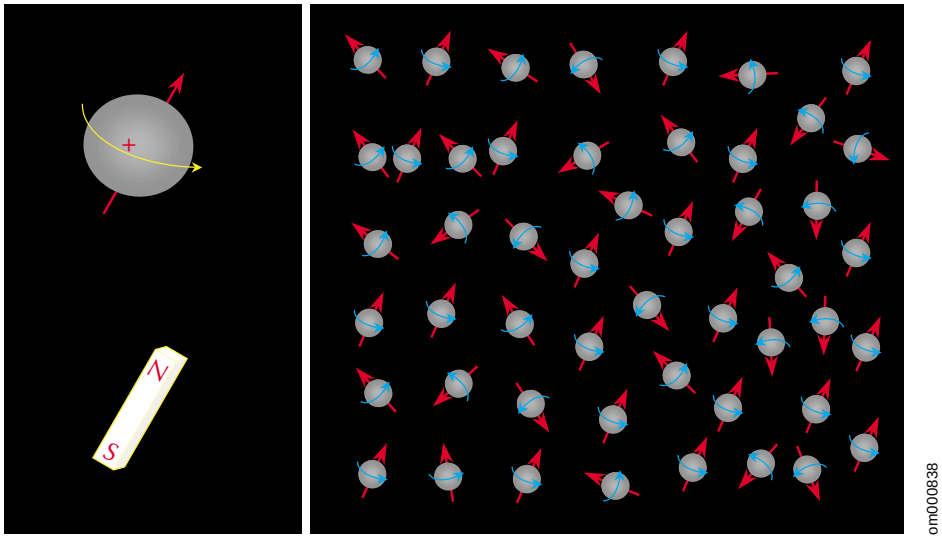

Figure 2.1—Because of their inherent nuclear magnetism, hydrogen nuclei (left) behave as though they are tiny bar magnets aligned with the spin axes of the nuclei. In the absence of an external magnetic field, the nuclear magnetic axes (right) are randomly aligned.

Larmor frequency associated with the nucleus is a function of the position of the nucleus. This observation is fundamental to medical MRI and oilfield MRIL measurements.

With both medical MRI and oilfield MRIL measurements, a gradient magnetic field is applied. Because the strength of such a field is position-dependent, the Larmor frequency of a nucleus will be a function of the position of the nucleus. In medical MRI, linear gradient fields (mostly pulsed fields) are used to fully map the hydrogen population in three-dimensional (3D) spaces. In the oilfield, the MRIL tool produces a primary static gradient field whose strength is a function of the radial distance from the tool surface.[2] Hence, the location of the spatial region investigated by the tool is determined by the Larmor frequency to which the MRIL tool responds.

According to quantum mechanics, when a proton is subjected to an external magnetic field, the proton is forced into one of two energy states. As indicated in Fig. 2.2 (right), the energy state of a particular proton depends on the orientation of the precessional axis of the proton with respect to the direction of the external field. When the precessional axis is parallel to $\mathbf{B}_0$, the proton is in the low-energy state, which is the preferred state. When the precessional axis is anti-parallel to $\mathbf{B}_0$, the proton is in the high-energy state. The direction of $\mathbf{B}_0$ is designated as the longitudinal direction.

When a large number of spinning protons are precessing about $\mathbf{B}_0$, as illustrated in **Fig. 2.3**, more spins are precessing parallel to $\mathbf{B}_0$ than anti-parallel. The difference between the number of protons aligned parallel and anti-parallel to the $\mathbf{B}_0$ field forms the bulk magnetization $\boldsymbol{M}_0$ that provides the signal measured by NMR and MRI devices.

The macroscopic magnetization $\boldsymbol{M}_0$ is defined as the net magnetic moment per unit volume. For the case of N nuclei per unit volume, the magnetization is given by Curie's Law as[3]

$$\boldsymbol{M}_0 = N\frac{\gamma^2 h^2 I(I+1)}{3(4\pi^2)kT}\mathbf{B}_0 \qquad (2.2)$$

where

k = Boltzman's constant
T = absolute temperature (Kelvin)
h = Planck's constant
I = the spin quantum number of the nucleus

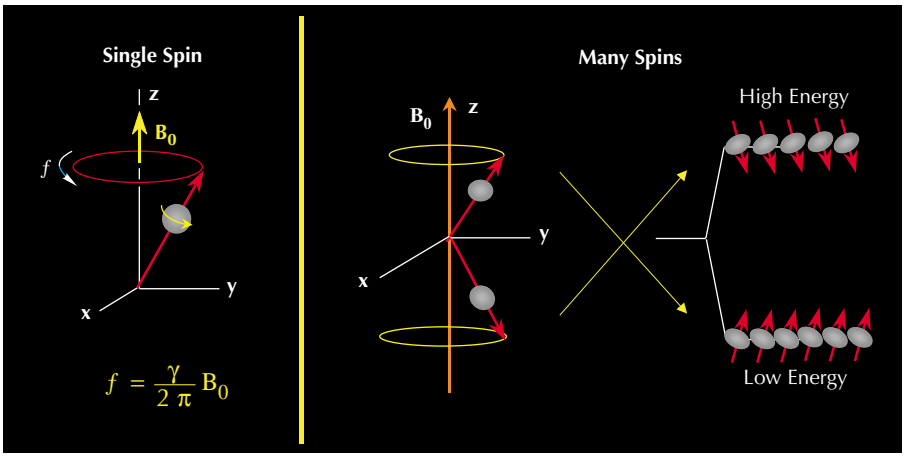

Figure 2.2—In an external magnetic field (left), the precessional frequency of a nucleus depends on the gyromagnetic ratio of the nucleus and the strength of the external field. The alignment of the precessional axis of the nucleus with respect to the direction of the external field (right) determines the energy state of the nucleus.

$\boldsymbol{M_0}$ is observable and, according to Eq. 2.2, is proportional to the number of protons, the magnitude $\mathbf{B_0}$ of the applied magnetic field, and the inverse of the absolute temperature.

After the protons are aligned in the static magnetic field, they are said to be polarized. Polarization does not occur immediately but rather grows with a time constant,[4] which is the longitudinal relaxation time, T_1:

$$M_z(t) = M_0(1 - e^{\frac{-t}{T_1}}) \tag{2.3}$$

where

t	=	the time that the protons are exposed to the $\mathbf{B_0}$ field
$M_z(t)$	=	the magnitude of magnetization at time t, when the direction of $\mathbf{B_0}$ is taken along the z axis
M_0	=	the final and maximum magnetization in a given magnetic field

T_1 is the time at which the magnetization reaches 63% of its final value, and three times T_1 is the time at which 95% polarization is achieved. A T_1 relaxation or polarization curve is illustrated in **Fig. 2.4**. Different fluids, such as water, oil, and gas, have very different T_1 relaxation times.

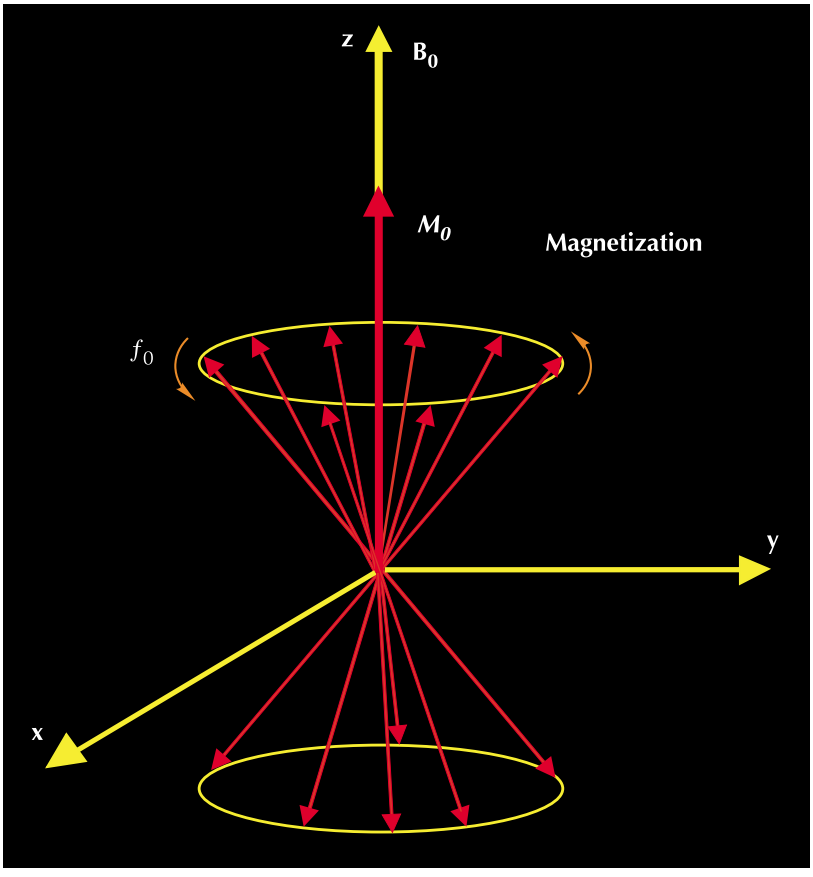

Figure 2.3— When many protons are precessing in an external magnetic field, a net magnetization ($\boldsymbol{M_0}$) will be exhibited.

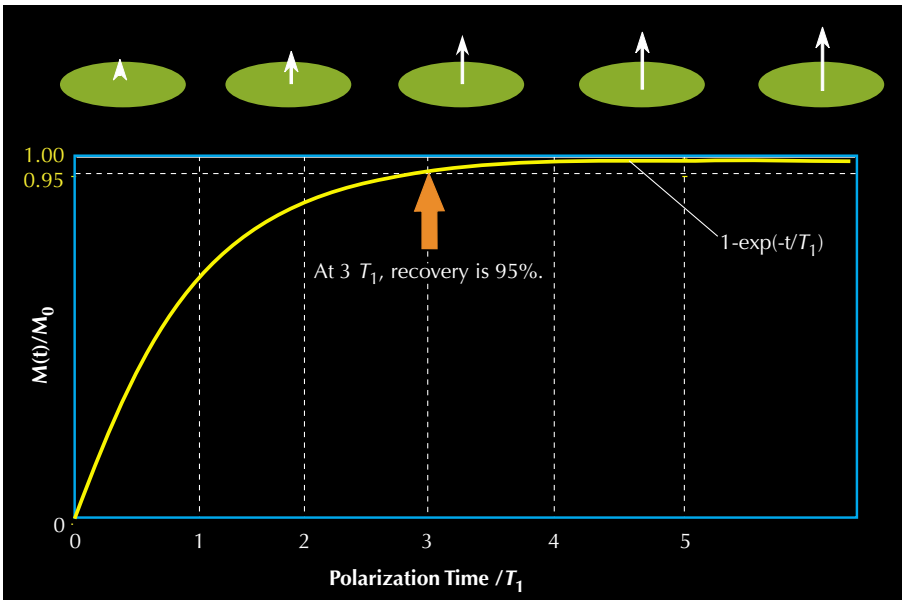

om000841

Figure 2.4— T_1-relaxation (polarization) curves indicate the degree of proton alignment, or magnetization, as a function of the time that a proton population is exposed to an external magnetic field.

Pulse Tipping and Free Induction Decay

The second step in the NMR measurement cycle is to tip the magnetization from the longitudinal direction to a transverse plane. This tipping is accomplished by applying an oscillating magnetic field ($\mathbf{B}_1$) perpendicular to $\mathbf{B}_0$, the static magnetic field. For effective tipping, the frequency of $\mathbf{B}_1$ must equal the Larmor frequency of the protons relative to $\mathbf{B}_0$.

An oscillating magnetic field interacting with protons is illustrated in **Fig. 2.5**. From the quantum mechanics point of view, if a proton is at the low-energy state, it may absorb energy provided by $\mathbf{B}_1$ and jump to the high-energy state. The application of $\mathbf{B}_1$ also causes the protons to precess in phase with one another. This change in energy state and in-phase precession caused by $\mathbf{B}_1$ is called nuclear magnetic resonance.

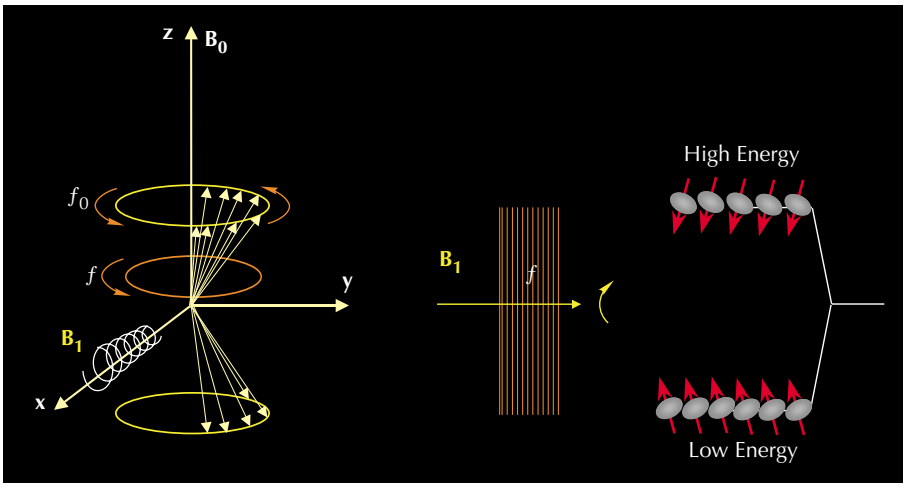

om000844

Figure 2.5—For effective interaction with protons (left), the oscillating magnetic field $\mathbf{B}_1$ must have a substantial component perpendicular to the static field $\mathbf{B}_0$ and must have frequency f equal to the proton's Larmor frequency f_0 in the static field. In this case (right), the protons will precess in phase with one another and may absorb energy from the oscillating field and change to the high-energy state. Nuclear magnetic resonance thus occurs.

On a macroscopic level, resonance results in the tipping of the magnetization, which precesses about $\mathbf{B}_0$ at the Larmor frequency. The angle through which the magnetization is tipped is given by[5,6]

$$\theta = \gamma B_1 \tau \tag{2.4}$$

where

θ = tip angle (degrees)
B_1 = amplitude of the oscillating field
τ = time over which the oscillating field is applied

The tip angle is thus proportional to the product $B_1\tau$, which reflects the energy that $\mathbf{B}_1$ supplies to the proton spin system. Increasing the strength of the oscillating field or increasing the time over which the oscillating field is applied increases the tip angle. The tipping-angle relationship of Eq. 2.4 is illustrated in **Fig. 2.6**.

The $\mathbf{B}_1$ field used in NMR logging is a pulsed oscillating magnetic field. Angular-pulse terms, such as a π pulse (or 180° pulse) and a π/2 pulse (or 90° pulse), refer to the angle through which magnetization is tipped by $\mathbf{B}_1$.

When an NMR tool applies a 90° $\mathbf{B}_1$ pulse to the proton population that the tool has polarized, the protons precess in phase in transverse planes (relative to $\mathbf{B}_0$). Macroscopically, magnetization is tipped 90° and precesses in the transverse plane.

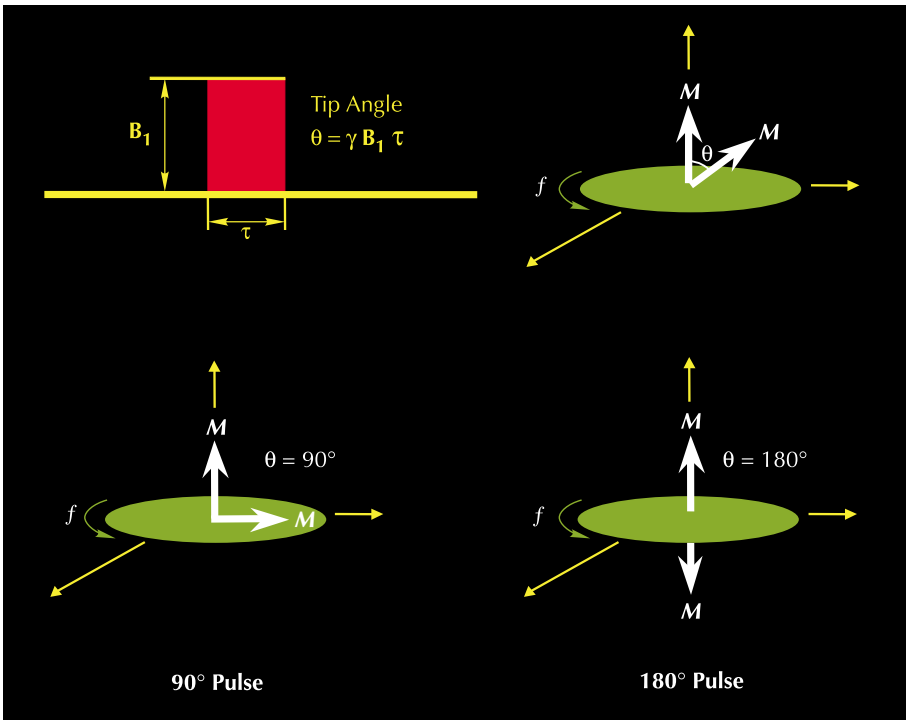

Figure 2.6— The tip angle θ depends on the strength of the oscillating field $\mathbf{B}_1$ and on the time τ over which the field is applied.

When the $\mathbf{B}_1$ field is turned off, the proton population begins to dephase, or lose phase coherency—that is, the precessions of the protons will no longer be in phase with one another. Therefore, as dephasing progresses, the net magnetization decreases. In this situation, a receiver coil that measures magnetization in the transverse direction will detect a decaying signal (**Fig. 2.7**). This decay is usually exponential and is called free induction decay (FID). The FID time constant (T_2*) is very short—a few tens of microseconds. FID is caused by magnetic-field inhomogeneities that are due to the magnetic field gradient and to certain molecular processes that occur in the measured material. Because of the inhomogeneities in the $\mathbf{B}_0$ field, protons at different locations will precess with different Larmor frequencies, thereby producing this very rapid decay.

Spin-Echo Detection

The dephasing caused by the inhomogeneity of the static magnetic field $\mathbf{B}_0$ is reversible. The proton magnetization vectors in the transverse planes can be re-phased when a 180° $\mathbf{B}_1$ pulse is applied. If a transverse magnetization vector has phase angle α, then application of a 180° $\mathbf{B}_1$ pulse will change the phase angle to $-\alpha$. In effect, the phase order of the transverse magnetization vectors is reversed, so that the slower (phasewise) vectors are ahead (phasewise) of the faster vectors. The faster vectors overtake the slower vectors, rephasing occurs, and a signal is generated that is detectable in the receiver coil. This signal is called a spin echo.[7] If time τ (not the same time as in Eq. 2.4*)* transpires between the application of the 90° $\mathbf{B}_1$ pulse and the 180° $\mathbf{B}_1$ pulse, then the same time τ will transpire between the application of the 180° $\mathbf{B}_1$ pulse and the peak of the spin echo. That is, rephasing time equals dephasing time, and the spin echo peak occurs at 2τ, which is defined as *TE*. Spin-echo generation is illustrated in **Fig. 2.8**.

Although a single spin echo decays very quickly, 180° pulses can be applied repeatedly to rephase the magnetization components and generate a series of spin echoes. Thus, a spin-echo train can be recorded, as illustrated in **Fig. 2.9**. A spin echo forms midway between each pair of 180° pulses. The inter-echo spacing (*TE*) is the time between the peaks of adjacent echoes. The number of pulses in the pulse train is *NE*. The entire pulse sequence—a 90°

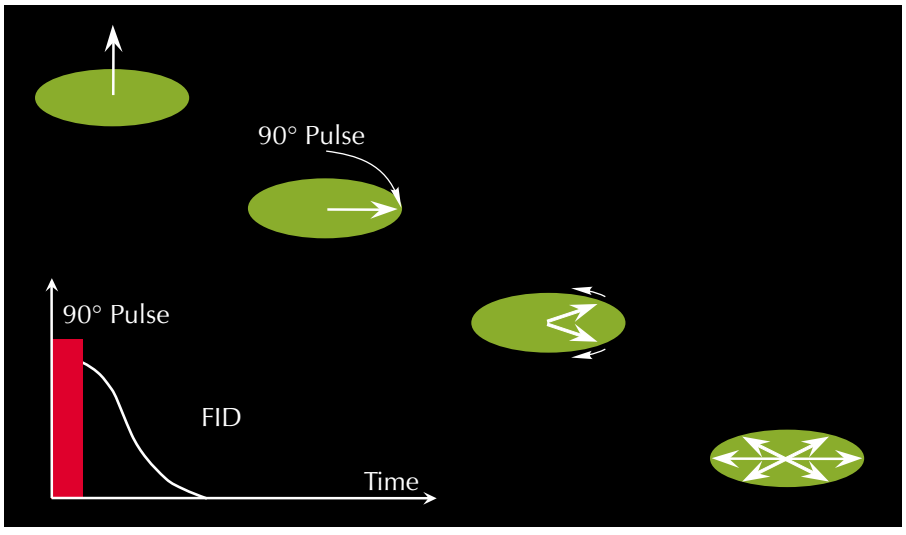

Figure 2.7—After application of a 90° pulse, the proton population dephases, and a free induction decay (FID) signal can be detected.

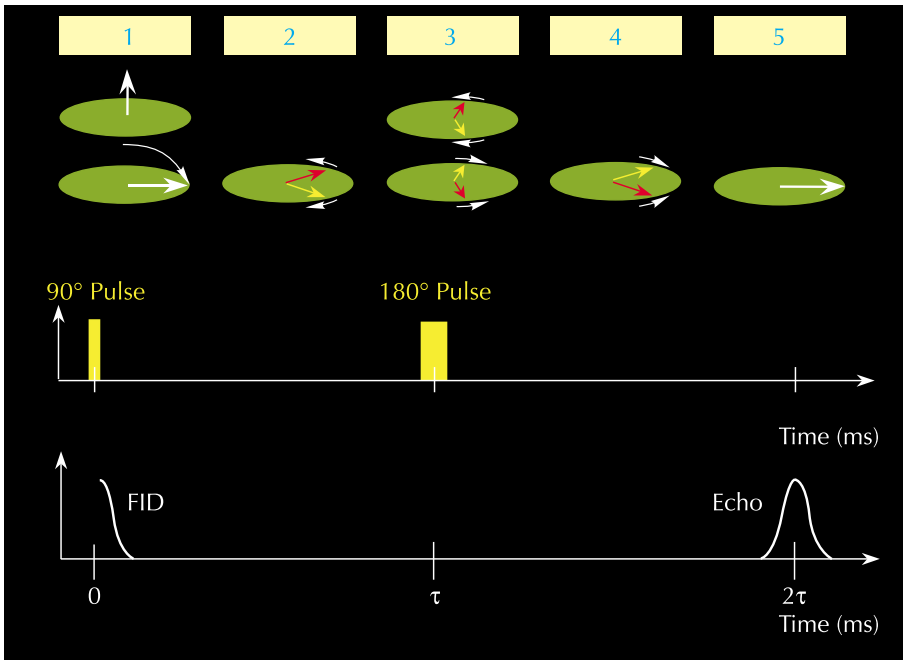

Figure 2.8— (1) To generate a spin echo, a 90° $\mathbf{B}_1$ pulse is first applied. (2) After cessation of the 90° pulse, dephasing starts. (3) At time τ, a 180° $\mathbf{B}_1$ pulse is applied to reverse the phase angles and thus initiates rephasing. (4) Rephasing proceeds. (5) Rephasing is complete, and a measurable signal (a spin echo) is generated at time 2τ.

pulse followed by a long series of 180° pulses—is called a CPMG sequence after its inventors, Carr, Purcell, Meiboom, and Gill.[8]

To the extent that the diffusion can be ignored, the CPMG pulse sequence negates the dephasing caused by the inhomogeneity of the $\mathbf{B}_0$ field; however, the dephasing resulting from molecular interactions and diffusion is irreversible. Once this irreversible dephasing occurs, the protons can no longer be completely refocused, and the CPMG spin-echo train will decay. As shown in **Fig. 2.10**, an NMR logging tool measures the amplitude of the spin echoes in the CPMG sequence to monitor the transverse magnetization decay and thus the irreversible dephasing.

The time constant of the transverse magnetization decay is called the transverse relaxation time, referred as to T_2. The amplitude of the spin-echo train at time t, which is the amplitude of the transverse magnetization $M_x(t)$, is given by[9]

$$M_x(t) = M_{0x} e^{\frac{-t}{T_2}} \tag{2.5}$$

where M_{ox} is the magnitude of the transverse magnetization at $t = 0$ (the time at which the 90° pulse ceases). The T_2 decay from the formation contains most of the petrophysical information obtainable from NMR logging and therefore is the prime objective of NMR logging measurements. As mentioned at the beginning of Chapter 1, the raw data obtained from the NMR logging are the spin-echo trains.

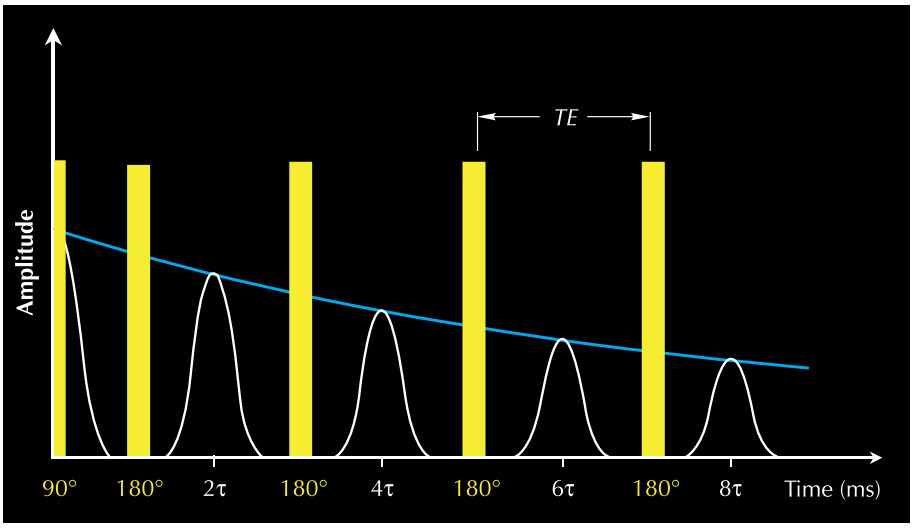

Figure 2.9— To generate a spin-echo train, the CPMG pulse sequence is used, which consists of a 90° $\mathbf{B}_1$ pulse followed by a sequence of 180° $\mathbf{B}_1$ pulses. Spin echoes of decreasing amplitude follow the 180° $\mathbf{B}_1$ pulses.

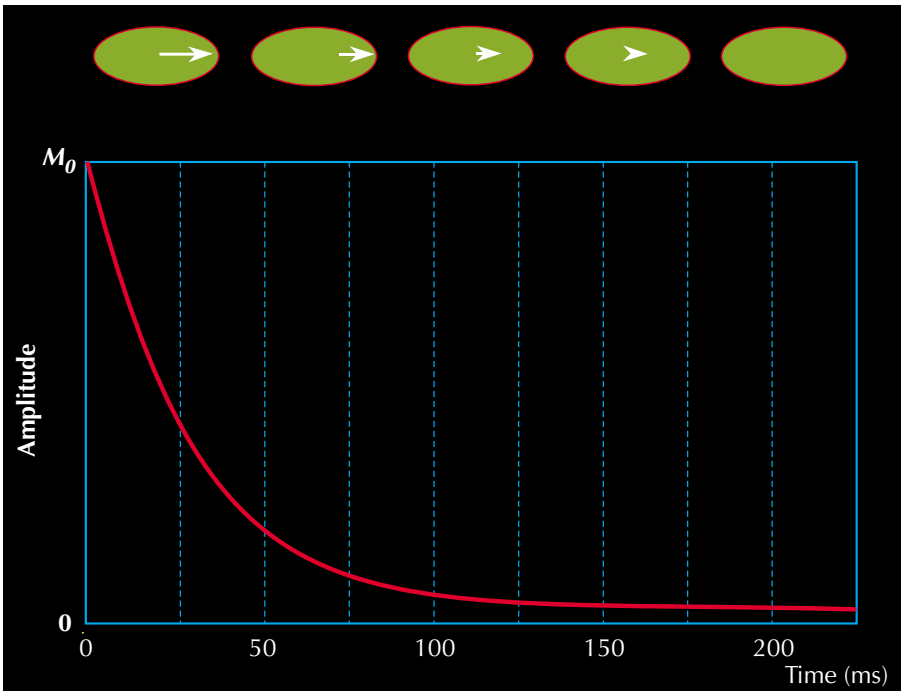

Figure 2.10— The amplitudes of the decaying spin echoes yield an exponentially decaying curve with time constant T_2.

NMR-Measurement Timing

After a period equal to several times T_2, the decay of the transverse magnetization is essentially complete, and further rephasing is not possible. During a CPMG sequence, the 90° pulse reorients the polarization so that there is no longer any longitudinal polarization of the protons, and the 180° pulses suppress the buildup of new longitudinal polarization. Hence, the protons are completely randomized at the end of a CPMG sequence. To start the next CPMG sequence, the protons must be polarized again. So, a wait time (*TW*) during which repolarization occurs is necessary between the end of one CPMG sequence to the start of the next.

A typical NMR-measurement timing diagram is illustrated in **Fig. 2.11**. The upper section of the figure depicts two CPMG sequences, each consisting of a 90° $\mathbf{B}_1$ pulse, followed by a series of 180° pulses. The bottom section represents polarization events (T_1-relaxation curves), and illustrates the spin-echo trains (T_2-relaxation curves) associated with the two CPMG sequences. Polarization time (*TW*), inter-echo spacing (*TE*), and number of echoes (*NE*) can be controlled manually.

To determine the magnitude of $\boldsymbol{M_0}$, the amplitude of the spin-echo train at $t = 0$ is estimated from the spin-echo-train measurements. To avoid underestimating M_0, full polarization or nearly full polarization (95%) is required. To achieve 95% polarization, *TW* should equal three times T_1.

As *TE* decreases, spin echoes will be generated and detected earlier and more rapidly, and the effective signal-to-noise ratio is increased because of the greater density of data points. As *NE* increases, spin echoes will be generated and detected longer, but more $\mathbf{B}_1$ power is required.

The CPMG measurement sets are always collected in pairs. After the first set is acquired, the second set is acquired with the phase of the transmitter pulse changed to give spin echoes of negative amplitude. The second set is then subtracted from the first set to produce a phase-alternate pair (PAP). This procedure preserves the signal and eliminates low-frequency electronic offsets.

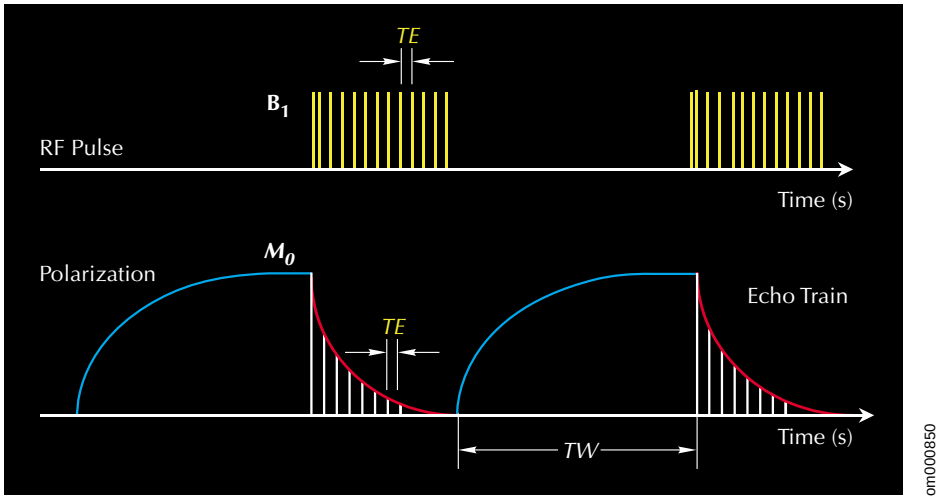

Figure 2.11—This NMR-measurement timing diagram shows (top) CPMG pulse sequences and (bottom) polarization (T_1-relaxation) curves and spin-echo-train acquisition.

References

1. Cowan, B., 1997, *Nuclear magnetic resonance and relaxation*, Cambridge University Press, Cambridge, U.K., p. 7.
2. Miller, M.N., et al., 1990, Spin-echo magnetic-resonance logging-porosity and free-fluid index, SPE 20561, SPE Annual Technical Conference and Exhibition Proceedings, v. Ω, (Formation evaluation and reservoir geology), p. 321–324.
3. Cowan, *Nuclear magnetic resonance and relaxation*, p. 21–22, 128–129.
4. Fukushima, E. and Roeder, S.B.W., 1981, *Experimental Pulse NMR: A Nuts and Bolts Approach*, Addison-Wesley Publishing Company, Advanced Book Program, Reading, Massachusetts, U.S.A., p. 22, 164, 242.
5. Cowan, *Nuclear magnetic resonance and relaxation*, p. 33–37.
6. Fukushima and Roeder, *Experimental Pulse NMR*, p. 54.
7. Cowan, *Nuclear magnetic resonance and relaxation*, p. 100–103.
8. Ibid., p. 111–117.
9. Ibid., p. 26.

Chapter 3

Fundamentals of NMR Petrophysics

Petrophysical information, such as porosity, pore-size distribution, bound water, and permeability, can be extracted from NMR relaxation measurements. Understanding the nature of the NMR relaxation of fluids in rock pores is critical for the proper application of NMR in formation evaluation. This chapter discusses the issues associated with NMR petrophysics and the models used for obtaining petrophysical properties from NMR measurements.

NMR Relaxation Mechanisms of Fluids in Rock Pores

Longitudinal (T_1) and transverse (T_2) relaxations are caused by magnetic interactions between protons. From an atomic point of view, T_1 relaxation occurs when a precessing proton system transfers energy to its surroundings. The donor proton relaxes to its low-energy state, in which the protons precess along the direction of $\mathbf{B}_0$. The same transfer also contributes to T_2 relaxation. In addition, dephasing contributes to T_2 relaxation without a transfer of energy to surroundings being involved. Therefore, transverse relaxation is always faster than longitudinal relaxation; consequently, T_2 is always less than or equal to T_1.[1] In general,

- For protons in solids, T_2 is much smaller than T_1.[2]
- For protons in reservoir fluids,
  - When the fluid is in a homogeneous static magnetic field, T_2 is approximately equal to T_1.
  - When the fluid is in a gradient magnetic field and a CPMG measurement process is used, T_2 is smaller than T_1. The difference is largely controlled by the field gradient, inter-echo spacing, and fluid diffusivity.[3]
- When a wetting fluid fills a porous medium, such as a rock, both T_2 and T_1 are dramatically decreased, and the relaxation mechanisms are different from those of the protons in either the solid or the fluid.

For fluids in rock pores, three independent relaxation mechanisms are involved:

- bulk fluid processes, which affect both T_1 and T_2 relaxation
- surface relaxation, which affects both T_1 and T_2 relaxation
- diffusion in the presence of magnetic field gradients, which only affects T_2 relaxation

All three processes act in parallel; therefore, the T_1 and T_2 times of pore fluids are given by[4]

$$\frac{1}{T_2} = \frac{1}{T_{2\text{bulk}}} + \frac{1}{T_{2\text{surface}}} + \frac{1}{T_{2\text{diffusion}}} \tag{3.1}$$

$$\frac{1}{T_1} = \frac{1}{T_{1\text{bulk}}} + \frac{1}{T_{1\text{surface}}} \tag{3.2}$$

where

T_2 = transverse relaxation time of the pore fluid as measured by a CPMG sequence

$T_{2\text{bulk}}$ = T_2 relaxation time of the pore fluid as it would be measured in a container so large that container effects would be negligible

$T_{2\text{surface}}$ = T_2 relaxation time of the pore fluid resulting from surface relaxation

$T_{2\text{diffusion}}$ = T_2 relaxation time of the pore fluid as induced by diffusion in the magnetic field gradient

T_1 = the measured longitudinal relaxation time of the pore fluid

$T_{1\text{bulk}}$ = T_1 relaxation time of the pore fluid as it would be measured in a container so large that container effects would be negligible

$T_{1\text{surface}}$ = T_1 relaxation time of the pore fluid resulting from surface relaxation

The relative importance of the three relaxation mechanisms depends on the type of fluid in the pores (water, oil, or gas), the sizes of the pores, the strength of the surface relaxation, and the wettability of the rock surface. In general, for a water-wet rock,

- For brine, T_2 is dominated by $T_{2\text{surface}}$.
- For heavy-oil, T_2 has $T_{2\text{bulk}}$ as its main contributor.
- For intermediate-viscosity and light oil, T_2 is a combination of $T_{2\text{bulk}}$ and $T_{2\text{diffusion}}$ and is dependent on viscosity.
- For gas, T_2 is dominated by $T_{2\text{diffusion}}$.

Bulk Relaxation

Bulk relaxation is the intrinsic relaxation property of a fluid. It is controlled by the physical properties of the fluid, such as viscosity and chemical composition. It can be measured by placing the fluid in a large container (thereby eliminating surface relaxation) and then subjecting the fluid to a homogeneous magnetic field and a CPMG pulse sequence. Other environmental conditions such as temperature and pressure affect the bulk relaxation of a fluid. Bulk relaxation times (in seconds) for water, gas, and oil are given by

Water[5]

$$T_{1\text{bulk}} \cong 3\left(\frac{T_K}{298\eta}\right) \tag{3.3}$$

$$T_{2\,\text{bulk}} \cong T_{1\text{bulk}} \tag{3.4}$$

Gas[6]

$$T_{1\text{bulk}} \cong 2.5\times 10^{4}\left(\frac{\rho_g}{T_K^{\,1.17}}\right) \tag{3.5}$$

$$T_{2\,\text{bulk}} \cong T_{1\text{bulk}} \tag{3.6}$$

Dead Oil[7]

$$T_{1\text{bulk}} \cong 0.00713\,\frac{T_K}{\eta} \tag{3.7}$$

$$T_{2\text{bulk}} \cong T_{1\text{bulk}} \tag{3.8}$$

where

T_K = temperature (°K)

η = fluid viscosity (cp)

ρ_g = gas density (gm/cm^3)

Surface Relaxation

Surface relaxation occurs at the fluid-solid interface, i.e., at the grain surface of rocks. Theoretical analysis shows that in what is known as the fast diffusion limit,† the dominant term in T_2 and T_1 surface relaxation times is given by [4, 8, 9]

$$\frac{1}{T_{2\text{surface}}} = \rho_2 \left(\frac{S}{V} \right)_{\text{pore}} \tag{3.9}$$

$$\frac{1}{T_{1\text{surface}}} = \rho_1 \left(\frac{S}{V} \right)_{\text{pore}} \tag{3.10}$$

where

ρ_2 = T_2 surface relaxivity (T_2 relaxing strength of the grain surfaces)

ρ_1 = T_1 surface relaxivity (T_1 relaxing strength of the grain surfaces)

$(S/V)_{\text{pore}}$ = ratio of pore surface to fluid volume

For simple shapes, S/V is a measure of pore size. For example, for a sphere, the surface-to-volume ratio is $3/r$, where r is the radius of the sphere.

Surface relaxivity varies with mineralogy. For example, carbonate surfaces exhibit weaker surface relaxivity than quartz surfaces.[10] Estimates of surface relaxivity can be determined in the laboratory. Fluids controlled by surface relaxation exhibit T_2 times that are not dependent on temperature and pressure.[11] For this reason, laboratory NMR measurements made at room conditions are commonly used to calibrate formulas used to estimate petrophysical parameters such as permeability and bound water. Because the measurement-acquisition process used in the laboratory is identical to the measurement-acquisition process used during logging, models determined from laboratory measurements can be directly transferred to the interpretation of NMR logging data, thus simplifying the interpretation process.

Diffusion-Induced Relaxation

Gas, light oil, water, and some medium-viscosity oils exhibit significant diffusion-induced relaxation when they are in a gradient magnetic field and are subjected to a CPMG sequence with long inter-echo spacing. For these fluids, $T_{2\text{diffusion}}$, the relaxation time constant associated with the diffusion mechanism becomes an important tool for their detection. When a significant gradient exists in the static magnetic field, molecular diffusion causes additional dephasing and, therefore, increases the T_2 relaxation rate ($1/T_2$). This dephasing is caused by the molecule moving into a region in which the magnetic field strength is different, and thus in which the precession rate is different. Diffusion has no influence on the T_1 relaxation rate ($1/T_1$).

† The fast diffusion limit essentially says that pores are small enough and surface relaxation mechanisms slow enough that a typical molecule crosses the pore many times before it relaxes.

The diffusion-induced relaxation rate ($1/T_{2diffusion}$) is given by [3]

$$\frac{1}{T_{2diffusion}} = \frac{D(\gamma GTE)^2}{12} \tag{3.11}$$

where

D = molecular diffusion coefficient

γ = gyromagnetic ratio of a proton

G = field-strength gradient (G/cm)

TE = inter-echo spacing used in the CPMG sequence

As with bulk relaxation, physical properties such as viscosity and molecular composition control the diffusion coefficient. Again, environmental conditions, temperature, and pressure affect diffusion. Water at room temperature has a diffusion coefficient of about $2 \leftrightarrow 10^{-5}$ cm^2/s. Gas, oil, and water diffusion coefficients are given by

Gas[6]

$$D_g \cong 8.5 \times 10^{-2} \left(\frac{T_K^{0.9}}{\rho_g} \right) \times 10^{-5} \text{cm}^2 / s \tag{3.12}$$

Oil[12]

$$D_o \cong 1.3 \left(\frac{T_K}{298\eta} \right) \times 10^{-5} \text{cm}^2 / s \tag{3.13}$$

Water[12]

$$D_w \cong 1.2 \left(\frac{T_K}{298\eta} \right) \times 10^{-5} \text{cm}^2 / s \tag{3.14}$$

As shown in Eqs. 3.12 through 3.14, the diffusion coefficients for gas, oil, and water increase with temperature (viscosity η decreases with temperature). The diffusion coefficient for gas decreases with increasing pressure because the gas density increases with pressure. The diffusion coefficient for oils varies significantly because different oils exhibit a wide range of molecular compositions, which results in a wide range of viscosities.

Three factors control the strength of the magnetic field gradient G in a formation when the formation is logged by the NMR tool. The first factor is a function of the tool design and configuration (i.e., tool size and tool frequency). The second factor accounts for environmental conditions, such as formation temperature. These first two factors are considered in the published gradient charts for each type of MRIL tool. The high degree to which this field gradient has been characterized has made diffusion applications for hydrocarbon typing possible. The third factor addresses gradients induced by the applied $\mathbf{B_0}$. These gradients

arise when a difference exists between the magnetic susceptibility of rock grains and pore fluids.[13] These gradients are known as internal gradients and can cause further reduction in relaxation times.

Molecular movement in wetting fluids is often restricted at the interface between rock grains and fluids and/or by the interfacial tension between fluids. Because of this restriction, the diffusion coefficient for a fluid in a rock differs from the diffusion coefficient of the bulk fluid at the same pressure and temperature.[6] Diffusion effects become unimportant at short inter-echo spacings for most fluids, with the exception of hydrocarbon gas, which exhibits significant diffusion characteristics even at small inter-echo spacings. The inter-echo spacing in the CPMG sequence is a parameter that can be selected by the logging engineer during the NMR job setup. If necessary, diffusion effects can be enhanced or minimized by selecting the appropriate inter-echo spacing for the desired application.

Integration of Eqs. 3.3, 3.4, and 3.11 into Eqs. 3.1 and 3.2 yields

$$\frac{1}{T_2} = \frac{1}{T_{2\text{bulk}}} + \rho_2 \left(\frac{S}{V}\right)_{\text{pore}} + \frac{D(\gamma G\, TE)^2}{12} \tag{3.15}$$

$$\frac{1}{T_1} = \frac{1}{T_{1\text{bulk}}} + \rho_1 \left(\frac{S}{V}\right)_{\text{pore}} \tag{3.16}$$

Fig. 3.1 illustrates the basic relaxation mechanisms.

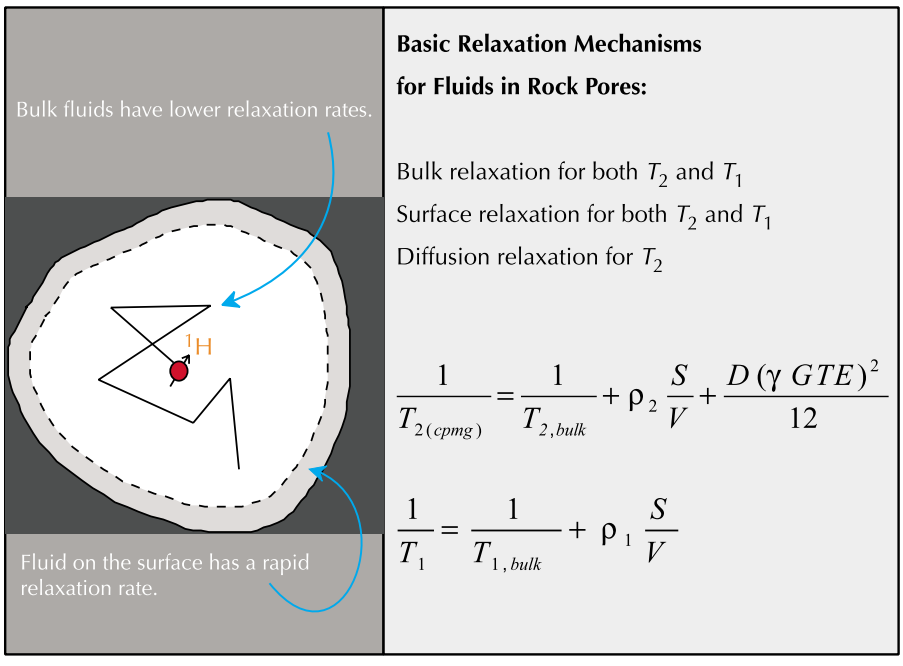

Figure 3.1—The relaxation of pore fluids is due to bulk, surface, and diffusion mechanisms.

Multi-Exponential Decay

Reservoir rocks commonly exhibit a distribution of pore sizes and frequently contain more than one fluid type. Therefore, the spin-echo train (transverse-magnetization measurements) recorded with a CPMG sequence does not decay with a single T_2 value but instead with a distribution of T_2 values that can be described by Eq. 3.17.[14]

$$M(t) = \sum M_i(0)\, e^{-\frac{t}{T_{2i}}} \qquad (3.17)$$

where

$M(t)$ = measured magnetization at time t

$M_i(0)$ = initial magnetization from the i^{th} component of relaxation

T_{2i} = decay constant of the i^{th} component of transverse relaxation

The summation is over the whole sample; i.e., all pores and all different types of fluid.

Fig. 3.2 illustrates the multi-exponential decay character of a porous medium containing pores of different sizes and a single wetting phase.

Surface relaxation becomes dominant when a short inter-echo spacing is used and the formation is only brine-saturated. Under this condition, T_2 is directly proportional to pore size. When all pores are assumed to have the similar geometric shape, the largest pores (left column of Fig. 3.2) have the lowest S/V and thus the longest T_2. Medium-size pores have smaller S/V, yielding shorter T_2 values. The smallest pores have the highest S/V and the

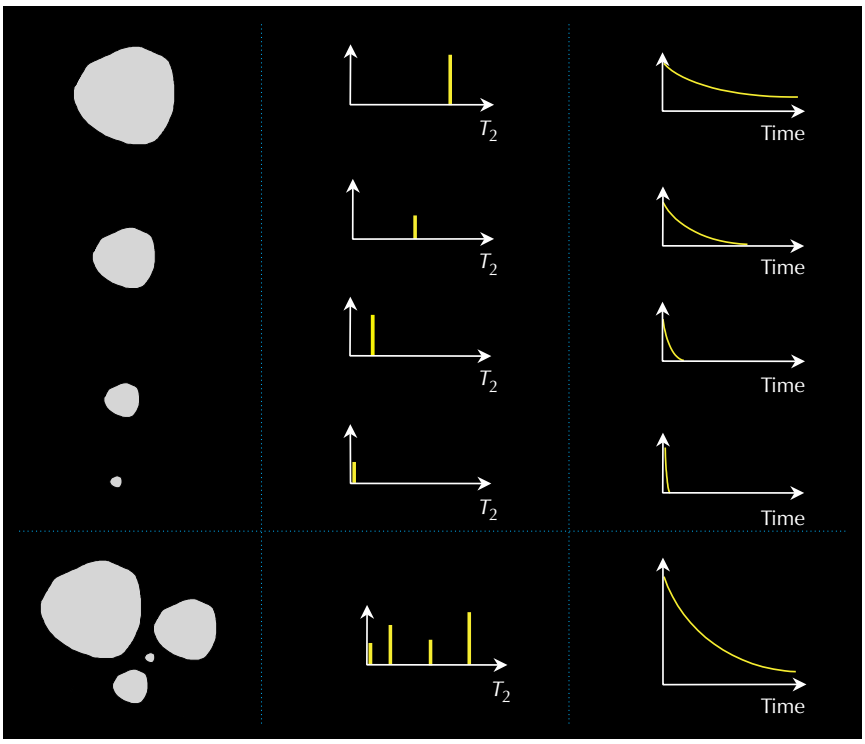

Figure 3.2—A 100% water-saturated pore (upper left) has a single T_2 value (upper center) that depends on pore size, and thus its spin-echo train exhibits a single-exponential decay (upper right) that also depends on pore size. Multiple pores at 100% water saturation (bottom left) have multiple T_2 values (bottom center) that depend on the pore sizes, and thus their composite spin-echo train exhibits multi-exponential decay (bottom right) that also depends on the pore sizes.

shortest T_2 values. For a single pore, the magnetization decays exponentially, and the signal amplitude is given by[15]

$$M(t) = M_0 e^{-\rho_2\left(\frac{S}{V}\right)t} \tag{3.18}$$

M_0 is proportional to the volume of fluid in the pore. When the complete distribution of the 100% water-saturated pores is considered (bottom left of Fig. 3.2), these pores exhibit a distribution of T_2 values (bottom center of Fig. 3.2). The associated signal amplitude is the sum of the signal amplitudes arising from the fluid in individual pores (bottom right of Fig 3.2), and the signal amplitude is given by

$$M(t) = \sum M_{0i} e^{-\rho_2\left(\frac{S}{V}\right)_i t} \tag{3.19}$$

where $(S/V)_i$ is the surface-to-volume ratio of the i^{th} pore. Obviously,

$$M(0) = \sum M_{0i} \tag{3.20}$$

If $M_{100\%}(0)$ (the measured magnetization for 100% bulk water with the same sensitive volume) is known, then $M(0)$ and M_{0i} can be calibrated to porosity:

$$\phi = \frac{M(0)}{M_{100\%}(0)} = \frac{\sum M_{0i}}{M_{100\%}(0)} = \sum \frac{M_{0i}}{M_{100\%}(0)} = \sum \phi_i \tag{3.21}$$

where

ϕ = calibrated porosity of the formation

ϕ_i = calibrated porosity associated with all pores of the i^{th} pore size (also known as the incremental porosity)

Therefore, the T_2 distribution (in the form of the amplitudes M_{0i} associated with the time constants T_{2i}) is calibrated to the porosity distribution (the individual pores ϕ_i with the associated time constants T_{2i}).

If the pores are partially saturated, i.e., the pores contain oil and/or gas in addition to water, then the oil and gas contribute to the measured magnetization as follows:

$$M(t) = \sum M_{0i} e^{-\rho_2\left(\frac{S}{V}\right)_i t} + M_{\text{oil}} e^{-\frac{t}{T_{2\text{oil}}}} + M_{\text{gas}} e^{-\frac{t}{T_{2\text{gas}}}} \tag{3.22}$$

where

M_{oil} = magnetization produced by oil protons in the pores

M_{gas} = magnetization produced by gas protons in the pores

$T_{2\text{oil}}$ = T_2 of oil measured with a CPMG sequence

$T_{2\text{gas}}$ = T_2 of gas measured with a CPMG sequence

Eq. 3.22 assumes that the rock is water-wet and that the spin-echo decays of both oil and gas can be characterized by using a single exponential expression which represents the bulk and diffusion relaxation properties of the non-wetting fluids. Actually, many crude oils are

composed of multiple hydrocarbon types and thus have complex decay spectra that must be represented by multi-exponential sums. Furthermore, if oil or gas occupies part of a pore, then the volume of water in the pore is reduced. Because the volume of water decreases while the surface area of the pore remains the same, the ratio *V/S* decreases. Because the corresponding T_2 of the pore water is proportional to *V/S*, it follows that *V/S* also decreases. Thus, when a non-wetting fluid is present, the T_2 spectrum no longer represents a pore-size distribution because it contains a bulk response from the non-wetting fluid. Pores containing the non-wetting fluid either appear in the spectrum at a decay time that is faster than is normally associated with the pores, or do not appear at all if the surface layer is too thin. The porosity in these pores is accounted for in the non-wetting bulk fluid response; thus, although the distribution is distorted, the porosity is not affected.

Because, in practice, it is difficult to consider each pore individually, all pores with similar surface-to-volume ratios and non-wetting fluids having similar T_2 values are grouped together. With this grouping, the sums in the magnetization equations have a manageable number of terms.

Echo-Fit for T_2 Distribution

One of the most important steps in NMR data processing is to determine the T_2 distribution that produces the observed magnetization. This step, called echo-fit or mapping, is a mathematical inversion process. **Fig. 3.3** illustrates the input (echo train) and output (T_2 distribution) of the mapping process. Eq. 3.23 displays the system of equations that represent the individual echoes. Normally, the T_2 distribution of rocks is a continuous function. However, to simplify fitting the echo train, the mapping process uses a multi-exponential model that assumes that the T_2 distribution consists of *m* discrete relaxation times T_{2i} with corresponding porosity components ϕ_i. The values of T_{2i} are pre-selected (for example, 0.5, 1, 2, 4, 8, 16, 32, 64, 128, 256, 512, 1024 ms …), and the mapping process focuses on determining the porosity components of each distribution.

$$
\begin{aligned}
echo(1) &= \phi_1 e^{-\left[t(1)/T_{2,1}\right]} + \phi_2 e^{-\left[t(1)/T_{2,2}\right]} + \phi_3 e^{-\left[t(1)/T_{2,3}\right]} + \cdots + \phi_m e^{-\left[t(1)/T_{2,m}\right]} + noise \\
echo(2) &= \phi_1 e^{-\left[t(2)/T_{2,1}\right]} + \phi_2 e^{-\left[t(2)/T_{2,2}\right]} + \phi_3 e^{-\left[t(2)/T_{2,3}\right]} + \cdots + \phi_m e^{-\left[t(2)/T_{2,m}\right]} + noise \\
&\vdots \\
echo(n) &= \phi_1 e^{-\left[t(n)/T_{2,1}\right]} + \phi_2 e^{-\left[t(n)/T_{2,2}\right]} + \phi_3 e^{-\left[t(n)/T_{2,3}\right]} + \cdots + \phi_m e^{-\left[t(n)/T_{2,m}\right]} + noise
\end{aligned}
\tag{3.23}
$$

where $t(i) = i\ TE$ and $i = 1, \ldots n$, is the time when the i^{th} echo was acquired.

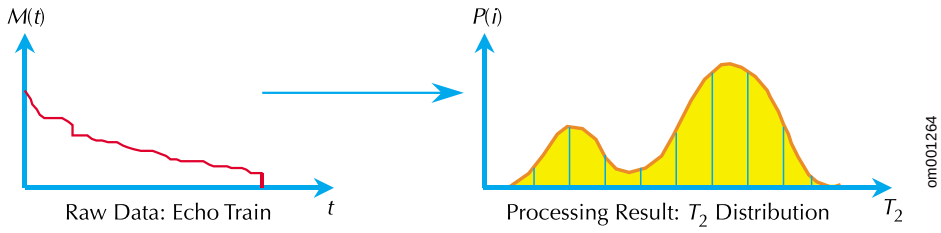

Figure 3.3—Through echo fitting, the echo train (echo amplitude as a function of time) is mapped to a T_2 distribution (porosity as a function of T_2).

Eq. 3.23 is a system of n linear equations in m unknowns, $\phi_1, \ldots, \phi_m$, where n is much larger than m. Typically m, the number of T_2 values or bins, can range from 2 in some log data, to 50 in high-quality laboratory data. The number of echoes n ranges from 10 in partial-polarization measurements for clay-bound water, to several thousands for some laboratory data. There are numerous methods to invert such an equation set for the "best" set of ϕ_i.[16] The solution of Eq. 3.23 is complicated by the fact that ϕ_i must be constrained to be greater than or equal to zero and by the fact that the fit to a sum of multi-exponentials is unstable. Therefore, the inversion of Eq. 3.23 must involve regularization to stabilize the solution. The inverse is thus a function of both the measured echo data and the chosen regularization, i.e., the chosen smoothness for the inversion. Regularization is at least in part controlled by the signal-to-noise ratio of the data. As a consequence, the set of ϕ_i is not unique (i.e., distributions with different shapes can all appear to be good fits to the decay curve); thus, care must be taken in interpreting the fine details of the distribution. In general, though, the area under the curve (this area represents the porosity) and the general location in time of the high-porosity bins are robust.

Pore Size Distribution

As discussed earlier, when a water-wet rock is fully saturated with water, the T_2 value of a single pore is proportional to the surface-to-volume ratio of the pore, which is a measure of the size of the pore. Thus, the observed T_2 distribution of all the pores in the rock represents the pore-size distribution of the rock. **Fig. 3.4** compares the T_2 distribution of a brine-saturated rock with the pore throat size distribution of the rock obtained from mercury-injection data. The information from the mercury porosimetry incremental injection curve is difficult to quantify exactly, but it is essentially pore throat sizes weighted by the pore

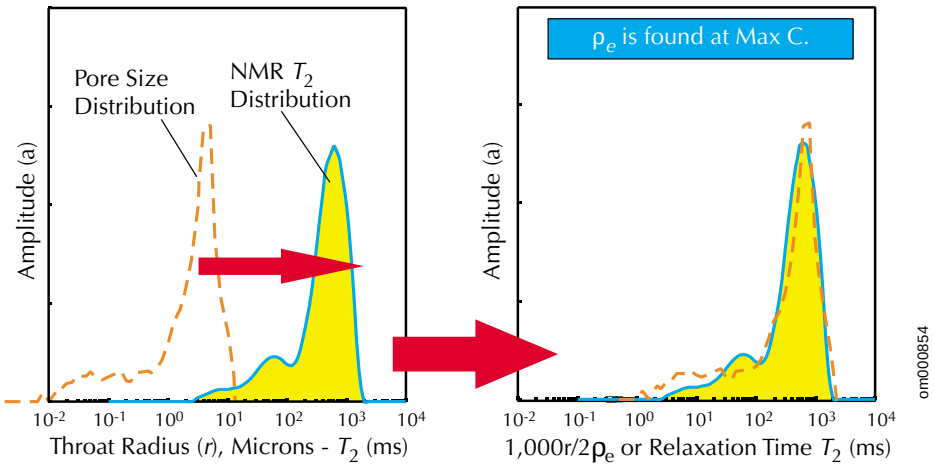

Figure 3.4—When shifted by the effective surface relaxivity, the pore-size distribution from mercury-injection data nearly overlays the NMR T_2 distribution.

volumes to which the pore throats control access. As seen in the left of the figure, when a shift is applied to account for factors such as surface relaxivity, the T_2 distribution shows a remarkable correlation with the pore throat size distribution. Although distributions from NMR and mercury can often be shifted to closely overlay each other, the distributions represent somewhat different rock properties. This good quantitative agreement is due to the correlations often seen among some properties of sedimentary rocks.

Mappings such as Fig. 3.4 produce an effective relaxivity (ρ_e). Effective relaxivity is introduced to account for the fact that NMR responds to pore "body" size whereas mercury-injection capillary pressure (MICP) is controlled mainly by the pore throat sizes. Thus, ρ_e is proportional to the product of the intrinsic surface relaxivity (ρ) and the ratio of pore throat size to pore body size.[17]

Fig. 3.5 shows how relaxation-time distributions compare to MICP pore size distributions for three types of lithologies. The relaxivity of sandstones is commonly greater than the relaxivity of carbonates, which is the case for the sample data depicted in the figure.

The T_2 distribution from NMR data offers a reasonable estimate of a zone's pore size distribution when the zone is 100% water-saturated, as shown in **Fig. 3.6** for sandstone and carbonate samples. Even when hydrocarbons are present, *BVI* delineates fine-grained sands from coarse-grained sands. This information is very helpful when evaluating reservoir quality and depositional environment.

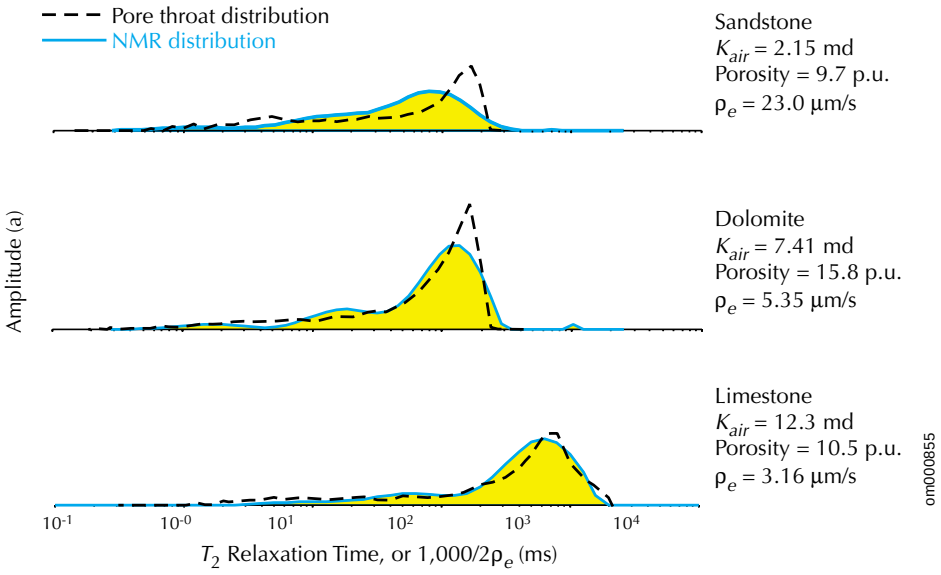

Figure 3.5—For a particular rock, the T_2 distribution can be compared with the mercury-injection pore-size distribution to determine the effective surface relaxivity.

Figure 3.6—The correlation between MCIP and T_2 distributions offers a reasonable assurance that the T_2 distributions estimate a sensible pore size distribution when pores are 100% water-saturated.

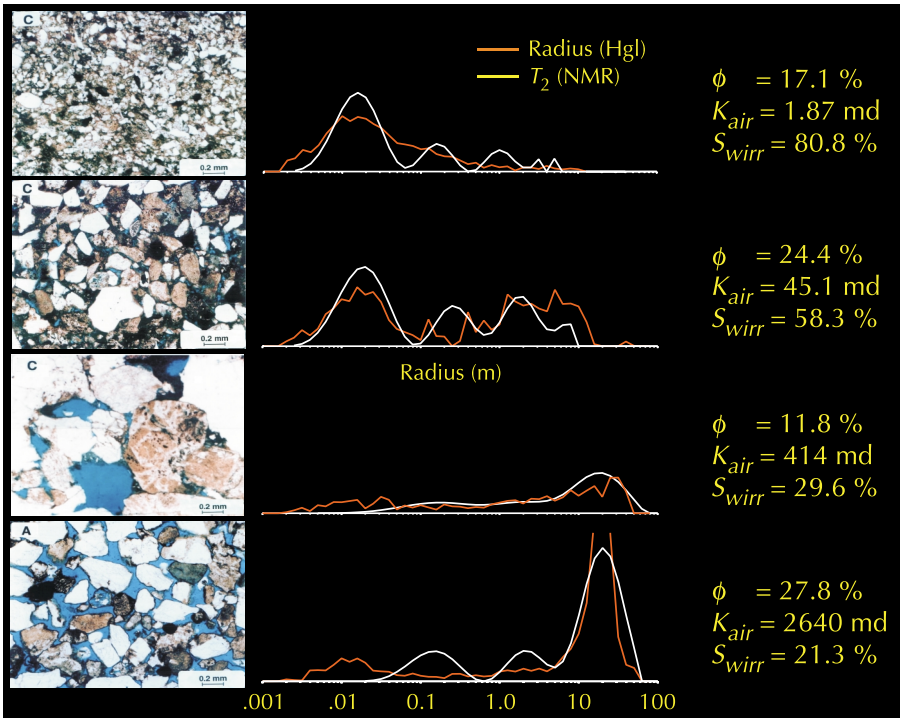

om001265

Sandstone Samples

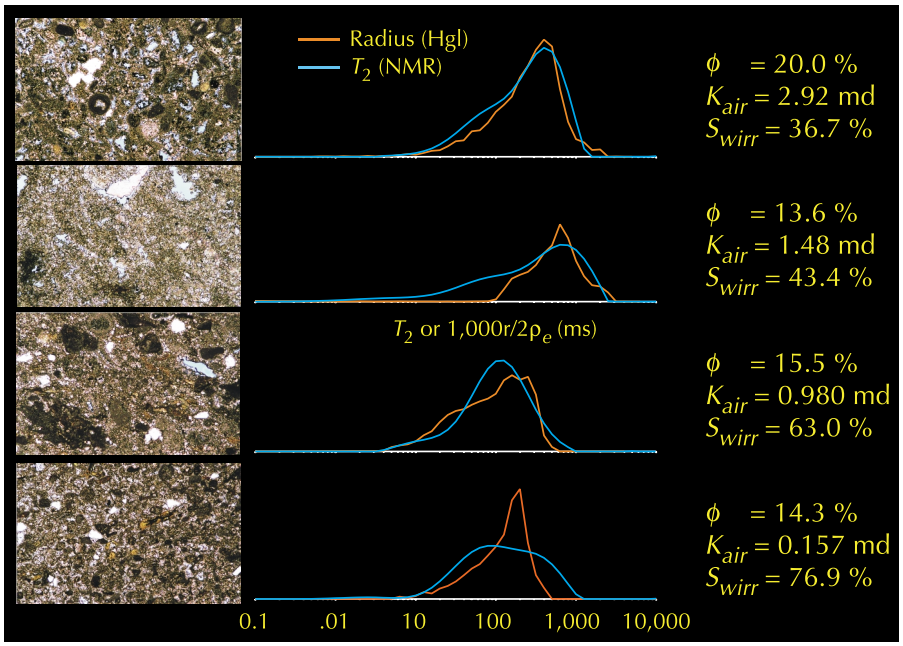

om001266

Carbonate Samples

Determination of BVI

Estimating *BVI*, the bulk volume of irreducible water in a formation, is one of the earliest and still one of the most widely used applications of NMR logging. Currently, two methods are available for *BVI* determination. The first method, cutoff *BVI* (*CBVI*), is based on a fixed T_2 value ($T_{2cutoff}$) that divides the T_2 distribution into two components, one consisting of pore sizes containing bound water and the other consisting of pore sizes containing free fluids. The second method for *BVI* determination, called spectral *BVI* (*SBVI*), is based on the recognition that a given pore can contain both free and bound fluids.

In the NMR literature, the concept of bound water (*BVI*) is used in two different ways. The first refers to the water contained in the pore space that will not flow out of the rock and into the wellbore during production. This volume is accurately determined only by a relative permeability measurement, but can be reasonably estimated from a capillary-pressure saturation curve. This water volume is primarily a property of the rock and the wetting conditions. The second use of *BVI* refers to the water that is not displaced by hydrocarbons during the filling of the reservoir. This volume is a function of both the capillary-pressure curve for the rock and the height above free water. In a transition zone, this water volume can include water that can be produced. However, for a sufficient height above free water, capillary forces can drive water saturation to levels well below the point at which the relative permeability to water is effectively zero. In many reservoirs, the transition zone occupies only a small fraction of the hydrocarbon column, and the hydrocarbon column is short enough that no significant difference exists between the two *BVI* values. If the two *BVI* values do differ significantly, then it is important to decide whether *BVI* is being used to estimate water production or to estimate permeability. For permeability estimation, especially when drilling with oil-based mud, the *BVI* must be the volume of remaining water not displaced by oil.

Cutoff *BVI*

Fig. 3.7 shows the *CBVI* concept. The NMR estimate of *BVI* is based on the assumption that bound fluids reside in small pores and producible fluids reside in large pores. This assumption is based on the fact that pore throat size and pore body size are often related. Because T_2

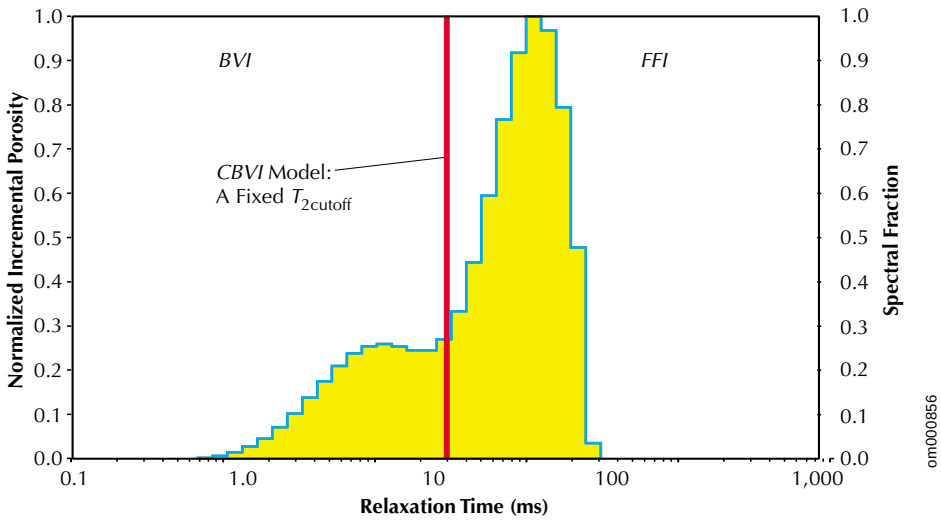

Figure 3.7—When a *CBVI* model is used for NMR log interpretation, a fixed $T_{2cutoff}$ is selected to calculate *BVI*.

values can be related to pore body size, a T_2 value can be selected below which the corresponding fluids are expected to reside in small pores and are thus immobile, and above which the corresponding fluids are expected to reside in larger pores and thus can move freely. This T_2 value is called the T_2 cutoff ($T_{2cutoff}$). Through its partitioning of the T_2 distribution, the $T_{2cutoff}$ divides *MPHI* into two parts, *BVI* and *FFI*, as shown in Fig. 3.7. The *BVI* portion is referred to as the cutoff *BVI* (*CBVI*).[18]

Instead of assuming a relaxation-time cutoff, a $T_{2cutoff}$ can be determined in the laboratory with NMR measurements on core samples. Core samples are analyzed for NMR characteristics at two saturation conditions, S_w = 100% and (after establishing the appropriate value of saturation from a capillary-pressure curve, or directly desaturating the sample to the appropriate capillary pressure) S_w = irreducible. A centrifuge technique or a porous-plate technique at a specified capillary pressure is used to achieve the latter condition. The T_2 distributions are compared as illustrated in **Fig. 3.8**. The two T_2 distributions are displayed in two ways: incremental porosity and cumulative porosity. (The cumulative porosity at a particular T_2, say $T_{2,U}$, is the integral of the incremental porosity for all T_2 values less than or equal to $T_{2,U}$.) The cumulative curves are used to determine $T_{2cutoff}$. To determine $T_{2cutoff}$ from a plot of T_2 vs. cumulative porosity, enter the plot from the cumulative porosity axis at the porosity at which the sample is at irreducible condition. Project horizontally to the cumulative porosity curve for S_w = 100%. Upon intersecting this curve, project down to the T_2 axis. The T_2 value of the intersection of this projection with the T_2 axis is the $T_{2cutoff}$.[18]

In the absence of laboratory data, default values based on lithology are used for $T_{2cutoff}$. A $T_{2cutoff}$ of 33 ms is used for sandstones and 92 ms for carbonates. These values work very well in the Gulf of Mexico area. $T_{2cutoff}$ values, however, are affected not only by lithology, but also by several other factors, such as pore-wall chemistry, minor paramagnetic or ferromagnetic components, texture, pore throat to pore body ratios, and other factors not well understood.

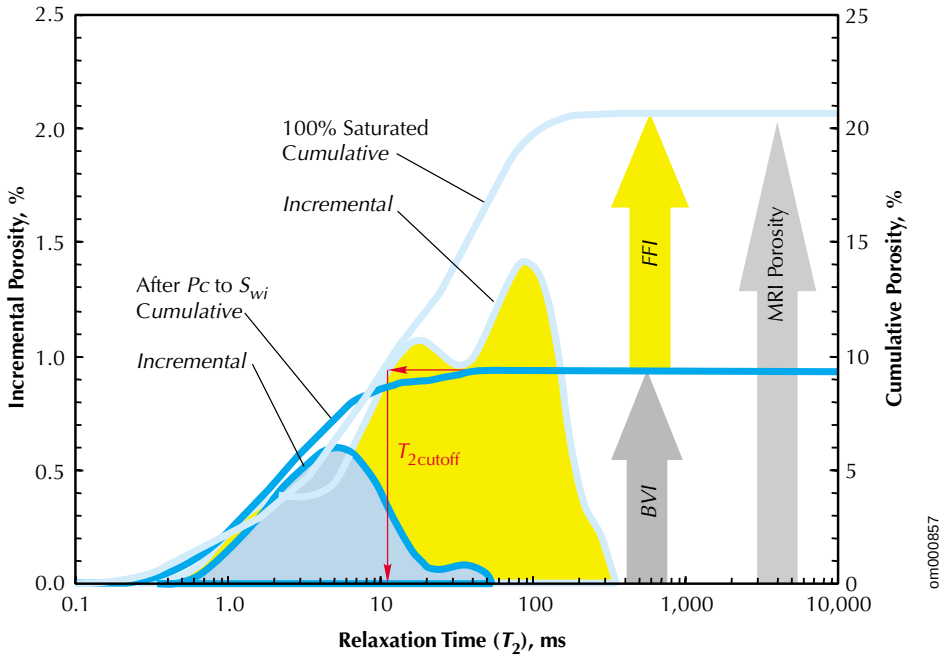

Figure 3.8—NMR measurements on fully saturated (S_w = 100%) core samples and on samples at irreducible saturation (S_{wi}) can be used to establish a $T_{2cutoff}$ for use in a *CBVI* model.

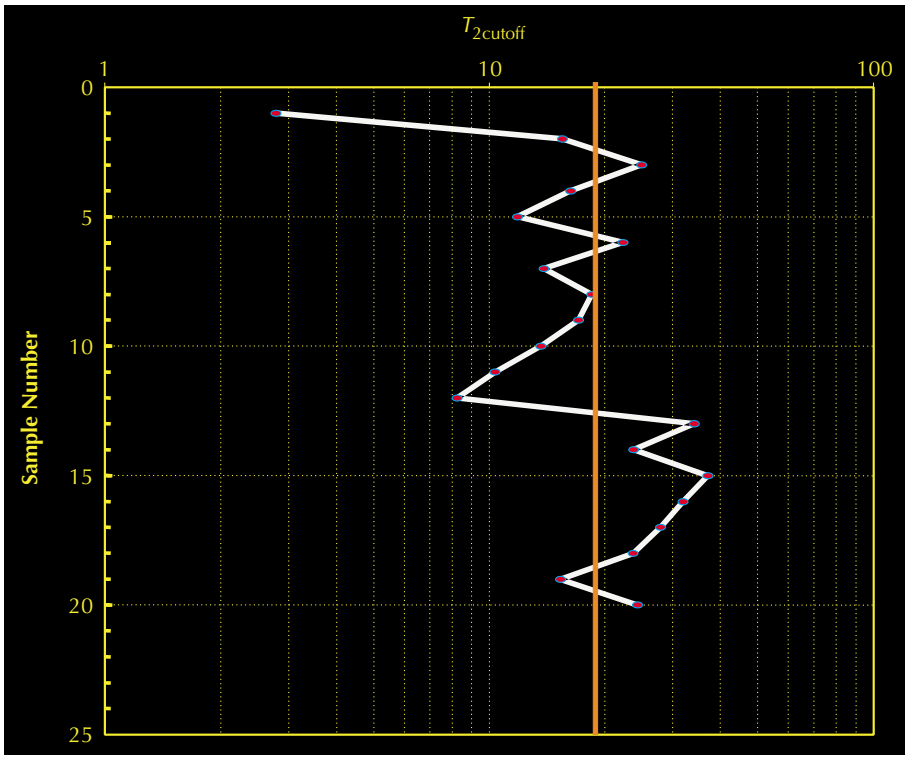

Figure 3.9—In core samples from an apparently homogeneous reservoir, laboratory-derived $T_{2cutoff}$ values can vary. The red line represents the average value of the cutoff.

These factors can cause $T_{2cutoff}$ to vary among samples within a single lithology, as illustrated in **Fig. 3.9**.

Given the fact that T_2 is directly proportional to pore size, a cutoff T_2 represents a pore-size cutoff or a capillary-pressure cutoff. Thus, $T_{2cutoff}$ values are a function of capillary pressure along with the surface relaxivity. Laboratory examination of core samples to determine $T_{2cutoff}$ by the method illustrated in Fig. 3.8 is dependent on the capillary pressure chosen to create the irreducible condition. This pressure depends on whether *BVI* is being used for producible water or permeability. In the second case, it depends on the height above free water along with the capillary-pressure curve of the rock.

Even though a $T_{2cutoff}$ may have been determined that best represents the irreducible saturation condition of a particular rock type at the appropriate capillary pressure, this single relaxation time may not properly represent the irreducible saturation condition of a different rock type. One reason for this difference in $T_{2cutoff}$ values is the different capillary pressure at which irreducible water condition is achieved in different rocks. This situation is illustrated in **Fig. 3.10**. In this figure, the capillary pressure appropriate for rock type A is too low for rock type B. Thus, a cutoff value established for rock type B using this capillary pressure would identify an overly high irreducible water saturation. Establishment of a $T_{2cutoff}$ using the capillary pressure needed for rock type B may not give the same cutoff value found for rock type A.

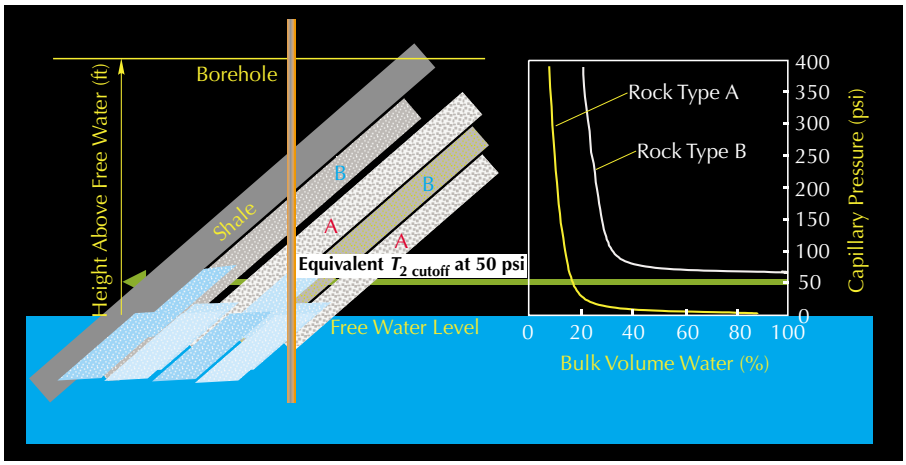

Figure 3.10—Proper interpretation of NMR data often requires capillary-pressure data to select a pressure that best represents an irreducible condition for all rock types encountered. Even so, it is possible that no single pressure will satisfactorily represent the irreducible condition of all the rock types encountered.

Spectral *BVI*

The application of a fixed cutoff to the 100% water-saturated spectra will sometimes give a significantly incorrect value for *BVI*. This error occurs because pores are not simple geometrical shapes such as cylinders or spheres. The pore walls may be rough and the pore may contain many tiny irregularities. NMR sees as a single pore all the pore space through which the water molecules of the pore fluid diffuse before relaxing by interacting with the pore walls. Thus, the micro-porosity contained in the rough surface and in the irregularities will often be included by the NMR measurement as part of the total volume of the large pore. However, when brine is displaced by hydrocarbons or when fluid flows through a rock, the water in these micro-pores usually remains in place and so should be included in the *BVI*. Furthermore, during desaturation of a water-wet rock, a very thin layer of water covering the pore wall always remains. This water also needs to be included in the *BVI*. In the fixed-cutoff model, these effects are partly accounted for by effectively using a slightly larger cutoff, but better results are often obtained by using a spectral cutoff rather than a sharp cutoff.

The standard cutoff model seems to fail most dramatically when the 100% brine-saturated NMR response has a very narrow spectrum that can be fit fairly well by a single-exponential decay. This failure has been seen in coarse-grained, high-permeability sandstones, as well as in the North Sea chalks with relatively small pores.[18] Scanning electronic microscope (SEM) analysis of the chalks suggests that their pore walls are uniformly rough. **Fig. 3.11** presents what is often seen in a North Sea chalk. As hydrocarbons displace brine in these chalks and in some coarse-grained sandstones, small pores appear in the resulting NMR spectrum that do not appear in the 100% brine-saturated spectrum. This effect is less obvious when the original 100% brine-saturated spectrum is broad and thus contains pores of the same size range as the small pores that become visible during desaturation.

To address the problems encountered with a fixed-cutoff *BVI*, the spectral *BVI* (*SBVI*) method has been developed.[18] This method has its primary use in quantifying movable water, but it has also been applied to determining permeability. In this method, each pore size seen in the 100% brine-saturated spectra is assumed to contain some bound water. This is defined by a weighting function $W(T_{2,i})$, where $0 \le W(T_{2,i}) \le 1$, that defines the fraction of bound

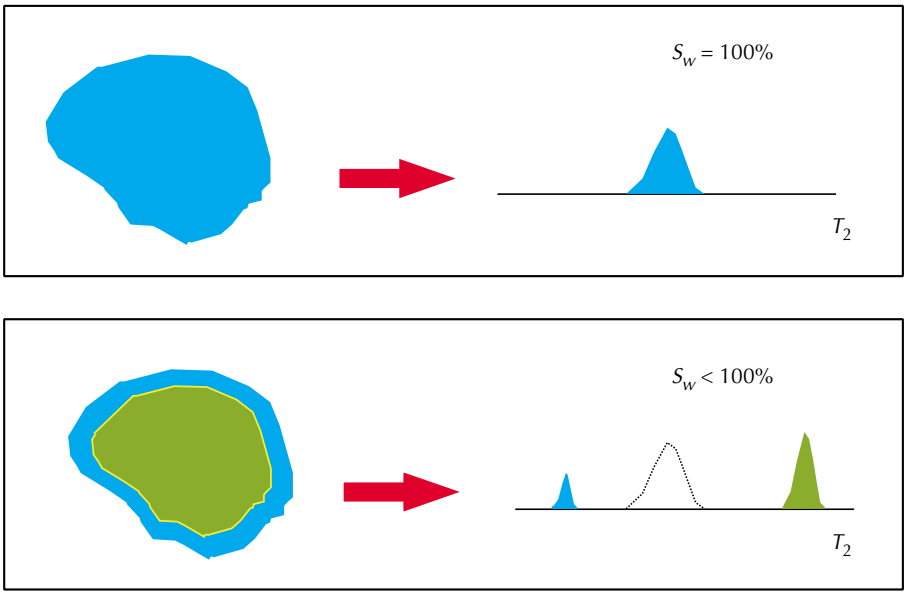

om000860

Figure 3.11—In a coarse-grained rock that is fully water-saturated (upper panel), the T_2 distribution will exhibit a single sharp peak. No signal is observed below the $T_{2cutoff}$ value; hence, *CBVI* = 0. After oil displaces most of the movable water in the same rock (lower panel), two peaks are found in the T_2 distribution. One appears below the $T_{2cutoff}$ value and is due to irreducible water on the pore surface. The other appears above the $T_{2cutoff}$ value and is due to the oil. The T_2 value of the second peak is close to the T_2 of bulk oil. Hence, after most of the water has been displaced, *CBVI* can be calculated.

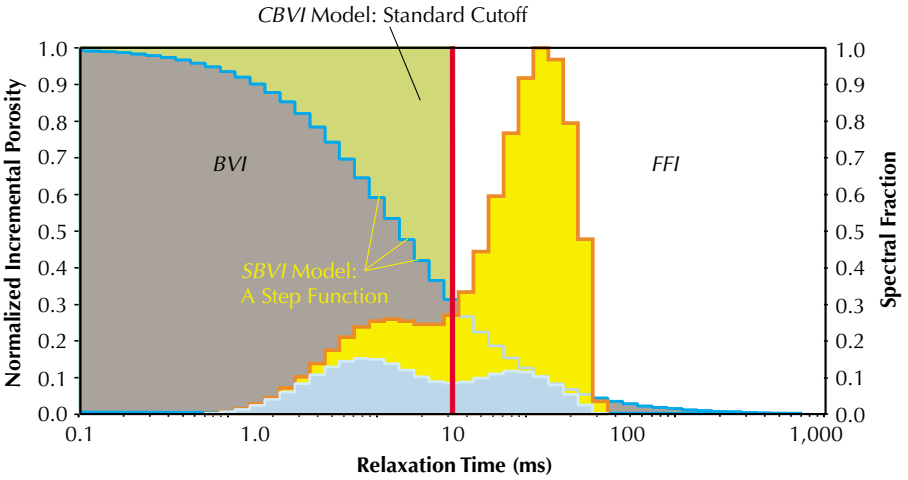

om000861

Figure 3.12—For a given T_2, the *SBVI* weighting factor gives the fractional volume of irreducible fluids in the pores whose size is associated with that T_2. The model shown is a step function and is commonly used to describe the weighting factors.

water associated with each pore size, as shown in **Fig. 3.12**. Various methods have been proposed in the literature to obtain the weighting functions.[19, 20] One class of methods is based on models in which the pores have a simple geometrical shape and in which the bound water forms a thin film on the pore walls. These models give similar weighting functions for the various simple pore shapes. However, the methods in this class all suffer from the simplistic nature of the models.

Another class of models takes a more phenomenological approach. Comparison of formulas for permeability, examination of thin-film models, study of experimental data, and general considerations suggest a weighting function of the form

$$\frac{1}{W_i} = mT_{2,i} + b \tag{3.24}$$

$T_{2,i}$ is the T_2 relaxation time associated with the i^{th} bin, and m and b are parameters that depend on pore geometry and height above free water established from core capillary desaturation measurements and NMR measurements on the partially saturated cores. Then

$$SBVI = \sum_{i=1}^{n} W_i \phi_i \tag{3.25}$$

where n is the number of bins and ϕ_i is the porosity associated with each bin.

Fig. 3.13 provides a motivation for Eq. 3.24. For a set of core samples, the figure shows a linear relationship between $1/S_{wirr}$ and T_{2gm}, where S_{wirr} is the water saturation at a given capillary pressure, and T_{2gm} is the geometric mean of the relaxation spectra. The functional form for the weight function makes sense in the limits of small and large pores.

In almost any reasonable pore model, the percentage of bound water in a pore decreases as pore size increases. In its simplest functional form, this property is expressed as

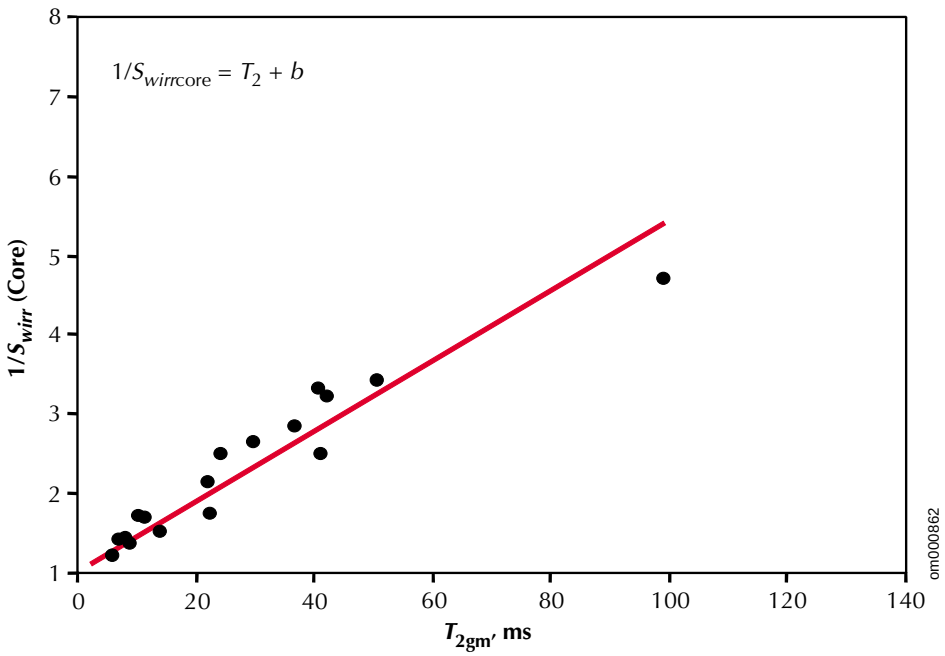

Figure 3.13—This example comparing core-measured irreducible water saturation ($1/S_{wirr}$) to the geometric mean (T_{2gm}) of core T_2 spectra illustrates that a linear relationship exists between relaxation time and $1/S_{wirr}$.

$$\frac{1}{W_i} \sim T_{2,i} \tag{3.26}$$

For small pores, a pore size exists below which W_i must be equal to 1. Thus, for all T_2 values above a certain small T_2, a constant term b must be added to the right side of the simple relationship given by Eq. 3.26. Taking $b = 1$ implies every pore has some movable water, but this implication is never correct at a given height above free water.

In general, for a particular value of m and b, a value k exists such that W_k will be 1 for the time bin $T_{2,k}$. Then for all $T_{2,i}$ less than $T_{2,k}$, W_i is assumed to be 1. Although the best method for establishing m and b is measurements on cores from the zone being logged, work by Coates et al.[18] on a set of 340 sandstone and 71 carbonate samples has established generic values. In this work, b was taken as 1, and the value of m for sandstones and limestones was found to be 0.0618/ms and 0.0113/ms, respectively.

Models with $b = 1$ are most prone to error when there is a significant porosity in small pores (such as in clay pores) that must be weighted as one.

A method to determine m and b from laboratory measurements on s core samples is to solve the set of equations 3.27.

$$\begin{aligned}
S_{wirr,1}\phi_1 &= W_1\phi_{1,1} + W_2\phi_{1,2} + \cdots + W_n\phi_{1,n} \\
S_{wirr,2}\phi_2 &= W_1\phi_{2,1} + W_2\phi_{2,2} + \cdots + W_n\phi_{2,n} \\
&\vdots \\
S_{wirr,s}\phi_s &= W_1\phi_{s,1} + W_2\phi_{s,2} + \cdots + W_n\phi_{s,n}
\end{aligned} \tag{3.27}$$

W_i, $i = 1, \ldots, n$, are the weighting functions. $S_{wirr,i}$, $i = 1, \ldots, s$, are the water saturations of the samples at a chosen capillary pressure. ϕ_i, $i = 1, \ldots, s$, are the porosities of the samples. $\phi_{i,j}$, $j = 1, \ldots, n$, are the components of the porosity of the i^{th} sample in j^{th} bin of the m-term exponential fit to the NMR decay curve. Eq. 3.25 can also be solved for other forms of the weighting function.

In general, for a 100% water-saturated rock, determining *SBVI* with a correct set of weighting functions is a superior method of obtaining bound water from NMR measurements.

Application of the *SBVI* method becomes more complicated when the pores contain hydrocarbons and water. If the rock is water-wet, two major effects must be considered. First, because the weighting functions are non-zero over a wide range of relaxation times, hydrocarbons will more likely be counted as bound water, driving *SBVI* to be too large. Second, although the small pores that appear in the NMR spectra when hydrocarbons fill the center of the pore body should be counted as 100% filled with bound water, the model may associate them with weightings less than one, making *SBVI* too small. This effect is particularly important when a sensitive zone of the logging tool is at irreducible water saturation. Counting bound water as free water can only happen when a weighting function is used that is inappropriate for the rock type or for the height above free water. Currently, the suggested best practice for determining *BVI* is to compute two bound-water values—one from the fixed-cutoff and one from the *SBVI* method—and take the larger of the two. It should be noted that this practice is strongly dependent on the weighting function used and is based on studies that used functions for which $b = 1$.

MRIL Permeability Model

The NMR estimate of permeability is based on a combination of experimental and theoretical models and relationships.[14] When all other factors are kept constant in these models and relationships, permeability increases as connected porosity increases. The unit of permeability, the Darcy, has dimensions of area, and from practical considerations in petrophysical applications, permeability can be considered as being proportional to the square of some geometrical size. The correlation between capillary pressure curves and permeability strongly support that the pertinent size is that of the pore throat.[21, 22] NMR measures pore body size, but in almost all sandstones and some carbonates, a strong correlation exists between pore body size and pore throat size.

The two most commonly used expressions for permeability both vary as ϕ^4. This power of ϕ is somewhat arbitrary but is loosely derived from Archie's Law, the relationship of permeability to resistivity, and with an additional factor to account for NMR measuring pore body size not pore throat size. In one expression, the Free Fluid (or Coates) model, the size parameter enters implicitly through $T_{2cutoff}$, which determines the ratio of *FFI* to *BVI*, where *FFI* is the free fluid volume and $FFI = \phi - BVI$. In the other expression, the Mean T_2 (or SDR) model, the size parameter enters through the geometrical mean of the relaxation spectra, T_{2gm}.[4] The use of these particular size parameters in the respective expressions is based on empirical considerations. Other size measures have also been used. **Fig. 3.14** illustrates both models. Both models correlate very well to permeability from laboratory data on 100% brine-saturated samples. The Mean T_2 model, however, fails when the pore contains hydrocarbons because then T_{2gm} is not controlled exclusively by pore size.

The Free Fluid Model

In the Free Fluid (or Coates) model in its simplest form the permeability k is given by

$$k = \left[\left(\frac{\phi}{C}\right)^2\left(\frac{FFI}{BVI}\right)\right]^2 \tag{3.28}$$

MPHI (MRIL porosity, which is discussed in the next section) is usually used for ϕ, and *BVI* is obtained through the *CBVI* or *SBVI* method.[18] The coefficient C is a variable that is dependent on the processes that created the formation and can be different for each formation.

Experience has shown that the Coates model is more flexible than the Mean T_2 model. Through careful core calibration, the Coates model has been customized for successful use in different formations and reservoirs. As long as *BVI* does not include any hydrocarbon contribution, *BVI* is not affected by an additional liquid phase such as oil or oil filtrates, which is very important when analyzing hydrocarbon-bearing formations.

In unflushed gas zones, the *MPHI* used for porosity in the Coates formula may be too low because of the low hydrogen index in such zones. Thus, *MPHI* must be corrected, or an alternative porosity source should be used. Zones that maintain high residual gas saturation at sufficient reservoir pressure will have *SBVI* and *CBVI* values that are too high and thus, to a small degree, will yield permeability values that are too low. Heavier oils, which normally have very short T_2 values, may be counted as *BVI*, thus causing permeability to be underestimated.

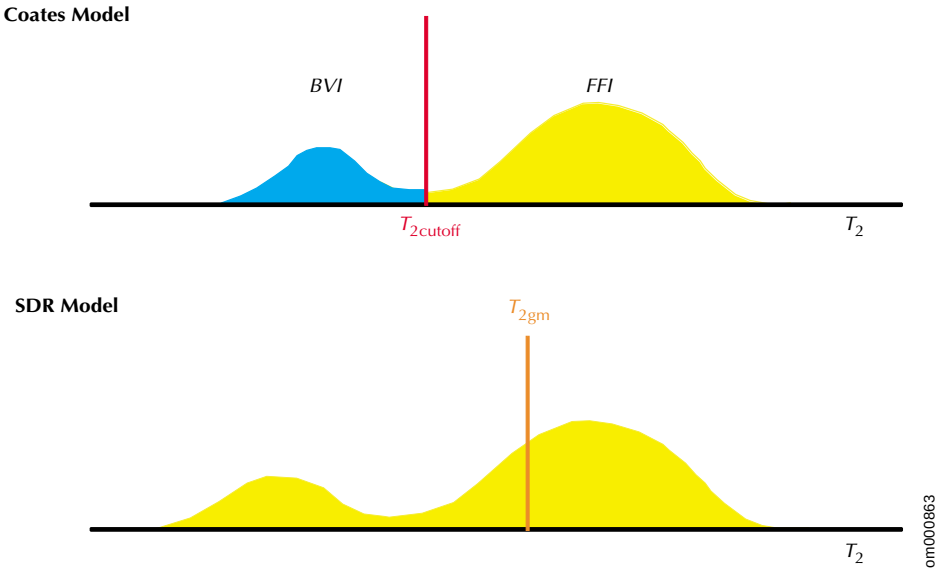

Figure 3.14—The Coates permeability model (top) uses the *FFI*/*BVI* ratio to describe changes in the surface-to-volume ratio. The SDR permeability model (bottom) uses an average T_2 value to describe changes in surface-to-volume ratio.

The Mean T_2 Model

The Mean T_2 (or SDR) model is given by

$$k = a\, T_{2gm}{}^{2}\, \phi^{4} \tag{3.29}$$

In Eq. 3.29, NMR effective porosity is substituted for ϕ. As before, T_{2gm} is the geometric mean of the T_2 distribution. As with the Coates model, the value a is a coefficient that depends on the formation type.

Experience has shown that the Mean T_2 model works very well in zones containing only water. However, if oils or oil filtrates are present, the mean T_2 is skewed toward the bulk-liquid T_2, and permeability estimates are erroneous. In unflushed gas zones, mean T_2 values are too low relative to the flushed gas zone, and permeability is consequently underestimated. Because hydrocarbon effects on T_{2gm} are not correctable, the Mean T_2 model fails for hydrocarbon-bearing formations.

In fractured formations, permeability estimates from both the Coates and SDR models are too low because these models can only represent matrix permeability.

MRIL Porosity Model

The initial amplitude of the NMR spin-echo train, or the area under the T_2 distribution curve, is proportional to the number of hydrogen protons that are contained in the pore fluids within the sensitive volume. Thus, this amplitude can be calibrated to give a porosity value. **Fig. 3.15** shows the NMR porosity model for a water-wet formation. The upper part of the figure is a typical volumetric model of the virgin zone, which consists of matrix and dry clay, clay-bound water, capillary-bound water, movable water, oil, and gas. The middle part of the

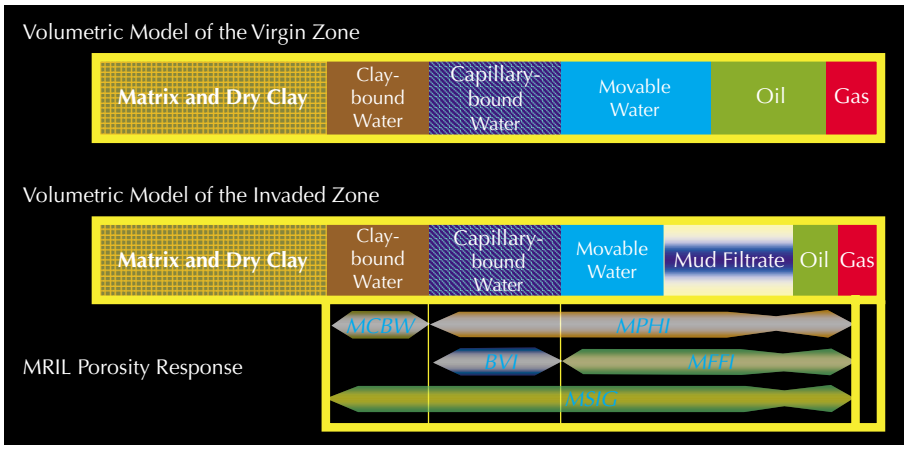

Figure 3.15—MRIL tools respond to the flushed-zone (bottom volumetric model), in which mud filtrate has displaced some of the free fluids that were present in the virgin zone (top volumetric model). MRIL responses (bottom) are sensitive to fluids but not to matrix materials and dry clay. MRIL porosity is affected by hydrogen index (*HI*), polarization time (*TW*), and inter-echo spacing (*TE*).

figure is the corresponding volumetric model for the invaded zone, which is the region in which MRIL measurements are made; all model elements remain the same as in the virgin zone except that the mud filtrate now displaces some of the movable water, oil, and gas. The bottom part of the figure illustrates the MRIL response to porosity elements. Note that *MFFI* refers to the same quantity as *FFI*, and *MPHI* does not include the contribution from some of the water that is associated with clay porosity and perhaps other materials with clay-size pores.

Fig 3.15 shows sharp divisions between the porosity elements associated with *MFFI*, *BVI*, and *MCBW*. These sharp divisions in porosity elements do necessarily correspond to sharp divisions in the T_2 spectra. For *BVI*, this has already been discussed in detail. In the case of clays, the water associated with clays has a range of decay times that can overlap decay times for capillary-bound water; thus, a sharp division may not exist between *MCBW* and *BVI* in the T_2 spectra.

Both matrix minerals and dry clay can contain hydrogen atoms in the form of hydroxyl groups (OH). Because the T_1 relaxation times of these nuclei are too long to be polarized by a moving MRIL tool, and their T_2 relaxation times are too short to be recorded, hydrogen in OH groups and in water of hydration is invisible to the MRIL tool.[23] The hydrogen nuclei of clay-bound water are adsorbed on the surfaces of clay grains. These hydrogen protons in clay-bound water can be polarized by the MRIL tool and can be recorded as long as a sufficiently short *TE* is used. The clay-bound water is measured by an MRIL CPMG sequence with *TE* = 0.6 ms and with polarization time *TW* set for partial or full recovery. The measurement yields the component of porosity referred to as *MCBW*, which provides an estimate of clay-bound water. Similarly, hydrogen protons exist in capillary-bound water and movable fluids, such as movable water, mud filtrates, oil, and gas. These hydrogen protons are measured using a standard T_2-logging CPMG sequence with *TE* = 1.2 ms and with *TW* set for full polarization. This measurement yields *MPHI*.

The measured echo-train amplitude, and thus *MPHI*, is affected by the hydrogen index *HI* of the fluids. *MPHI* is calibrated to the number of protons in water having a hydrogen index of 1. If the hydrogen index of any of the fluids in the pore space is significantly different from 1, then a correction to *MPHI* is required.

Both *MPHI* and *MCBW* are affected by the polarization time *TW*. Both light oil and gas have very long T_1 relaxation times. If the polarization time is too short, then *MPHI* may underestimate effective porosity.

Both *MPHI* and *MCBW* are affected by inter-echo spacing *TE*. As *TE* decreases, faster T_2 relaxation components can be detected. Conversely, increasing *TE* causes the loss of fast T_2 components, which in turn causes *MPHI* and *MCBW* to be too low.

In addition, *MPHI* and *MCBW* measurements are both affected by the 90° $\mathbf{B}_1$ pulse in their CPMG sequences. If the pulse angles are less than 90°, the magnetization will be under-tipped, the measured amplitude thus will be too small, and both *MPHI* and *MCBW* will be underestimated. If their pulse angles are greater than 90°, then the magnetization will be over-tipped, the measured amplitude will once more be too small, and both *MPHI* and *MCBW* will be underestimated again. Calibration usually solves this problem.

References

1. Cowan, B., 1997, *Nuclear Magnetic Resonance and Relaxation*, Cambridge, Cambridge University Press, Cambridge, U.K., p. 207–234.
2. Guimaraes, A.P., 1998, *Magnetism and Magnetic Resonance in Solids*, New York, John Wiley & Sons, Inc., New York, p. 203–225.
3. Bendel, P., 1990, Spin-echo attenuation by diffusion in non-uniform field gradients, *Journal of Magnetic Resonance*, v. 86, p. 509–515.
4. Kenyon, W.E., 1992, Nuclear magnetic resonance as a petrophysical measurement, *Nuclear Geophysics*, v. 6, no. 2, p. 153–171. Later revised and published in 1997 as Petrophysical principles of applications of NMR logging, The Log Analyst, v. 38, no. 2, p. 21–43.
5. Vinegar, H., 1995, Relaxation mechanisms, chapter 3, in Georgi, D.T., ed., *36th Annual SPWLA Logging Symposium: Nuclear magnetic resonance logging short course notes*, variously paginated.
6. Prammer, M.G., et al., 1995, Lithology-independent gas detection by gradient-NMR logging, SPE 30562, *1999 SPE Annual Technical Conference and Exhibition Proceedings*, v. Ω (Formation evaluation and reservoir geology), p. 325–336.
7. Zhang, Q., et al., 1998, Some exceptions to default NMR rock and fluid properties, *SPWLA 39th Annual Logging Symposium Transactions*.
8. Brownstein, K.R., and Tarr, C.E., 1979, Importance of classical diffusion in NMR studies of water in biological cells, *Physical Review*, Series A, v. 19, p. 2446–2453.
9. Kleinberg, R.L., Kenyon, W.E., and Mitra, P.P., 1994, Mechanism of NMR relaxation of fluids in rock, *Journal of Magnetic Resonance*, Series A, v. 108, no. 2, p. 206–214.
10. Chang, D., et al., 1994, Effective porosity, producible fluid and permeability in carbonates from NMR logging, paper A, *35th Annual SPWLA Logging Symposium Transactions*, 21 p. Later published in 1997 in The Log Analyst, v. 38, no. 2, p. 60–72.
11. Chen, R., et al., 1994, Effects of hydrostatic pressure on proton and deuteron magnetic resonance of water in natural rock and artificial porous media, *Journal of Magnetic Resonance, Series A*, v. 110, p. 77–81.

12. Mardon, D., Prammer, M.G., and Coates, G.R., 1996, Characterization of light hydrocarbon reservoirs by gradient-NMR well logging, *Magnetic Resonance Imaging*, v. 14, no. 7/8, p. 769–777.

13. Appel, M., Freeman, J.J., Perkins, R.B., Hofman, J.P., 1999, Restricted diffusion and internal field gradients paper, *SPWLA 40th Annual Logging Symposium Transactions*.

14. Kenyon, W.E., et al., 1986, Compact and consistent representation of rock NMR data from permeability estimation, SPE 15643, 1986 SPE Annual Technical Conference and Exhibition preprint, 22 p. Later published in 1988 as a three-part study of NMR longitudinal relaxation properties of water-saturated sandstones, *SPE Formation Evaluation*, v. 3, no. 3, p. 622–636.

15. Kenyon, W.E., et al., 1989, Pore-size distribution and NMR in microporous cherty sandstones, paper LL, in, *30th Annual SPWLA Logging Symposium Transactions*, 24 p.

16. Golub, G.H., and Van Loan, C.F., 1983, *Matrix computation*, The Johns Hopkins University Press.

17. Marschall, D., Gardner, J.S., Mardon, D., and Coates, G.R., 1995, *Method for correlating NMR relaxometry and mercury injection data*, SCA 9511 *International SCA Symposium proceedings: SPWLA Society of Core Analysts Chapter-at-Large*, 12 p.

18. Coates, G., et al., 1997, *A new characterization of bulk-volume irreducible using magnetic resonance*, paper QQ, 38th Annual SPWLA Logging Symposium Transactions, 14 p. Also published in 1997 in *DiaLog*, London Petrophysical Society, v. 5, no. 6, p. 9–16.

19. Chen, S., et al., 1998, Methods for computing Swi and *BVI* from NMR logs, *HI*, 39th SPWLA Annual Logging Symposium.

20. Kleinberg, R.L., and Boyd, A., 1997, Tapered cutoffs for magnetic resonance bound water volume, SPE 38737, *1997 SPE Annual Technical Conference and Exhibition Proceedings*, v. Ω (Formation evaluation and reservoir geology), part 2, p. 197–202.

21. Pittman, E.D., 1992, Relationship of porosity and permeability to various parameters derived from mercury injection-capillary pressure curves for sandstone, *AAPG Bulletin*, v. 76, no. 2, p. 191–198.

22. Thompson, A., Katz, A.J., and Krohn, C.E., 1987, The micro-geometry and transport properties of sedimentary rock, *Advances in Physics*, v. 36, p. 625–694.

23. Prammer, M.G., et al., 1996, Measurements of clay-bound water and total porosity by magnetic resonance logging, SPE 36522, *1996 SPE Annual Technical Conference and Exhibition Proceedings*, v. Ω (Formation evaluation and reservoir geology), p. 111–118. Also published in 1996 in *The Log Analyst*, v. 37, no. 5, p. 61–69.

More discussion on fluid properties and NMR petrophysics can be found in the following literature:

Ahmed, U., Crary, S.F., and Coates, G.R., 1989, Permeability estimation; the various sources and their interrelationship, SPE 19604, *SPE Annual Technical Conference and Exhibition Proceedings*, v. Ω (Formation evaluation and reservoir geology), p. 649-662. Later published in 1990 as The interrelationship between various permeability measurements, *1990 SPWLA International Well Logging Symposium Transactions, Beijing Chapter*, 21 p. Later published in 1991 in *Journal of Petroleum Technology*, v. 43, no. 5, p. 578–587. Later reprinted in 1994 in *Petrophysics*, SPE Reprint Series No. 39, p. 118–127.

Allen, D., et al., 1988, Probing for permeability—An introduction of measurements, *The Technical Review*, v. 36, no. 1, p. 6–20.

Baldwin, B.A., 1993, Immobile water determination in shaly sandstone, SCA 9314, in Annual technical conference proceedings: Society of Professional Well Log Analysts, Society of Core Analysts Chapter-at-Large, 14 p. Later published in 1994 in *The Log Analyst*, v. 35, no. 3, p. 31–37.

Banavar, J.R., and Schwartz, L.M., 1987, Magnetic resonance as a probe of permeability in porous media, *Physical Review Letters*, v. 58, no. 14, p. 1411–1414.

Banavar, J.R., and Schwartz,L.M., 1989, Probing porous media with nuclear magnetic resonance, in Klafter, J., and Drake, J.M., eds., *Molecular dynamics in restricted geometries*, Wiley, New York, p. 273–310.

Basan, P., et al., 1994, Variations in NMR relaxivity and its relationship to pore size in sandstones from the South Morecambe Field, Irish Sea, paper AA, *16th SPWLA European Formation Evaluation Symposium Transactions, Aberdeen Chapter*, 39 p.

Bergman, D.J., and Dunn, K.J., 1994, Theory of diffusion in a porous medium with applications to pulsed-field-gradient NMR, *Physical Review*, Series B, v. 50, p. 9153.

Bergman, D.J., and Dunn, K.J., 1995, NMR of diffusing atoms in a periodic porous medium in the presence of a nonuniform magnetic field, *Physical Review*, Series E, v. 52, no. 6, p. 6516.

Bergman, D.J., Dunn, K.J., and LaTorraca, G.A., 1995, Magnetic susceptibility contrast and fixed field gradient effects on the spin-echo amplitude in a periodic porous medium diffusion, *Bulletin of the American Physical Society*, v. 40, p. 695.

Blackband, S., et al., 1984, Discrimination of crude oil and water in sand and in bore cores using NMR imaging, SPE 13401: Society of Petroleum Engineers, 17 p. Later published in 1986 in *SPE Formation Evaluation*, v. 1, no. 1, p. 31–34.

Bobroff, S., et al., 1996, Quantitative porosity profiles and wettability contrast visualization in sandstone by CPMG imaging, *Magnetic Resonance Imaging*, v. 14, no. 7/8, p. 907–909.

Borgia, G.C., et al., 1990, Specific surface and fluid transport in sandstones through NMR studies, SPE 20921, *1990 SPE European petroleum conference [Europec 90] Proceedings*. Later published in 1992 in *SPE Formation Evaluation*, v. 7, no. 3, p. 206–210.

Borgia, G.C., et al., 1996, Developments in core analysis by NMR measurements, *Magnetic Resonance Imaging*, v. 14, no. 7/8, p. 751–760.

Borgia, G.C., et al., 1991, Proceedings of the first international conference on recent advances in NMR applications to porous media, *Magnetic Resonance Imaging*, v. 9, no. 5, p. 639–888.

Borgia, G.C., et al., editors, 1994, Proceedings of the second international meeting on recent advances in MR applications to porous media, *Magnetic Resonance Imaging*, v. 12, no. 2.

Borgia, G., Brancolini, A., Brown, R.J.S., Fantazzini, P., and Ragazzini, G., 1994, Water-air saturation changes in restricted geometries studied by proton relaxation, *Magnetic Resonance Imagin*g, v. 12, p. 191–195.

Borgia, G.C., et al., 1994, Capillary water determination in core plugs; a combined study based on imaging techniques and relaxation analysis, *Magnetic Resonance Imaging*, v. 12, no. 2, p. 221–224.

Borgia, G.C., et al., 1990, Specific surface and fluid transport in sandstones through NMR studies, SPE 20921, *1990 SPE European petroleum conference [Europec 90] Proceedings*. Later published in 1992 in *SPE Formation Evaluation*, v. 7, no. 3, p. 206–210.

Borgia, G.C., Brown, R.J.S., and Fantazzini, P., 1995, The effect of diffusion and susceptibility differences on T_2 measurements for fluids in porous media and biological tissues, *Magnetic Resonance Imaging*, v. 14, no. 7/8, p. 731–736.

Borgia, G.C., Brown, R.J.S., and Fantazzini, P., 1995, Scaling of spin-echo amplitudes with frequency, diffusion coefficient, pore size and susceptibility difference for the NMR of fluids in porous media and biological tissues, *Physical Review*, Series E, v. 51, p. 2104.

Bowers, M.C., et al., 1993, Determination of porosity types from NMR data and their relationship to porosity types derived from thin section, SPE 26307, unsolicited paper, 45 p. Later published in 1995 in *Journal of Petroleum Science and Engineering*, v. 13, p. 1–14.

Brown, R. J. S., 1961, Proton Relaxation in Crude Oils, *Nature*, v. 189, no. 4762, 387–388.

Brownstein, K.R., and Tarr, C.E., 1977, Spin-lattice relaxation in a system governed by diffusion, *Journal of Magnetic Resonance*, v. 26, p. 17–24.

Carr, M.B., et al., 1996, Correlation of porosity types derived from NMR data and thin section image analysis in a carbonate reservoir, *Journal of Petroleum Science and Engineering*, v. 14, p. 115–131.

Chen, Q., Wang, W., and Cai, X., 1996, Application of NMR imaging to steam foam flooding in porous media, *Magnetic Resonance Imaging*, v. 14, no. 7/8, p. 949–950.

Chen, S., and Georgi, D.T., 1997, Improving the accuracy of NMR relaxation distribution analysis in clay-rich reservoirs and core samples, SCA 9702, in 1997 international symposium proceedings: Society of Professional Well Log Analysts, Society of Core Analysts Chapter-at-Large, 10 p.

Chen, S., et al., 1992, Quantitative NMR imaging of multiphase flow in porous media, *Magnetic Resonance Imaging*, v. 10, p. 815–826.

Chen, S., Liaw, H.K., and Watson, A.T., 1993, Fluid saturation-dependent nuclear magnetic resonance spin-lattice relaxation in porous media and pore structure analysis, *Journal of Applied Physics*, v. 74, no. 3, p. 1473–1479.

Chen, S., Liaw, H.-K., and Watson, A.T., 1994, Measurements and analysis of fluid saturation-dependent NMR relaxation and linebroadening in porous media, *Magnetic Resonance Imaging*, v. 12, no. 2, p. 201–202.

Chen, S., et al., 1993, Characterization of rock pore structures using NMR restricted diffusion measurements and analyses, SCA 9313, in Annual technical conference proceedings: Society of Professional Well Log Analysts, Society of Core Analysts Chapter-at-Large, 15 p.

Chen, S., et al., 1992, NMR imaging of multiphase flow in porous media, SPE 24760, *1992 SPE Annual Technical Conference and Exhibition Proceedings*, v. Ω (Formation evaluation and reservoir geology), p. 1013–1026. Also published in 1993: *AIChE Journal* (American Institute of Chemical Engineers), v. 39, no. 6, p. 925–934.

Chen, S., Qin, F., and Watson, A.T., 1994, Determination of fluid saturations during multiphase flow experiments using NMR imaging techniques, *AIChE Journal*, v. 40, p. 1238–1245.

Chen, S., et al., 1994, Characterization of fractures and multiphase flow in fractured permeable rocks using NMR imaging techniques, SCA 9402, in SCA international symposium proceedings: Society of Professional Well Log Analysts, Society of Core Analysts, Chapter-at-Large, p. 17–28. Also published in 1994 as, NMRI characterization of fractures and multiphase transport in fractured porous media, SPE 28369, *1994 SPE Annual Technical Conference and Exhibition Proceedings*, v. Ω (Formation evaluation and reservoir geology), p. 65–79.

Chen, S., Ostroff, G., Georgi, D., 1998, Improving estimation of NMR log $T_{2cutoff}$ value with core NMR and capillary pressure measurements, SCA 9822.

Coates, G., et al., 1997, A new characterization of bulk-volume irreducible using magnetic resonance, paper QQ, *38th Annual SPWLA Logging Symposium Transactions*, 14 p. Also published in 1997 in DiaLog (London Petrophysical Society), v. 5, no. 6, p. 9–16.

Coates, G. R., et al., 1993, Restrictive diffusion from uniform gradient NMR Well Logging, SPE 26472.

Curwen, D.W., and Molaro, C., 1995, Permeability from magnetic resonance imaging logs, paper GG, in *36th Annual SPWLA Logging Symposium Transactions*, 12 p.

Davies, S., et al., 1990, Pore-size distributions from NMR spin-lattice relaxation measurements of fluid saturated porous solids, part 2, Application to reservoir core samples, *Journal of Applied Physics*, v. 67, no. 6, p. 3171–3176.

Davies, S., and Packer, K.J., 1990, Pore-size distributions from NMR spin-lattice relaxation measurements of fluid-saturated porous solids, part 1, Theory and simulation, *Journal of Applied Physics*, v. 67, p. 3163–3170.

Dodge, W.S., Shafer, J., and Klimentidis, R., 1996, Capillary pressure—the key to producible porosity, paper J, in *37th Annual SPWLA Logging Symposium Transactions*,13 p.

D'Orazio, F., et al., 1989, Application of nuclear magnetic resonance pore structure analysis to porous silica, *Journal of Applied Physics*, v. 65, p. 742–751.

Dawson, R., Khoury, F., and Kobayashi, R., 1970, Self-Diffusion Measurements in Methane by Pulsed Nuclear Magnetic Resonance, *AIChEJ*, Vol. 16, No. 5, 725–729.

Dunn, K-J., et al., 1994, On the calculation and interpretation of NMR relaxation time distributions, SPE 28367, *1994 SPE Annual Technical Conference and Exhibition Proceedings*, v. Ω (Formation evaluation and reservoir geology), p. 45–54.

Foley, I., Farooqui, S. A., and Kleinberg, R. L., 1996, Effect of paramagnetic ions on NMR relaxation of fluids at solid surfaces, *Journal of Magnetic Resonance*, Series A, v. 123, 95–104.

Freedman, R., and Morriss, C.E., 1995, Processing data from an NMR logging tool, SPE 30560, *1995 SPE Annual Technical Conference and Exhibition Proceedings*, v. Ω (Formation evaluation and reservoir geology), p. 301–316.

Gallegos, D.P., Munn, K., Douglas, M.S., and Stermer, D.L., 1988, NMR technique for the analysis of pore structure application to materials with well-defined pore structure, *Journal of Colloid and Interface Science*, v. 119, no. 1, p. 127–140.

Gallegos, D.P., and Smith, D.M., 1988, A NMR technique for the analysis of pore-structure—determination of continuous pore size distributions, *Journal of Colloid and Interface Science*, v. 122, no. 1, p. 143–153.

Gallegos, D.P., Smith, D.M., and Brinker, C.J., 1988, An NMR technique for the analysis of pore structure—application to mesopores and micropores, *Journal of Colloid and Interface Science*, v. 124, p. 186–198.

Glasel, J.A., 1970, NMR relaxation in heterogeneous systems, *Nature*, v. 227, p. 704—705.

Glasel, J.A., and Lee, K.H., 1979, On the interpretation of water nuclear magnetic resonance relaxation times in heterogeneous systems, *Journal of the American Chemical Society*, v. 96, p. 970–978.

Godefroy, S., et al., 1999, NMR surface relaxivity and diffusion effects in grain packs, SCA 9920.

Harris, K. R., 1978, The Density Dependence of the Self-Diffusion Coefficient of Methane at -50°, 25°, and 50°C, Physica, v. 94A, 448–464.

Hawkins, J.M., Skopec, R.A., 1998, Nuclear magnetic resonance versus air/brine capillary pressure permeability correlations: how good are our assumptions in the empirical determination of permeability, SCA 9824.

Howard, J. J., Kenyon, W. E., and Straley, C., 1993, Proton magnetic resonance and pore–size variation in reservoir sandstones, *SPE Formation Evaluation*, p. 194.

Howard, J.J., and Kenyon, W.E., 1992, Determination of pore size distribution in sedimentary rocks by proton nuclear magnetic resonance, *Marine and Petroleum Geology*, v. 9, no. 2, p. 139–145.

Howard, J.J., Kenyon, W.E., and Straley, C., 1990, Proton-magnetic-resonance and pore-size variations in reservoir sandstones, SPE 20600, *1990 SPE Annual Technical Conference and Exhibition Proceedings*, v. Ω (Formation evaluation and reservoir geology), p. 733–742. Later published in 1993 in SPE Formation Evaluation, v. 8, no. 3, p. 194–200.

Hurlimann, M.D., et al., 1994, Restricted diffusion in sedimentary rocks—determination of surface-area-to-volume ratio and surface relaxivity, *Journal of Magnetic Resonance*, Series A, v. 111, p. 169.

Hurlimann, M.D., Latour, L.L., and Sotak, C.H., 1994, Diffusion measurement in sandstone core—NMR determination of surface-to-volume ratio and surface relaxivity, *Magnetic Resonance Imaging*, v. 12, p. 325–327.

Hurlimann, M. D., et al., 1994, Restricted diffusion in sedimentary rocks—determination of surface-area-to-volume ratio and surface relaxivity, *Journal of Magnetic Resonance*, Series A, v. 111, p. 169–178.

Hurlimann, M. D., 1998, Effective gradients in porous media due to susceptibility differences, *Journal of Magnetic Resonance*, v. 131, p. 232–240.

Jerosch-Herold, M., Thomann, H., and Thompson, A.H., 1991, Nuclear magnetic resonance relaxation in porous media, SPE 22861, *1991 SPE Annual Technical Conference and Exhibition Proceedings*.

Karger, J., and Pfeifer, H., 1987, NMR self-diffusion studies in zeolite science and technology, *Zeolites*, v. 7, p. 90–107.

Karger, J., Pfeifer, H., and Heink, W., 1988, Principles and application of self-diffusion measurements by nuclear magnetic resonance, in Waugh, J.S., editor, *Advances in magnetic resonance*, v. 12, Academic Press, New York, p. 1–89.

Karger, J., and Ruthven, D.M., 1992, *Diffusion in zeolites and other microporous solids*, Wiley, New York.

Katz, A.J., and Thompson, A.H., 1986, Quantitative prediction of permeability in porous rock, *Physical Review*, Series B, v. 34, p. 8179–8191.

Keller, Paul J. Glossary, 1991, *Basic Principles of MR Imaging*, Chapter 4, GE Medical Systems.

Kenyon, W.E., and Kolleeny, J.A., 1995, NMR surface relaxivity of calcite with adsorbed Mn2+, *Journal of Colloid and Interface Science*, v. 170, p. 502–514.

Kenyon, W.E., et al., 1989, Pore-size distribution and NMR in microporous cherty sandstones, paper LL, in, *30th Annual SPWLA Logging Symposium Transactions*, 24 p.

Kenyon, W.E., et al., 1995, A laboratory study of nuclear magnetic resonance relaxation and its relation to depositional texture and petrophysical properties—carbonate Thamama Group, Mubarraz field, Abu Dhabi, SPE 29886, *9th SPE Middle East Oil Show and Conference Proceedings*, v. 2, p. 477–502.

Klein, J., Martin, P., and Widjanarko, W., 1997, Log water saturation model validation using NMR log and core data, paper TT, *38th Annual SPWLA Logging Symposium Transactions*, 13 p.

Kleinberg, R. L. and Vinegar, H. J., 1996, NMR Properties of Reservoir Fluids, *The Log Analyst*, November-December, 20–32.

Kleinberg, R.L., 1994, Pore size distributions, pore coupling, and transverse relaxation spectra of porous rocks, *Magnetic Resonance Imaging*, v. 12, no. 2, p. 271–274.

Kleinberg, R.L., 1995, Petrophysics of the nuclear magnetic resonance tool, chapter 5, in Georgi, D.T., ed., Nuclear magnetic resonance logging short course notes, 36th Annual SPWLA Logging Symposium, variously paginated.

Kleinberg, R.L., Farooqui, S.A., and Horsfield, M.A., 1993, T_1/T_2 ratio and frequency dependence of NMR relaxation in porous sedimentary rocks, *Journal of Colloid and Interface Science*, v. 158, no. 1, p. 195–198.

Kleinberg, et al., 1993, Nuclear magnetic resonance of rocks—T_1 vs. T_2, SPE 26470, *1993 SPE Annual Technical Conference and Exhibition Proceedings*, v. Ω (Formation evaluation and reservoir geology), p. 553–563.

Kleinberg, R. L., 1996, Utility of NMR T_2 Distributions, Connections with Capillary Pressure, Clay Effect, and Determination of the Surface Relaxivity Parameter r_2, *Magnetic Resonance Imaging*, v. 14, no. 7/8, 761–767.

Krynicki, K., 1966, Proton Spin-Lattice Relaxation in Pure Water Between 0°C and 100°C , *Physica*, v. 32, 167–178.

Kubica, P., 1995, Statistical tests of permeability estimates based on NMR measurements, paper VVV, *36th Annual SPWLA Logging Symposium Transactions*, 11 p.

LaTorraca, G.A. Dunn, K.J., and Bergman, D.J., 1995, Magnetic susceptibility contrast effects on NMR T2 logging, paper JJ, *36th Annual SPWLA Logging Symposium Transactions*, 8 p.

LaTorraca, G.A., Dunn, K.J., and Brown, R.J.S., 1993, Predicting permeability from nuclear magnetic resonance and electrical properties measurements, SCA 9312, in Annual technical conference proceedings: Society of Professional Well Log Analysts, Society of Core Analysts Chapter-at-Large, 12 p.

LaTorraca, G. A., et al., 1999, Heavy Oil Viscosity Determination Using NMR Logs, paper PPP, *40th Annual SPWLA Logging Symposium Transactions*, Oslo, Norway, May 30-June 3.

Latour, L.L., Kleinberg, R.L., and Sezginer, A., 1992, Nuclear magnetic resonance properties of rocks at elevated temperatures, *Journal of Colloid and Interface Science*, v. 150, p. 535.

Lipsicas, M., Banavar, J.R., and Willemsen, J., 1986, Surface relaxation and pore sizes in rocks—a nuclear magnetic resonance analysis, *Applied Physics Letters*, v. 48, no. 22, p. 1544–1546.

Lo, S.-W., et al., 1998, Relaxation Time and Diffusion Measurements of Methane and n-Decane Mixtures, *The Log Analyst*, November-December, p. 43–47.

Lyne, A., Varini, G., and Ghilardotti, G., 1996, Determination of petrophysical properties of carbonate rocks by NMR relaxometry, SPE 36852, *1996 SPE European Petroleum Conference Proceedings*, v. 1, p. 331–339.

Mardon, D., et al., 1996, Experimental study of diffusion and relaxation of oil-water mixtures in model porous media, paper K, *37th Annual SPWLA Logging Symposium Transactions*.

Marschall, D.M., 1997, Laboratory MRI investigation in the effects of invert oil muds on primary MRI log determinations, SPE 38739, *1997 SPE Annual Technical Conference and Exhibition Proceedings*, v. Ω (Formation evaluation and reservoir geology), part 2, p. 203–215.

Marschall, D.M., and Coates, G., 1997, Laboratory MRI investigation in the effects of invert oil muds on primary MRI log determinations, SCA 9701, in 1997 international symposium proceedings: Society of Professional Well Log Analysts, Society of Core Analysts Chapter-at-Large, 11 p.

Matteson, A., et al., 1998, "NMR Relaxation of Clay-Brine Mixtures," SPE 49008, *1998 ATCE of SPE Annual Technical Conference and Exhibition Proceedings*, New Orleans, LA.

Morris, C. E., et al., 1997, Hydrocarbon Saturation and viscosity estimation from NMR logging in the Belridge diatomite, *The Log Analyst*, March-April, p. 44–59.

Neretin, V.D., Belorai, Y.L., and Kononenko, I.Y., 1992, A study of permeability and porosity using nuclear magnetic resonance methods, *Nuclear Geophysics*, v. 6, no. 1, p. 121–124.

Ohen, H.A., Ajufo, A., and Curby, F.M., 1995, A hydraulic (flow) unit based model for the determination of petrophysical properties from NMR relaxation measurements, SCA 9514, in International SCA symposium proceedings: Society of Professional Well Log Analysts, Society of Core Analysts Chapter-at-Large, 12 p. Also published in 1995 as SPE 30626, *1995 SPE Annual Technical Conference and Exhibition Proceedings*, v. Ω (Formation evaluation and reservoir geology), p. 983–996.

Prammer, M.G., 1994, NMR pore size distributions and permeability at the well site, SPE 28368, *1994 SPE Annual Technical Conference and Exhibition Proceedings*, v. Ω Formation evaluation and reservoir geology), p. 55–64.

Prammer, M., 1995, Principles of signal processing—NMR data and T_2 distributions, chapter 4, in Georgi, D.T., ed., Nuclear magnetic resonance logging short course notes, *36th Annual SPWLA Logging Symposium Transactions*, variously paginated.

Rueslatten, H., et al., 1998, NMR studies of an iron-rich sandstone oil reservoir, SCA 9821.

Sakurai, S., Loucks, R.G., and Gardner, J.S., 1995, NMR core analysis of Lower San Andres/Glorieta/Upper Clear Fork (Permian) carbonates—central basin platform, west Texas, paper M, *36th Annual SPWLA Logging Symposium Transactions*, 12 p.

Sandor, R., et al., 1994, Frequency dependence of NMR measurements on rock samples, paper L, *16th SPWLA European Formation Evaluation Symposium Transactions*, 8 p.

Seziner, A., et al., 1999, An NMR high-resolution permeability indicator, paper NNN, *40th Annual SPWLA Logging Symposium Transactions*, Oslo, Norway.

Shafer, J. L., Mardon, D., and Gardner, J., 1999, Diffusion effects on NMR response of oil & water in rock: impact of internal gradients, SCA 9916.

Straley, C., et al., 1991, NMR in partially saturated rocks: laboratory insights on free fluid index and comparison with borehole logs, paper CC, *32nd Annual SPWLA Logging Symposium Transactions*, 25 p. Later published in 1994 in *The Log Analyst*, v. 36, no. 1, p. 40 56.

Straley, C., et al., 1994, Core analysis by low field NMR, SCA 9404, in SCA international symposium proceedings: Society of Professional Well Log Analysts, Society of Core Analysts, Chapter-at-Large, p. 43–56. Later published in 1997 in *The Log Analyst*, v. 38, no. 2, p. 84–93.

Taicher, Z., et al., 1994, A comprehensive approach to studies of porous media (rocks) using a laboratory spectrometer and logging tool with similar operating characteristics, *Magnetic Resonance Imaging*, v. 12, no. 2, p. 285–289.

Tariq, S.M., Denoo, S., and Cordes, M., 1997, Permeability estimation from modern NMR logging measurements; experiences and applications in the Rocky Mountain area, SPE 38378, 1997 *SPE Rocky Mountain Regional Meeting/Geological Association Field Conference Proceedings*.

Timur, A., 1967, Pulsed nuclear magnetic resonance studies of porosity, movable fluid and permeability of sandstones, SPE 2045, SPE 42nd annual meeting preprint. Later published in 1969 in *Journal of Petroleum Technology*, v. 21, no. 6, p. 775–786.

Timur, A., 1968, An investigation of permeability, porosity, and residual water saturation relationships for sandstone reservoirs, paper J, *9th Annual SPWLA Logging Symposium Transactions*, 18 p. Later published in 1968 in *The Log Analyst*, v. 9, no. 4, July-August, p. 8–17. Later reprinted in 1994 in *Petrophysics*, SPE Reprint Series No. 39, p. 128–137.

Timur, A., 1968, Effective porosity and permeability of sandstones investigated through nuclear magnetic principles, paper K, *9th Annual SPWLA Logging Symposium Transactions*, 18 p. Later published in 1969 in *The Log Analyst*, v. 10, no. 1, January-February, p. 3–11.

Timur, A., 1972, Nuclear magnetic resonance study of carbonates, paper N, *13th Annual SPWLA Logging Symposium Transactions*, 15 p. Later published in 1972 in *The Log Analyst*, v. 13, no. 5, p. 3–11.

Tutunjian, P.N., et al., 1993, Characterization of pore microgeometry by NMR diffusion measurements, paper II, in *34th Annual SPWLA Logging Symposium Transactions*, 13 p.

Vinegar, H. J., et al., 1991, Whole-Core Analysis by ^{13}C NMR, *SPE Formation Evaluation*, p. 183–189.

Volokitin, Y., et al., 1999, Constructing capillary pressure curves from NMR log data in the presence of hydrocarbons, *40th Annual SPWLA Logging Symposium Transactions*.

Xiao, L.Z., 1998, *NMR imaging logging principles and applications*, Science Press (in Chinese), Beijing, 328 p.

Zhang, Q., et al., 1998, Some exceptions to default NMR rock and fluid properties, FF, *39th Annual SPWLA Logging Symposium Transactions*.

Zhang, Q., Hirasaki, G. J., and House, W. V., 1998, Diffusion in internal field gradients, SCA 9823.

Chapter 4

Fundamentals of NMR Hydrocarbon Typing

The NMR properties of different reservoir fluids are quite different from one another. These differences make it possible to type hydrocarbons and sometimes to quantify their volumes. This chapter first reviews NMR properties of hydrocarbons and NMR hydrocarbon-typing techniques based on T_1 relaxation and/or diffusivity contrast. The chapter then discusses qualitative forward modeling of oil and gas effects on T_2 distributions under different conditions.

NMR Properties of Hydrocarbons

NMR properties, such as the T_1 and T_2, of oil and gas at reservoir conditions in a water-wet rock, can be calculated based on the equations introduced in Chapter 3. The T_1 and T_2 of dead oil and gas are given in Eqs. 4.1 through 4.4.

Dead Oil

$$T_1 = 0.00713\,\frac{T_k}{\eta} \tag{4.1}$$

$$T_2^{-1} = \left(0.00713\,\frac{T_k}{\eta}\right)^{-1} + 2.5\times10^{-5}\,\frac{T_K}{298\eta}\,\frac{(\gamma G\,TE)^2}{12} \tag{4.2}$$

Gas

$$T_1 = 2.5\times10^{4}\left[\frac{\rho_g}{T_k^{\,1.17}}\right] \tag{4.3}$$

$$T_2^{-1} = \left[2.5\times10^{4}\left(\frac{\rho_g}{T_k^{1.17}}\right)\right]^{-1} + 8.5\times10^{-7}\left(\frac{T_k^{0.9}}{\rho_g}\right)\frac{(\gamma G\,TE)^2}{12} \tag{4.4}$$

Eqs. 4.1 through 4.4 assume that the relaxation is given by the bulk fluid relaxation for T_1, and that the T_2 relaxation is composed of a bulk relaxation term and a diffusion term. The expressions for the diffusion coefficients—Eqs. 3.12 and 3.13—have been used in Eqs. 4.2 and 4.4. In the absence of diffusion, T_1 and T_2 are taken to be equal. The water-wet condition implies that a layer of water coats the rock grains and thus prevents contact between the rock grain and any hydrocarbon fluid. Consequently, there is no surface relaxation term. The lack of surface relaxation for oil in water-wet rocks is confirmed by numerous laboratory and field observations. However, in a series of experiments, Straley in 1997[1] unexpectedly found an apparent surface relaxation component for the relaxation of methane in both a sandstone sample and a carbonate sample. At this time, the results have not been confirmed by work at other laboratories, and no theoretical explanation for this observation has been published. The surface relaxation component reported by Straley would have a minimal effect on gas detection using the TDA method discussed in Chapter 6. That this effect would be minimal can be verified by examination of the TDA equations found in the Chapter 6 Appendix.

In reality, the T_2 of crude oil is a distribution of values rather than a single value and depends on viscosity.[2,3] As viscosity increases, the hydrogen protons become less mobile and thus relax more quickly. Therefore, increases in viscosity shorten the T_2 geometric mean. More viscous oils usually also have broader T_2 distributions. The broadening is due to the different mobilities of the protons in the different oil components. More viscous oils are often composed of a wider variety of hydrocarbons. Even some light oils have multiple components and can exhibit a broadened T_2 distribution. NMR T_2 measurements on several crude oils with different viscosities are illustrated in **Fig. 4.1**.

The NMR response of gas is quite different from the responses of water and oil under typical reservoir conditions.[4, 5] NMR measurements can thus be used to quantify the gas phase in a reservoir. Dry natural gas is composed mostly of methane (CH_4), along with other light hydrocarbons and often with small amounts of non-hydrocarbon substances. **Fig. 4.2** shows how the hydrogen index, diffusion coefficient, and T_1 and T_2 relaxation times of methane vary with pressure and temperature.[1, 6, 7]

Table 4.1 is an example of NMR properties of bulk fluids, such as brine, oil, and gas, at reservoir conditions.[6] The differences in T_1, T_2, and D among these fluids at reservoir condition form the foundation for NMR fluid typing. Two methods of hydrocarbon typing have been developed: dual-*TW* and dual-*TE*. The dual-*TW* method is based on the T_1 contrast between water and light hydrocarbons. The dual-*TE* method is based on the diffusivity difference between water and medium viscosity oil or between liquid and gas.

Table 4.1—NMR Properties of Reservoir Fluids

Fluid	T_1 (ms)	T_2 (ms)	Typical T_1/T_2	*HI*	η (cp)	$D_0 \times 10^{-5}$ (cm^2/s)
Brine	1 - 500	1 - 500	2	1	0.2 - 0.8	1.8 - 7
Oil	3,000 - 4,000	300 - 1,000	4	1	0.2 - 1,000	0.0015 - 7.6
Gas	4,000 - 5,000	30 - 60	80	0.2 - 0.4	0.011 - 0.014 methane	80 - 100

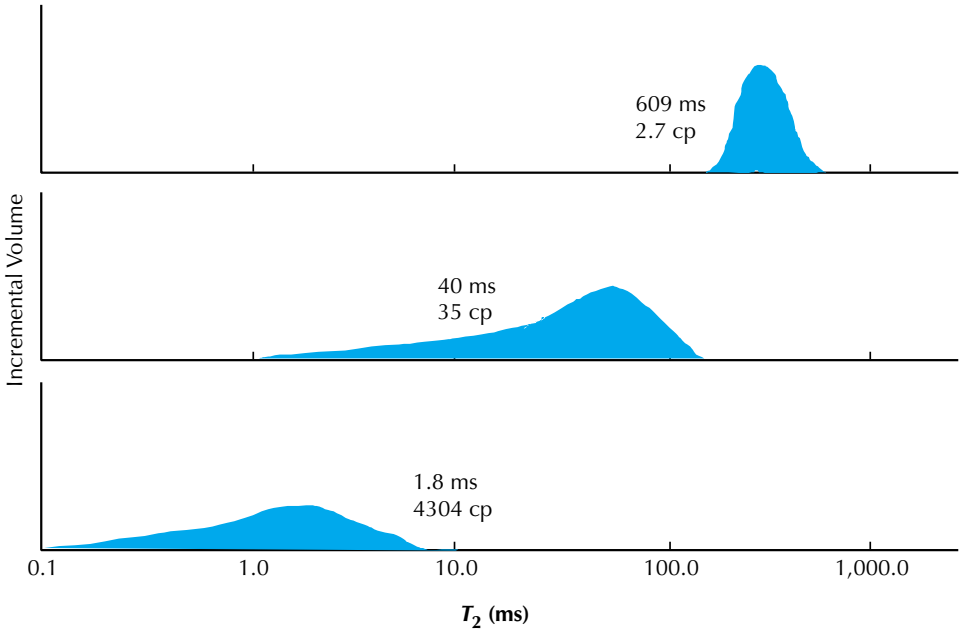

om000866

Figure 4.1—The T_2 of crude oil varies with viscosity, as shown in these T_2 distributions for three oil samples. For the light oil (top), which has a viscosity of 2.7 cp, the measured T_2 values are clustered tightly about a single value, namely, 609 ms. For the medium-viscosity oil (middle), which has a viscosity of 35 cp, the measured T_2 values form a broad distribution with a lower-end tail and a geometric mean of 40 ms. For a much heavier crude oil (bottom), which has a viscosity of 4304 cp, the measured T_2 values also form a broad distribution with a lower-end tail but with a geometric mean of only 1.8 ms.

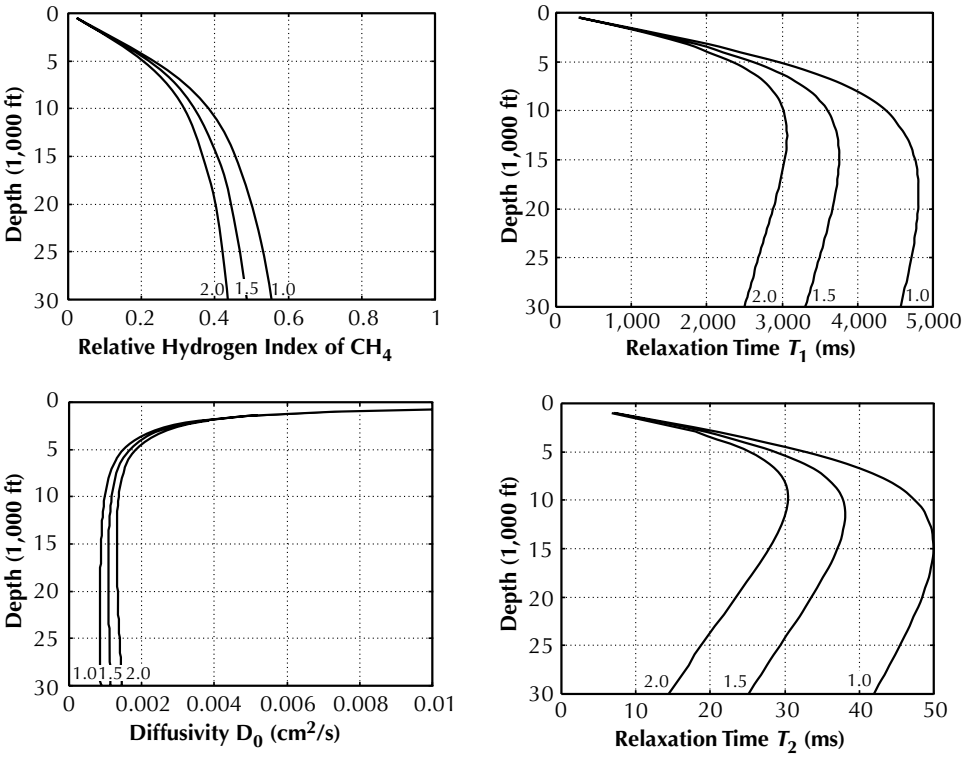

om000867

Figure 4.2—The hydrogen index, bulk diffusion coefficient, and T_1 and T_2 relaxation times of methane vary with pressure (depth) and temperature. In these charts, curves correspond to different temperature gradients, expressed in °F/100 ft. The hydrogen index and T_1 charts assume a pressure gradient of 43.3 psi/100 ft. The T_2 chart is based on the bulk diffusion chart and assumes (1) TE = 0.6 ms, (2) a magnetic field gradient of 18 gauss/cm, and (3) a diffusion restriction (D/D_g) of 0.7 in rock pores, where D is the diffusion coefficient of methane situated in the rock pores and D_g is the bulk diffusion coefficient of methane. According to these charts, at a depth of 25,000 ft, a temperature gradient of 1.5 °F/100 ft, and a pressure gradient of 43.3 psi/100 ft, methane will have a hydrogen index of 0.48, a bulk diffusion coefficient of 0.0015, a T_1 of 3,500 ms, and a T_2 of 29 ms. Under these conditions, a gas signal will be detectable by an MRIL tool.

NMR Hydrocarbon Typing

T_2 Distribution of a Partially Saturated Rock

As was illustrated in Fig. 3.11, a single pore, fully saturated with water, exhibits a sharp peak at a moderate T_2 value on the T_2 distribution. As the movable water is displaced by oil, the single peak on the T_2 distribution separates into two peaks. One peak often appears as a very low amplitude peak below the original T_2 value and is attributable to irreducible water in smaller pores and on the pore surface. The other peak, which appears above the original T_2 value, is attributable to the oil, and the T_2 value of this peak is close to the T_2 of bulk oil. This phenomenon is shown in **Fig. 4.3** for a North Sea chalk. North Sea chalks exhibit an unusually large amount of irreducible water associated with the pore surface.

T_1 Relaxation Contrast

Table 4.1 and Eqs. 4.1 and 4.3 show that gas and oil each have T_1 relaxation times much longer than that of brine. Therefore, for full polarization, a longer TW is needed for hydrocarbons than for water. Dual-TW measurements are based on the T_1 contrast between water and light hydrocarbons, and are made using two TW values, TW_{short} and TW_{long}.

For the short TW,

$$M_{TW_{short}}(t) = \sum M(0_i)\left(1 - e^{-TW_{short}/T_{1wi}}\right)e^{-t/T_{2wi}} + M_{oil}\left(1 - e^{-TW_{short}/T_{1oil}}\right)e^{-t/T_{2oil}} + M_{gas}\left(1 - e^{-TW_{short}/T_{1gas}}\right)e^{-t/T_{2gas}} \quad (4.5)$$

For the long TW,

$$M_{TW_{long}}(t) = \sum M(0_i)\left(1 - e^{-TW_{long}/T_{1wi}}\right)e^{-t/T_{2wi}} + M_{oil}\left(1 - e^{-TW_{long}/T_{1oil}}\right)e^{-t/T_{2oil}} + M_{gas}\left(1 - e^{-TW_{long}/T_{1\,gas}}\right)e^{-t/T_{2gas}} \quad (4.6)$$

where, $T_{1\text{wi}}$ and $T_{2\text{wi}}$ are the T_1 and T_2 of water in the i^{th} bin respectively.

Fig. 4.4 illustrates the dual-TW method. A TW of three times T_1 is required to achieve 95% polarization. The maximum T_1 of water in sandstone pores is about 0.5 s, and the minimum T_1 of light hydrocarbons is about 3 s. Therefore, water will be fully polarized by using a TW_{short} at least 1.5 s (Fig. 4.4, upper left), and hydrocarbons will be adequately polarized in many cases by using a TW_{long} of 9 s (Fig. 4.4, upper right). (TW_{long} may need to be adjusted for the hydrocarbon pressure and temperature, and for gas it may not be practical to achieve complete polarization.) Because water is fully polarized at both the short and long polarization

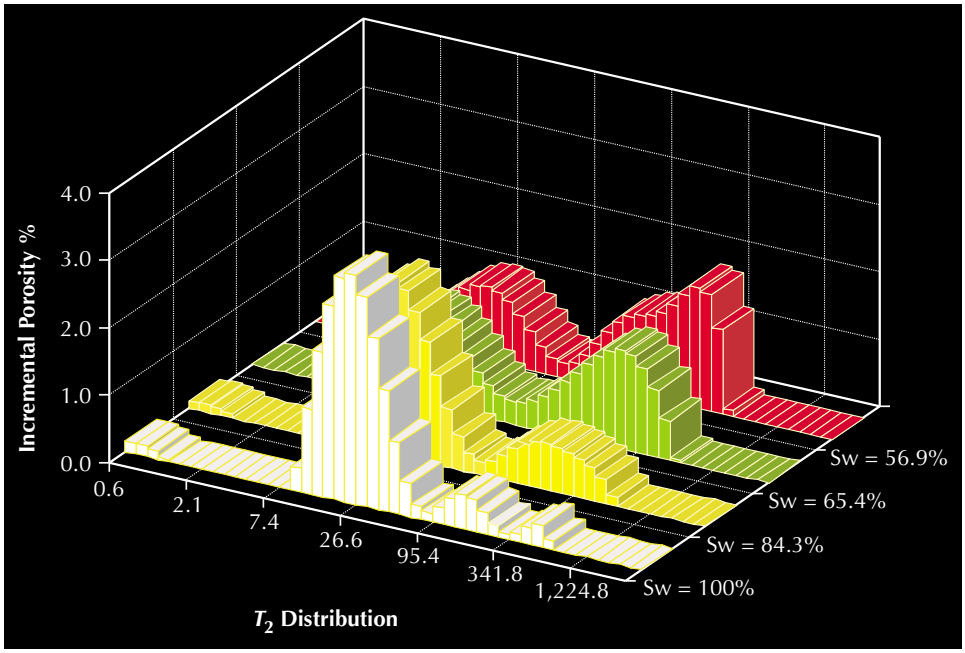

om000865

Figure 4.3—A North Sea chalk sample demonstrates how T_2 distributions vary with water saturation. At S_w = 100%, the sample exhibits a simple pore-size distribution: the signal is mainly focused at T_2 = 27 ms, indicating essentially one pore size. As S_w decreases (oil saturation increases), the amplitude of the water peak of the T_2 distribution decreases because of the decreasing volume of water. The amplitude of the oil peak at about 200 ms increases because of the increasing oil volume. Furthermore, because the surface-to-volume ratio of the water signal is changing (assuming that pore surface area remains the same and that surface relaxivity does not change, but that water volume is decreasing), the T_2 value for the water also decreases.

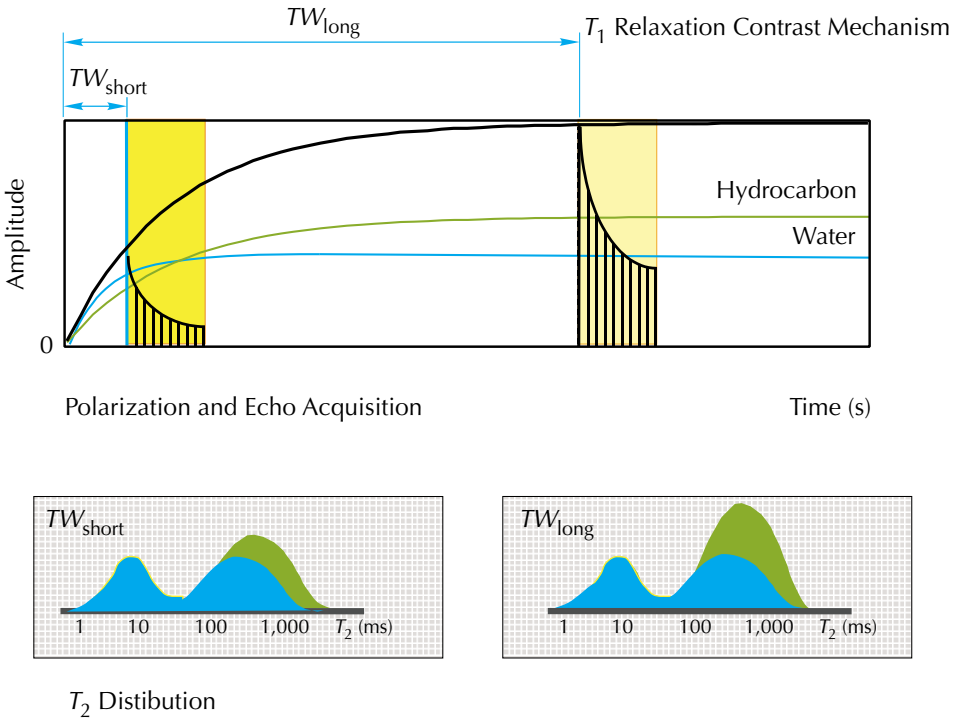

om000869

Figure 4.4—In the dual-*TW* measurement, only water can fully polarize during TW_{short}, while both water and hydrocarbons can fully polarize during TW_{long}. Results obtained by taking the difference between the resulting T_2 distributions are used to detect and quantify hydrocarbons.

times, it will have the same amplitude on the resulting T_2 distributions (Fig. 4.4, bottom). However, light hydrocarbons will be fully polarized only when TW_{long} is used. Therefore, the difference of the two T_2 distributions acquired with TW_{long} and TW_{short} will leave only the hydrocarbon components. Thus, light hydrocarbons can be detected and quantified, the methods of which will be discussed in Chapter 6.

Diffusivity Contrast

$T_{2diffusion}$ depends on D, G, and TE. For brines, medium-viscosity oils, and heavy oils, D_{gas} is much greater than D_w, and the D_w is much greater than D_{oil}. (See **Table 4.1**.) Thus, $T_{2diffusion}$ will be very different among these fluids, and the differences can be amplified by NMR measurements made with different TE. Dual-TE measurements use two TE values, TE_{short} and TE_{long}.

For the short TE,

$$M_{TE_{short}}(t) = \sum M(0_i)\left(1 - e^{-TW/T_{1wi}}\right) e^{-t\left(\frac{1}{T_{2w}} + \rho\frac{S}{V} + D_w\frac{(\gamma G\, TE_{short})^2}{12}\right)} + M_{oil}\left(1 - e^{-TW/T_{1oil}}\right) e^{-t\left(\frac{1}{T_{2oil}} + D_{oil}\frac{(\gamma G\, TE_{short})^2}{12}\right)} + M_{gas}\left(1 - e^{-TW/T_{1gas}}\right) e^{-t\left(D_{gas}\frac{(\gamma G\, TE_{short})^2}{12}\right)} \tag{4.7}$$

When $TW >> 3\times\max(T_{1w}, T_{1oil}, T_{1gas})$,

$$M_{TE_{short}}(t) = \sum M(0_i) e^{-t\left(\frac{1}{T_{2w}} + \rho\frac{S}{V} + D_w\frac{(\gamma G\, TE_{short})^2}{12}\right)} + M_{oil}\, e^{-t\left(\frac{1}{T_{2oil}} + D_{oil}\frac{(\gamma G\, TE_{short})^2}{12}\right)} + M_{gas}\, e^{-t\left(D_{gas}\frac{(\gamma G\, TE_{short})^2}{12}\right)} \tag{4.8}$$

For the long TE,

$$M_{TE_{long}}(t) = \sum M(0_i)\left(1 - e^{-TW/T_{1wi}}\right) e^{-t\left(\frac{1}{T_{2w}} + \rho\frac{S}{V} + D_w\frac{(\gamma G\, TE_{long})^2}{12}\right)} + M_{oil}\left(1 - e^{-TW/T_{1oil}}\right) e^{-t\left(\frac{1}{T_{2oil}} + D_{oil}\frac{(\gamma G\, TE_{long})^2}{12}\right)} + M_{gas}\left(1 - e^{-TW/T_{1gas}}\right) e^{-t\left(D_{gas}\frac{(\gamma G\, TE_{long})^2}{12}\right)} \tag{4.9}$$

When $TW >> 3\text{x}\max(T_{1w}, T_{1oil}, T_{1gas})$,

$$M_{TE_{long}}(t) = \sum M(0_i) e^{-t\left(\frac{1}{T_{2w}} + \rho\frac{S}{V} + D_w\frac{(\gamma G TE_{long})^2}{12}\right)} + M_{oil}\, e^{-t\left(\frac{1}{T_{2oil}} + D_{oil}\frac{(\gamma G TE_{long})^2}{12}\right)} + M_{gas}\, e^{-t\left(D_{gas}\frac{(\gamma G TE_{long})^2}{12}\right)} \quad (4.10)$$

Fig. 4.5 illustrates a dual-*TE* measurement in which $TE_{long} = 3\ TE_{short}$. The pore fluid is assumed to be composed of two phases, one with large *D* (the green component of the echo trains in the figure) and one with small *D* (the red component of the echo trains). The difference in the decay of a particular component between the TE_{short} and TE_{long} measurements is greater for the component with the larger *D*. Specifically, the large-*D* component decays much more quickly during the TE_{long} measurements than during the TE_{short} measurements, while the small-*D* component decays only slightly faster during the TE_{long} measurements than during the TE_{short} measurements. This distinction between the two components is reflected in the corresponding T_2 distributions and can be used to distinguish the fluids.

Numerical Simulations

NMR responses for dual-*TW* or dual-*TE* measurements can be numerically simulated with the equations presented earlier in this section.[8] This simulation is important for job planning (Chapter 8) and for interpreting dual-*TW* and dual-*TE* logs (Chapter 6).

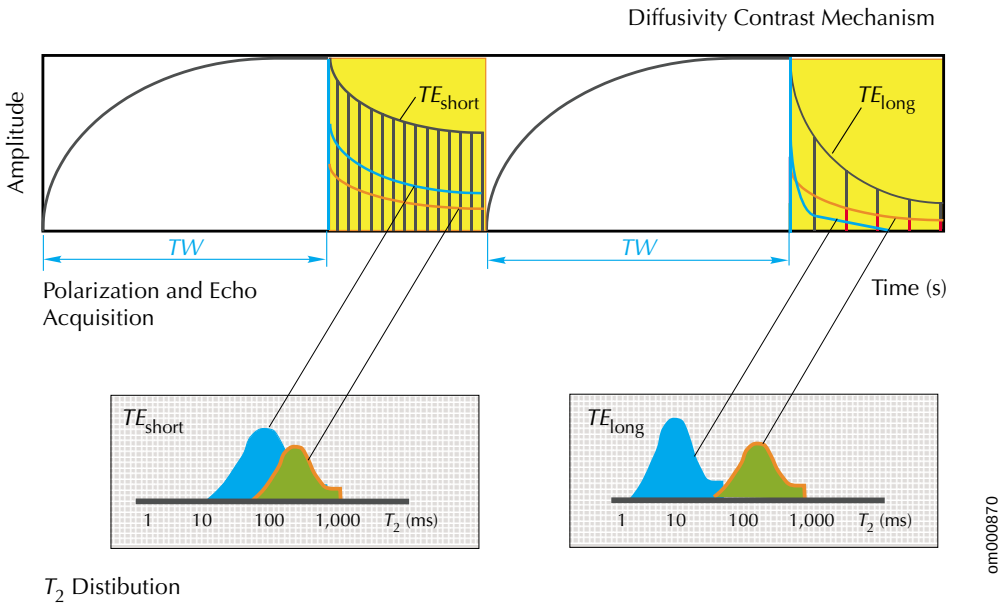

Figure 4.5—In this dual-*TE* measurement of a two-phase pore fluid, the echo-train of the large-*D* fluid (green curve) decays much faster during TE_{long} measurements than during TE_{short} measurements. The decay of the fluid with the small-*D* component (red curve) increases only slightly during TE_{long} measurements. These decay differences are reflected in the T_2 distributions and can be used to distinguish the fluids.

Oil Effects on T_2 Distributions

The effects of oil on T_2 distributions vary with the fluids present in the pores.

Water and Light Oil

Fig. 4.6 (top) is a volumetric model of a water-wet formation filled with water and light oil. The sharp boundaries between the various components in the model do not imply sharp boundaries between the corresponding decay spectra. If a short *TE* and long *TW* are used to measure the echo train, then water will have a broad T_2 distribution, while light oil tends to display a much more narrow distribution around a single T_2 value.[3] Little difference exists between the diffusion coefficients of water and light oil; therefore, the *D* contrast between the two fluids will not be very obvious. The T_1 values for light oil and pore water are very different; thus, the T_1 contrast between the two fluids will be detectable.

The middle and bottom sections of Fig. 4.6 show how dual-*TW* measurements can be used to distinguish between water and light oil. Because of the large T_1 contrast between water and

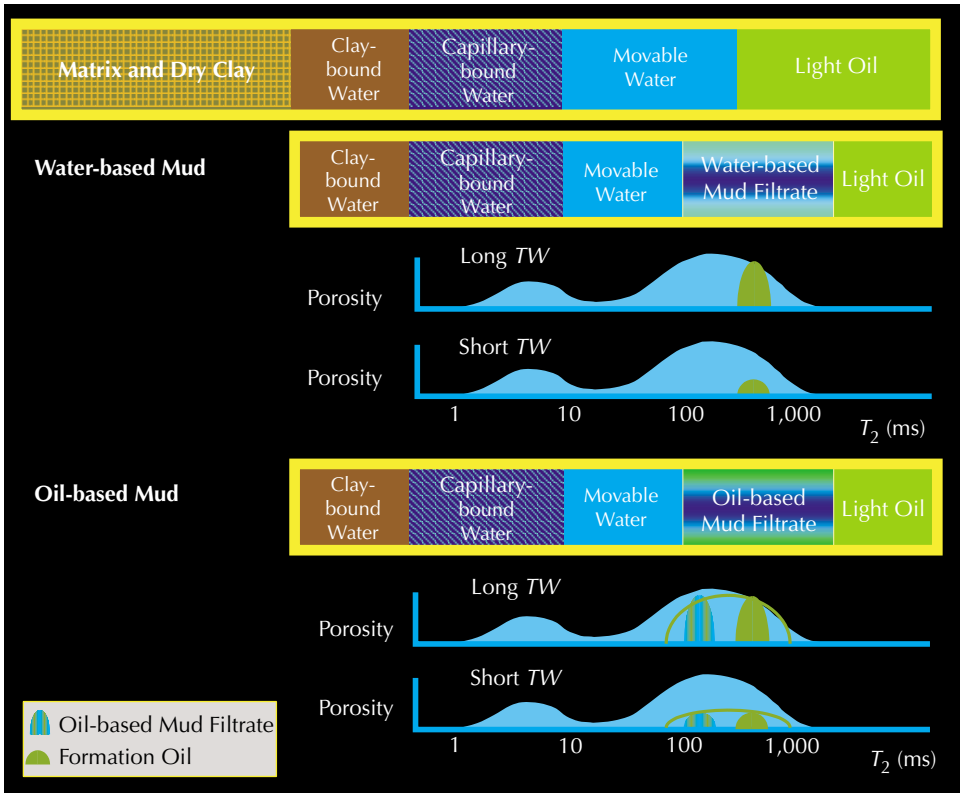

Figure 4.6—In these volumetric models of a light-oil reservoir, the virgin zone (top model) contains no mud filtrate. When the reservoir is logged with an MRIL tool, invasion will have occurred, and part of the tool response will be attributable to mud filtrate in the flushed zone (middle and bottom models). The MRIL tool does not respond to matrix and dry clay. The two T_2 distributions obtained with dual-*TW* measurements will both contain an oil signal. When a water-based mud is used (middle model), the oil signal will be concentrated around a single peak (here, at about 500 ms). When an oil-based mud is used (bottom model), theoretically two oil peaks may exist, one for the reservoir oil (here, at about 500 ms) and one for the filtrate oil (here, at about 200 ms). In practice, however, both oil signals normally overlap on the T_2 distribution, as the green curve seen in the figure. Whether water-based mud or oil-based mud is used, oil signals will remain after one T_2 distribution is subtracted from the other.

light oil, the water signal will disappear when the TW_{short} and TW_{long} T_2 distributions are subtracted from one another. The resulting differential "spectrum" will contain only part of the light-oil signal. The amplitude of this signal in the differential spectrum will be highly dependent on both the T_1 difference between the two kinds of fluids and the difference between TW_{short} and TW_{long}. Normally, TW_{short} and TW_{long} are selected so that $TW_{short} \geq 3T_{1,bulk\ water}$ and $TW_{long} \geq 3T_{1,light\ oil}$. If oil-based mud is used, a signal from the mud filtrate will appear on the T_2 distribution. In Fig. 4.6, the T_2 of light oil is concentrated at about 500 ms. The T_2 of oil-based mud filtrate is about 200 ms. The signals from both light oil and oil-based mud filtrate will remain in the differential spectrum. Normally, it is difficult to distinguish the native oil and oil-based mud filtrate because of the mixture of these two kinds of oil and their NMR signals.

Water and Viscous Oil

When both water and viscous oil fill the pores of a water-wet formation, the volumetric model of the formation can be illustrated as in **Fig. 4.7**. If a small *TE* and long *TW* are used, the spin-echo signal from water measured with the MRIL gradient field will usually have a broad T_2 distribution, and the signal from viscous oil will also typically have a broad T_2 distribution. The bulk decay time T_2 for viscous oil and the contribution to the decay time of water from surface relaxation usually are not very different. The diffusion coefficients for both water and viscous oil, however, are very different; therefore, the diffusion contrast between the two fluids is detectable.

Fig. 4.7 shows how dual-*TE* measurements can be used to distinguish between water and viscous oil. Because of the diffusion contrast between water and viscous oil, the T_2 distribution measured with TE_{long} will show a much larger shift to the left (to lower T_2 values) for water than for viscous oil, as compared to the T_2 distribution measured with TE_{short}. The fast T_2 times of water will shift very little. When oil-based mud is used, normally it has lower viscosity than viscous oil at reservoir conditions. The T_2 components of an oil-based mud filtrate measured with TE_{short} will be clustered around a single peak with T_2 longer than that of viscous oil. The T_2 peak of an oil-based mud filtrate measured with TE_{long}, however, may be shorter than that of viscous oil because of the high diffusivity of the filtrate. Careful selection of TE_{long} makes it possible to separate the T_2 components of viscous oil and water, whether water-based or oil-based mud is used in the well. In general, because the diffusion shift is non-linear, relaxation times longer than the diffusion relaxation time will shift much more to the left than those shorter than the diffusion relaxation time. This non-linear shifting thus causes the spectra to become more sharply peaked as diffusion increases.

Effects of Viscosity and Wettability on the Oil Signal in a T_2 Distribution

In the discussion thus far, the formations have been assumed to be water-wet. If the formation logged by an NMR tool is not water-wet but instead is partially or completely oil-wet, then the oil T_2 values will be different and the T_2 distributions will be different from those discussed earlier.[8, 9] Rocks are probably never completely oil-wet; some are of intermediate and/or mixed wettability. Mixed wettability most likely occurs in reservoir rocks where oil has been trapped and comes into contact with the grain surfaces in the larger pores to form an oil film or coating on the grains. Crude oils vary in their ability to alter the wettability of a pore surface. The pore surfaces of the smaller pores or in the crevices of larger pores are not in contact with the oil and remain water-wet. For NMR, the essential condition for water wettability is the existence of a protective layer of water between the rock grain and the

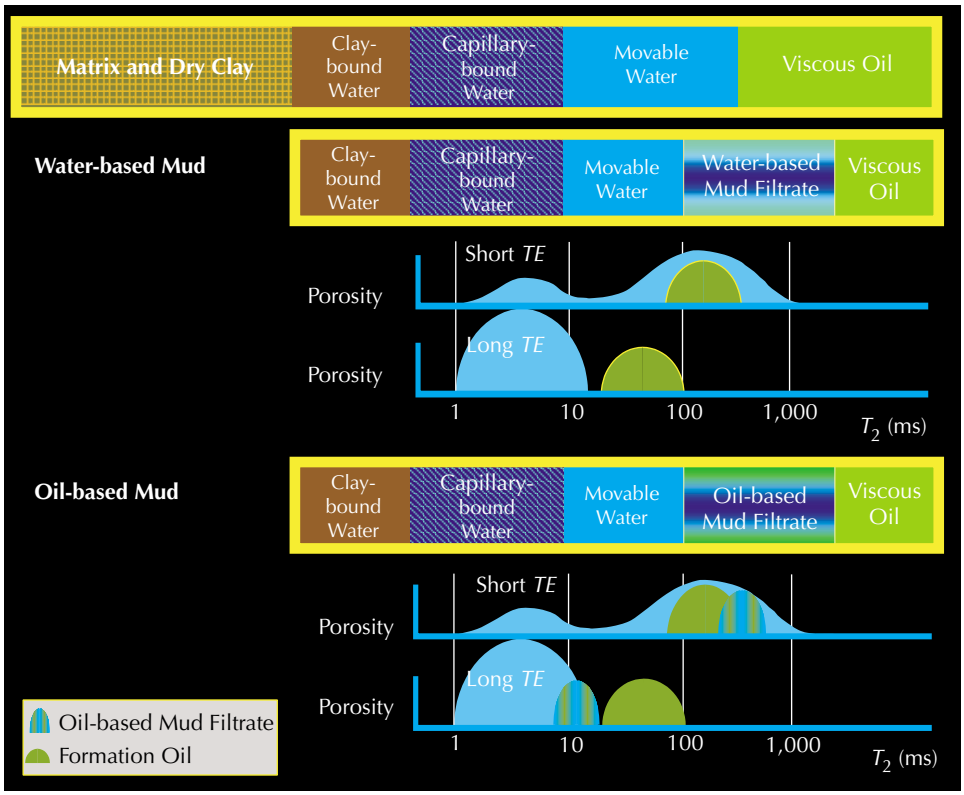

Figure 4.7—In a viscous-oil reservoir, the virgin zone (top volumetric model) contains no mud filtrate. During MRIL logging, part of the tool response will be attributable to mud filtrate in the flushed zone. If water-based mud is used (middle model), T_2 distributions obtained with dual-*TE* measurements allow oil to be differentiated from water. With the long-*TE* measurement, fast water components in the T_2 distribution are shifted farther to the left than the oil components. If oil-based mud is used (bottom model), the filtrate may give rise to an additional oil signal.

hydrocarbon fluid. However, this condition is not identical to the condition measured by other wettability tests. For example, part of the protective coating could be absent and the rock could still be considered water-wet by a USBM test (a commonly used test developed by the United States Bureau of Mines).

When oil molecules directly contact grain surfaces, the oil molecules exhibit surface relaxivity, which makes the T_2 relaxation mechanism more complicated. If a formation is completely oil-wet, then water and oil switch roles compared to the water-wet situation, and overall behavior is very similar. However, the details of the spectra could be different because the surface relaxivity to oil is probably different than the surface relaxivity to water. If a formation exhibits mixed wettability, then the situation is much more complex, and differentiating between oil and water is very difficult.

Fig. 4.8 shows how, in an oil-bearing formation, both oil viscosity and formation wettability affect the location of the oil component in the T_2 distribution of the formation.[7] The figure assumes (1) *TW* is sufficiently long so that T_1 effects need not be considered and (2) *TE* is sufficiently short so that diffusion effects need not be considered.

As previously discussed, for a water-wet formation, the oil component of the T_2 distribution is dependent mainly on oil viscosity (water-wet row in Fig. 4.8). Notice that for any

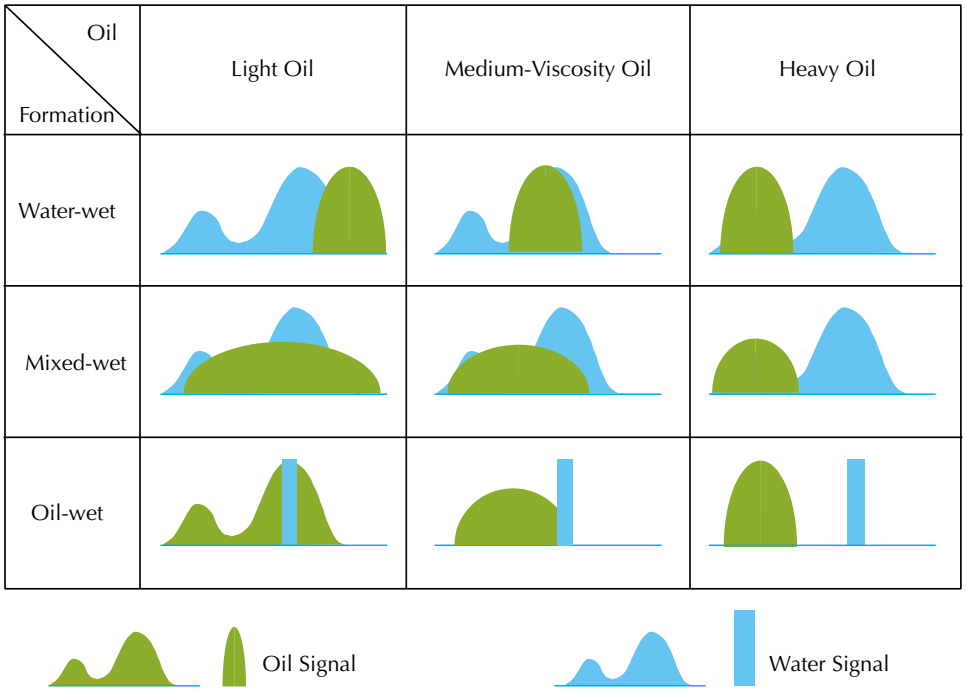

Figure 4.8—The position and breadth of the oil component in the T_2 distribution of a formation depends on oil viscosity and formation wettability. Oil typing is easiest in water-wet formations because of the moderate breadth and distinct positions of the different oil components in the T_2 distribution. Oil typing is most difficult in mixed-wet formations because the oil and water components are broad and overlap each other.

wettability, the heavy-oil component of the T_2 distribution is broad and fills the BVI portion of the distribution (heavy-oil column in Fig. 4.8), which makes detecting heavy oil with MRIL measurements difficult. For a mixed-wet formation, which poses one of the greatest challenges for MRIL applications, the oil and water components of the T_2 distribution are broad and overlap each other (mixed-wet row in Fig. 4.8). Although this overlapping does not affect the total porosity estimation, it will affect the determination of BVI, free fluid, permeability, and, of course, the hydrocarbon type. For the rare oil-wet formation, oil molecules will be adsorbed on all pore surfaces. In this case, BVI will be the bulk volume irreducible of oil. The water component will be always in the free-fluid portion of the distribution (oil-wet row of Fig. 4.8) and should exhibit bulk characteristics. The T_1 and T_2 of water are both single-valued and quite long compared to the corresponding relaxation times of the oil in contact with the pore wall.

Gas Effects on T_2 Distribution Under Different Conditions

Gas is always a non-wetting phase in the pore space of a formation. Hence, the T_1 of gas is taken as that of bulk gas (Straley's work[1] suggests that sometimes this assumption may be too simple), which is much longer than the T_1 of water in contact with the pore wall. The $T_{2diffusion}$ of gas will dominate the T_2 of gas. These characteristics and the gradient field of the MRIL tool make the gas signal detectable through MRIL measurements.

Water and Gas

Fig. 4.9 presents volumetric models for rocks saturated by water and gas. The models depict a virgin zone and zones invaded by water-based and oil-based muds. If a small *TE* and long *TW* are used, the spin-echo signal from water will have a broad T_2 distribution, while the signal from gas will have almost a single T_2 value. The T_1 times for water and gas are very different; therefore, the T_1 contrast can be used to differentiate water and gas, as shown in the middle and bottom models of Fig. 4.9.

As with water and light oil, a large T_1 contrast exists between gas and water in contact with the pore wall. Thus, when dual-*TW* measurements (see Chapter 6) are used, and the resulting T_2 distributions are subtracted from one another, the water component will be eliminated, and part of the gas component will remain in the differential spectrum. The amplitude of the partial gas component in the differential spectrum will be highly dependent on both the difference between T_{1gas} and T_{1w} and the difference between TW_{short} and TW_{long}. Normally, logging parameters are set so that $TW_{long} \geq T_{1gas}$ and $TW_{short} \geq 3T_{1w}$. In addition, when gas is present, hydrogen index and polarization effects must be considered because gas has low hydrogen index and long T_1.

If oil-based mud is used, a signal from the oil-based mud filtrate appears on the T_2 distribution. In Fig. 4.9, the T_2 of the gas is concentrated at about 40 ms, and the T_2 of oil-based mud filtrate is at about 200 ms. The signals from both gas and oil-based mud filtrate will remain in the differential spectrum.

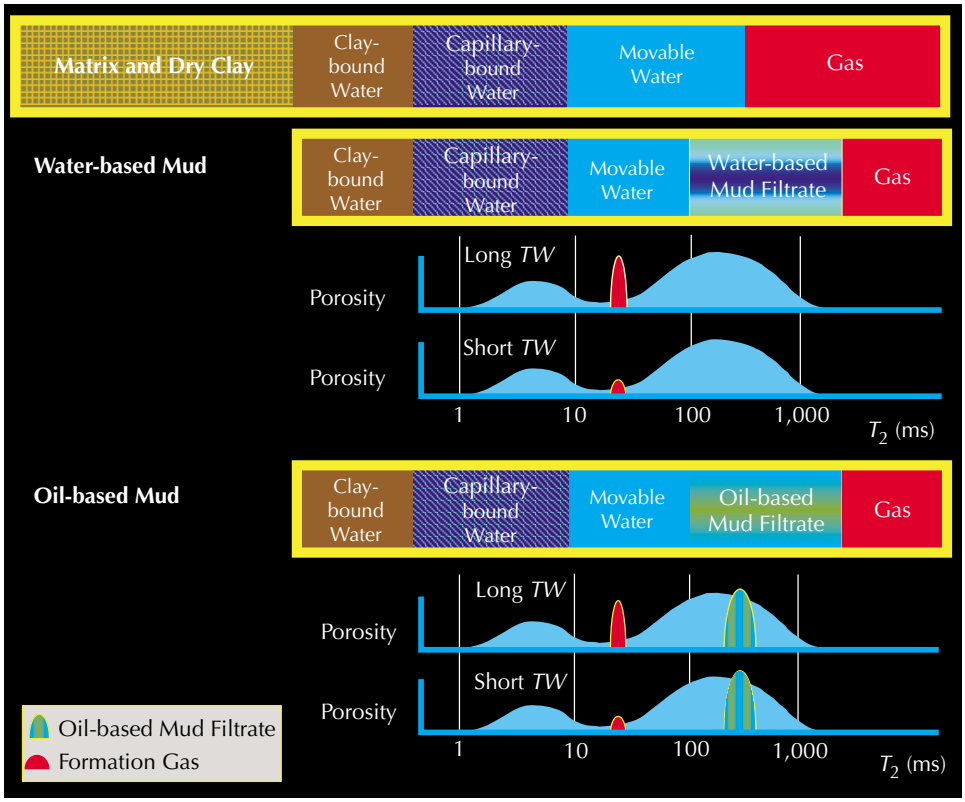

Figure 4.9—In a gas reservoir, the virgin zone (top volumetric model) contains no mud filtrate. During NMR logging, part of the tool response will be attributable to mud filtrate in the flushed zone. When water-based mud and dual-*TW* measurements are used (middle model), gas can be detected by subtracting the two resulting T_2 distributions. If oil-based mud is used (bottom model), the resulting differential spectrum will also contain a component attributable to the oil-based filtrate that has invaded the formation.

Water, Light Oil, and Gas

When water, light oil, and gas occupy the same pore system in the formation rocks (**Fig. 4.10**), both light oil and gas can still be detected through their T_1 contrast. Dual-*TW* measurements are used, and TW_{long} should be greater than three times of the maximum T_1 of light oil, gas, and (if oil-based mud is used) the oil-based mud filtrate. When oil-based mud is used, the signals from light oil, gas, and oil-based mud filtrate will remain in the differential spectrum.

Although the difference in diffusivity between gas and liquid is large, this contrast is seldom applied to separate the signals of two fluids. Generally, the T_2 of gas is very small. In most cases, the gas T_2 component may fill the *BVI* window. When a longer *TE* is used, the gas component may disappear from the T_2 distribution. The T_2 of gas is strongly affected by inter-echo spacing in a gradient field. By carefully choosing *TE* and gradient strength (which is related to frequency), the gas signal can be separated from *BVI*, light oil, and oil-based mud filtrate. This choice is one of the keys for designing a T_1-contrast (i.e., dual-*TW*) NMR logging job.

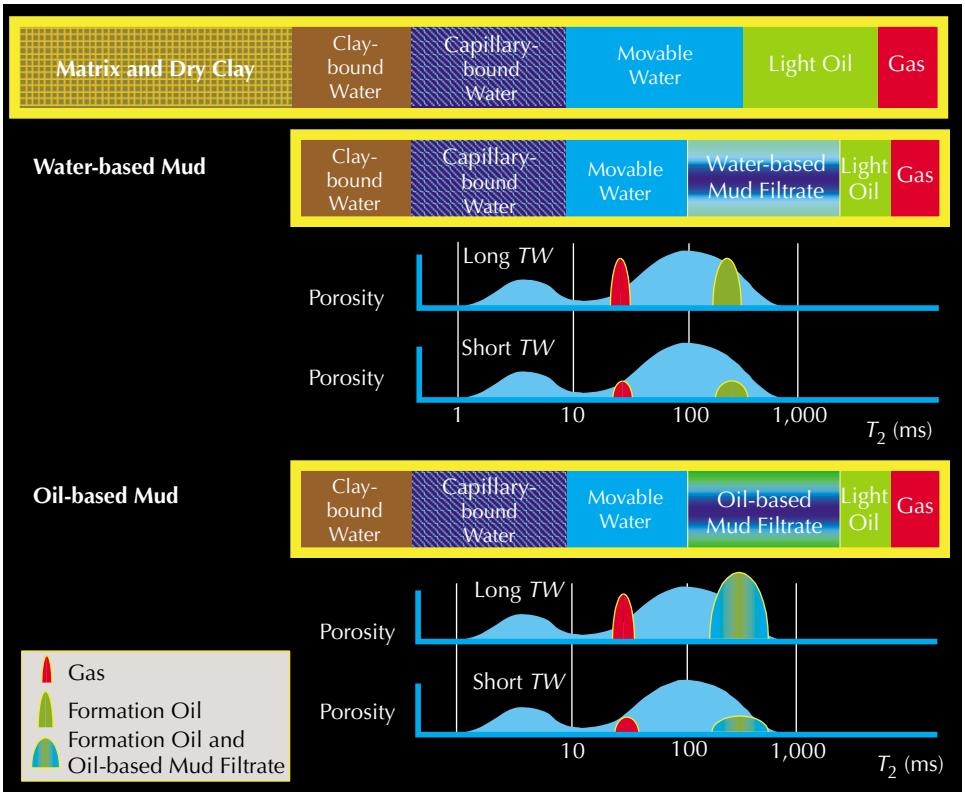

Figure 4.10—In a reservoir containing gas and light oil, the virgin zone (top volumetric model) contains no mud filtrate. During NMR logging, part of the tool response will be attributable to mud filtrate in the flushed zone. When water-based mud and dual-*TW* measurements are used (middle model), gas and light oil can be differentiated from water by subtracting the two resulting T_2 distributions. If oil-based mud is used (bottom model), the resulting differential spectrum may also contain a component attributable to the oil-based filtrate that has invaded the formation. The differentiation between gas and light oil/oil-based mud filtrate is dependent on resolvable T_2 differences in the differential spectrum.

References

1. Straley, C., 1997, An experimental investigation of methane in rock materials, paper AA, *38th Annual SPWLA Logging Symposium Transactions*, 14 p.

2. Kleinberg, R.L., and Vinegar, H.J., 1996, NMR properties of reservoir fluids, *The Log Analyst*, v. 37, no. 6, p. 20–32.

3. Morris, C. E., et al., 1997 Hydrocarbon saturation and viscosity estimation from NMR logging in the Belridge diatomite, *The Log Analyst*, March-April, p. 44–59.

4. Gerritsma, C.J., Oosting, P.H., and Trappeniers, N.J., 1971, Proton spin-lattice relaxation and self-diffusion in methane, part 2—Experimental results for proton spin-lattice relaxation times, *Physica*, v. 51, p. 381–394.

5. Gerritsma, C.J., and Trappeniers, N.J., 1971, Proton spin-lattice relaxation and self-diffusion in methanes, part 1—Spin-echo spectrometer and preparation of the methane samples, *Physica*, v. 51, p. 365-380.

6. Akkurt, R., et al., 1995, NMR logging of natural gas reservoirs, paper N, *36th Annual SPWLA Logging Symposium Transactions*, 12 p. Later published in 1996, as Akkurt, R., et al. in *The Log Analyst*, v. 37, no. 5, p. 33–42.

7. Prammer, M.G., Mardon, D., Coates, G.R., and Miller, M.N., 1995, Lithology-independent gas detection by gradient-NMR logging, SPE 30562, *1995 SPE Annual Technical Conference and Exhibition Proceedings*, v. Ω (Formation evaluation and reservoir geology), p. 325–336.

8. Xiao, L.Z., 1998, NMR Imaging Logging Principles and Applications (in Chinese), Science Press, Beijing, 328 p.

9. Howard, J.J., and Spinler, E.A., 1993, Nuclear magnetic resonance measurements of wettability and fluid saturations in chalk, SPE 26471, *1993 SPE Annual Technical Conference and Exhibition Proceedings*, v. Ω (Formation evaluation and reservoir geology) p. 565–573. Later published in *1995 in SPE Advanced Technology Series*, v. 3, no. 1, p. 60–65.

Chapter 5

MRIL Tool Principles

The MRIL measurement process consists of four basic steps:

1. Polarizing the nuclei
2. Tipping the magnetization
3. Detecting spin echoes
4. Re-polarizing the nuclei

This chapter discusses the MRIL measurement process and associated issues, such as vertical resolution, depth of investigation, signal-to-noise ratio, and activation.

Polarization

An MRIL tool contains a large permanent magnet that produces a static magnetic field.[1,2] Before an earth formation is logged with an MRIL tool, the hydrogen nuclei of the formation are aligned with the earth's magnetic field. Because the magnitude of the earth's field is relatively small, the magnitude of the magnetization induced in the protons is also small. As an MRIL tool moves through the formation, the high-magnitude field $\mathbf{B}_0$ of the tool dominates and polarizes the protons (that is, it aligns them with the $\mathbf{B}_0$ field). For example, the strength of the earth's field is about 0.5 gauss, while the strength of the MRIL-produced magnetic field at the sensitive volume is about 176 gauss, which is 350 times stronger than the earth's magnetic field. For protons in pore fluids, "full" polarization requires up to several seconds and can be achieved as the tool moves through the wellbore. Reliable measurements are made provided the protons are exposed to the same static magnetic field throughout the entire measurement cycle. **Fig. 5.1** shows the increase in polarization with time. Once the protons are polarized, they are in an equilibrium state and will remain polarized unless disturbed. The net magnetic moment of the polarized proton population is $\boldsymbol{M}_0$, which was discussed in Chapter 2.

Magnetization Tipping and Spin-Echo Detection

The MRIL technique of tipping the magnetization and acquiring spin echoes from a formation is illustrated in **Fig. 5.2**. An MRIL tool produces a static magnetic field with gradient in the radial direction; therefore, the Larmor frequency of protons will vary with the radial

Figure 5.1— (1) Before protons are subjected to the MRIL static magnetic field, their spin axes are randomly aligned. (2) Upon initial exposure of the protons to the MRIL static magnetic field, their spin axes begin to precess, with the precessional axes being aligned with the direction of the static field $\mathbf{B}_0(\mathbf{r})$. (3 and 4) As exposure continues, the spin axes approach the precessional axes, and the net magnetization of the proton population increases, as the graph indicates.

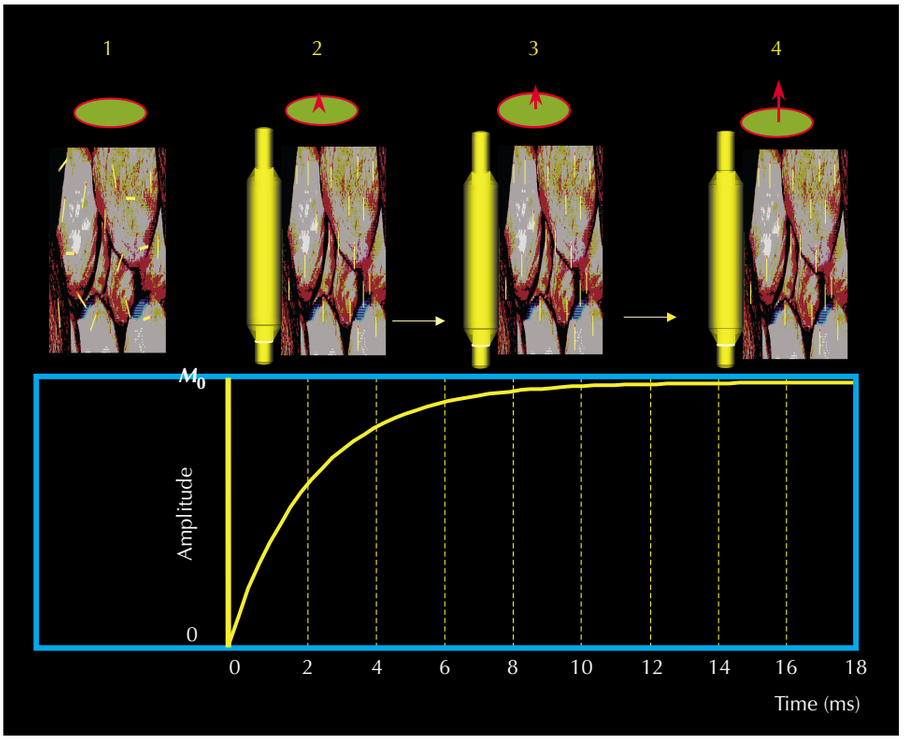

om000853

Figure 5.2— The MRIL antenna (left) applies a 90° oscillating $\mathbf{B}_1$ pulse to phase-synchronized protons and tips the magnetization 90°. As the protons dephase, the MRIL antenna (middle) applies a 180° oscillating $\mathbf{B}_1$ pulse to re-phase the protons. When the protons re-phase (right), they generate a signal—a spin echo—which is measurable by the MRIL antenna.

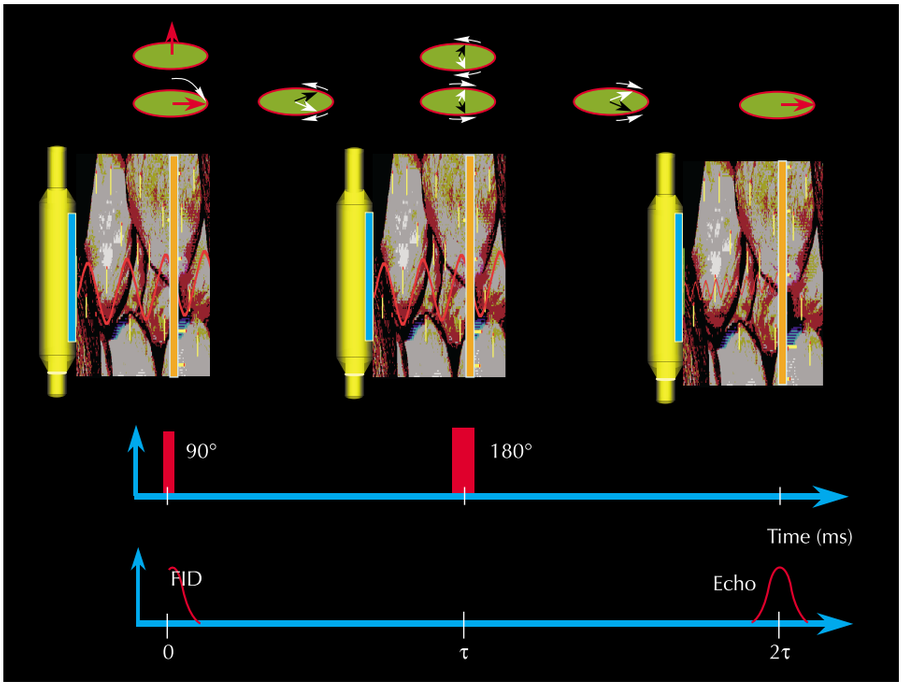

om000876

distance from the tool.[1,2] An antenna, which surrounds the magnet of the tool, serves as oscillating-field transmitter and spin-echo receiver. The antenna produces a $\mathbf{B}_1$ field that is perpendicular to $\mathbf{B}_0$ and that rotates the magnetization vector into the transverse plane. The values selected for the frequency and bandwidth of the $\mathbf{B}_1$-field pulses determine the geometry of the sensitive volume and, thus, the depth of investigation of the tool.

The MRIL tool records a spin-echo train, as illustrated in **Fig. 5.3**. The CPMG pulse sequence negates the dephasing caused by the gradient effects of the $\mathbf{B}_0$ field; however, the dephasing that results from molecular interaction or diffusion processes is irreversible. When this irreversible dephasing occurs, the protons can no longer be completely refocused, and the CPMG spin-echo train decays. An MRIL tool measures the amplitude of the spin echoes in the CPMG sequence to monitor the transverse magnetization decay and thus the irreversible dephasing. After a spin-echo train is acquired, the magnet repeats the polarization for the next CPMG measurement, as illustrated in **Fig. 5.4**.

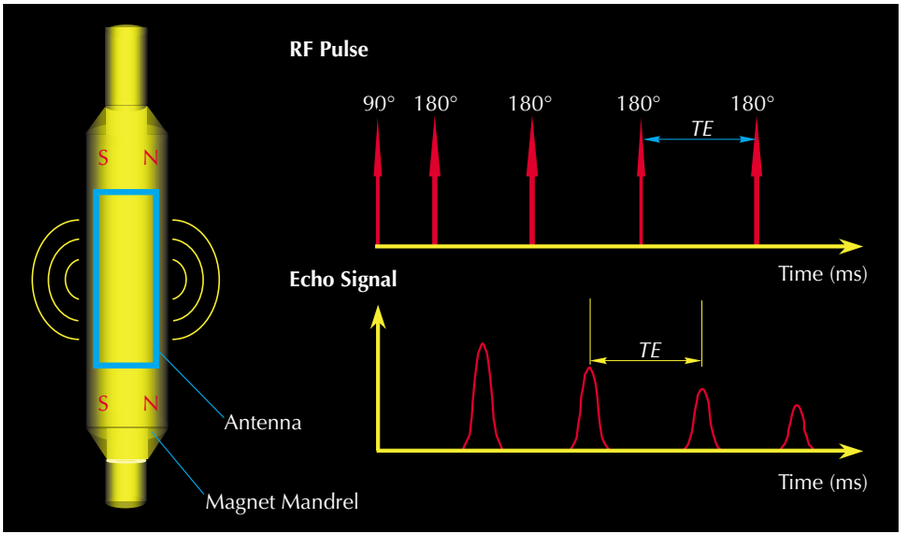

Figure 5.3—To generate and receive a spin-echo train, an MRIL tool emits a 90° $\mathbf{B}_1$ pulse followed by a sequence of 180° $\mathbf{B}_1$ pulses.

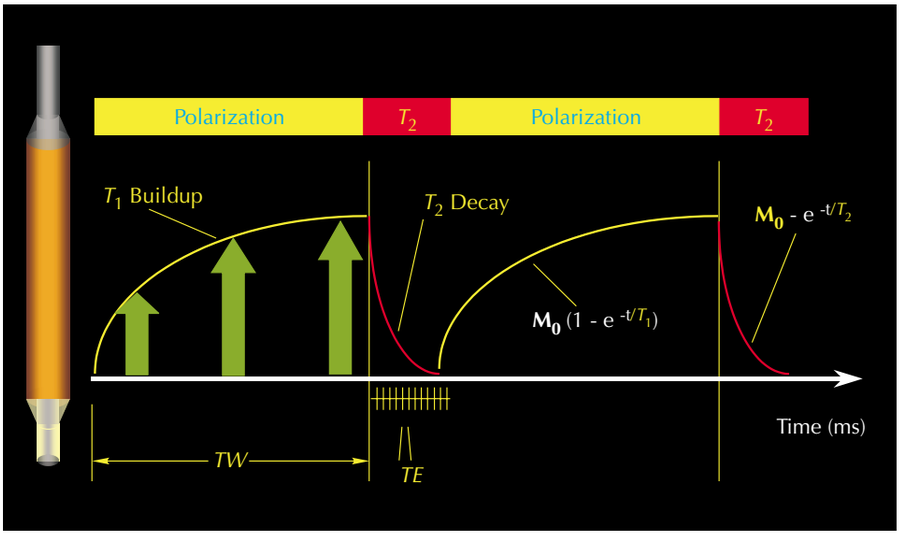

Figure 5.4—The MRIL measurement cycle, which is repeated continuously during logging, consists of proton polarization followed by echo-train acquisition. The decaying echo train reflects the dephasing that follows polarization.

Logging Speed and Vertical Resolution

As an MRIL tool moves through the borehole, the proton population with which the tool interacts changes continuously. This changing population affects tool characteristics and logging parameters in two ways, as shown in **Fig. 5.5**.

First, the tool encounters "new" and unpolarized protons and leaves behind "old" and polarized protons. The time required for the new protons to become fully polarized before they enter the sensitive volume of the tool is controlled by the T_1 relaxation times. The polarization time *TW* is directly related to the length of the magnet and to the logging speed. To allow the tool to run at a faster logging speed, the magnet of an MRIL tool extends 24 in. (for the C-type tool) above and below the antenna (for up-logging and down-logging). With this design, the tool polarizes the protons before they enter the sensitive volume of the tool's measurement.

Second, during the CPMG sequence, protons whose magnetization vectors have already been tipped into the transverse plane leave the sensitive volume, while polarized protons that have not yet been tipped enter the sensitive volume. This situation reduces the measured amplitude of later echoes if the antenna is too short or if the logging speed is too fast. To maintain an acceptable logging speed, a 10% loss of accuracy is typically accepted—that is, the surveyed volume can change 10% during a CPMG sequence. Because the antenna length determines the surveyed volume, a longer antenna will allow faster logging, but at the expense of vertical resolution. The MRIL antenna is 24 in. long.

If the tool does not move during the measurement cycle (that is, a stationary reading is obtained), the vertical resolution (*VR*) equals the length of the antenna (*L*). If the tool moves during measurement, vertical resolution will decrease at a rate proportional to logging speed.

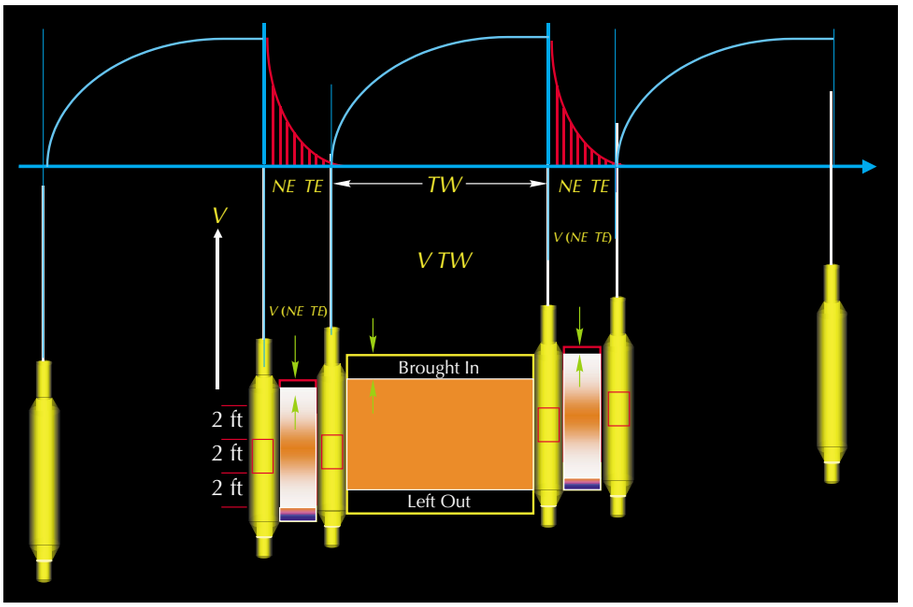

Figure 5.5—(1) As the MRIL tool moves through the borehole, it polarizes part of the surrounding formation. If the logging speed is *V* and the polarization time is *TW*, then the tool will move a distance of *V TW* during one polarization event. (2) Following a polarization event, a CPMG sequence induces and measures spin echoes. If the echo spacing is *TE* and the number of echoes is *NE*, then the tool will move a distance *V* (*TE NE*) during echo acquisition. (3) The CPMG sequence ends, and the next polarization/ CPMG cycle begins.

To correct measurements for signal-to-noise effects, results from several experiments are combined, or stacked. The number of experiments needed to produce a measurement with a particular improvement in signal-to-noise effect is called the running average (*RA*). The cycle time (*TC*) is the time required to perform a CPMG measurement plus the polarization time (or wait time) before the next CPMG sequence can start. As **Fig. 5.6** illustrates, for a tool operating at a single frequency, *TC* is given by

$$TC = TW + TE \ NE \tag{5.1}$$

For a tool operating at a single frequency, moving at a logging speed *V*, the vertical resolution can be expressed as

$$VR = L + V \ (TC \ RA - TW) \tag{5.2}$$

Eq. 5.2 shows that:

- For a stationary measurement ($V = 0$), the vertical resolution is the length of the RF antenna. Thus, a shorter antenna gives better vertical resolution.
- Vertical resolution degrades as logging speed increases.
- Vertical resolution degrades as experiment time increases. Experiment time comprises mainly polarization time *TW*.
- As more experiments are stacked, the signal-to-noise ratio improves, but the vertical resolution degrades.

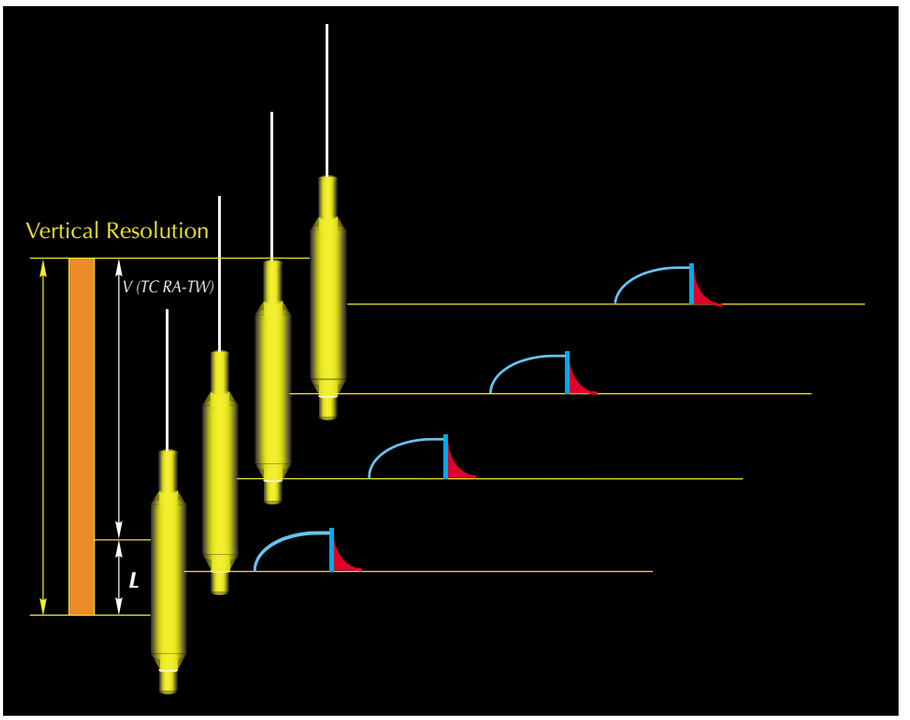

Figure 5.6—The vertical resolution of the MRIL tool is equal to sum of the antenna length and the product of the logging speed, cycle time, and running average.

Depth of Investigation

The static magnetic field produced by the MRIL magnet is a gradient field $\mathbf{B_0(r)}$ whose magnitude is a function of the radial distance *r* from the tool surface.[3] In particular, $\mathbf{B_0(r)} \propto 1/r^2$. For example, along a thin cylinder with a diameter of 16 in. that is concentric with the axis of a 6-in. OD tool, field strength is approximately 155 gauss (**Fig. 5.7**).

The MRIL gradient magnetic field $\mathbf{B_0}$ decreases as the distance from the tool surface increases. Because the Larmor frequency is proportional to $\mathbf{B_0}$, the Larmor frequency of protons in the formation will also decrease as the distance from the tool surface increases.

Thus, for an MRIL tool to investigate at a particular distance into the formation, the frequency of the oscillating field ($\mathbf{B_1}$) is selected to match the Larmor frequency of the protons at that distance. In practice, a narrow frequency band is chosen so that the sensitive volume is a thin cylindrical shell.

Fig. 5.8 contains a cross-sectional view of an MRIL tool, the borehole, the surrounding formation, and the sensitive volume.[4] The graph below this view depicts the decrease in $\mathbf{B_0}$ strength (hence, the decrease in Larmor frequency) with distance from the tool. The $\mathbf{B_0}$ gradient and the selection of the $\mathbf{B_1}$ frequency band thus determine the diameter and thickness of the sensitive volume of the tool. This volume is very well defined. Protons on either side of the sensitive volume will be polarized by the $\mathbf{B_0}$ field but will not be tipped by the $\mathbf{B_1}$ field because of the frequency mismatch between the precession of these protons and the $\mathbf{B_1}$ field.

Theoretically, the depth of investigation increases with decreasing $\mathbf{B_1}$ frequency. In reality, increasing the depth of investigation requires higher $\mathbf{B_1}$ power to tip the protons 90° and 180°. Furthermore, increasing the depth of investigation decreases the signal-to-noise ratio.

Because of the radial character of MRIL responses, the tool must be well centralized in the wellbore. When a washout does not intersect the sensitive volume, the washout will have no effect on measurements except for the loading effect of the mud on the $\mathbf{B_1}$ field. Because of this loading effect, more $\mathbf{B_1}$ power is needed for 90° tipping in the sensitive volume in a salty-mud environment than in a resistive-mud environment.

If a washout does intersect the sensitive volume, then wellbore fluids will also affect the measurement. In some cases, decentralization will expose the sensitive volume to wellbore fluids, and MRIL measurements will include some mud signal. In both situations, the MRIL determinations of effective porosity (*MPHI*) and bulk volume irreducible (*BVI*) will be much higher than the actual formation values because (1) the liquid in the mud system is rich in protons and (2) the relaxation times of the protons in the mud are very fast because of the high surface area of the mud grains. Generally, wellbore-fluid effects on MRIL signals are easy to identify, especially when caliper data are available.

No washout or borehole-fluid corrections are available for MRIL measurements. Thus, when wellbore fluids affect MRIL signals, MRIL measurements no longer represent formation conditions and cannot be used for formation evaluation.

The static magnetic field of an MRIL tool is generated by a permanent magnet made from ferromagnetic materials, and the magnetization is temperature-dependent. Therefore, the strengths of both the static magnetic field and the field gradient are also temperature-dependent, as shown in **Fig. 5.9**. As the magnet becomes hotter, $\mathbf{B_0}$ decreases and, for a given $\mathbf{B_1}$ frequency, the depth of investigation also decreases. Because the temperature dependence of the MRIL magnet is well characterized, knowledge of the magnet's temperature and of the $\mathbf{B_1}$ frequency uniquely determines the depth of investigation of the tool.

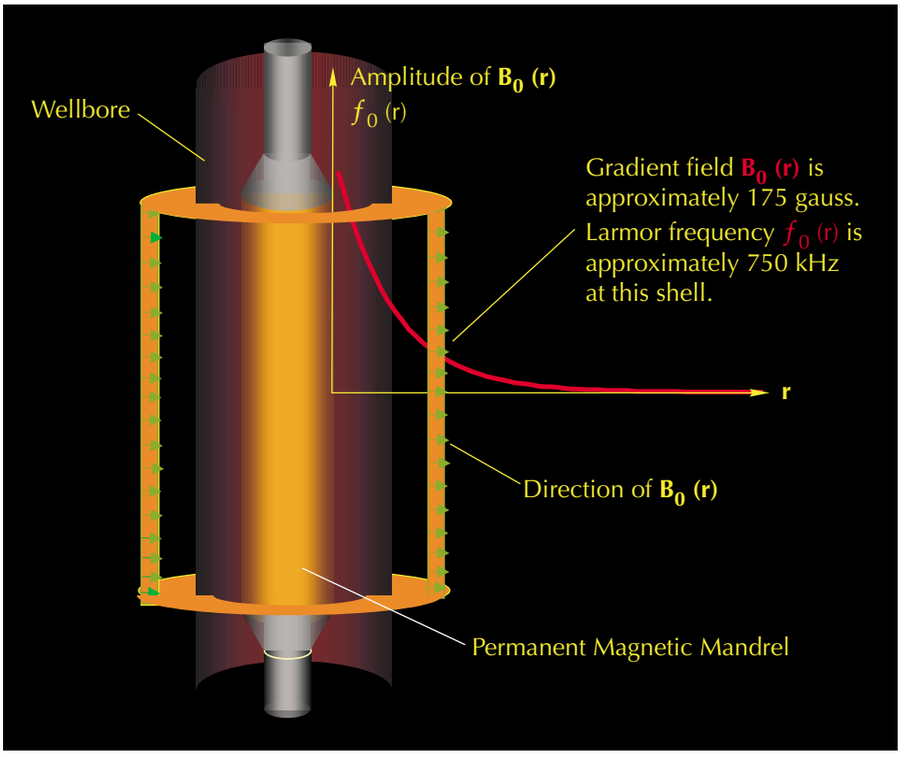

Figure 5.7—The permanent magnet of the MRIL tool produces a gradient field whose magnitude decreases with radial distance from the tool.

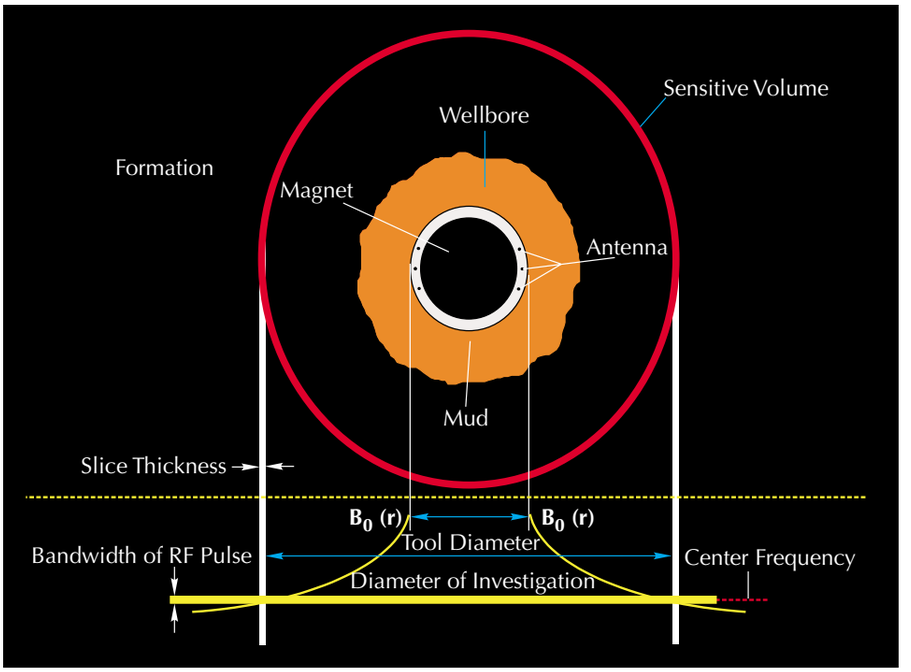

Figure 5.8—The diameter and thickness of the sensitive volume of the MRIL tool are determined by the gradient of the permanent $\mathbf{B}_0$ field and the frequency band of the oscillating $\mathbf{B}_1$ field.

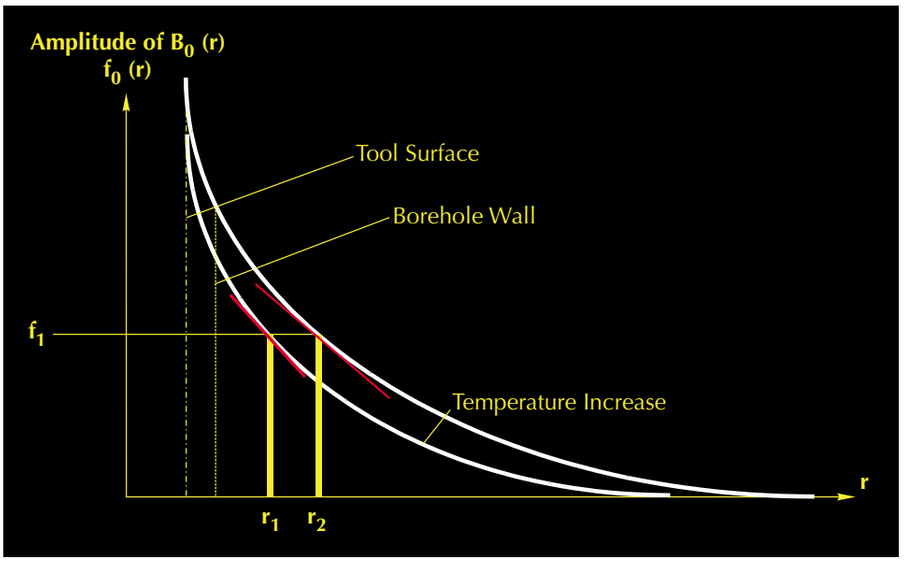

Figure 5.9—The strength of both the $\mathbf{B}_0$ field and the field gradient are temperature-dependent. For an RF field of frequency f_1, the depth of investigation will thus vary with temperature.

MRIL tools are available in 6- and 4 $^1/_2$- (or 4 $^7/_8$- for the Prime tool) in. OD versions, both of which can operate at high frequency (about 750 kHz) or low frequency (about 600 kHz). As seen in **Fig. 5.10**, the depths of investigation of the 6-in. probe at 200°F are about 14.5 and 16.5 in., at the high and low frequencies, respectively. For the 4 $^1/_2$-in. probe, the corresponding depths of investigation are about 10 and 11.5 in. For typical borehole sizes (for example, holes drilled with an 8 $^1/_2$-in. bit), a 16-in. diameter of investigation corresponds to a region of investigation located about 3 to 4 in. from the borehole wall. Therefore, the sensitive volume is generally within the flushed zone.

Multi-Frequency Measurement and RF Pulse Bandwidth

According to NMR theory, only those protons that precess at the Larmor frequency will contribute to the CPMG measurement signal. The Larmor frequency is directly proportional to strength of the $\mathbf{B}_0$ magnetic field. Therefore, in the presence of a gradient magnetic field, pulses with different frequencies can be applied to cause protons in different regions of space to resonate. This principle has been successfully used for slice selection in medical MRI and in MRIL logging. **Figs. 5.11** and **5.12** illustrate the sensitive volumes and timing for multi-frequency MRIL measurements.[5]

The protons excited by an MRIL RF signal will have Larmor frequency equal to the frequency of the RF signal, and these protons will lie in a distinct volume. Protons outside this volume will not be influenced by the MRIL RF signal and will repolarize with respect to the external magnetic field.

Cycling through several frequencies excites protons in different cylindrical volumes in space, thus allowing measurements to be made more quickly. The time between frequencies can be as little as the time of an echo train, typically 0.5 s, while the time between measurements made at a single frequency is essentially the time to re-polarize (*TW*), which is often on the order of 10 s. If the frequencies of multi-frequency measurements are very similar, then the sensitive volumes are very close to one another and, for practical purposes, the rocks sampled can be considered to be the same.

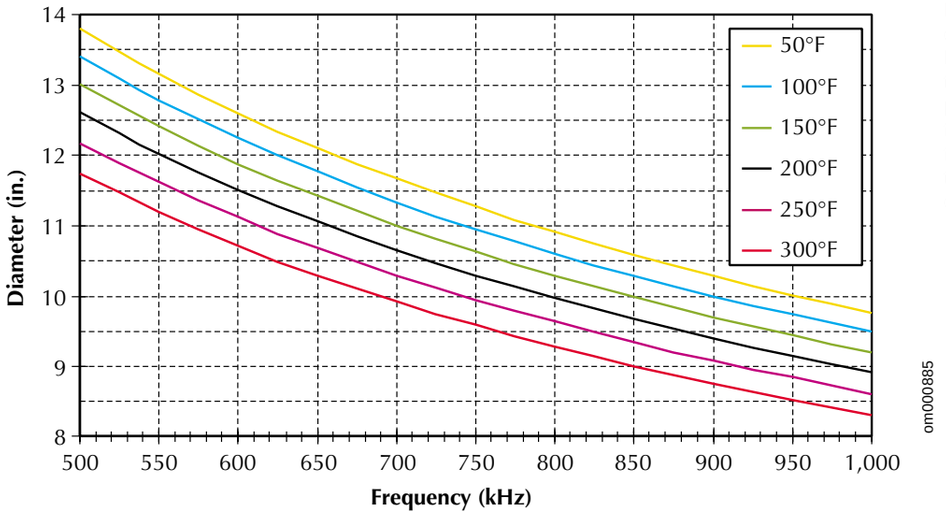

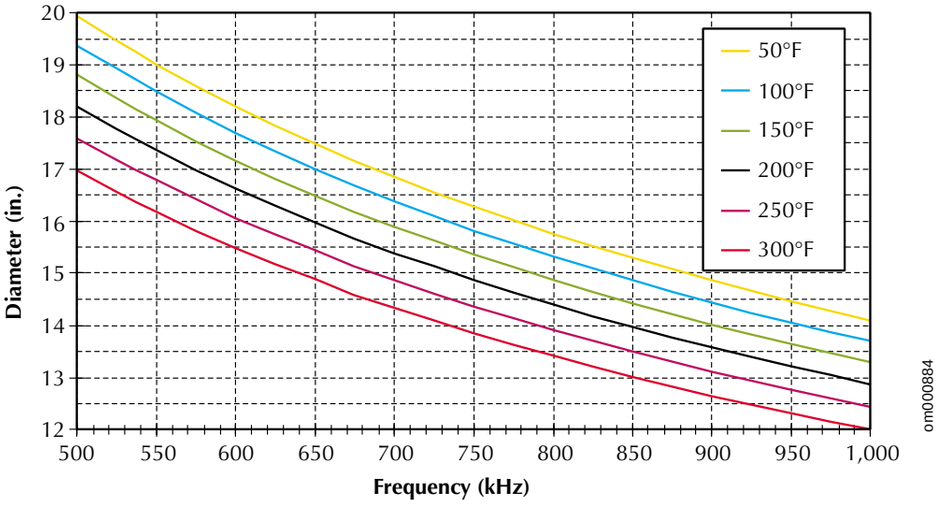

Figure 5.10—The diameter of investigation of an MRIL tool is dependent on the temperature of the permanent magnet and the frequency of the oscillating field. The upper chart is for the 4 ½-in. tool. The lower chart is for the 6-in. tool.

Thus, logging speed can be increased accordingly while maintaining the same signal-to-noise ratio. For example, if two frequencies are used, the number of CPMG measurements with full polarization will double, and the logging speed can be increased by a factor of two with no decrease in signal-to-noise ratio.

When multi-frequency acquisition with F frequencies is used, the cycle time and vertical resolution are given by

$$TC = \frac{TW + TE\ NE}{F} \tag{5.3}$$

$$VR = L + \frac{V\ (TC\ RA - TW)}{F} \tag{5.4}$$

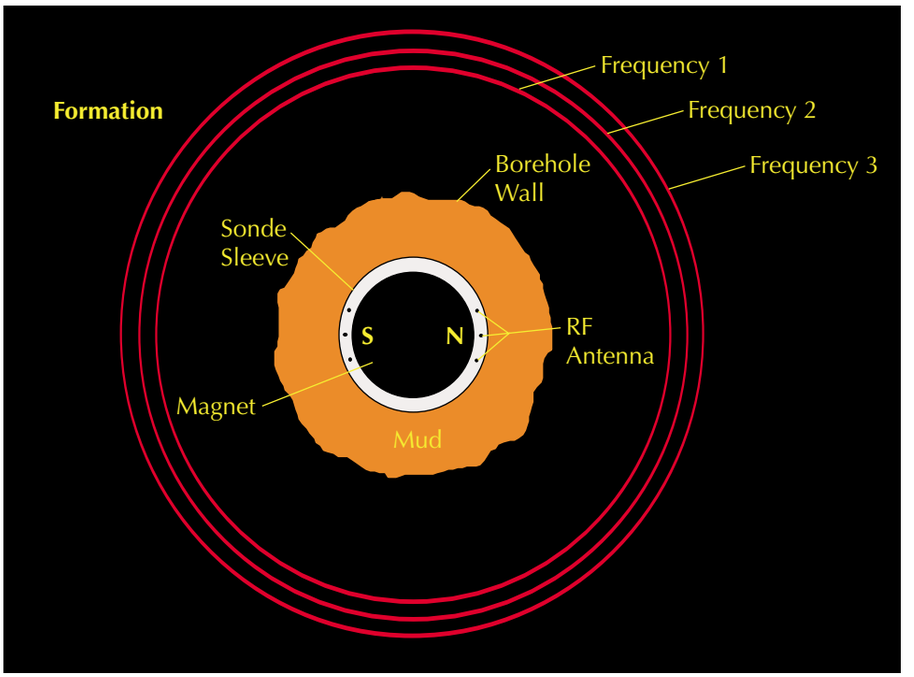

Figure 5.11—The sensitive volume of a multi-frequency MRIL measurement comprises several closely spaced cylindrical regions. The radii of the regions decrease as the frequencies increase.

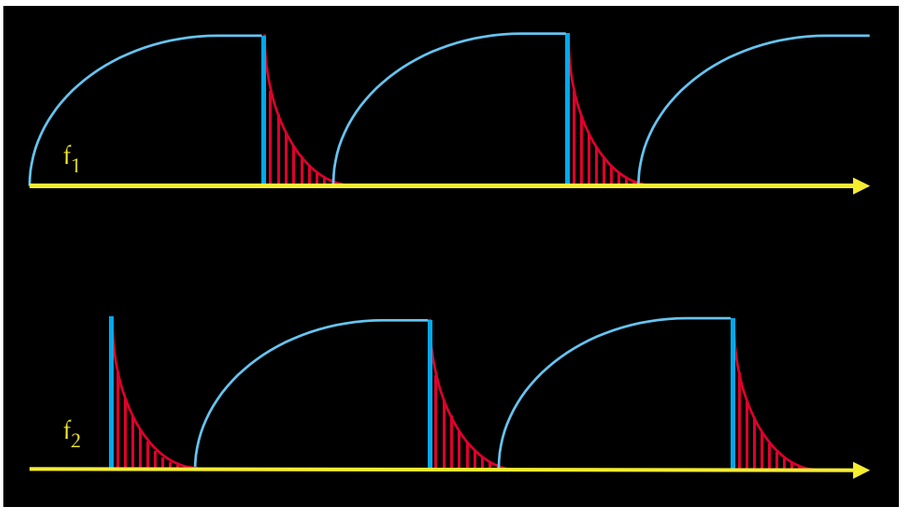

Figure 5.12—When two frequencies (f_1 and f_2) are used in MRIL measurements, the frequencies are alternated. While protons whose Larmor frequency is f_1 are being polarized, CPMG echo trains are being acquired from protons whose Larmor frequency is f_2. Similarly, while protons whose Larmor frequency is f_2 are being polarized, CPMG echo trains are being acquired from protons whose Larmor frequency is f_1.

The $\mathbf{B}_1$ field is an RF pulse whose center frequency is selected according to the Larmor frequency of the sensitive volume. The frequency response of any RF pulse, however, is not just a single frequency but rather is a frequency range defined by the bandwidth of the pulse.

Fig. 5.13 shows that the bandwidth (Δf) of an RF pulse and the strength of the field gradient (G) determine the thickness (Δr) of the sensitive volume associated with that pulse:

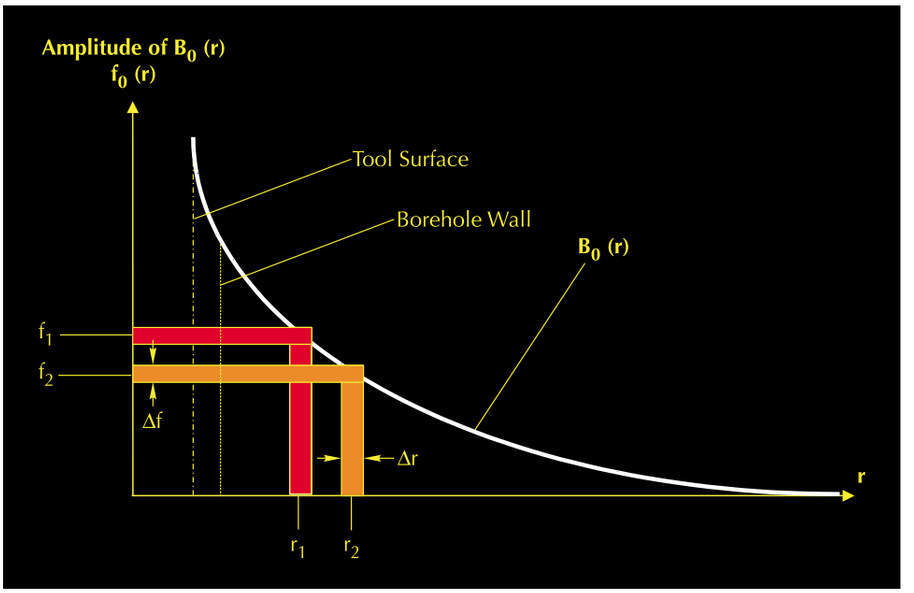

Figure 5.13— The pulse used in MRIL logging excites a narrow range of frequencies of uniform amplitude and thus has very good frequency selectivity (hence, very good sensitive-volume selectivity).

$$\Delta r = \frac{\Delta f}{\gamma\, G} \tag{5.5}$$

The bandwidth of each MRIL soft pulse is about 12 kHz, and the MRIL field gradient is about 17 gauss/cm; therefore, the thickness of the sensitive volume is about 1 mm. When an MRIL tool is run in dual-frequency mode, the difference between the two center frequencies thus should be greater than or equal to 12 kHz for avoiding overlap of the two sensitive volumes. For example, for a 750-kHz tool, f_1 is set to 756 kHz, and f_2 is set to 744 kHz. Consequently, the corresponding two sensitive volumes do not intersect.

As **Fig. 5.14** indicates, the MRIL-Prime tool uses nine RF signals to produce nine sensitive volumes,[6,7] all located in a cylindrical band approximately 1 in. thick. These signals are in five frequency ranges. The highest frequency range yields the shallowest depth of investigation and is used only for determining clay-bound water. In this application, the tool operates in single-frequency mode. Eight frequencies selected from the remaining four bands (two frequencies per band) can be used for dual-*TW*, dual-*TE*, or any standard T_2 measurements.

Ringing Effect

The MRIL magnet is a highly magnetic, ceramic material. When an oscillating electric current flows through the antenna surrounding the magnet, an electromechanical effect, called ringing, occurs in the tool. **Fig. 5.15** shows that the interaction of an electric current **I** flowing through the antenna coil and the magnetic field $\mathbf{B_0}$ of the permanent magnet produces a force **F** on the surface of the magnet and a net torque on the tool. Because this current is not constant, the torque varies, producing vibration in the tool. In turn, this vibration induces electrical noise in the antenna. Although this “ringing noise” decays quite rapidly, it can still be present during the echo detection period.

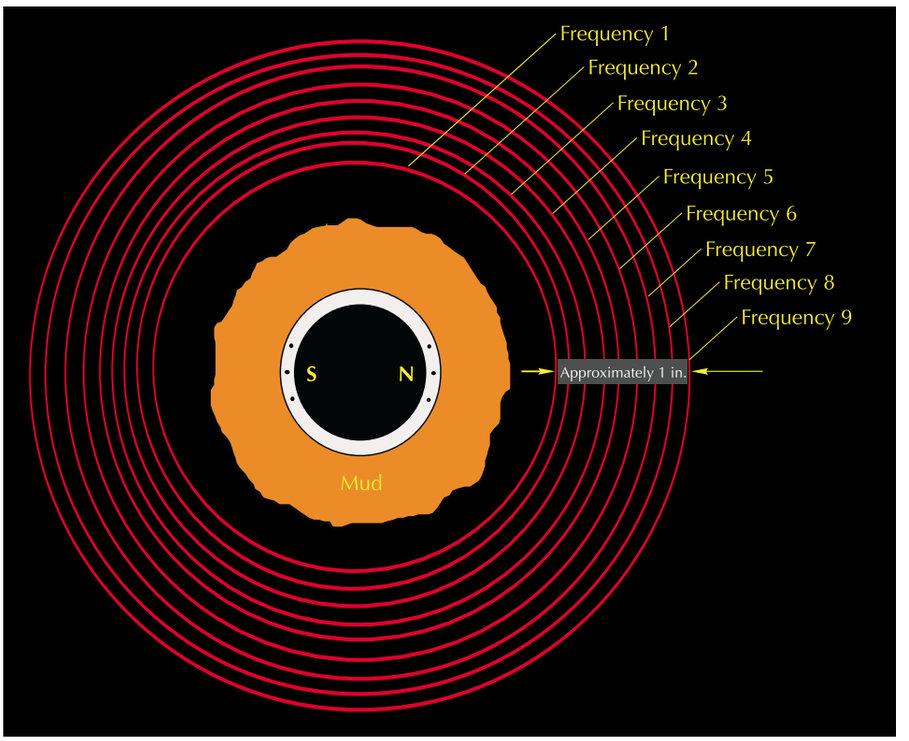

Figure 5.14—The MRIL-Prime tool can be operated with nine frequencies to make measurements in nine closely spaced sensitive volumes.

The ringing amplitude is usually very high and particularly affects the first echo (Echo 1) because of the ringing combination produced by both the 90° and the 180° pulses. Experience has shown that the ringing is frequency-dependent and is not consistent between tools. Ringing effects are more prevalent at shorter *TE* because of the limited time available for the ringing to die away.

Alternating the phase of the 90° pulse, such as is done in the phase-alternate pulse sequence (PAPS) technique discussed in Chapter 2, effectively reduces both measurement-system offset and ringing noise. When the phase of the 90° pulse is 0°, the echo amplitudes will be positive, and when the phase of the 90° pulse is 180°, the echo amplitudes will be negative. However, both system offset and ringing noise will be unaffected by the phase of the 90° pulse. Thus, the measured echoes of two echo trains having a 180° phase difference between their 90° pulses can be expressed as follows:

For a 90° pulse at 0° phase: measured echoes = signal + ringing + offset (5.6)

For a 90° pulse at 180° phase: measured echoes = -signal + ringing + offset (5.7)

Hence, subtracting the two measured echoes and dividing the result by two yields the true signal. Adding the two measured echoes and dividing the result by two (i.e., averaging the two echoes) yields ringing and offset information useful in quality control.

Fig. 5.16 illustrates the pulse timing used with the PAPS technique (which is always applied in MRIL logging) when an MRIL tool is operated in a dual-frequency mode.

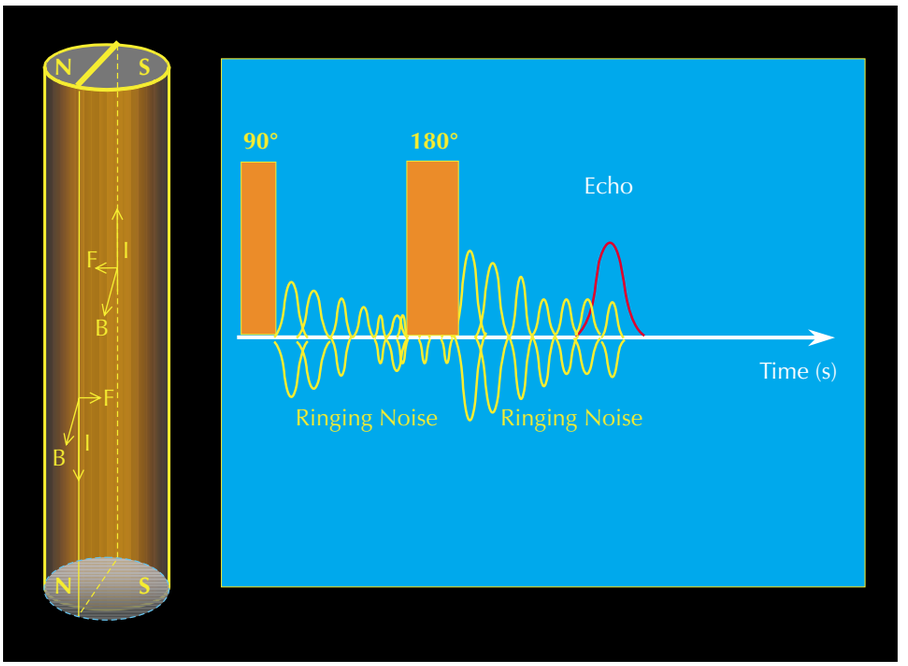

om000891

Figure 5.15—Ringing occurs during CPMG measurements because of the torque associated with a variable force **F** produced by the interaction of the electric current **I** flowing through the antenna coil and the magnetic field $\mathbf{B}_0$.

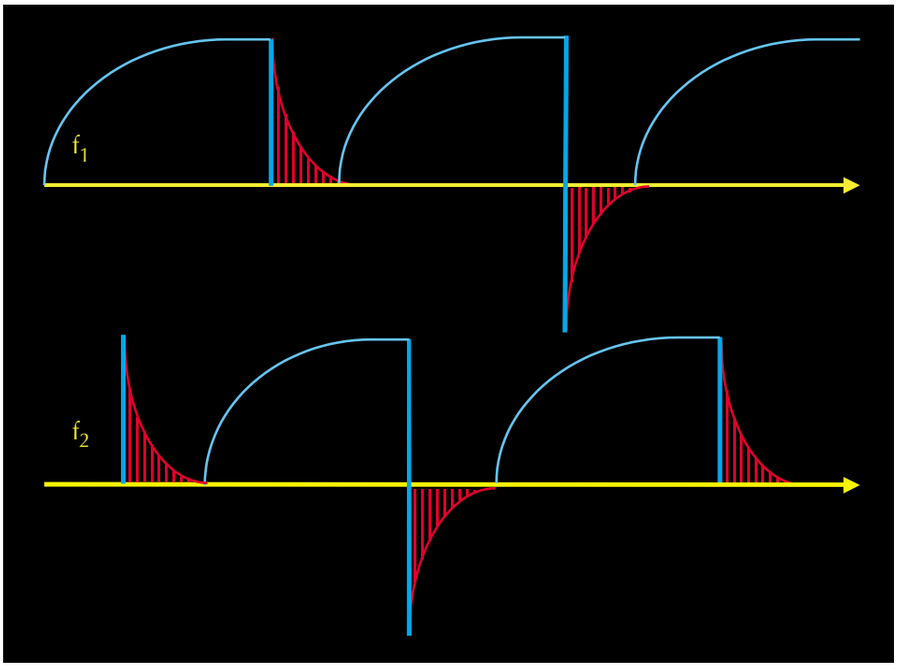

om000893

Figure 5.16—When the PAPS method is used, the phase angle between the 90° pulses for each frequency is 180°.

Signal-to-Noise Ratio and Running Average

An NMR signal is always very weak. In particular, the amplitudes of the echo signals received by an MRIL tool are on the order of a nanovolt (10^{-9} volt), which makes these signals difficult to distinguish from noise. Thus, the raw signal-to-noise ratio (*S/N*) is very poor. A single CPMG echo train from an MRIL tool is shown in the top panel of **Fig. 5.17**.

If an echo measurement is repeated, the amplitude and position in time of an echo signal will repeat, but the noise will not, because noise is randomly distributed. Stacking and averaging several echo trains reduces the noise level and improves the *S/N*. The running average (*RA*) represents the total number of individual echo trains needed to produce a stacked, averaged echo train with a particular improvement in *S/N* over the raw *S/N*. If the number of echo trains that are stacked and averaged is n (that is, $RA = n$), then the resulting *S/N* will be $\sqrt{n}$ times the *S/N* of an individual echo train.

When the PAPS technique and a multi-frequency operational mode are used, the selection of *RA* is not arbitrary. Because a phase-alternated pair of echoes is associated with each frequency, *RA* in current implementations is an even multiple of the number of frequencies used in acquiring the echo trains.

Activations

An activation is a set of parameters that controls the pulse sequence of an MRIL tool during a logging job. The activation chosen thus determines the type of NMR measurement that is made. Activation parameters are contained in a table that is transmitted from the surface system of the logging unit to the digital signal processor (DSP) in the MRIL tool.

Some activation parameters can be changed easily by the field engineer—for example, number of echoes (*NE*), polarization time (*TW*), and running average (*RA*). Some other parameters are "invisible," being built into the activation, and, therefore, impossible to change—for example, pulse type, number of gain or noise cycles, and number of $\mathbf{B}_1$ measurements. Furthermore, some parameters can be changed only by selecting another activation, and these parameters include echo spacing (*TE*) and number of operating frequencies (*XF*).

For third-generation MRIL tools (MRIL-C/TP[8]), activations can be selected based on

- the information to be obtained from tool measurements
  - effective porosity (Use a standard-T_2 activation.)
  - direct hydrocarbon typing through Differential Spectrum/Time Domain Analysis (Use a dual-*TW* activation.)
  - direct hydrocarbon typing through Shifted Spectrum/Diffusion Analysis (Use a dual-*TE* activation.)
  - total porosity (Use a total-porosity activation.)
- the environment surrounding the tool
  - high-resistivity borehole (Use an activation with high *Q*, where *Q* is an antenna loading factor.)
  - medium-resistivity borehole (Use an activation with medium *Q*.)
  - low-resistivity borehole (Use an activation with low *Q*.)

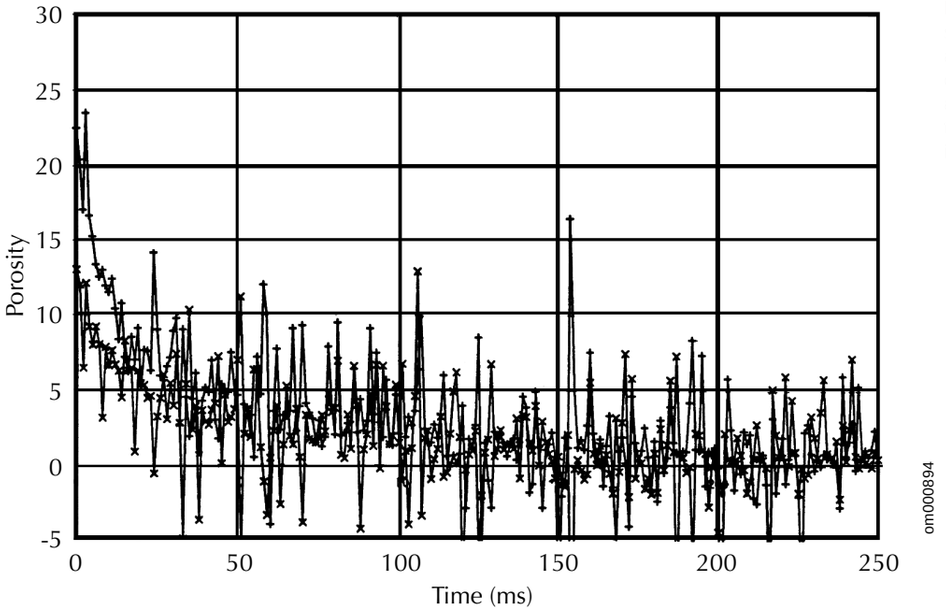

Figure 5.17—A single spin-echo train (top) acquired by an MRIL tool exhibits poor *S/N*. Stacking and averaging eight echo trains (bottom) significantly improves the *S/N*.

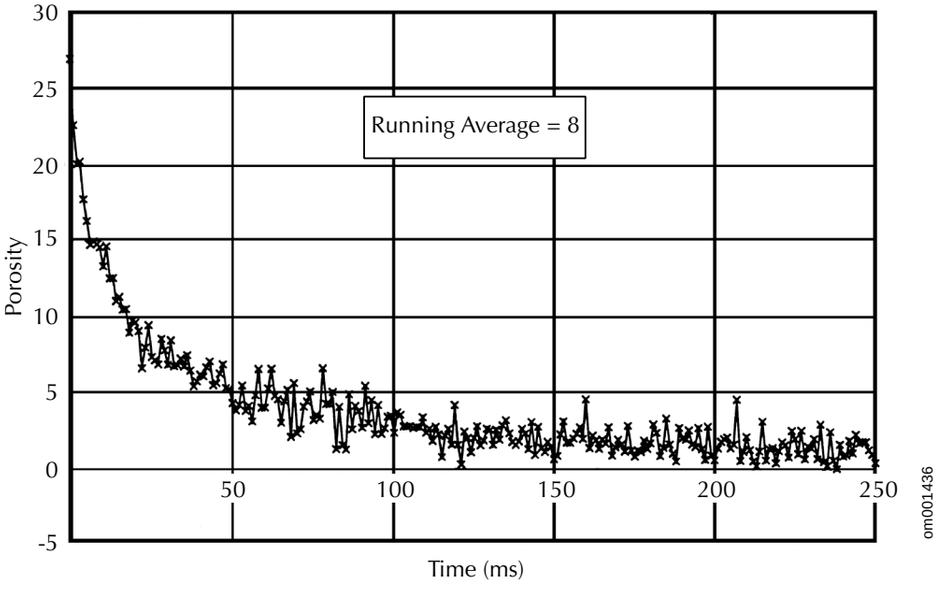

- the number of operating frequencies used by the tool
  - one frequency (Use an activation that employs one frequency.)
  - two frequencies (Use an activation that employs two frequencies.)
  - three frequencies (Use an activation that employs three frequencies.)

Each activation contains several parameters that must be chosen carefully to obtain accurate data without exceeding the operational limits of the tool. Some of these parameters are

- polarization or wait time (*TW*)
- echo spacing (*TE*)
- number of echoes (*NE*)
- running average (*RA*)

Activation sets are tool-dependent. The actual choice of proper activations for an MRIL job is a part of job planning, which is discussed in Chapter 8.

The nine frequencies of the MRIL-Prime tool allow it to obtain more data in a particular period than if only one frequency were used. **Fig. 5.18** illustrates the application of these frequencies,[7] which are selected from five bands, designated as bands 0, 1, 2, 3, and 4. A frequency chosen from band 4 can be used to measure clay-bound water with a partial-polarization activation in single-frequency mode. Frequencies from the other four bands can be used to run different activation sets, such as standard T_2, dual *TW*, and/or dual *TE*, in dual-frequency mode. **Fig. 5.19** shows the five frequency bands and their typical center frequencies.

Fig. 5.18 also illustrates the concept of measurement efficiency, $[XF \times (NE \times TE)]/TW$, under the assumption $NE \times TE = 500$ ms and $TW = 12$ s, where *XF* is the number of frequencies used and $NE \times TE$ is the pulse time. Measurement efficiency is thus only 4% for a single-frequency measurement but 36% for a nine-frequency measurement.

Fig. 5.20 contains a simplified timing diagram for a dual-*TW* activation for the MRIL-Prime tool.[6] The activation initiates three different CPMG pulse sequences at various operating frequencies:

- For the first sequence, $TE = 1.2$ ms and $TW = 12$ s.
- For the second sequence, $TE = 1.2$ ms and $TW = 1$ s.
- For the third sequence, $TE = 0.6$ ms and $TW = 0.02$ s.

The cycle repeats every 14 s. At a logging speed of 1,000 ft/hr (16.7 ft/min), two samples per foot are produced for each *TW* of 1 and 12 s in frequency bands 3, 2, 1, and 0, and one sample per foot is produced for the *TE* of 0.6 ms in frequency band 4.

MRIL-Prime 6-in. sondes are equipped with additional pairs of magnets located above and below the main magnet to achieve accelerated pre-polarization by their higher magnetic fields.[6] The main magnet is three times longer than the antenna aperture, which allows for proper recovery from the higher polarization. At stationary or slow logging conditions, these magnets offer no advantage, but at normal- or high-logging speeds, they effectively halve the time needed for complete polarization, as shown in **Fig. 5.21**.

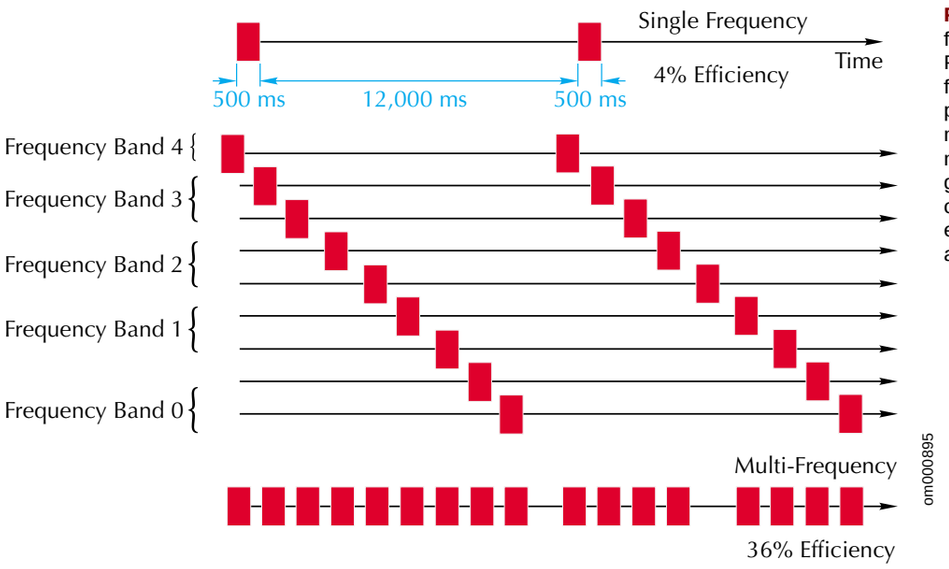

Fig. 5.18—The nine frequencies of the MRIL-Prime tool are selected from five bands. When polarization time is 12,000 ms and pulse time is 500 ms, the nine frequencies give an efficiency of 36% compared to the 4% efficiency obtainable with a single frequency.

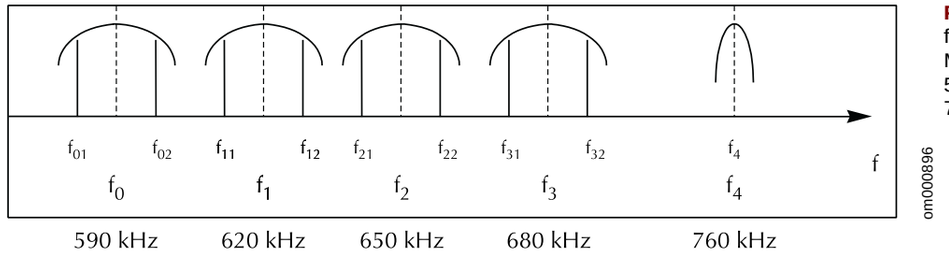

Fig. 5.19—Typical center-frequencies of the five MRIL frequency bands are 590, 620, 650, 680, and 760 kHz.

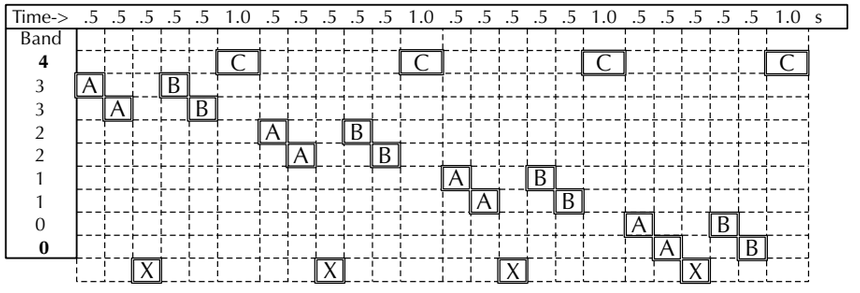

Figure 5.20—This timing diagram for a dual-*TW* activation for an MRIL-Prime tool shows that three different CPMG sequences are used repeatedly, two of them at various operating frequencies.

Legend:

- A — CPMG Sequence: *TE* = 1.2 ms, *TW* = 12 s, *NE* = 400.
- B — CPMG Sequence: *TE* = 1.2 ms, *TW* = 1 s, *NE* = 400.
- C — CPMG Sequence: *TE* = 0.6 ms, *TW* = 0.02 s, *NE* = 10. (Repeated 24 Times)
- X — Data Transfer

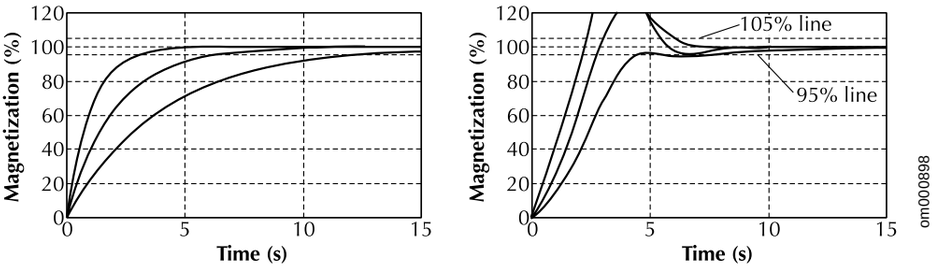

Fig. 5.21—These three curves (left) show how fast magnetization can be achieved without accelerated pre-polarization. The curves correspond to T_1 = 1, 2, and 4 s. If 5% underpolarization can be tolerated, 12 s are needed to polarize the slowest component. With accelerated polarization as used in the MRIL-Prime 6-in. sonde (right), magnetization can be achieved more quickly. The most critical case of logging at 24 ft/min is shown. The same T_1 distribution of 1, 2, and 4 s as was studied in the left graph is assumed. After 6 s, all components have stabilized within a ±5% band of the nominal magnetization.

Tool Configuration

In basic configuration, an MRIL tool consists of a magnetic mandrel with a diameter of 4 $^1/_2$, 4 $^7/_8$, or 6 in.; an electronics cartridge; and one or two energy-storage cartridges (capacitors), as illustrated in **Fig. 5.22**. A fluid excluder, centralizers, and standoffs are optional items but are always recommended and must be selected according to hole size.

The use of a fluid excluder reduces the loading effect of mud and increases the signal-to-noise ratio. Centralizers and standoffs both help centralize the tool in the borehole. Furthermore, standoffs may protect the tool's fiberglass body by keeping it away from the casing/borehole wall.

MRIL tools are fully combinable with Halliburton's other openhole logging tools, such as the High-Resolution Array Induction (HRAI) tool, the Electrical Micro Imaging (EMI) tool, and the Circumferential Acoustic Scanning Tool (CAST-V).

References

1. Taicher, Z., et al., 1986, Nuclear magnetic resonance sensing apparatus and techniques, U.S. patent 4,717,877.

2. Taicher, Z., and Shtrikman, S., 1986, Nuclear magnetic resonance sensing apparatus and techniques, U.S. patent 4,717,878.

3. Miller, M.N., et al., 1990, Spin-echo magnetic-resonance logging—porosity and free-fluid index, SPE 20561, *1990 SPE Annual Technical Conference and Exhibition Proceedings*, v. Ω (Formation evaluation and reservoir geology), p. 321–334.

4. Coates, G.R., et al., 1993, Restrictive diffusion from uniform gradient NMR well logging, SPE 26472, *1993 SPE Annual Technical Conference and Exhibition Proceedings*, v. Ω (Formation evaluation and reservoir geology), p. 575–590.

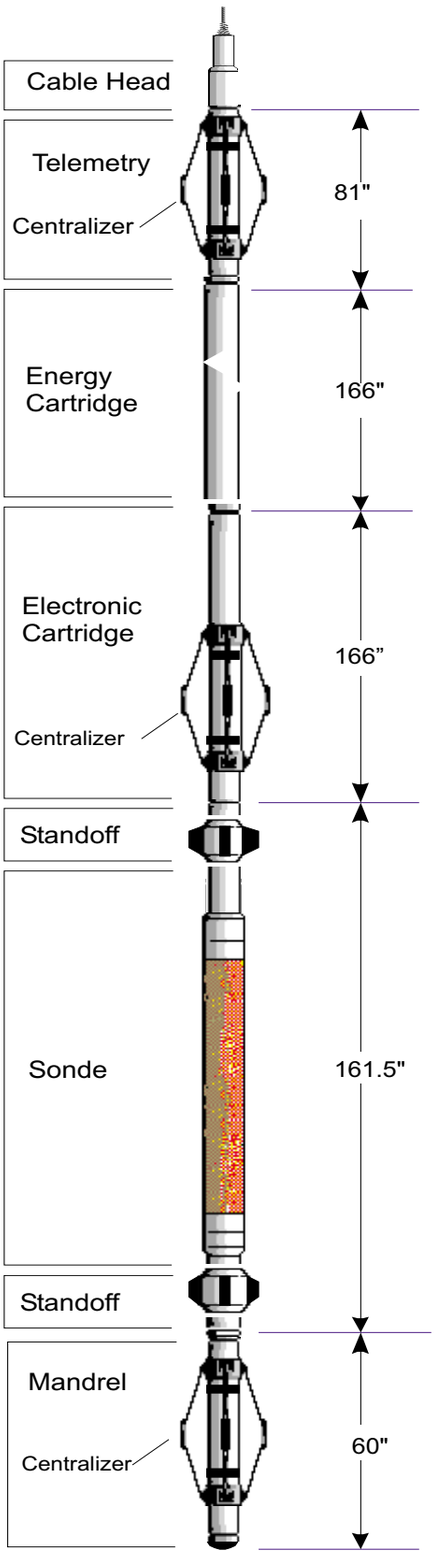

Figure 5.22—In its basic configuration, the MRIL tool consists of a magnetic mandrel, an electronics cartridge, and one or two energy-storage cartridges.

5. Chandler, R.N., et al., 1994, Improved log quality with a dual-frequency pulsed NMR tool, SPE 28365, *1994 SPE Annual Technical Conference and Exhibition Proceedings*, v. Ω (Formation evaluation and reservoir geology), p. 23–35.

6. Prammer, M.G., et al., 1999, Theory and operation of a new, multi-volume, NMR logging system, paper DD, *40th Annual SPWLA Logging Symposium Transactions*, 12 p.

7. Prammer, M.G., et al., 1998, A new multiband generation of NMR logging tools, SPE 49011, *1998 SPE Annual Technical Conference and Exhibition Proceedings*, v. Ω (Formation evaluation and reservoir geology), p. 237–243.

8. Prammer, M.G., et al., 1996, Measurements of clay-bound water and total porosity by magnetic resonance logging, SPE 36522, *1996 SPE Annual Technical Conference and Exhibition Proceedings*, v. Ω (Formation evaluation and reservoir geology), p. 111–118. Also published in 1996 in *The Log Analyst*, v. 37, no. 5, p. 61–69.

Additional information on NMR logging tool principles can be found in following literature.

Akkurt R., 1990, *Effects of Motion in Pulsed NMR Logging*, Colorado School of Mines, Golden, Colorado, unpublished Ph.D. dissertation, 165 p.

Allen, D., et al., 1997, How to use borehole nuclear magnetic resonance, *Oilfield Review*, v., 9, no. 2, p. 2–15.

Brown, J.A., Brown, L.F., and Jackson, J.A., 1981, NMR (nuclear magnetic resonance) measurements on western gas sands core, SPE/DOE 9861, *1981 SPE/DOE Low Permeability Gas Reservoirs Symposium Proceedings*, p. 321-326. Also published in 1981 as Los Alamos National Laboratory Report No. LA-UR-81-736, 16 p.

Brown, J.A., et al., 1982, NMR Logging Tool Development—Laboratory Studies of Tight Gas Sands and Artificial Porous Material, Los Alamos National Laboratory Report No. LA-UR-82-447, 20 p. Also published in 1982 as SPE 10813 in *1982 SPE/DOE Unconventional Gas Recovery Symposium Proceedings*, p. 203–209.

Brown, J.A., Jackson, J.A., and Koelle, A.R., 1985, Western Gas Sands Project Los Alamos NMR Well Logging Tool Development, Los Alamos National Laboratory Report LA-10374-PR, 77 p.

Chandler, R., 1995, NML hardware history and MRIL, chapter 6, in Georgi, D.T., ed., Nuclear Magnetic Resonance Logging Short Course Notes, *36th Annual SPWLA Logging Symposium*, Paris, France, 12 p.

Edwards, C., 1997, Effects of tool design and logging speed on T_2 NMR log data, paper RR, *38th Annual SPWLA Logging Symposium Transactions*, 13 p.

Georgi, D.T., et al., 1995, Vertical resolution and signal-to-noise characteristics of nuclear magnetic resonance imaging logs, paper OOO, in Georgi, D.T., ed., Nuclear Magnetic Resonance Logging Short Course Notes, *36th Annual SPWLA Logging Symposium Transactions*, Paris, France, 12 p.

Jackson, J.A., 1984, Nuclear magnetic resonance logging, *The Log Analyst*, v. 25, no. 5, September-October, p. 16.

Jackson, J.A., Brown, J.A., and Crawford, T.R., 1981, Remote Characterization of Tight Gas Formations with a New NMR Logging Tool: Los Alamos National Laboratory Report No. LA-UR-81-735, 18 p. Also published in 1981 as SPE/DOE 9860, in *1981 SPE/DOE Symposium on Low Permeability Gas Reservoirs Proceedings*, p. 313–320.

Jackson, J.A., Brown, J.A., and Koelle, A.R., 1982, Western Gas Sands Project, Los Alamos NMR (Nuclear Magnetic Resonance) Well Logging Tool Development, Progress Report, April 1, 1980–September 30, 1981, Los Alamos National Laboratory Report No. LA-9151-PR, 24 p. Also published in 1982 as U.S. Department of Energy Fossil Energy Report No. DOE/BC/10018-20, 34 p.

Jackson, J.A., Brown, J.A., and Koelle, A.R., 1982, Western Gas Sands Project, Los Alamos NMR (Nuclear Magnetic Resonance) Well Logging Tool Development, Progress Report, October 1, 1981–September 30, 1982, Los Alamos National Laboratory Report.

Mardon, D., et al., 1995, Improved environmental corrections for MRIL pulsed NMR logs run in high-salinity boreholes, paper DD, *36th Annual SPWLA Logging Symposium Transactions*, 12 p.

Morriss, C.E., et al., 1996, Operating guide for the Combinable Magnetic Resonance tool, *The Log Analyst*, v. 37, no. 6, p. 53–60.

Xiao, L.Z., 1998, NMR Imaging Logging Principles and Applications (in Chinese), Science Press, Beijing, 328 p.

Chapter 6

Answer Products Derived from MRIL Stand-Alone Analysis

NMR data can be analyzed independently or in combination with conventional data. When NMR data are interpreted independently, they can provide porosity and permeability as well as complete information on fluid types and fluid saturation in the invaded zone. Two computer-center models are available for stand-alone analysis of MRIL data, the Time Domain Analysis (TDA) model and the Diffusion Analysis (DIFAN) model. Another model called the Enhanced Diffusion Method (EDM) can be implemented during data acquisition and provides valuable information for viscous-oil detection. Complete descriptions of these models and their applications are discussed in this chapter.

Time Domain Analysis

Concept

Time Domain Analysis (TDA)[1–3] relies on the fact that different fluids have different rates of polarization, or different T_1 relaxation times. The T_1 of both gas and light oil (viscosity less than 5 cp) is normally much longer than the T_1 of water. Time Domain Analysis provides

- fluid types in the flushed zone
- corrected MRIL porosity in gas reservoirs (Without this correction, MRIL data underestimates porosity because of the long T_1 and low hydrogen index of gas.)
- corrected MRIL porosity in light oils
- complete fluid-saturation analysis in the flushed zone using only MRIL data

Principle

Differential Spectrum Method

TDA was an outgrowth of the Differential Spectrum Method (DSM),[4–6] which was developed as an earlier application of dual-*TW* logging. The DSM technique is used mostly to qualitatively investigate the existence of gas in a formation. The basis of the technique is represented in **Fig. 6.1**.

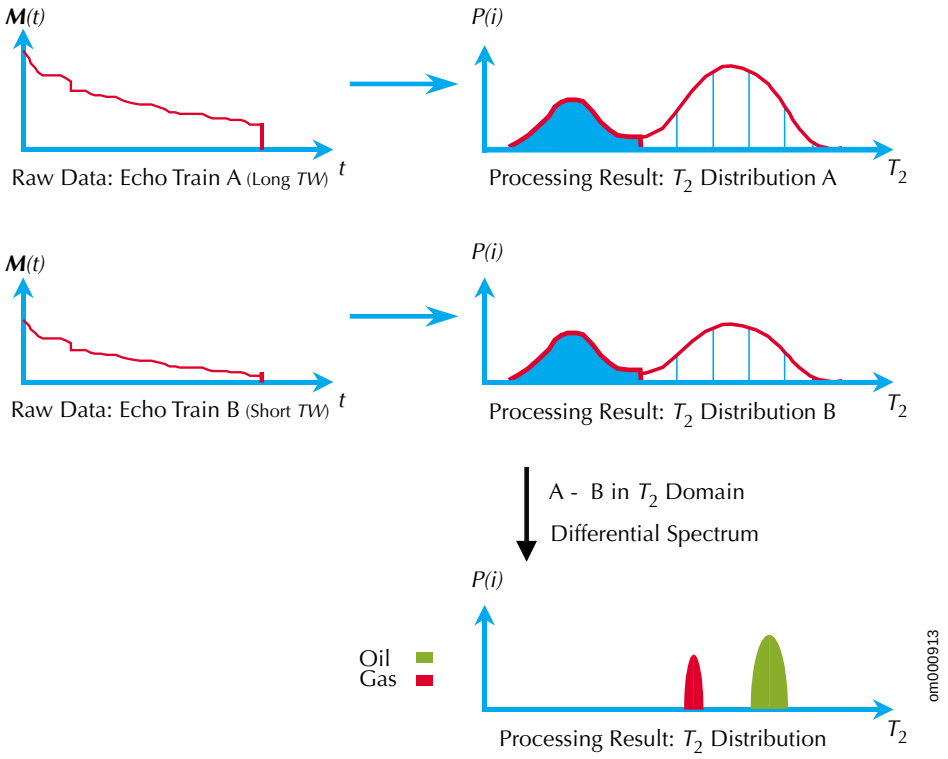

Figure 6.1—In the Differential Spectrum Method, the long-*TW* and short-*TW* echo trains are first converted to T_2 distributions, and the resulting T_2 distributions are subtracted from one another.

Time Domain Analysis

With TDA, the subtraction is performed in the ordinary time domain instead of the T_2 domain. The TDA method has two key advantages over the DSM.

- The difference between the two echo trains is calculated in the time domain, so the difference is more robust. The difference is then transformed to a T_2 distribution.
- TDA provides better corrections for underpolarized hydrogen and for hydrogen-index effects.

Fig. 6.2 illustrates the TDA principle. A complete mathematical derivation of the Time Domain Analysis technique is presented in the chapter Appendix.

Data Acquisition

TDA data are acquired with dual-*TW* activation. Dual-*TW* logging acquires two NMR decay curves by utilizing a long *TW* and a short *TW* with a single *TE*. A typical *TW* pair is 1 and 8 s, with a *TE* of 0.9 or 1.2 ms. Some of the TW_S/TW_L pairs for the dual-*TW* logging activations were introduced in Chapter 5.

Fig. 6.3 illustrates the principle of dual-*TW* logging. The top and middle sections show the polarization and echo acquisition with a dual-frequency mode using frequencies f_1 and f_2. In this illustration, the short-*TW* echo train is acquired in the f_1 shell, or f_1 sensitive volume, while the formation is being polarized in the f_2 shell. Then a long-*TW* echo train is acquired in

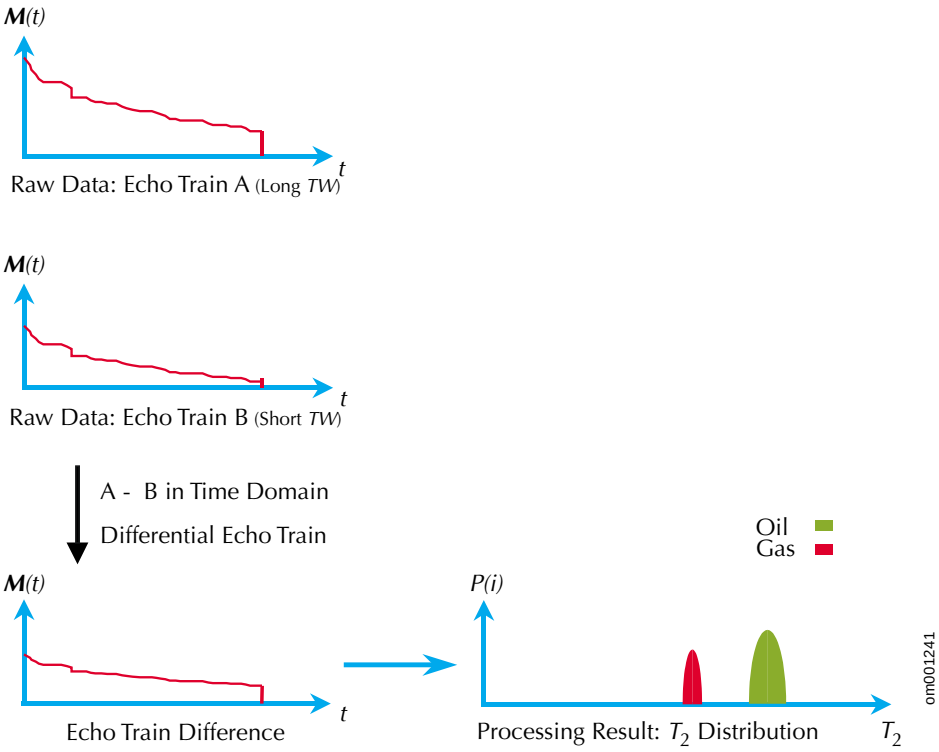

Figure 6.2—In Time Domain Analysis, the long- and short-*TW* echo trains are first subtracted, and the echo train difference is converted to a T_2 distribution.

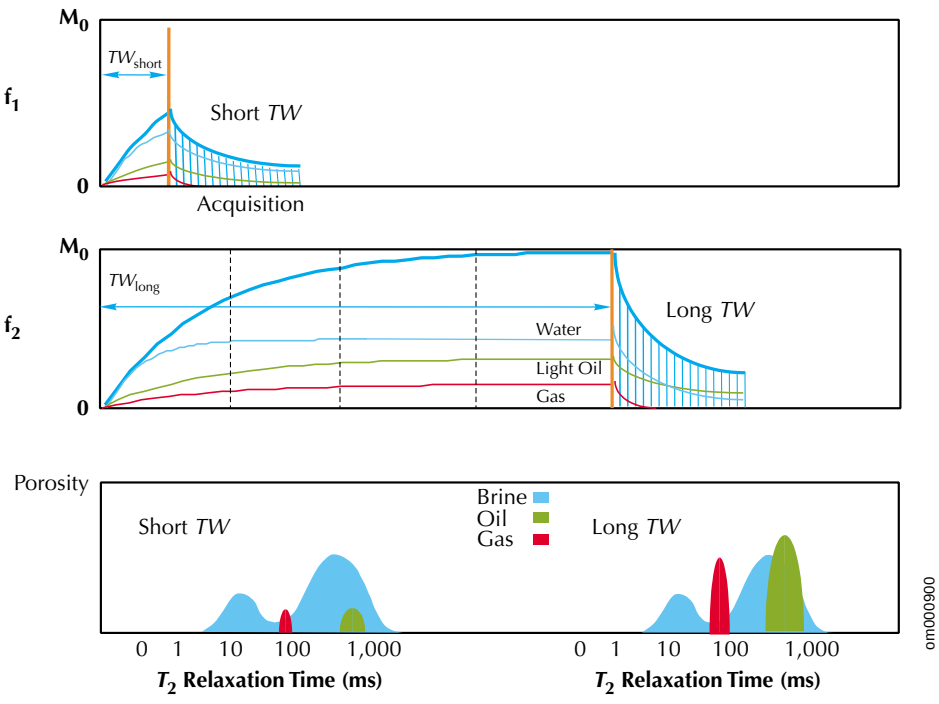

Figure 6.3—Dual-*TW* logging acquires a partially polarized echo train with a short *TW* (upper section) and a fully polarized echo train with a long *TW* (middle section). T_2 distributions corresponding to the two echo trains are generated (bottom section).

the f_2 shell. The short *TW* is selected so that the protons in water are fully polarized, but so that the protons of both gas and light oils are only partially polarized. During the long-*TW* cycle, all the protons from the water are fully polarized, and the protons from the gas and light oil are more completely polarized than during the short-*TW* cycle. The full polarization of the water implies that the difference between the long-*TW* and short-*TW* measurements is due to the gas and light oil signals. The bottom section in Fig. 6.3 shows the T_2 distributions from both echo trains.

Dual-*TW* logging results at the wellsite include short-*TW* and long-*TW* T_2 distributions; apparent *MPHI*, *BVI*, and *MFFI* from both the short-*TW* and long-*TW* echo trains; and *MPERM* from the long-*TW* measurements. **Fig. 6.4** shows a dual-*TW* log. By comparing the *BVI* and *MFFI* from both the short- and long-*TW* measurements, useful quick look information may be obtained. Both gas and light oil have a long T_1, and thus need a longer *TW* for full polarization. If light oil is present, the *MFFI* from the long *TW* will be greater than that from the short *TW*. In a gas zone, the *BVI* and *MFFI* from long *TW* will be greater than that from the short *TW*.

Applications

Example 1

Two wells from a field in Egypt show the importance of TDA in overcoming the effect of underpolarization of light hydrocarbons to provide correct formation porosity. In the subject field, the operator used a light oil-based mud, which has a T_1 value of about 5 s. Originally, the effect of the light oil-based mud was not taken into consideration, which resulted in underestimating the formation porosity. A comparison between core porosity and MRIL porosity on the first well is shown in **Fig. 6.5** and illustrates this underestimation as does a comparison between the neutron-density crossplot porosity and MRIL porosity shown in **Fig. 6.6**.

In the second well, TDA was run to correct for the light oil-based mud in the invaded zone, which affected the MRIL response because of the underpolarization of the hydrogen nuclei in the mud. **Fig. 6.7** compares core porosity with TDA-determined *MPHI*. **Fig. 6.8** compares neutron-density crossplot porosity with TDA-determined *MPHI*. The figures demonstrate that TDA processing corrected the *MPHI* underestimation problem that was observed in the previous well.

Example 2

Fig. 6.9 shows the result of applying TDA to the MRIL data of Fig. 6.4. Utilizing this technique, MRIL stand-alone analysis provides a complete solution for porosity, permeability and fluid saturation in the flushed zone. According to the TDA results, a very good water-free pay zone is located between XX685 and XX870 ft, although the resistivity is quite low from XX715 to XX870 ft. A water zone is located from XX870 to XX880 ft.

As discussed before, the data acquired with NMR tools always contain noise, which results in spectral broadening. The effects of spectral broadening when using the DSM can be severe when the difference between hydrocarbon-filled porosity obtained from the two echo trains ($\Delta\phi_h$) is small.[2] The signal may be smeared unequally into adjacent bins, and the differential spectrum may appear to contain no hydrocarbon signal.

Example 3

A gas well drilled with oil-based mud in the Gulf of Mexico provides an example of complete DSM and TDA processing.[3] The logging program in the well consisted of logging-while-drilling (LWD) gamma ray, resistivity, and neutron logs, and a wireline MRIL log. The MRIL

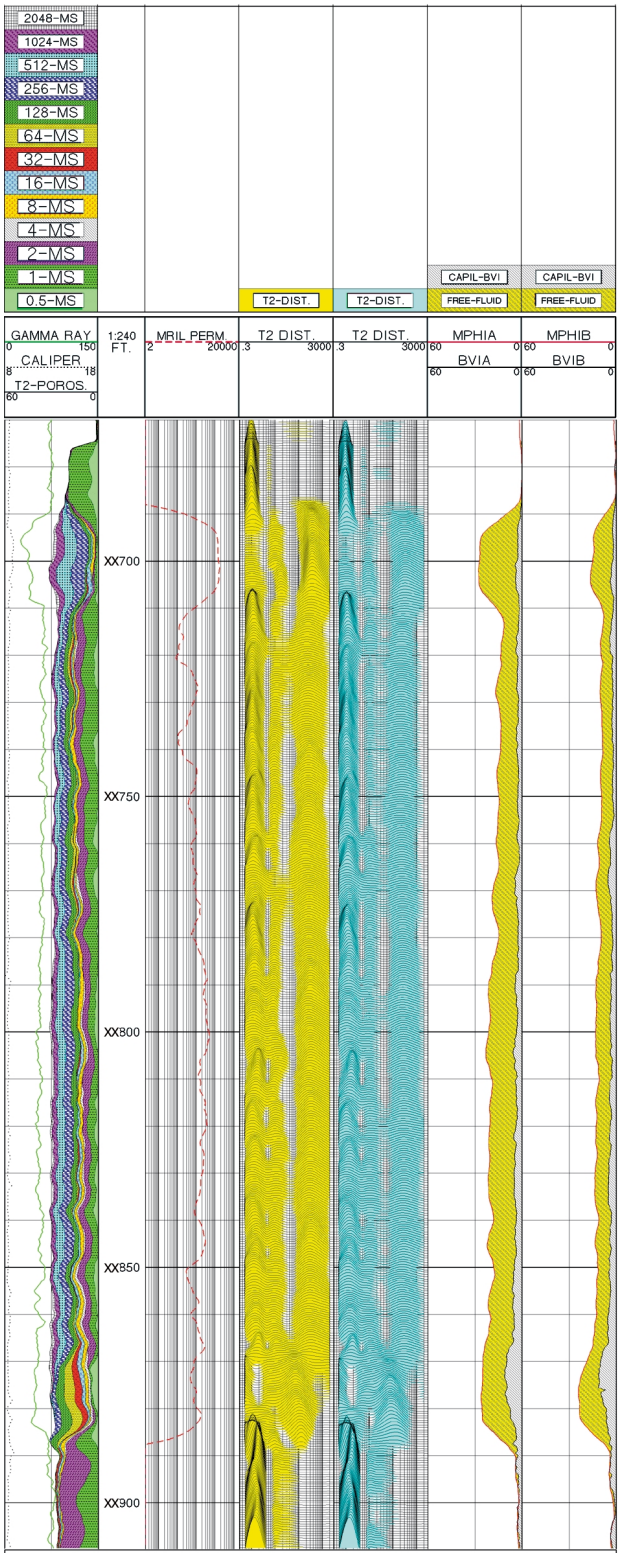

Figure 6.4—This log shows dual-*TW* wellsite results. Track 1 contains a conventional gamma ray correlation curve and long-*TW* T_2 bin data. Track 2 displays *MPERM*. Track 3 displays the long-*TW* T_2 distribution. Track 4 displays the short-*TW* T_2 distribution. Track 5 contains the long-*TW MPHI* and *BVI* curves. Track 6 contains the short-*TW MPHI* and *BVI* curves.

Figure 6.5—On this Egyptian well drilled with a light oil-based mud, a comparison of core porosity with *MPHI* determined without TDA shows that *MPHI* underestimates porosity.

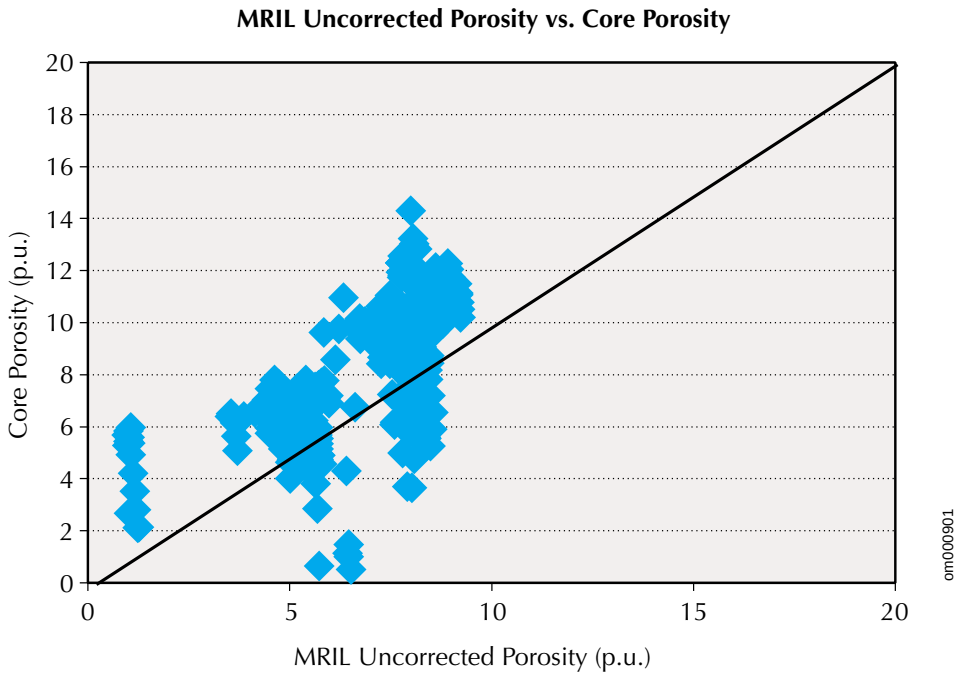

Figure 6.6—On the same well as described in Fig. 6.5, a comparison of neutron-density crossplot porosity with *MPHI* determined without TDA again shows that *MPHI* underestimates porosity.

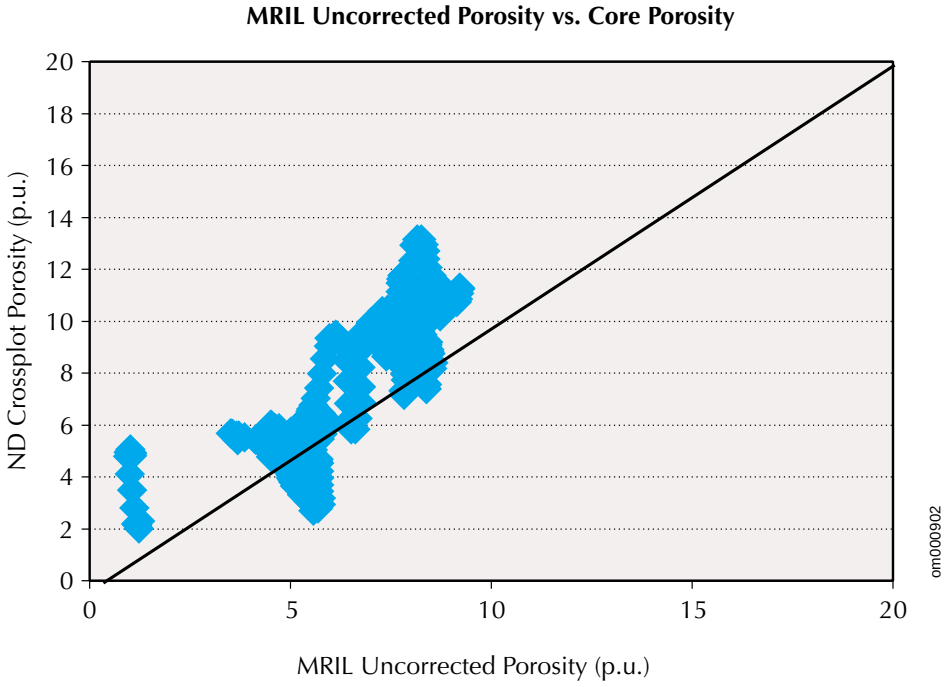

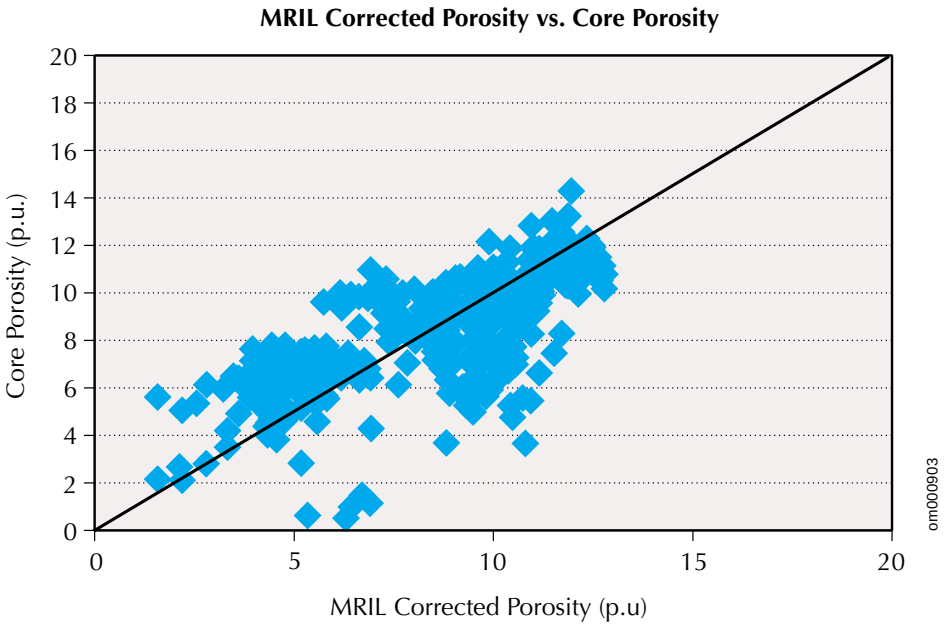

Figure 6.7—On this second Egyptian well drilled with a light oil-based mud, *MPHI* determined with TDA correlates well with core porosity.

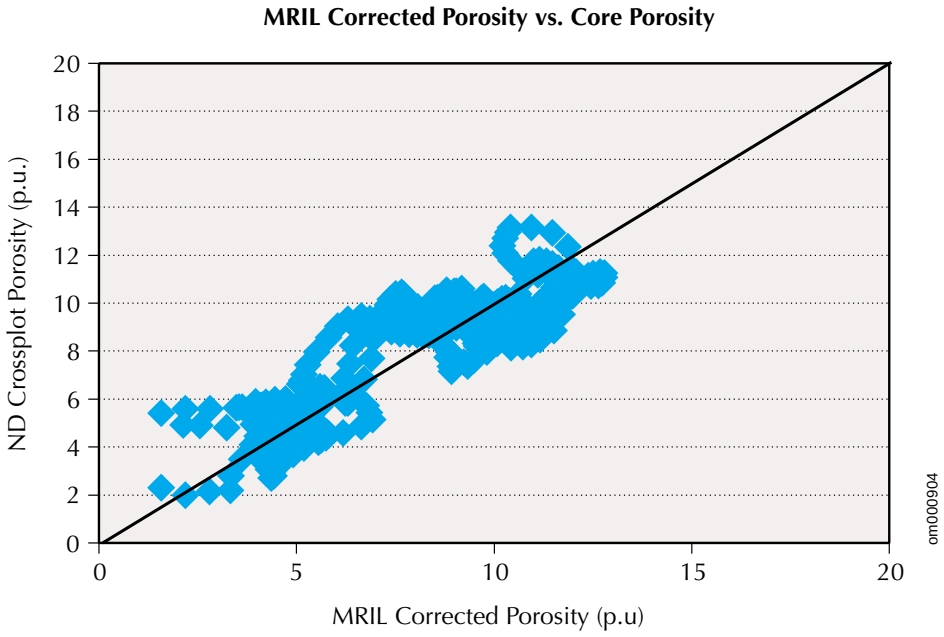

Figure 6.8—On the same well as described in Fig. 6.7, *MPHI* determined with TDA correlates well with neutron-density cross-plot porosity.

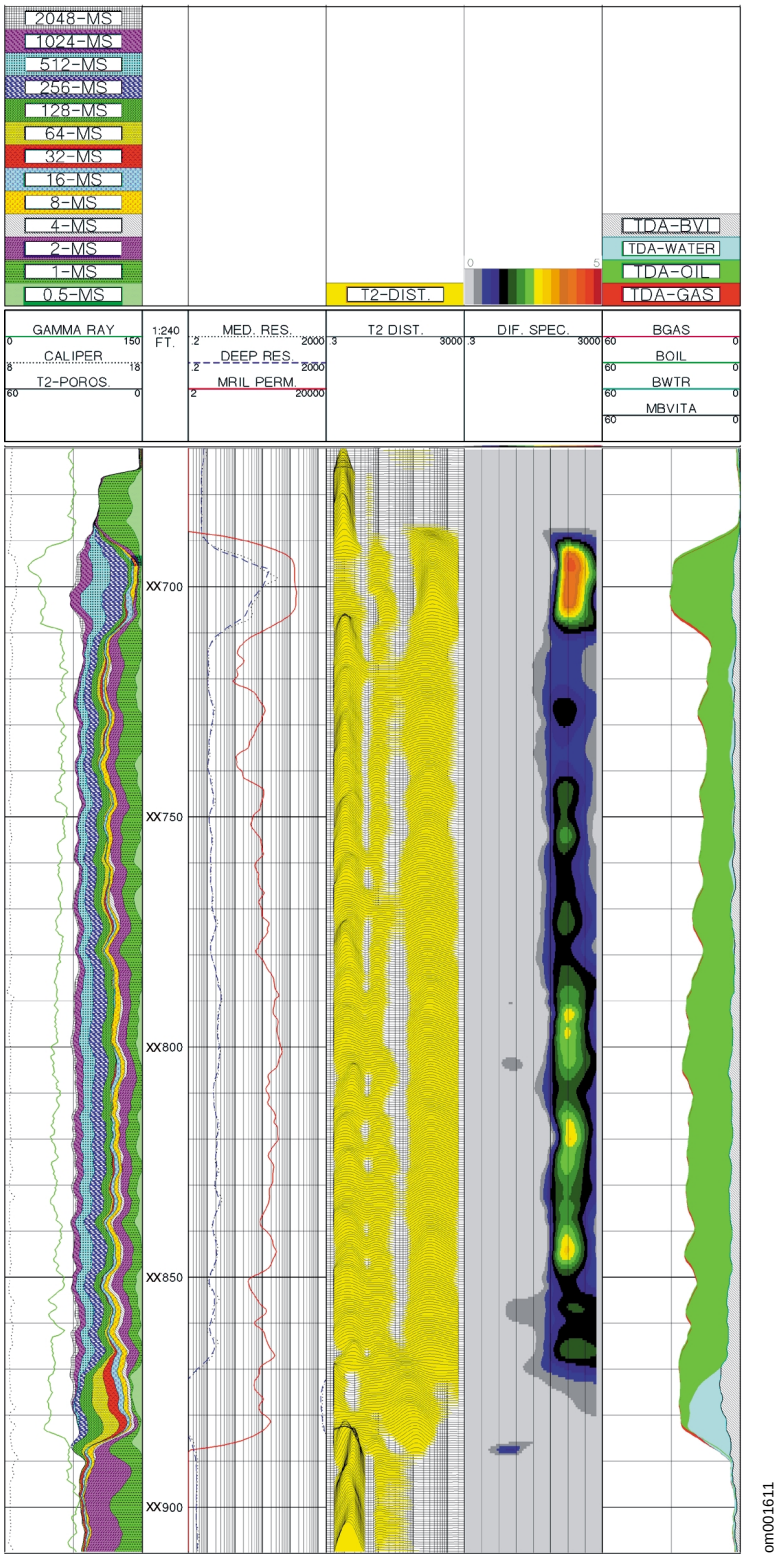

Figure 6.9—TDA was applied to the MRIL data of Fig. 6.4 to obtain the results shown here. Track 1 contains a conventional gamma ray correlation curve and long-*TW* T_2 bin data. Track 2 displays *MPERM* and resistivity data (both deep and shallow). Track 3 displays the long-*TW* T_2 distribution. Track 4 displays the differential spectrum (imaging). Track 5 contains TDA products: corrected effective porosity, *BVI*, and gas, as well as oil and movable-water porosity.

log was run with dual-*TW* activation using *TW* values of 1 and 8 s. The DSM was applied to the MRIL data: first, the T_2 distributions of both data sets were generated, and then the short-*TW* T_2 distribution was subtracted from the long-W T_2 distribution. The results are presented in the log of **Fig. 6.10**. The LWD gamma ray and resistivity logs are displayed in the first two tracks, and the differential spectrum is shown in the third track. Although the zone depicted on the log contains gas with T_2 = 60 ms, the differential spectrum shows no evidence of gas. The differential spectrum is dominated by the oil-based mud filtrate (right side of Track 3) with T_2 = 375 ms. In the *BVI* window (T_2 < 33 ms) of the differential spectrum, the strong energy across the depicted interval is interpreted as noise.

The TDA technique was then used to quantitatively analyze this well. Because the TDA technique analyzes the flushed zone, the technique is sensitive to the four types of fluid that were present in the reservoir at the time of MRIL logging. As depicted in the log of **Fig. 6.11**, these fluids were formation gas (coded red), invaded oil-based mud (light green), formation water (dark blue), and capillary-bound water (light blue). The TDA-calculated values for the T_1 and T_2 of the fluids in the flushed zone are shown in Tracks 2 and 3. In particular, Track 2 displays a gas signal with T_2 approximately 60 ms and an oil-based mud signal with T_2 approximately 375 ms. The gas/oil and oil/water contacts, which are apparent on the bottom half of Track 2 of this TDA log, were not evident on the DSM log of Fig. 6.9.

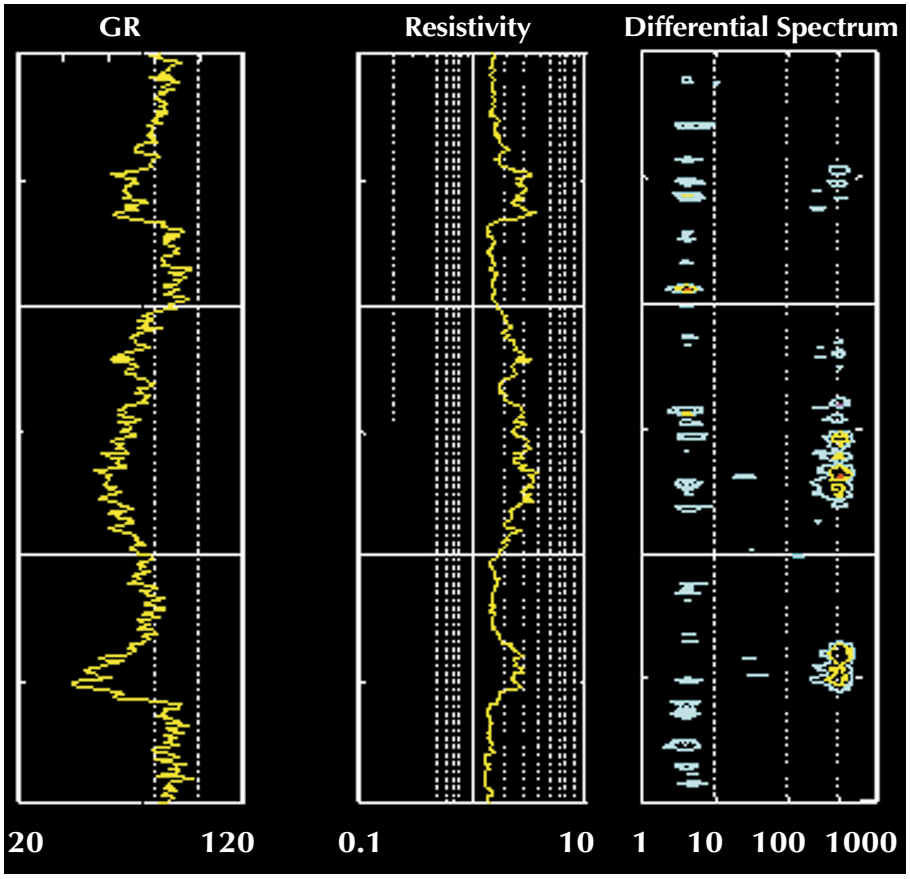

Figure 6.10—DSM processing was applied to MRIL data from a gas well drilled with oil-based mud in the Gulf of Mexico. Tracks 1 and 2 show, respectively, LWD gamma ray and resistivity data. Track 3 displays the differential spectrum in which oil signals are present in the higher T_2 range. No gas/oil or gas/water contacts are indicated on this log.

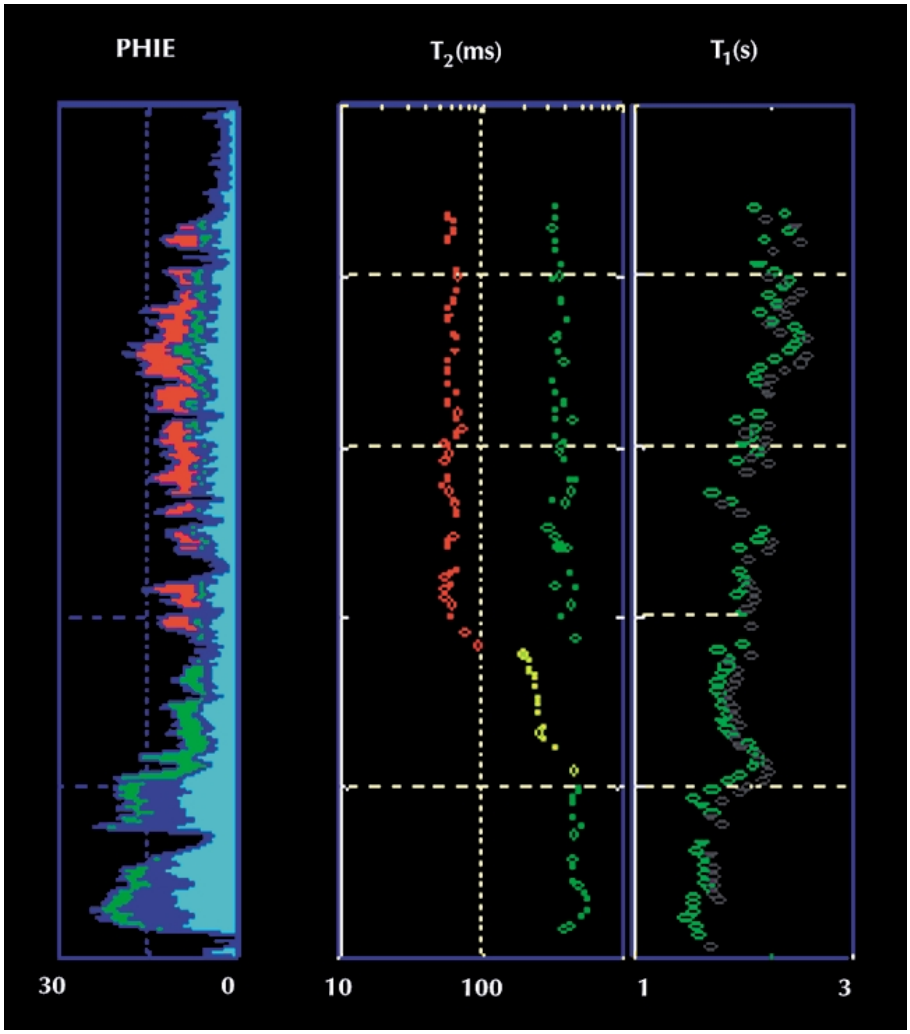

Figure 6.11—TDA was performed on MRIL data from the well described in Fig. 6.10. Track 1 shows the pore volumes for gas (red), oil-based mud filtrate and/or native oil (green), movable water (dark blue), and capillary-bound water (light blue) obtained from TDA quantitative analysis. Tracks 2 and 3 show, respectively, the T_2 and T_1 values of gas and light oil calculated through TDA. A hydrocarbon signal with an unclear origin (yellow) appears in Track 2. The lower part of Track 2 shows oil/water and gas/oil contacts, while the upper part of the track indicates the presence of gas and oil.

Diffusion Analysis

Concept

Diffusion Analysis depends on the diffusion contrast between fluids to type and quantify oils with viscosities ranging between 0.5 to 35 cp at temperatures and pressures of at least 200°F and at least 2,000 psi. As discussed in Chapter 3, the diffusion relaxation mechanism occurs because of the gradient of the MRIL magnetic field. The observed T_2 of a fluid changes with changes in the echo spacing TE.[7] The value of T_2 depends on the magnetic field gradient G, the gyroscopic constant γ of the hydrogen nuclei, the echo spacing TE, and the apparent diffusion coefficient D_a according to

$$1/T_2 = 1/T_{2\text{int}} + \left[C\, D_a \left(G\gamma TE\right)^2/12\right] \qquad (6.1)$$

where T_{2int} is the intrinsic relaxation time when the field gradient is zero. C accounts for the combined effects of restricted diffusion and spin dynamics associated with the mixing of direct and stimulated echoes in a gradient magnetic field.[8] For the MRIL tool, $C = 1.08$. For a given job, all the parameters in Eq. 6.1 are constants except for the echo spacing TE. Eq. 6.1 shows that increasing the echo spacing from 1.2 ms to a higher value will generate a lower T_2 value.

Data Acquisition

Diffusion analysis requires echo data from a dual-TE activation.[9] Dual-TE logging acquires two types of CPMG echo trains by utilizing a short and a long TE with a single TW. For full polarization, TW should be at least three times the maximum T_1 of all pore fluids. A typical TE pair is 1.2 and 4.8 ms.

The dual-TE activation allows the principle of diffusion-weighted measurements to be applied to distinguish water from medium-viscosity oil. The oil must have a significantly smaller D_a than the water, and in practice, the oil viscosities must range approximately from 0.5 to 35 cp. Through comparison of the CPMG echo trains derived from the short echo spacing (TE_S) and long echo spacing (TE_L), the oil signal is distinguished from the water signal.

Fig. 6.12 illustrates the principle of dual-TE logging. The top and middle sections show the polarization and echo acquisition using a dual-frequency mode with frequencies f_1 and f_2. While the f_2 shell is being re-polarized, data is acquired in the f_1 shell. The process then reverses. In this illustration, a long TE echo train is acquired in the f_1 shell, and a short TE echo train is acquired in the f_2 shell. For the long-TE measurement, the decay of the water signal is much faster than the decay of the medium-viscosity-oil signal. By careful selection

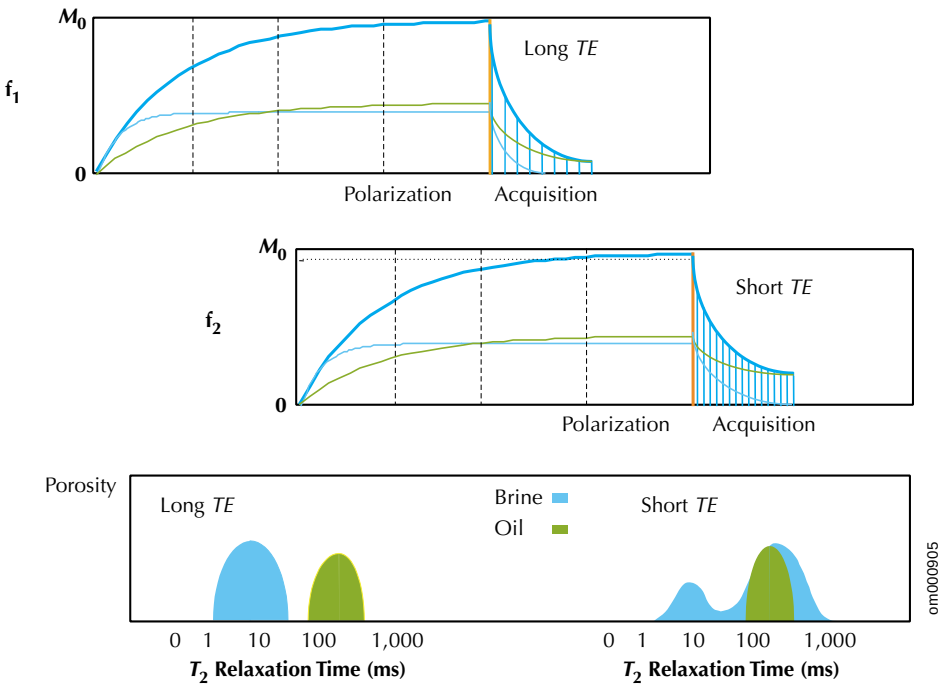

Figure 6.12—Dual-*TE* logging acquires two fully polarized echo trains, one from a long-*TE* measurement (top) and the other from a short-*TE* measurement (middle). The resulting T_2 distributions (bottom) can be used to distinguish water from oil.

of the long *TE*, the signals from water and oils can be separated. For the short-*TE* measurement, the water T_2 distribution overlaps much of the oil T_2 distribution. The bottom section shows T_2 distributions from both echo trains.

At the wellsite, products from dual-*TE* logging include two T_2 distributions, *MPHI* and *BVI* from both the short-*TE* and long-*TE* echo trains, and *MPERM* from the short-*TE* measurements, as shown in **Fig. 6.13**. (The log in this figure was calculated with the default parameters $T_{2cutoff}$ = 33 ms and C = 10, where C is the Coates-model coefficient.) Later results may differ from the wellsite results because of subsequent refinements in measurement parameters and computational assumptions. For example, both the polarization time *TW* and the hydrogen index *HI* will affect *MPHI* and *BVI*. Additionally, $T_{2cutoff}$ affects *BVI* and *MFFI*. *MPERM* is affected by the same factors as *BVI* as well as by the Coates-model coefficient. From a comparison of the T_2 distributions and of *BVI* and *MFFI* from both the short- and long-*TE* measurements, useful quick look information may be obtained. Gas has a high diffusivity, viscous oil has a low diffusivity, and the diffusivity of water is between the gas and viscous-oil diffusivities. Therefore, gas, water, and viscous oil will exhibit different shifts on the T_2 distributions from the short-*TE* to the long-*TE* MRIL measurements.

Shifted Spectrum Method

The Shifted Spectrum Method[4] (SSM) is a qualitative technique used to represent the changes in the T_2 values of fluids, and hence changes in their T_2 distributions, when different echo spacings are used. Consider a formation that contains fluids composed of water and medium-viscosity oil. The diffusion coefficient for water is about 10 times larger than that for the medium-viscosity oil. When *TE* is increased, the diffusion process will decrease the T_2 of water more than the T_2 of oil. Long- and short-*TE* values (TE_L and TE_S) can be selected so that the reduction in water and oil T_2 values measured with TE_L relative to those measured with TE_S can be used to separate the water signal from the oil signal. Comparison of the T_2 distributions determined with TE_L and TE_S demonstrates the relative diffusion-induced shifts of the water and oil T_2 values, which were seen in Chapters 1 and 4.

Quantitative Diffusion Analysis: DIFAN

DIFAN is an empirical model for quantitative diffusion analysis that has been used successfully in many oil fields. It was developed to address problems where there is insufficient T_1 contrast to use the TDA method or too little diffusion contrast to use the more straightforward dual-*TE* or EDM methods. It uses the different shifting of the T_2 values for different fluids produced by the diffusion phenomenon to provide quantitative values of the water-filled and hydrocarbon-filled porosity. For hydrocarbon liquids with very low viscosities, i.e., light oil and condensates, DIFAN is not recommended because the differences between the diffusion coefficients of hydrocarbons and water are too small. For high-viscosity oil (heavy oil), DIFAN is also not recommended because the difference between the T_{2int} values of dead oil and irreducible water is too small.

The DIFAN model generates two T_2 distributions using the two echo trains generated from dual-*TE* logging. The apparent T_2 geometric means of the free-fluid windows of the TE_L and TE_S T_2 distributions are calculated and are designated as T_{2L} and T_{2S}, respectively. The two means are then correlated to the diffusion parameters through the following two equations:

$$1/T_{2S} = 1/T_{2int} + \left[C\,D_a\,(G\gamma\,TE_S)^2/12\right] \tag{6.2}$$

$$1/T_{2L} = 1/T_{2int} + \left[C\,D_a\,(G\gamma\,TE_L)^2/12\right] \tag{6.3}$$

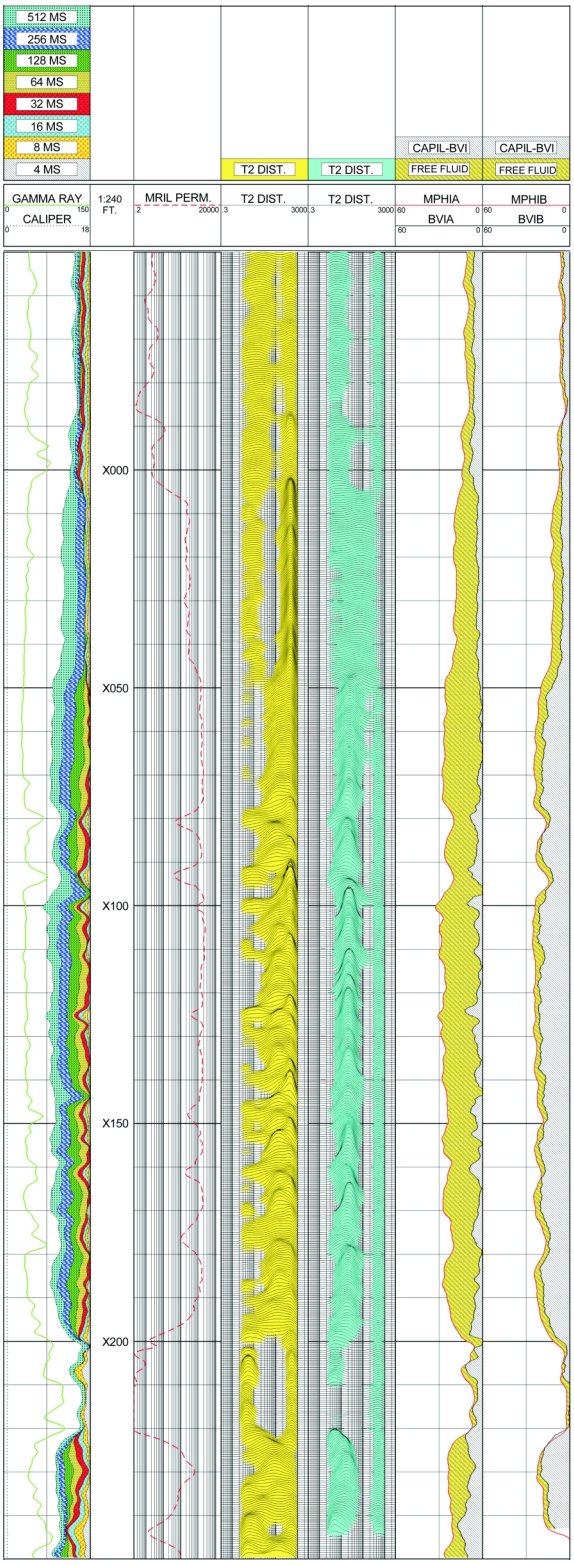

Figure 6.13—This log shows dual-*TE* wellsite products. Track 1 contains a conventional gamma ray correlation curve and T_2 bin data from short-*TE* echo trains. Track 2 shows the calculated *MPERM*. Track 3 displays the short-*TE* T_2 distribution. Track 4 displays the long-*TE* T_2 distribution. Track 5 contains the short-*TE MPHI* and *BVI* curves. Track 6 contains the long-*TE MPHI* and *BVI* curves.

where

T_{2int} = intrinsic T_2 of the pore fluid ($1/T_{2int} = 1/T_{2bulk} + 1/T_{2surface}$)

D_a = apparent diffusion coefficient of the pore fluid

C = a constant that accounts for the combined effects of restricted diffusion and spin dynamics associated with the mixing of direct and stimulated echoes in a gradient magnetic field (1.08 for MRIL tools)

Because T_{2S}, T_{2L}, TE_S, TE_L, G, γ, and C are known, the two equations can be solved simultaneously to obtain T_{2int} and D_a. The solution of the two equations is then used to construct a crossplot between $1/T_{2int}$ and D_a/D_w as shown in **Fig. 6.14**, from which S_{wa} is determined for calculating S_w.

Before the points (D_a/D_w,$1/T_{2int}$) are plotted, the S_{wa} = 100% and S_{wa} = 0% lines are constructed. For the construction, D_w, D_{oil}, and $T_{2bulk,oil}$ must be known.

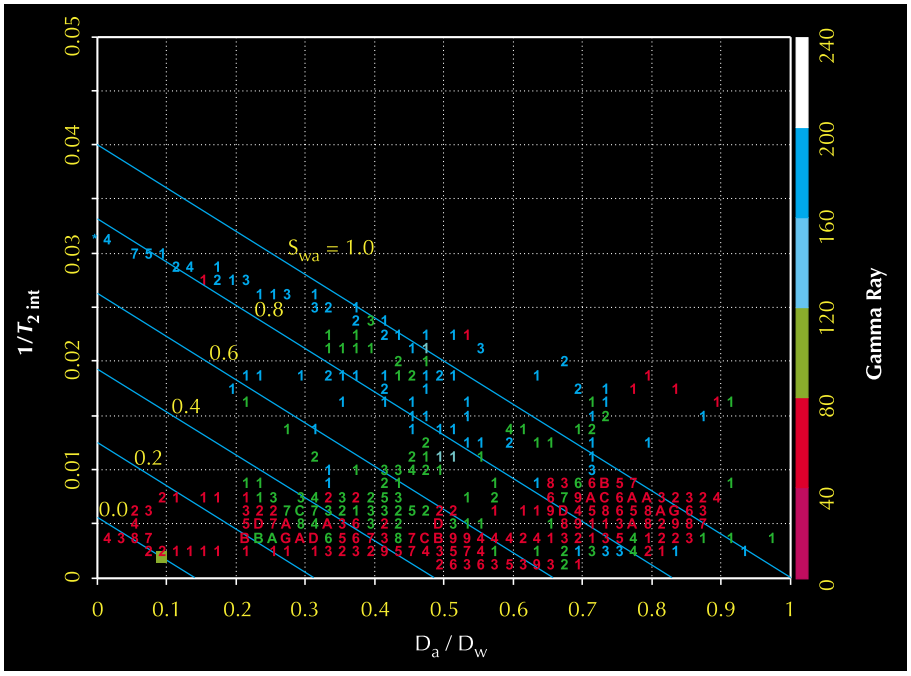

Figure 6.14—A $1/T_{2int}$ vs. D_a/D_w crossplot, such as shown here, is used in DIFAN analysis to determine S_{wa}, from which S_w is calculated.

The S_{wa} = 100% line is the line that forms the upper boundary of the data points in a water-saturated formation. This line passes through the bulk-water point (D_a/D_w = 1). Empirical results place the $1/T_{2int}$ intercept of this line at 0.04 ms^{-1}, or T_{2int} = 25 ms. The exact location of this intercept is not critical for most hydrocarbon-bearing formations because changes in saturation are primarily a function of D_a/D_w.

To determine the S_{wa} = 0% line, the formation is considered to be at irreducible water conditions so that the free fluid is oil. T_{2int} will then equal $T_{2bulk,oil}$, and D_a will equal D_{oil} at

reservoir conditions. Thus, the point (D_{oil}/D_w,$1/T_{2bulk,oil}$) will be on the S_{wa} = 0% line, and the line should be parallel to the S_{wa} = 100% line.

To map S_{wa} in the area between the 0% and the 100% S_{wa} lines, equally spaced lines that are parallel to the 0% and 100% S_{wa} lines are constructed between the 0% and the 100% S_{wa} lines. Thus, after T_{2int} and D_a are calculated at a particular depth, the point (D_a/D$_w$, $1/T_{2int}$) is plotted, and S_{wa} is determined from the crossplot. S_w is subsequently calculated from

$$S_w = \frac{S_{wa}\, FFI + BVI}{FFI + BVI} \tag{6.4}$$

In summary, the process of diffusion analysis using fluid diffusion properties and the DIFAN model is as follows:

1. Acquire two echo trains with dual-*TE* activation.
2. Estimate the bulk properties (T_{2int} and D) of oil and water at reservoir conditions (e.g., temperature, pressure, and oil viscosity).
3. Contruct the crossplot of $1/T_{2int}$ vs. D_a/D_w.
4. Calculate the T_2 geometric means for the free-fluids window of the TE_L and TE_S T_2 distributions.
5. Calculate T_{2int} and D_a from Eqs. 6.2 and 6.3.
6. Estimate S_{wa} by using the crossplot of $1/T_{2int}$ vs. D_a/D_w.
7. Use S_{wa} to calculate true S_w in the effective porosity system.

Fig. 6.15 is one of the many successful DIFAN examples from Indonesia. The MRIL data were acquired with dual-*TE* activation having TE_S = 1.2 ms and TE_L = 4.8 ms. The DIFAN answer products in Track 5 show that the intervals from X95 to X20 ft, XX05 to XX00 ft, and XX60 to XX30 ft are hydrocarbon zones with significant free water. Production data confirmed these results.

Enhanced Diffusion Method

The Enhanced Diffusion Method[8, 10] (EDM) types and quantifies oils with viscosities ranging between 1 and 50 cp. The EDM relies on diffusion contrasts to differentiate the fluids. Use of a properly selected long *TE* enhances the diffusion effect during echo-data acquisition and allows water and oil to be separated on a T_2 distribution generated from the logged data. The EDM can use CPMG measurements acquired with the following activations:

- standard-T_2 logging with a long *TE*
- dual-*TE* logging with a single long *TW*
- dual-*TW* logging with a single long *TE*

An understanding of the EDM principle depends on an understanding of the factors affecting the relaxation rates of water and oil in rock pores. If two echo trains are acquired during dual-*TE* logging, the resulting TE_L and TE_S T_2 distributions will both include water and oil signals. TE_L can be selected so that oil and water signals will separate on the TE_L T_2 distribution, thereby providing a quick-look EDM result at the wellsite.

As discussed in Chapter 3, the relaxation rates of fluids in rock pores observed with CPMG measurements are related to bulk, surface, and diffusion relaxation mechanisms:

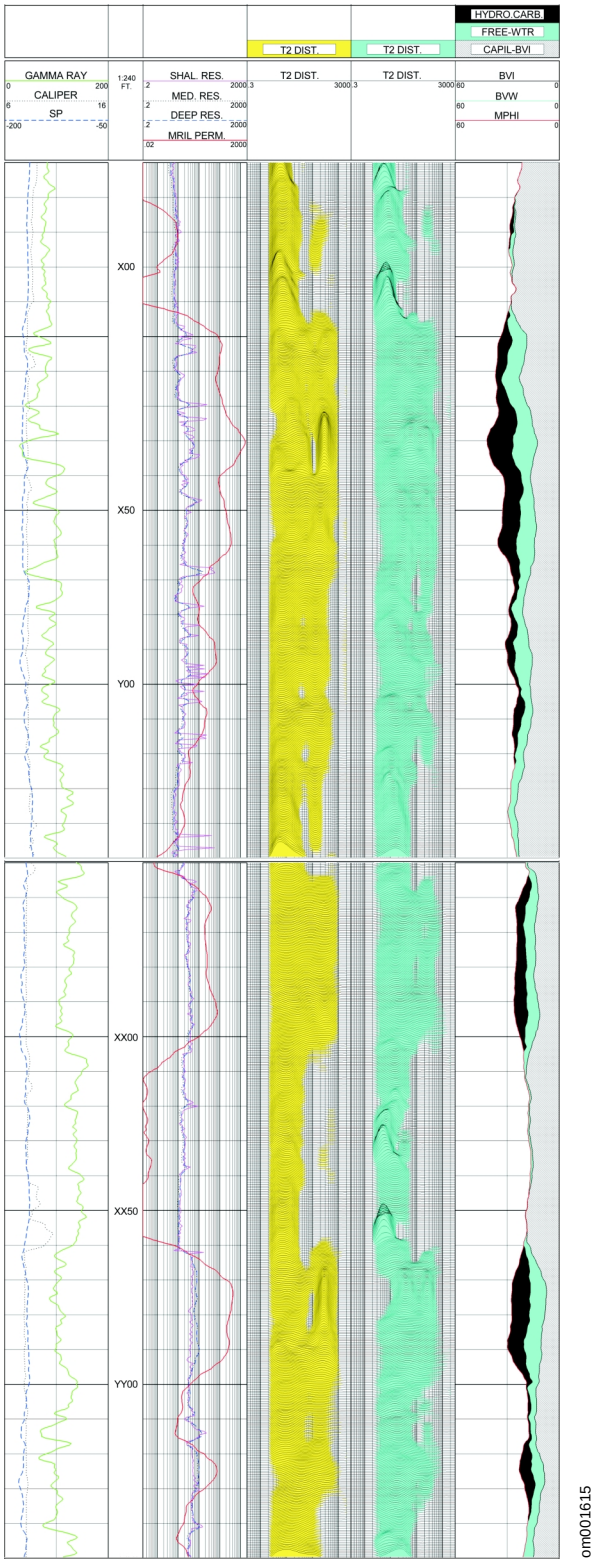

Figure 6.15—This log contains results from the application DIFAN to MRIL data from an Indonesian well. Track 1 includes conventional gamma ray, spontaneous potential (SP), and caliper curves. Track 2 presents deep, medium, and shallow resistivity data and MRIL permeability. Track 3 contains the long-*TE* T_2 distribution. Track 4 contains the short-*TE* T_2 distribution. Track 5 displays answer products from the DIFAN calculations.

$$1/T_{2\mathrm{CPMG}} = 1/T_{2\mathrm{bulk}} + 1/T_{2\mathrm{surface}} + 1/T_{2\mathrm{diffusion}} \quad (6.5)$$

The T_2 measured by a CPMG sequence is smaller than the T_2 calculated for any of the three relaxation mechanisms. Because $T_{2\mathrm{bulk}}$ is always much larger than $T_{2\mathrm{surface}}$ and $T_{2\mathrm{diffusion}}$, $T_{2\mathrm{bulk}}$ can be ignored in practical applications. If $T_{2\mathrm{surface}}$ is smaller than $T_{2\mathrm{diffusion}}$, then surface relaxation dominates the observed relaxation. Otherwise, diffusion relaxation dominates.

The diffusion effect can be manipulated to an extent by the choices of MRIL-tool operational parameters. In particular, the strength of the field gradient *G* is a function of the operating frequency and tool type, and the inter-echo spacing *TE* can be selected by the logging engineer at the wellsite. G and *TE* can be chosen so that the diffusion mechanism dominates water relaxation and thus so that the upper limit of T_2 for water in rock pores is $T_{2\mathrm{diffusion,w}}$. This upper limit, designated $T_{2\mathrm{DW}}$, is given by

$$T_{2DW} = 12 / \left[C\, D_w \left(G \gamma\, TE \right)^2 \right] \quad (6.6)$$

Therefore, $T_{2\mathrm{DW}}$ constitutes the absolute upper bound for the measured T_2 of water, and all T_2 relaxation times associated with water will be less than or equal to $T_{2\mathrm{DW}}$.

The T_2 of oil in water-wet rock pores is determined by both bulk and diffusion relaxation and is given by

$$1/T_{2\mathrm{oil}} = 1/T_{2bulk,oil} + 1/T_{2diffusion,oil} \quad (6.7)$$

The selection of *TE* and *G* can be often further refined so that

$$T_{2\mathrm{DW}} << \text{minimum } \{T_{2\mathrm{oil}} \text{ values expected over the formation}\} \quad (6.8)$$

In reality, because of noise effects, *TE* and *G* are usually selected so that

$$2T_{2\mathrm{DW}} << \text{minimum } \{T_{2\mathrm{oil}} \text{ values expected over the formation}\} \quad (6.9)$$

Thus, the existence of a signal on the T_2 distribution longer than $T_{2\mathrm{DW}}$ unambiguously indicates the presence of oil in the formation. **Fig. 6.16** shows how this observation is used to recognize pay on EDM log displays.

The use of the EDM is quite straightforward. A T_1 contrast is not necessary, and depending on oil NMR properties and the job objective, EDM data processing can be done in either T_2 domain or time domain. If the EDM objective is to discriminate pay from non-pay, then a single CPMG measurement with long *TW* (for full polarization) and long *TE* (for diffusion enhancement) is sufficient. Thus, standard-T_2 logging with a long *TE* can be used. If the EDM objective is to quantify fluids in a pay zone, then dual-*TE* logging will be required. The short-*TE* measurements will provide correct *MPHI* and *BVI*. If the T_2 contrast over the zone of interest is not expected to be large enough to separate the T_2 values of water and oil, then dual-*TW* logging with a single, long *TE* may be required to obtain data for TDA processing. Thus, job planning is critical for EDM success.

Appendix: TDA Mathematical Model[11]

An understanding of how TDA determines the oil- and gas-filled porosity from the differential spectrum can be based on discussions in Chapter 3. In particular, Eq. 3.17 indicates that

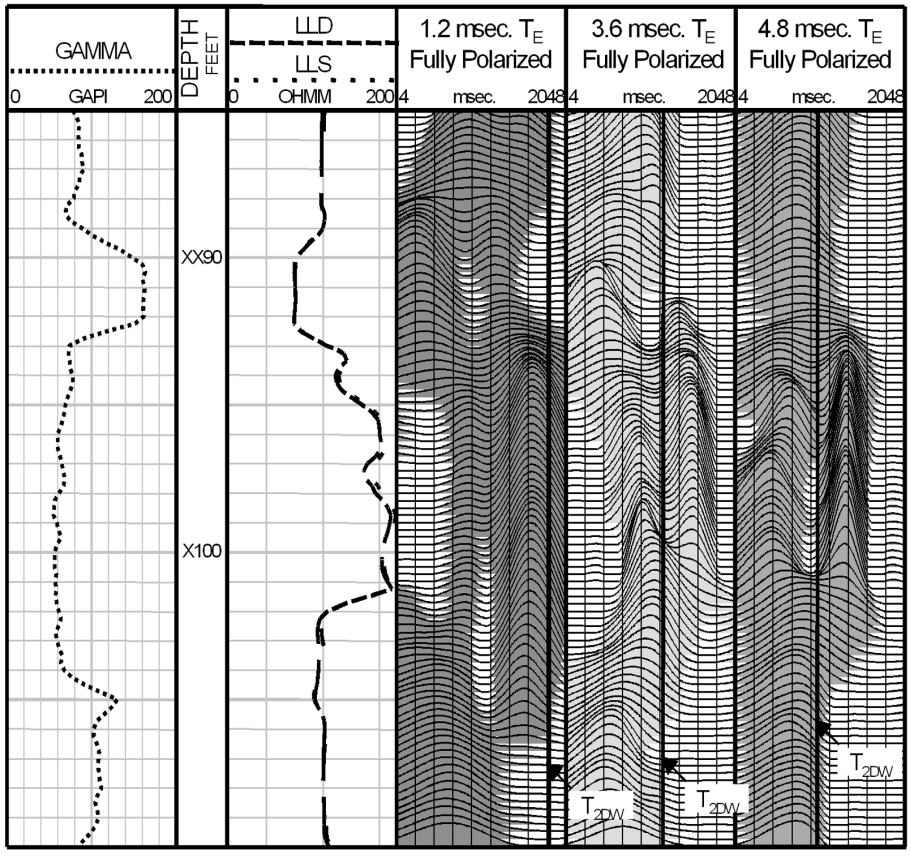

Figure 6.16—In this log display, the T_2 distributions from TE = 1.2, 3.6, and 4.8 ms are shown in Tracks 3, 4, and 5 respectively. On the EDM results in Track 4 and 5, significant energy to the right of the T_{2DW} line indicates obvious oil zones. Also note the increased separation in Track 5 because of the increased TE.

the amplitude of an echo train acquired with a CPMG sequence for a water-wet rock saturated with water, oil, and gas can be given by Eq. 6-A.1, when both oil and gas are assumed to have single T_2 values.

$$M(t) = \Sigma[M_{0i}\exp(-t/T_{2i})] + M_{oil}\exp(-t/T_{2\text{oil}}) + M_{\text{gas}}\exp(-t/T_{2\text{gas}}) \quad (6\text{-A.1})$$

When polarization effects are considered, M_{0i}, M_{oil}, and M_{gas} can be expressed as

$$M_{0i} = M_{0i}(0)[1 - \exp(-TW/T_{1i})]$$

$$M_{\text{oil}} = M_{\text{oil}}(0)[1 - \exp(-TW/T_{1\text{oil}})]$$

$$M_{\text{gas}} = M_{\text{gas}}(0)[1 - \exp(-TW/T_{1\text{gas}})] \quad (6\text{-A.2})$$

The amplitudes of echo trains for TW_{L} and TW_{S} are then given as

$$M_{TW_L}(t) = \Sigma\{M_{0i}(0)[1 - \exp(-TW_L/T_{1i})]\exp(-t/T_{2i})\}$$

$$+ M_{\text{oil}}(0)[1 - \exp(-TW_L/T_{1\text{oil}})]\exp(-t/T_{2\text{oil}})$$

$$+ M_{\text{gas}}(0)[1 - \exp(-TW_L/T_{1\text{gas}})]\exp(-t/T_{2\text{gas}}) \quad (6\text{-A.3})$$

and

$$M_{TW_S}(t)=\Sigma\{M_{0i}(0)[1-\exp(-TW_S/T_{1i})]\exp(-t/T_{2i})\}$$

$$+ M_{\text{oil}}(0)[1-\exp(-TW_S/T_{1\text{oil}})]\exp(-t/T_{2\text{oil}})$$

$$+ M_{\text{gas}}(0)[1-\exp(-TW_S/T_{1\text{gas}})]\exp(-t/T_{2\text{gas}}) \quad (6\text{-A.4})$$

$$\Delta M(t)=M_{\text{TWL}}(t) - M_{\text{TWS}}(t)$$

$$= \Sigma\{M_{0i}(0)\exp(-t/T_{2i}) [\exp(-TW_S/T_{1i})- \exp(-TW_L/T_{1i})] \}$$

$$+ M_{\text{oil}}(0)\exp(-t/T_{2\text{oil}}) [\exp(-TW_S/T_{1\text{oil}})- \exp(-TW_L/T_{1\text{oil}})]+$$

$$M_{\text{gas}}(0)\exp(-t/T_{2\text{gas}})[\exp(-TW_S/T_{1\text{gas}})- \exp(-TW_L/T_{1\text{gas}})] \quad (6\text{-A.5})$$

Polarization functions are then defined for water ($\Delta\alpha_{wi}$), oil ($\Delta\alpha_o$), and gas ($\Delta\alpha_g$) as follows:

$$\Delta\alpha_{wi}=[\exp(-TW_S/T_{1i})- \exp(-TW_L/T_{1i})] \quad (6\text{-A.6})$$

$$\Delta\alpha_o=[\exp(-TW_S/T_{1\text{oil}})- \exp(-TW_L/T_{1\text{oil}})] \quad (6\text{-A.7})$$

$$\Delta\alpha_g=[\exp(-TW_S/T_{1\text{gas}})- \exp(-TW_L/T_{1\text{gas}})] \quad (6\text{-A.8})$$

Eq. 6-A.5 subsequently becomes

$$\Delta M(t) =\Sigma[M_{0i}(0)\exp(-t/T_{2i})\,\Delta\alpha_{wi}]+ M_{\text{oil}}(0)\exp(-t/T_{2\text{oil}})\,\Delta\alpha_o + M_{\text{gas}}(0)\exp(-t/T_{2\text{gas}})\,\Delta\alpha_g \quad (6\text{-A.9})$$

If TW_S was selected to fully polarize the protons of water in rock pores, then $\Delta\alpha_{wi} \cong 0$. This condition allows the difference of the two echo trains to be written as

$$\Delta\text{M}(t) = M_{\text{oil}}(0)\exp(-t/T_{2\text{oil}})\,\Delta\alpha_o + M_{\text{gas}}(0)\exp(-t/T_{2\text{gas}})\,\Delta\alpha_g \quad (6\text{-A.10})$$

A differential porosity function is then defined by

$$\Delta\phi(t) = \phi^*_{\text{oil}}\exp(-t/T_{2\text{oil}}) + \phi^*_{\text{gas}}\exp(-t/T_{2\text{gas}}) + \text{noise} \quad (6\text{-A.11})$$

where

noise	=	noise during CPMG measurement of the two echo trains
$\Delta\phi$	=	difference in hydrocarbon-filled porosity obtained from the echo trains
ϕ^*_{oil}	=	apparent oil-filled porosity obtained from the difference of the two echo trains
ϕ^*_{gas}	=	apparent gas-filled porosity obtained from the difference of the two echo trains

Finally, the apparent porosities are related to the true porosities (ϕ_{oil} and ϕ_{gas}) by

$$\phi^*_{oil} = [M_{oil}(0)/M_{100\%}(0)]\,\Delta\alpha_o = \phi_{oil} HI_{oil} \Delta\alpha_o \quad (6\text{-A.12})$$

$$\phi^*_{gas} = [M_{gas}(0)/M_{100\%}(0)]\,\Delta\alpha_g = \phi_{gas} HI_{gas} \Delta\alpha_g \quad (6\text{-A.13})$$

where

$M_{100\%}(0)$ = amplitude of CPMG echo train at time zero obtained from an MRIL water-tank (i.e., 100% porosity) calibration

HI_{oil} = hydrogen index of oil

HI_{gas} = hydrogen index of gas

Therefore,

- If the values of T_{2oil} and T_{2gas} are known at reservoir conditions, then Eq. 6-A.11 can be used to calculate the apparent porosities, ϕ^*_{oil} and ϕ^*_{gas}.
- If the values of T_{1oil}, T_{1gas}, HI_{oil}, and HI_{gas} are also known, then Eqs. 6-A.12 and 6-A.13 can be used to calculate the true porosities, ϕ_{oil} and ϕ_{gas}.

The actual TDA procedure includes the following steps:

1. Acquire two echo trains with dual-*TW* activation.
2. Estimate the bulk properties (T_1, T_2, and HI) of oil and gas at reservoir conditions (e.g., temperature, pressure, and oil viscosity).
3. Subtract the echo trains from one another.
4. Search T_2 for gas and oil, and search T_1 for oil at reservoir conditions.
5. Calculate the apparent porosities (ϕ^*_{oil} and ϕ^*_{gas}) using Eq. 6-A.11.
6. Calculate the true porosities (ϕ_{oil} and ϕ_{gas}) using Eqs. 6-A.12 and 6-A.13, the bulk properties estimated in Step 2, and the apparent porosities found in Step 5. (Note that the T_1 values estimated in Step 2 or measured by a triple-TW[12] activation are used to calculate the oil and gas polarization functions.)
7. Calculate water porosity and effective porosity.

The following summarizes several TDA assumptions that were discussed earlier in this appendix:

- In Eq. 6-A.1, each of the oil and gas signals exhibits a single-exponential decay. This single-exponential decay is a reasonable approximation for the decay of gas and many low-viscosity oils.
- In Eq. 6-A.10, TW_S should be selected so that the water protons are fully polarized. Otherwise, a water-polarization correction is needed, and the analysis process will be more complicated.

- In Eq. 6-A.11, $\Delta\phi$, the difference between the porosities derived from the two individual echo trains is dependent on both the true porosity of the rock and the T_1 contrast between water and light hydrocarbons. If $\Delta\phi$ is not sufficiently large, say $\Delta\phi < 1.5$ p.u., then fitting the difference signal with a single- or two-exponential function may be difficult because of the noise level under which the MRIL data are acquired.
- A significant T_1 contrast must exist between water and light hydrocarbons.
- Gas and oil have significantly different T_2 values to allow separate signals to be recognized.

These assumptions are generally valid for high-porosity, water-wet reservoirs containing light hydrocarbons (gas and light oil). In such reservoirs, TDA should be possible, provided that TW_L and TW_S are carefully selected to magnify the T_1 contrast between water and light hydrocarbons. Thus, job planning is critical to the success of TDA. TDA requires only MRIL data to provide porosity, permeability, and hydrocarbon typing: no other conventional log data are needed.

References

1. Prammer, M.G., et al., 1995, Lithology-independent gas detection by gradient-NMR logging, SPE 30562, *1995 SPE Annual Technical Conference and Exhibition proceedings*, v. Ω (Formation evaluation and reservoir geology), p. 325–336.
2. Akkurt, R., Prammer, M., and Moore, A., 1996, Selection of optimal acquisition parameters for MRIL logs, paper TT, *37th Annual SPWLA Logging Symposium Transaction*s, 13 p. Later published in 1996 in *The Log Analyst*, v. 37, no. 6, p. 43–52.
3. Akkurt, R., Moore, A., and Freeman, J., 1997, Impact of NMR in the development of a deepwater turbidite field, paper SS, in *38th Annual SPWLA Logging Symposium Transactions*, 14 p.
4. Akkurt, R., et al., 1995, NMR logging of natural gas reservoirs, paper N, *36th Annual SPWLA Logging Symposium Transactions*, 12 p. Later published in 1996, as Akkurt, R., et al. in *The Log Analyst*, v. 37, no. 5, p. 33–42.
5. Moore, M.A., and Akkurt, R., 1996, Nuclear magnetic resonance applied to gas detection in a highly laminated Gulf of Mexico turbidite invaded with synthetic oil filtrate, SPE 36521, *1996 SPE Annual Technical Conference and Exhibition proceedings*, v. Ω (Formation evaluation and reservoir geology), p. 305–310.
6. Mardon, D., et al., 1996, Characterization of light hydrocarbon-bearing reservoirs by gradient NMR well logging—a Gulf of Mexico case study, SPE 36520, *1996 SPE Annual Technical Conference and Exhibition proceedings*, v. Ω (Formation evaluation and reservoir geology), p. 295–304. Also published in 1996 in condensed form in *Journal of Petroleum Technology*, v. 48, no. 11, p. 1035–1036.
7. Mardon, D., et al., 1996, Experimental study of diffusion and relaxation of oil-water mixtures in model porous media, paper K, *37th Annual SPWLA Logging Symposium transactions*, 14 p.

8. Akkurt, R., et al., 1998, Enhanced diffusion: expanding the range of NMR direct hydrocarbon-typing applications, paper GG, *39th Annual SPWLA Logging Symposium Transactions*.

9. Mardon, D., Prammer, M.G., and Coates, G.R., 1996, Characterization of light hydrocarbon reservoirs by gradient-NMR well logging, *Magnetic Resonance Imaging*, v. 14, nos. 7 and 8, p. 769–777.

10. Akkurt, R., et al., 1998, Determination of Residual Oil Saturation Using Enhanced Diffusion, SPE 49014.

11. Xiao, L.Z., 1998, *NMR imaging logging principles and applications* (in Chinese), Science Press, Beijing. 328 p.

12. Hou, L., et al., 1999, Enhanced NMR logging methods for accurately measuring volumes of gas and light oil in hydrocarbon reservoirs, SPE 56769, prepublication print, 14 p.

Chapter 7

Answer Products Derived from MRIL Combinations with Other Logs

As stated in Chapter 6, MRIL stand-alone analysis, such as Time Domain Analysis and Diffusion Analysis, provides interpretation of the invaded zone because of the shallow depth of investigation of MRIL measurements. If MRIL data are combined with other logs, analysis can furnish even more information about the reservoir. For example, a combination of MRIL and deep-resistivity data provides a complete analysis of the fluids in the virgin zone. MRIAN is one of the interpretation models that uses this data combination.[1] This chapter contains a complete discussion of MRIAN and its applications.

If MRIL data are combined with quad-combo data (neutron, density, sonic, and resistivity), then the combination can provide critical information for well completions. For example, when used in a model called StiMRIL™, such data can generate information about rock properties, formation lithology, and formation permeability. The StiMRIL model and its application in stimulation optimization are discussed in this chapter.

MRIAN Concept

MRIAN combines MRIL data and the deep-resistivity data from lateral or induction logs. MRIAN uses the dual-water model[2] to provide the volume of formation fluids in the virgin zone. The main data requirements for MRIAN processing are true formation resistivity (R_t), total porosity (ϕ_T), and clay-bound-water saturation (S_{wb}). MRIL data are used to provide two important parameters needed in the dual-water model: the clay-bound water porosity (*MCBW*) and effective porosity (*MPHI*). A similar analysis could be implemented with different resistivity models, such as Archie or Waxman-Smits.[3]

MRIAN Principles

Dual-Water Model

The Dual-water model is illustrated in the left panel of **Fig. 7.1** and can be expressed mathematically by

$$C_t = \left(\phi_T{}^m S_{wT}{}^n\right)\left[C_w\left(1-\frac{S_{wb}}{S_{wT}}\right)+C_{cw}\left(\frac{S_{wb}}{S_{wT}}\right)\right] \qquad (7.1)$$

where

C_t = formation conductivity

C_w = conductivity of formation water

C_{cw} = conductivity of clay-bound water

ϕ_T = total porosity (includes free fluids, capillary-bound water, and clay-bound water)

S_{wT} = total water saturation (as a fraction of total porosity)

S_{wb} = clay-bound-water saturation (as a fraction of total porosity)

m = cementation exponent

n = saturation exponent

C_{cw} is temperature-dependent and is given by

$$C_{cw} = 0.000216\,(T - 16.7)(T + 504.4) \tag{7.2}$$

where T is formation temperature in degrees Fahrenheit.

Coates modified the dual-water model to reduce the uncertainty of the exponents m and n by introducing a parameter W defined by

$$W = \frac{\log\left(\phi_T{}^m S_{wT}{}^n\right)}{\log\left(\phi_T S_{wT}\right)} \tag{7.3}$$

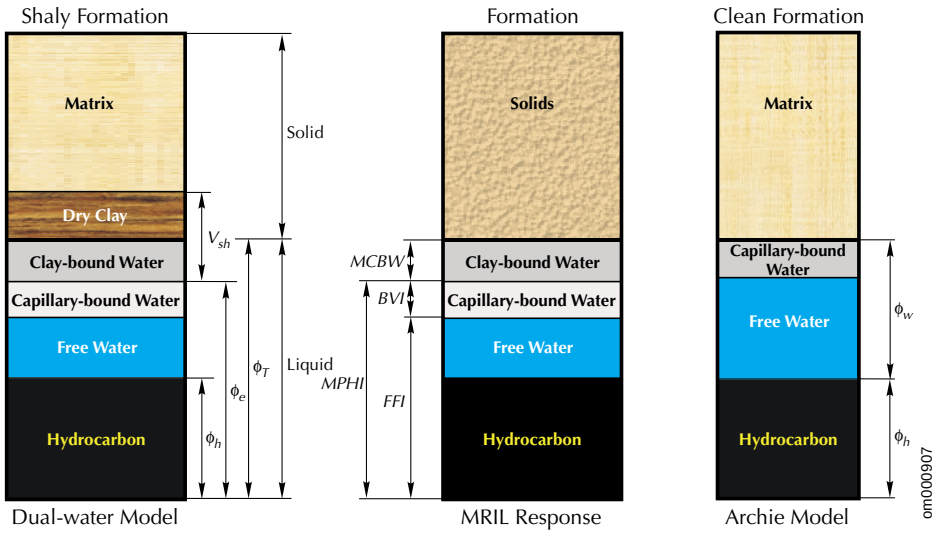

Figure 7.1— The dual-water model (left panel) provides a more comprehensive description of pore fluids for shaly formations than does the Archie model (right panel), which is applicable in clean formations. MRIL responses (middle panel) in this application provide two important parameters needed in MRIAN implementation of the dual-water model: clay-bound water porosity (*MCBW*) and effective porosity (*MPHI*).

With the *W* parameter, the dual-water model takes the form

$$C_t = \left(\phi_T S_{wT}\right)^W \left[C_w \left(1 - \frac{S_{wb}}{S_{wT}}\right) + C_{cw} \left(\frac{S_{wb}}{S_{wT}}\right) \right] \tag{7.4}$$

MRIAN calculates S_{wT} from Eq. 7.4 after other parameters in the equation are determined.

Determining S_{wb} for the Dual-Water Model

The clay-bound water saturation S_{wb} is calculated using the MRIL total and effective porosities (ϕ_T = *MSIG* and ϕ_e = *MPHI*) as follows

$$S_{wb} = \frac{\phi_T - \phi_e}{\phi_T} \tag{7.5}$$

Total porosity can be also obtained from conventional logs (e.g., neutron and density crossplot porosity).

The measurements underlying ϕ_T and ϕ_e can be underestimated when the hydrogen index is low (e.g., in gas-bearing formations) or when light hydrocarbons are incompletely polarized. In this case, ϕ_T and ϕ_e should be corrected using time domain analysis (discussed in Chapter 6) before being used in MRIAN computations.

MRIAN also uses other estimates of S_{wb} derived from conventional data such as gamma ray, neutron, density, sonic, and resistivity. In MRIAN, the average of the available secondary S_{wb} estimates is compared with the MRIL-based primary S_{wb} estimate, and the minimum of the two is selected for subsequent computations.

Quality Control on the Calculated S_{wb}

MRIAN provides the interpreter with robust quality control on the calculated S_{wb} values through construction of a crossplot of the apparent water conductivity (C_{wa}) versus the calculated S_{wb}. C_{wa} is calculated as

$$C_{wa} = \frac{1}{R_t \phi_t^W} \tag{7.6}$$

R_t is the true formation resistivity. As shown in **Fig. 7.2**, the plotted points should fall between two curves, the upper of which represents the condition S_{wT} = 100% and the lower of which represents the hydrocarbon-bearing condition.

The upper curve is calculated using the Dual-water model, assuming S_{wT} = 100%.

$$C_{wa} = C_w + S_{wb}\left(C_{cw} - C_w\right) \tag{7.7}$$

The lower curve is calculated using the irreducible (pure clay) condition, $S_{wT} = S_{wb} = S_{wirr}$

$$C_{wa} = \left(S_{wb}\right)^W C_{cw} \tag{7.8}$$

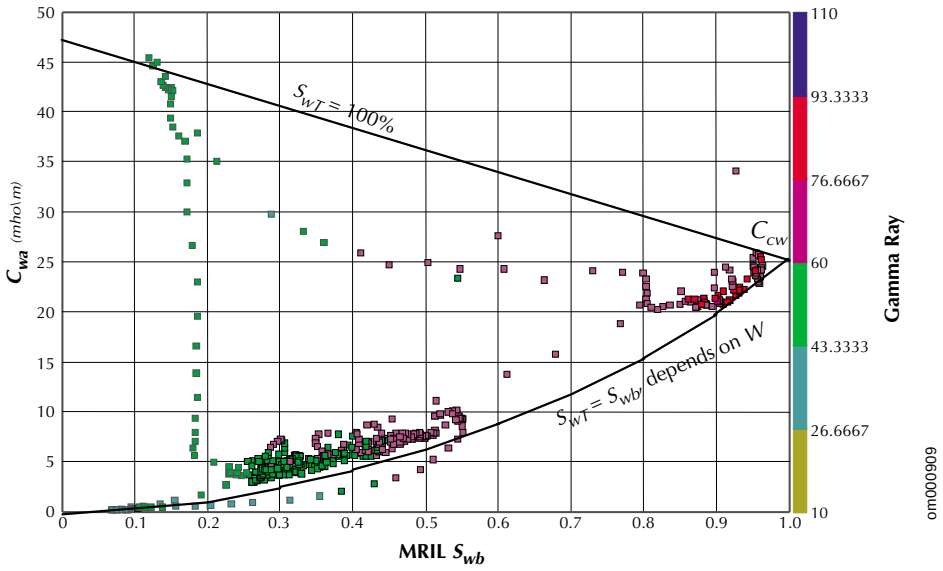

Figure 7.2— A crossplot of C_{wa} vs. S_{wb} serves as a quality check on the calculated S_{wb} values. Points in the plot should generally fall between two curves, the upper of which represents points with S_{wT} = 100% and the lower of which represents points with $S_{wT} = S_{wb}$.

Determination of the *W* exponent in MRIAN

The W exponent described in Eq. 7.3 is automatically determined throughout the MRIAN processing scheme. By solving Eq. 7.4, W can be estimated from

$$W = \frac{\log \dfrac{C_t}{C_w(1-S_{wb}/S_{wT}) + C_{cw}(S_{wb}/S_{wT})}}{\log(\phi_T S_{wT})} \qquad (7.9)$$

W will fall between values obtained from Eq. 7.9 at two extreme conditions:

- 100% water saturation
- Hydrocarbon bearing at irreducible condition

At 100% water saturation, the value of W is designated W_w and can be calculated from Eq. 7.9 using S_{wT} = 1.0:

$$W_w = \frac{\log \dfrac{C_t}{C_w + S_{wb}(C_{cw} - C_w)}}{\log(\phi_T)} \qquad (7.10)$$

At irreducible condition, the value of W is designated W_i and can be calculated from Eq. 7.9 using $S_{wT} = S_{wirr}$:

$$W_i = \frac{\log \dfrac{C_t}{C_w + S_{wb}(C_{cw} - C_w)/S_{wirr}}}{\log(\phi_T S_{wirr})} \qquad (7.11)$$

where

$$S_{wirr} = \frac{\phi_T S_{wb} + BVI}{\phi_T} \tag{7.12}$$

with BVI being obtained from an MRIL log.

In a normal hydrocarbon-bearing formation, W will always be less than W_w and greater than W_i.

$$W_i < W < W_w \tag{7.13}$$

MRIAN uses the following empirical relation to calculate W[4]:

$$W = W_Q = 1.65 + 0.4\left(\frac{BVI}{MPHI}\right) \tag{7.14}$$

If $W_Q > W_w$, then MRIAN sets $W_Q = W_w$ and recognizes the zone as being wet. If $W_Q < W_i$, then MRIAN sets $W_Q = W_i$ and recognizes the zone as being at irreducible water saturation.

Calculation of S_{wT} in MRIAN

MRIAN uses the S_{wb} and W_Q values to calculate S_{wT} from the Dual-Water model as described before. Using S_{wT}, MRIAN then calculates water-filled porosity (ϕ_{wT}), bulk volume of water in effective porosity ($CBVWE$), and hydrocarbon pore volume (ϕ_h). These parameters take the forms

$$\phi_{wT} = S_{wT}\phi_T \tag{7.15}$$

$$CBVWE = \phi_{wT} - MCBW \tag{7.16}$$

$$\phi_h = \phi_e - CBVWE \tag{7.17}$$

$MCBW$ is the MRIL-derived volume of clay-bound water, and ϕ_e is the effective porosity.

Parameters Affecting MRIAN Calculations

R_w is generally one of the most important parameters involved in the water saturation model, and every available source should be exploited to determine an accurate value for R_w. The salinity of a sample of formation water can be a good source. In addition, apparent R_w values can be obtained from Archie transforms of R_t and porosity, as well as from BVI information. Spontaneous potential (SP) measurements can be also used to estimate R_w.[5] However, it should be noted that SP, resistivity, and porosity measurements are affected by hydrocarbons.

MRIL Data Acquisition for MRIAN

The MRIL data required for MRIAN processing can be acquired with a total-porosity logging activation, which acquires two types of CPMG echo trains: fully polarized and partially polarized. The fully polarized echo train is acquired by using a long TW and a TE of 0.9 or 1.2 ms. These parameter values constitute a standard-T_2 logging activation as discussed before. The partially polarized echo train is acquired with a short TE (0.6 ms) and a short TW (20 ms).

After a long polarization time (*TW*), a fully polarized echo train is acquired. Then, a partially polarized sequence is recorded. This sequence consists of 50 echo trains with 10 echoes per train. The first two echo trains are used to stabilize the system and are subsequently discarded. The remaining trains are stacked and used for computing the part of the decay spectrum that falls in T_2 bins with $T_2 \leq 4$ ms. This part of the spectrum represents water in small pores and clay-bound water. The working assumption is that the partially polarized echo train represents the signal from clay-bound water. The two T_2 distributions (one from the fully polarized echo train and one from the partially polarized echo train) when combined, form a continuous T_2 distribution from 0.5 ms to more than 1,000 ms and provide a good estimation of total porosity.

The principle of total-porosity logging is illustrated in **Fig. 7.3**

At the wellsite, total-porosity logging provides bin data, a T_2 distribution from the fully polarized echo train, a T_2 distribution from the partially polarized echo train, apparent *MCBW*, *MPHI*, *BVI*, *MFFI*, and *MPERM*, as shown in **Fig. 7.4.** The wellsite products, such as *MFFI, BVI,* and *MPERM* are calculated with the default $T_{2cutoff}$ and permeability parameters.

MRIL data acquired with dual-*TW*, dual-*TE*, or standard-T_2 logging activations can also be used in MRIAN analysis. In the cases where dual-*TW* or dual-*TE* logging is used, the effective porosity *MPHI* should be taken from the long-*TW* echo train in dual-*TW* logging and from the short-*TE* echo train in dual-*TE* logging. Other porosity sources, such as a density/neutron crossplot, are needed for the total porosity.

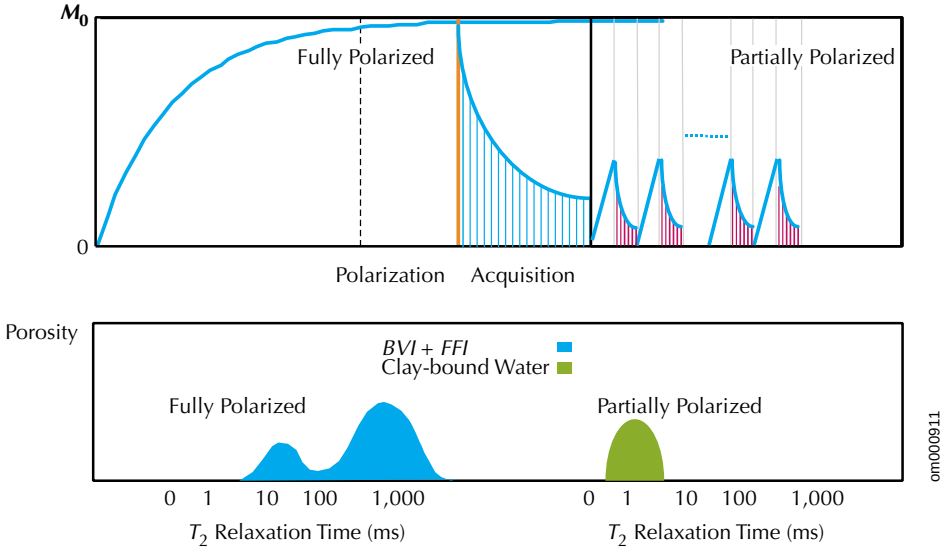

Figure 7.3—Total-porosity logging acquires fully polarized echo trains using short *TE* (0.9 or 1.2 ms) and partially polarized echo trains using very short *TE* (0.6 ms) and short *TW* (20 ms). The T_2 distributions corresponding to these echo trains are displayed at the bottom part of the figure.

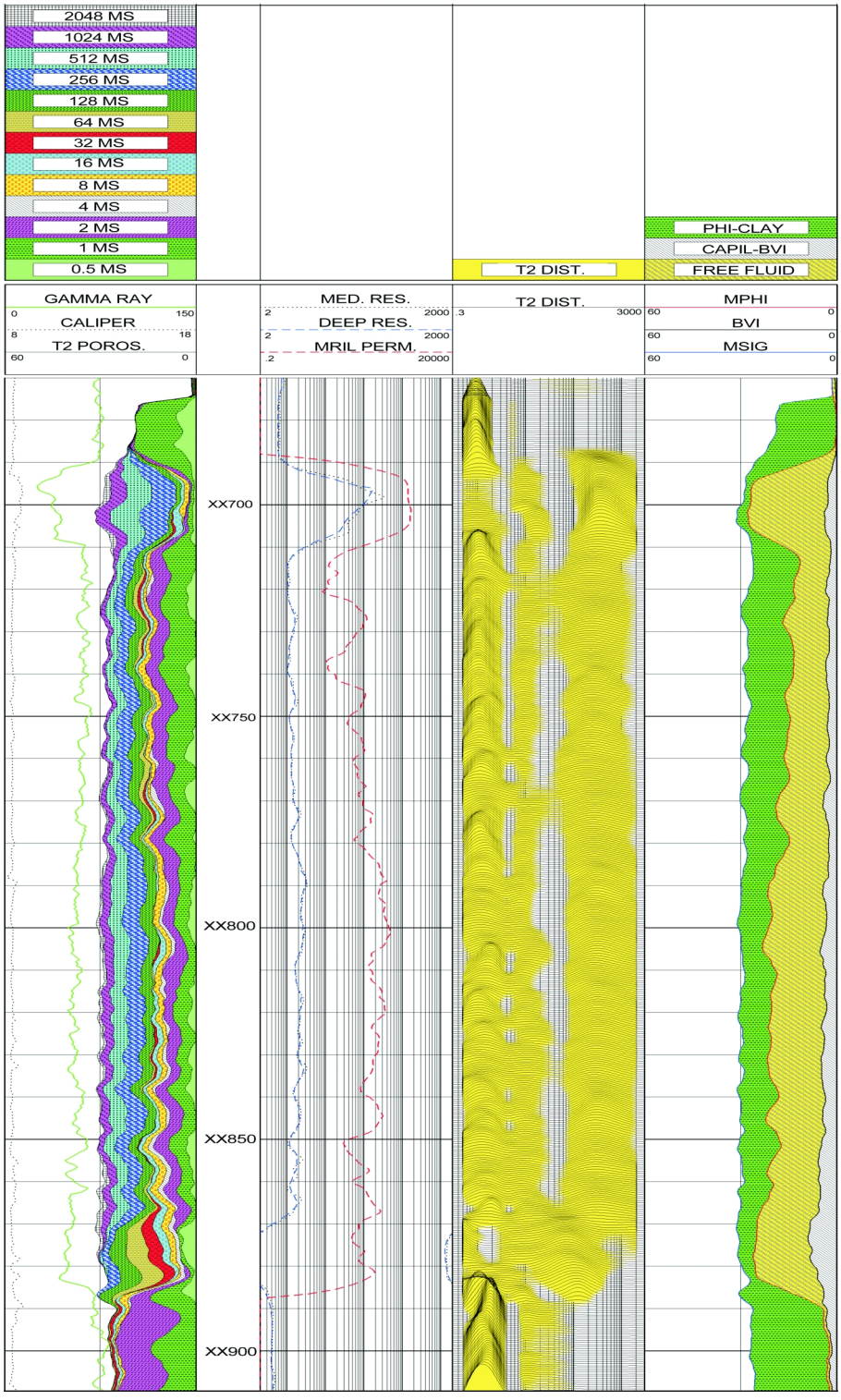

Figure 7.4—This log shows wellsite products from total-porosity logging. Track 1 contains a conventional gamma ray correlation curve and fully polarized T_2 bin data. Track 2 displays the *MPERM* calculated from the Coates permeability model. Track 3 displays the T_2 distribution spliced from fully polarized and partially polarized T_2 distributions. Track 4 contains *MCBW*, *MPHI*, and *BVI*.

MRIAN Applications

Low-Resistivity Reservoir 1

Fig. 7.5 shows a MRIAN example of the same well from the Gulf of Mexico, U.S.A., that was shown in Fig. 7.4. Track 1 contains gamma ray, caliper, and T_2 bin data. Track 2 contains resistivity data and MRIL permeability derived from the Coates model. Track 3 displays the T_2 distribution for clay-bound water and the long-*TW* echo trains. In the interval from XX690 to XX870, the hydrocarbons are oil, as indicated by the signals at long T_2. Track 4 displays the MRIAN results.

MRIL data for this example were acquired through total-porosity logging and through dual-*TW* logging. Total-porosity logging was used to determine clay-bound water, capillary-bound water, and free fluids. Dual-*TW* logging with *TW* values of 1 and 8 s was used to type the hydrocarbons and to make porosity corrections for under-polarization and hydrogen-index effects. Based on the MRIL *BVI*, *FFI*, and *CBW*, the observed reduction in resistivity from Zone A (XX690 to XX710) to Zone B (XX710 to XX870) was attributed to the increase in clay-bound water (Track 3) and not the presence of movable water. The MRIAN results suggested that Zone B was at irreducible water condition (Track 4) and had sufficient permeability (Track 2) to produce the movable hydrocarbons.

Fig. 7.6 shows the results of TDA (Track 5) and TDA/MRIAN (Track 6) for the same well as Fig. 7.4 and 7.5. In the TDA/MRIAN analysis, TDA provides a corrected effective porosity for MRIAN inputs. For this specific well, which was drilled with oil-based mud, both TDA and TDA/MRIAN results agree well.

Low-Resistivity Reservoir 2

Because MRIL data can provide estimates of irreducible water saturation, one of the advantages that MRIL logging has brought to petrophysical interpretation is the capability of more readily identifying low-resistivity pay zones, as seen in the previous example. If a rock contains a large amount of bound water, then formation resistivity is low, and in an initial analysis, the zone may appear wet. MRIL data, though, immediately shows the water to be bound and the zone as still having potential. In the conventional data presented in **Fig. 7.7**, the sand below XX200 has resistivity (Track 2) about 0.5 ohm-m and average neutron-density porosity (Track 4) about 38%. A standard first-pass analysis of S_w performed with these values would label this zone as wet.

Fig. 7.8 shows MRIL data acquired with a standard-T_2 logging activation for the same sand. Track 1 contains the T_2-distribution bin data, Track 2 contains formation permeability from the Coates model, and Track 3 contains the T_2 distribution in a variable-density display. Track 4 represents the irreducible water (*BVI*; shaded gray) and the free-fluid porosity (shaded yellow). *BVI* gradually increases with depth, suggesting that the sand is fining downward. (As sand grains become finer, the volume of capillary-bound water that they hold increases.) Also, comparison of the *BVI* with the resistivity profile shows that the resistivity decreases where the bound water increases. Because the initial MRIL data were encouraging, the sand was investigated further through MRIAN analysis. **Fig. 7.9** contains the MRIAN interpretation of the combination of MRIL and resistivity data. Track 1 shows gamma ray, caliper, SP, and T_2 bin data. Track 2 displays the resistivity and MRIL permeability. Track 3 contains the variable-density presentation of the T_2 distribution. Track 4 shows MRIAN fluid analysis, where capillary-bound water is shaded in gray, movable water in blue, and hydrocarbon in green. The MRIAN analysis clearly shows that the zone does not contain any movable water and will produce only oil. The interval below XX200 was tested and produced oil with no water.

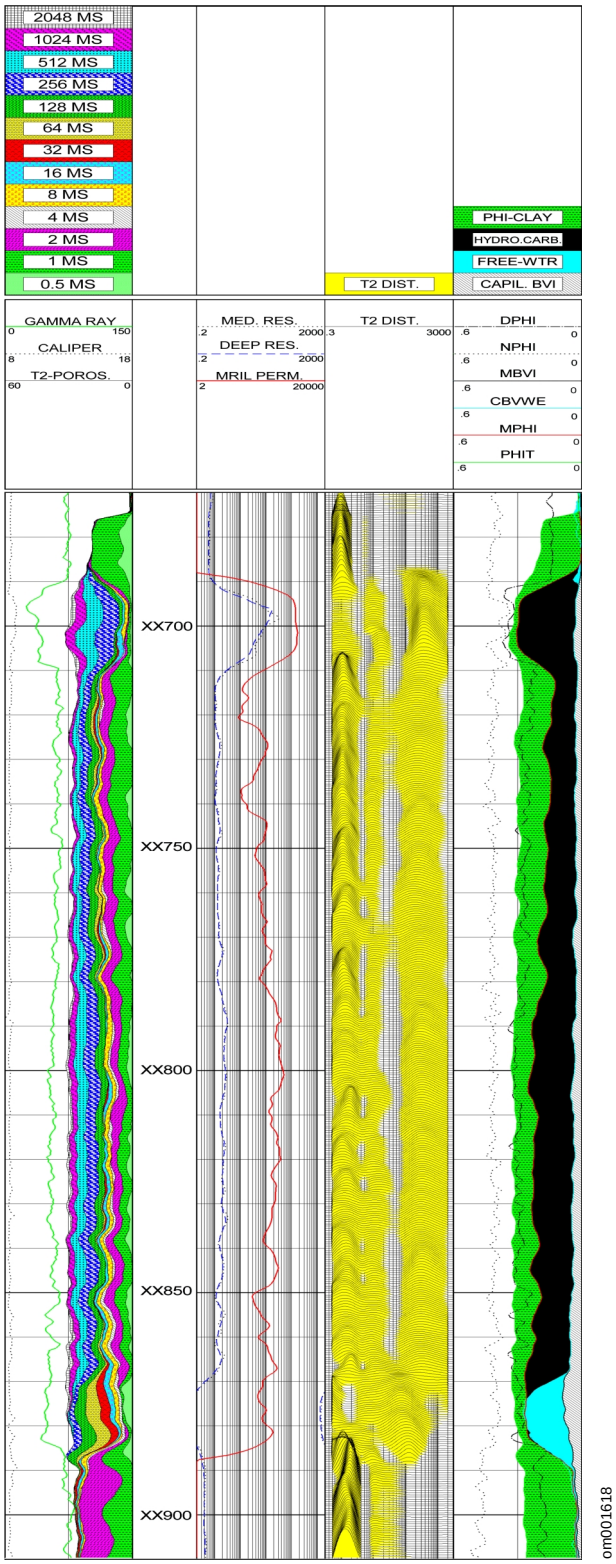

Figure 7.5—In this well from the Gulf of Mexico, U.S.A. (same well as shown in Fig. 7.4), conventional Archie S_w analysis indicated that the zone from xx710 to xx870 was wet. MRIAN analysis, however, suggested the zone was at irreducible water condition (Track 4) and had sufficient permeability (Track 2) to produce the movable hydrocarbons.

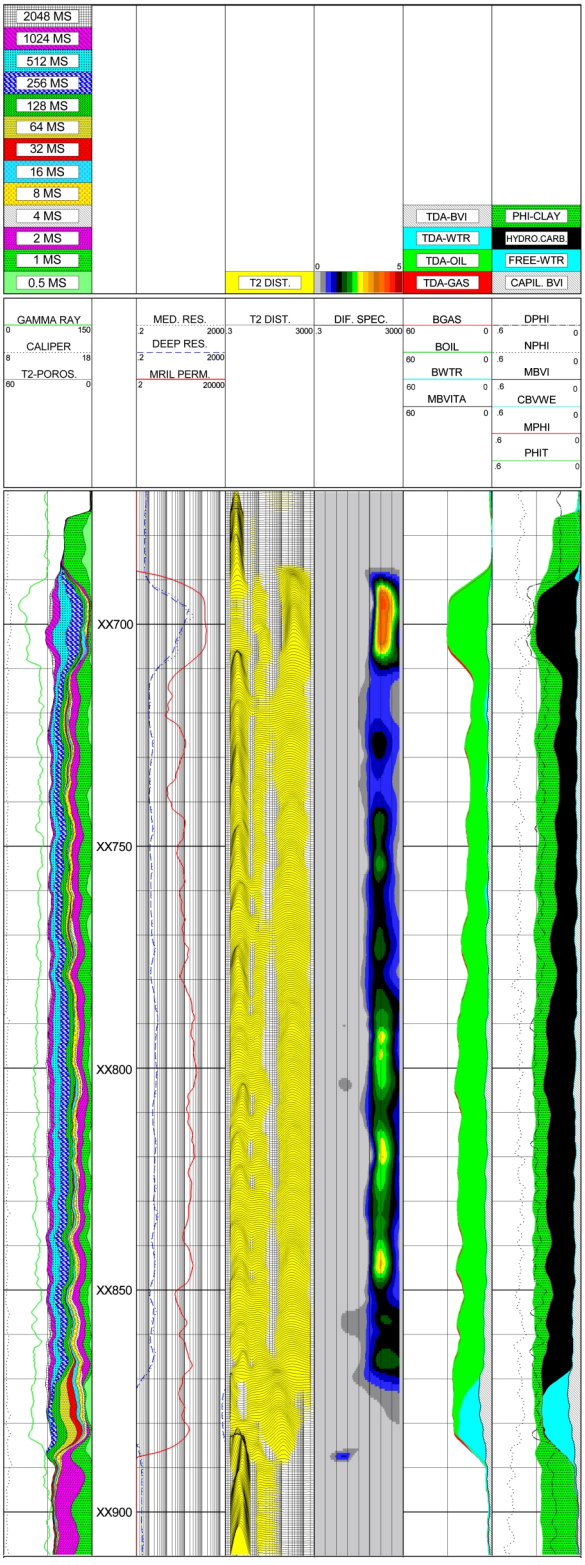

Figure 7.6—TDA and TDA/MRIAN results (Tracks 5 and 6, respectively) agree well in this oil well drilled with oil-based mud. This well is the same as the one depicted in Figs. 7.4 and 7.5.

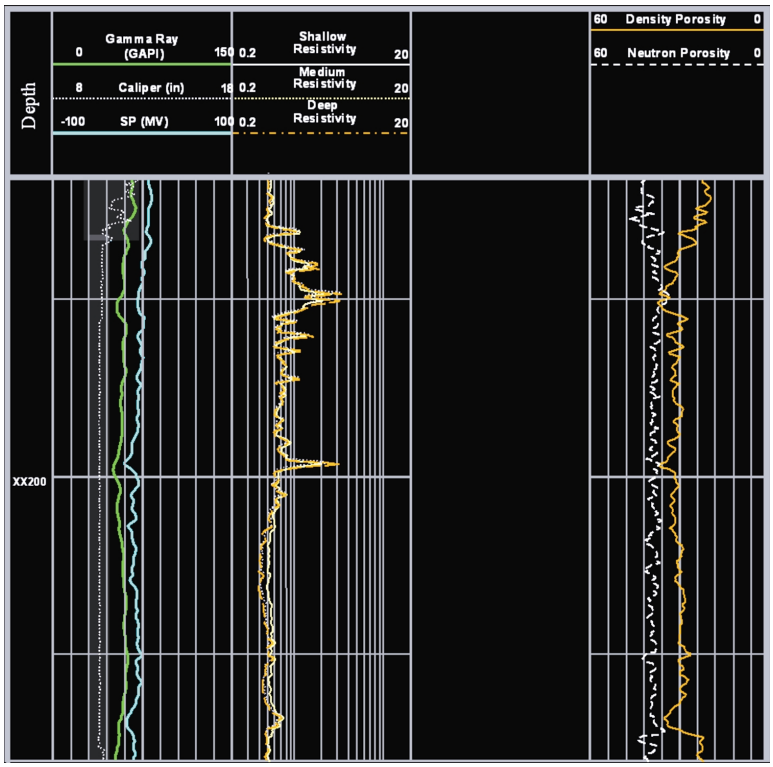

Figure 7.7—Conventional data shows the lower zone of this well (below XX200) to be water-wet because of the very low resistivity.

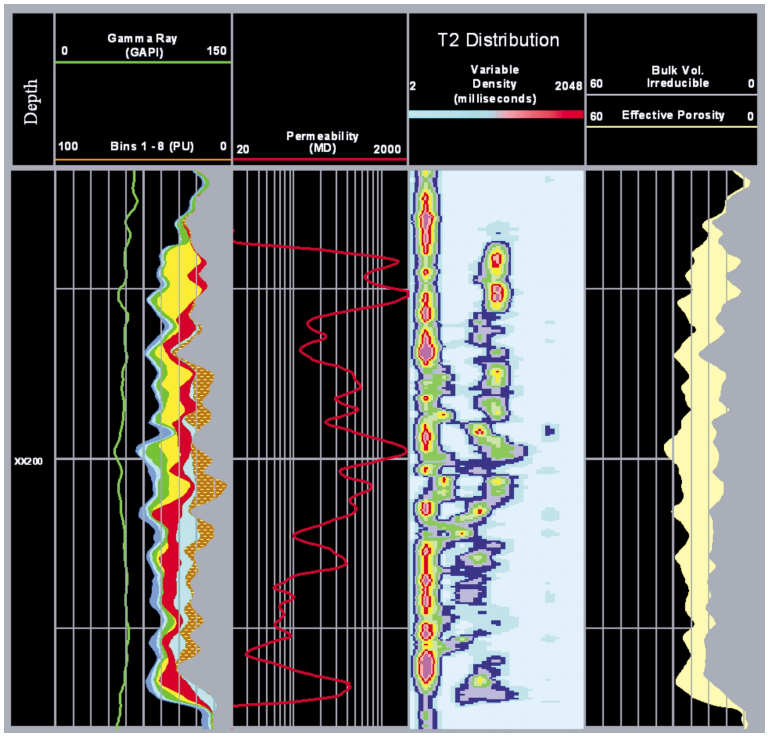

Figure 7.8—This MRIL log was run in the same well as the log of Fig. 7.7 and shows in Track 4 that *BVI* increases with depth.

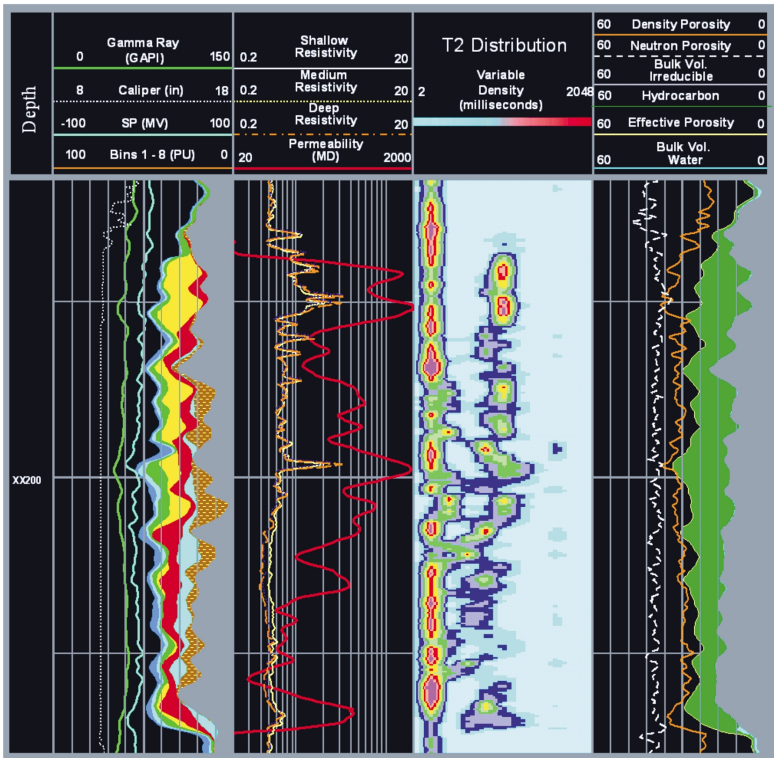

Figure 7.9—The MRIAN results shown in Track 4 of this log were obtained from a combined analysis of the conventional logging data in Fig. 7.7 and the MRIL data in Fig. 7.8. These results show that the whole zone is water-free pay, which testing confirmed.

Gas-Influx Monitoring with MRIL in an Arabian Gulf Carbonate

A gas-injection project was undertaken in a light-oil reservoir in the Arabian Gulf. Two problems facing gas monitoring on this project were the effect of salinity on wireline logs and the inadequate porosity measurements made by logging-while-drilling (LWD) devices. (The LWD porosity always underestimated the reservoir porosity by 3 to 4 p.u.)

MRIL logs were run in this reservoir because of the MRIL gas-monitoring capability through Time Domain Analysis and because of the negligible effect of formation water salinity on MRIL measurements. In particular, MRIL, LWD neutron, and LWD density logs were recorded in a re-entry well with 59° deviation. The original borehole was cored, but the re-entry borehole was not. MRIL, LWD, and core porosities were statistically compared. The average gas-corrected MRIL porosity over the cored zone was 21 p.u., which compared very well with the average core porosity of 20.8 p.u. The average LWD porosity over the same zone was 17.4 p.u.

Tracks 6 and 7 of the log in **Fig. 7.10** show the MRIL results for, respectively, both Time Domain Analysis and MRIAN analysis. TDA showed four types of fluids in the flushed zone: gas influx (shaded red), residual oil (green), movable water (blue), and irreducible water (gray). Track 7 shows the MRIAN analysis, which indicated that the reservoir was at irreducible water saturation and no movable water was present. Combining the results of both analyses suggests that the movable water interpreted by TDA was filtrate from the water-based mud.

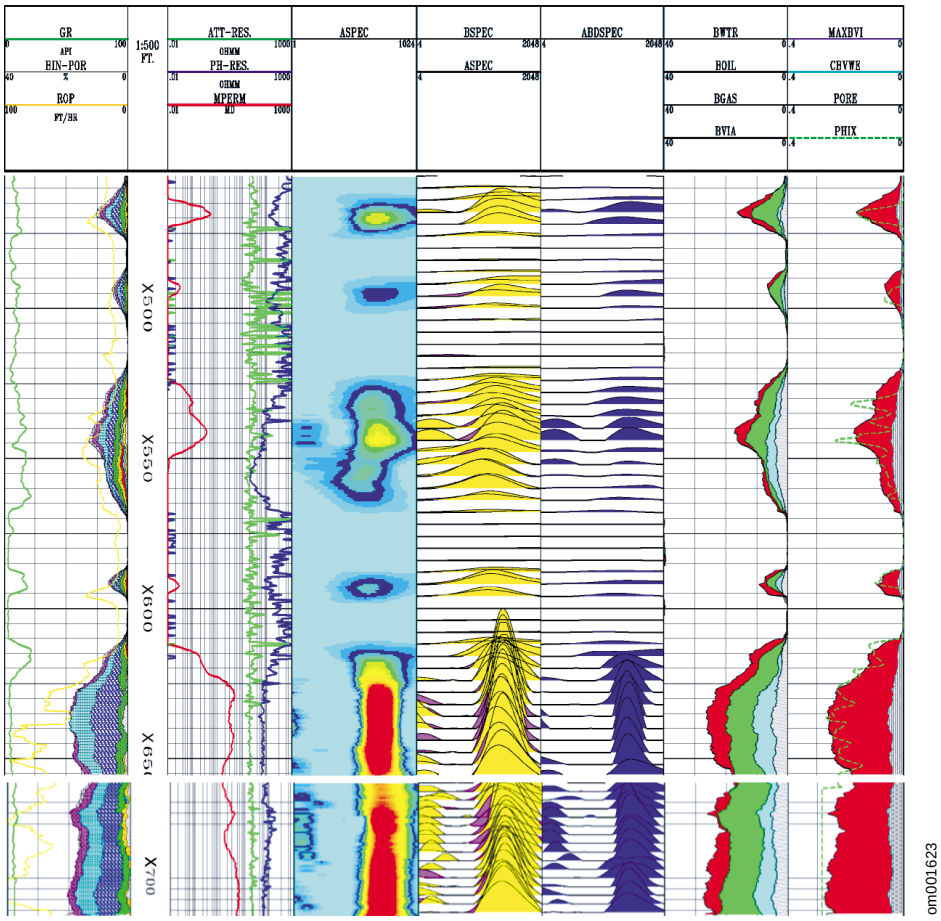

Figure 7.10—TDA and MRIAN analyses were performed on MRIL data acquired in a gas-injection well in a light-oil reservoir in the Arabian Gulf. Track 1 contains T_2 bin data and conventional SP and gamma ray curves. Track 2 shows permeability derived from the standard Coates model; this track also shows LWD resistivity data. Track 3 displays the T_2 distribution in variable density format. Track 4 contains T_2 distributions of data acquired with long *TW* and short *TW*. Track 5 is the differential spectrum. Track 6 contains TDA results. Track 7 contains MRIAN results. Because this display was customized for the client, it differs from most other displays in this book.

The differences in the results derived from TDA and MRIAN fluid identification are due to differences in the depths of investigation of the measurements that provided the data for the analyses. All data used for TDA are from measurements in the near-wellbore zone, which for water-based mud normally has a higher water saturation than the virgin zone. MRIAN uses the deep resistivity measurement, which is dominated by the virgin zone saturation, so MRIAN output is more representative of saturation there. When TDA is used together with MRIAN, the flushed-zone and virgin-zone saturations can be compared. TDA provides information for typing and quantifying fluids, and can furnish key data for MRIAN processing, such as effective porosity corrected for hydrogen-index and for polarization effects. If MRIL total-porosity measurements are available, then clay-bound water saturation and total porosity can be also derived from MRIL data alone, and a TDA/MRIAN combination can be run without conventional porosity data. Comparison of TDA and MRIAN answer products reveals changes in S_w between the invaded zone and the virgin zone. This change is dependent on mud type. **Fig. 7.11** illustrates the principles of the TDA/MRIAN combination when log data are acquired under water-based mud conditions.

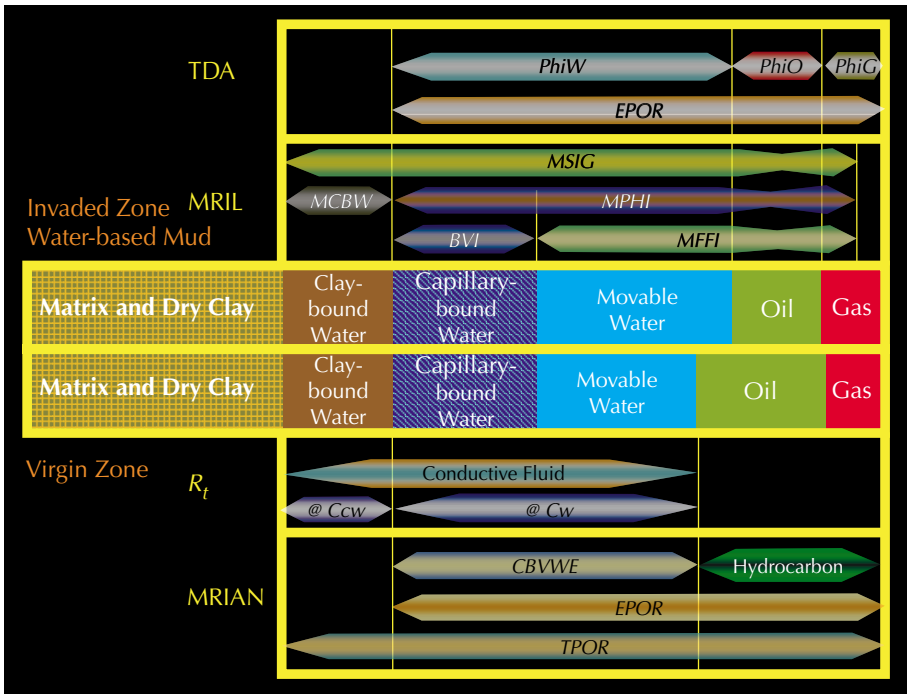

Figure 7.11—A comparison of TDA and MRIAN results can reveal differences in formation fluids between the flushed and virgin zones. The middle two panels in this figure represent volumetric models of the invaded and virgin zones. A water-based mud is assumed. The upper two panels represent MRIL standalone data and TDA results. *EPOR* is effective porosity corrected for polarization effects, *PhiW* is movable water volume, *PhiO* is oil volume, and *PhiG* is gas volume. The bottom two panels represent resistivity responses and MRIAN results. The differences between the TDA and MRIAN results shown here are caused by invasion of mud filtrate, which affects the data from the near-wellbore region used in both TDA and MRIAN but which has little effect on the deep-resistivity data used in MRIAN.

Evaluation of a Shaly, Tuff Sandstone Formation Containing Medium-Viscosity Oils

Fig. 7.12 is an EDM/MRIAN log from a field in the San Jorge Basin, Argentina. The formation consists of a series of medium- to fine-grained sandstones, which are thought to have originated from volcanic activities. The sands range between 5 and 20 ft in thickness and have lateral extents between 1 and 3 miles. Permeability ranges between 2 and 2,000 md, and porosity ranges between 10 and 30%. Resistivity in the sands is between 7 and 20 ohm-m, and shale volumes vary from 5 to 25%. The produced hydrocarbons consist of oils with viscosities of 20 to 50 cp. However, zones with oil of much higher viscosity (more than 100 cp) are also possible. The wells were drilled overbalanced with water-based mud. Mud resistivity was about 2 to 3 ohm-m.

Because individual well production in this area is very low, minimizing completion costs is essential. One of the primary problems for formation evaluation is identification of dry zones (tuff sandstones) with varying shale and zeolite volumes. When zeolite is present, its low matrix density (2.10 to 2.20 g/cm^3) causes the density porosity to read too high. Consequently, shale volumes may be underestimated, and porosity and permeability may be significantly overestimated. In many cases, these zones look potentially productive on logs, but are frequently dry or have very little oil production. Under these conditions, measurements with the potential to discriminate between low-permeability zones and dry zones and to identify hydrocarbon-bearing formations can significantly improve perforation and stimulation results. Because MRIL logs offered this potential, they were run in this area.

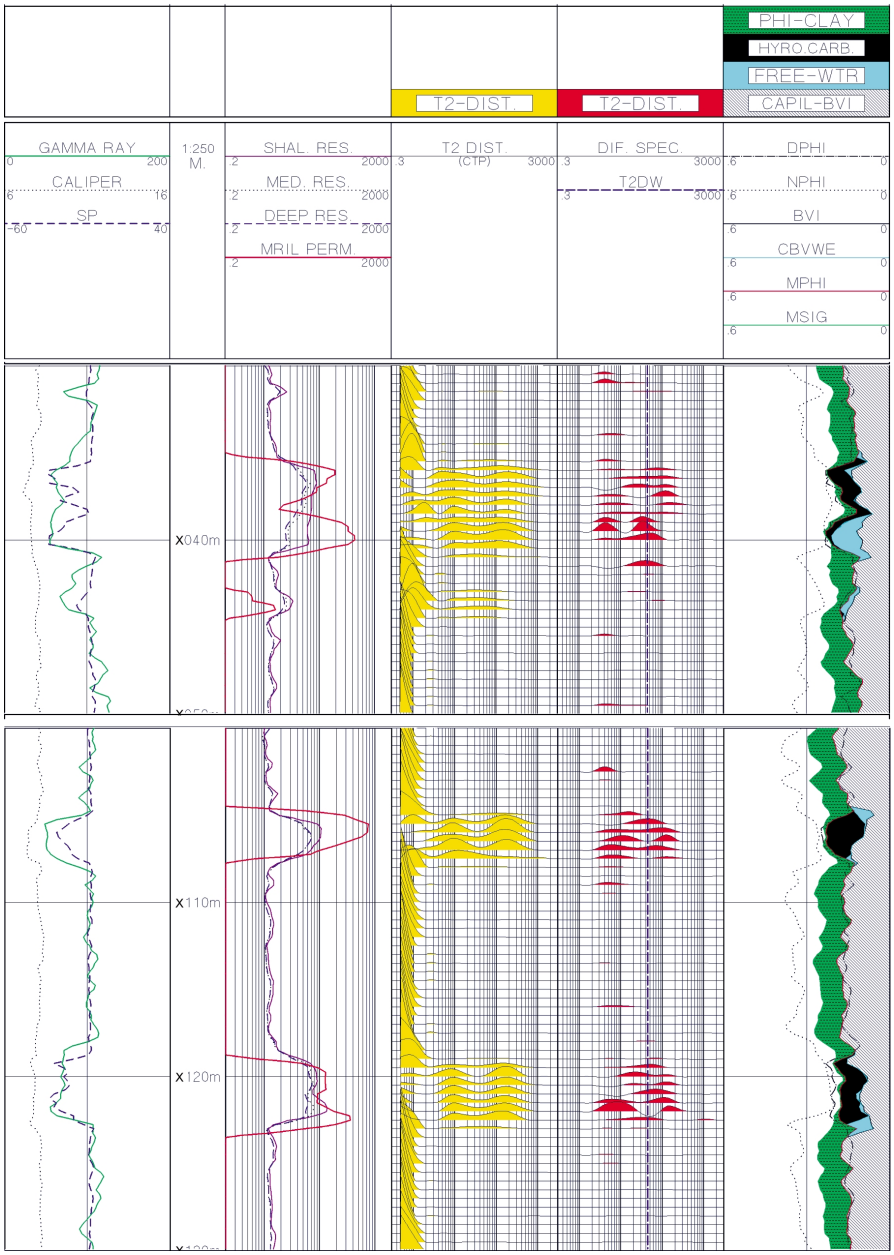

Figure 7.12—This log includes results of EDM/MRIAN processing. Track 1 contains conventional correlation log curves (gamma ray, SP, caliper) and T_2 bin data. Track 2 contains resistivity data and MRIL-derived permeability. The waveforms in Track 3 represent the T_2 distribution derived from the partially polarized echo trains used for determining clay-bound water and from the fully polarized echo trains acquired with short *TE*. The differential spectra in Track 4 are the difference between two T_2 distributions from echo trains acquired with *TE* = 3.6 ms and *TW* = 300 and 3,000 ms. The vertical line in Track 4 represents a maximum value for the water signal (T_{2DW} = 44 ms). Sharp changes in the T_2 spectra are evident at the oil/water contact. Track 5 contains the results of MRIAN analysis for fluid composition and volume (clay-bound water, hydrocarbon, free water, and capillary-bound water).

An MRIL total-porosity activation (*TE* = 0.6 and 1.2 ms, and *TW* = 3 s) was used to establish petrophysical properties such as clay-bound water, capillary-bound water, movable fluids, effective porosity, and permeability. A dual-*TW* activation (*TE* = 3.6 ms, and *TW* = 0.3 and 3 s) was used to supply measurements that would support the MRIL EDM technique for typing and quantifying the medium-viscosity oils in the reservoir. The zones of interest in this field often have porosity components of 256 and 512 ms in the standard T_2 distribution acquired with *TE* = 1.2 ms. These components imply the presence of large, water-filled pores. Utilizing the diffusion contrast between water and medium-viscosity oil, an upper T_2 limit of

water (T_{2DW}) was established to be 44 ms. Therefore, any signal with T_2 value greater than 44 ms could be attributed to oil, which has an average T_2 of approximately 90 ms. Based on this qualification, the MRIL data identified one zone from X036.5 to X042.5 that unambiguously contained oil. The standard T_2 distribution shown in Track 3 was unable to distinguish the oil/water contact in this zone. The EDM method shown in Track 4, however, clearly identified the contact. The operator completed this zone without stimulation and produced 554 B/D of fluid with a trace of water.

Utilizing the Coates equation with a customized $C = 6.0$, the MRIL tool provides a continuous permeability curve. The operator has observed that zones with permeability values less than 1 md are poor producers. By utilizing the MRIL permeability, fracture stimulation performance is significantly improved in this reservoir. The MRIL log was found to give a representative value of reservoir permeability within the drainage area of the well, and this permeability allowed a reasonable estimation of the after-fracture production. Zones with *kh* value (where *k* is zone permeability, and *h* is zone thickness) above 2 md/m and pressure at least 80% of the original reservoir pressure were targeted for treatment. However, the production in some zones above 2 md/m did not increase after fracturing, which suggested the possible influence of zeolite. These zones can easily be identified by comparing the MRIL-derived porosity to porosity derived from the neutron-density crossplot. Zones in which the MRIL effective porosity is substantially less than neutron-density porosity can be identified as tuff sands that will be non-productive.

As a result of the integration of MRIL into the logging program, the number of non-commercial completed zones decreased, and costs associated with production tests and stimulation were significantly reduced. The EDM results for the other two zones that appeared promising on the log of Fig. 7.12 have been also confirmed by production results.

MRIAN in a Light-Hydrocarbon Well

Fig. 7.13 shows MRIAN results from a well logged with dual-*TE* activation. (The dual-*TE* log was shown in Fig. 6.13.) Track 1 includes conventional gamma ray and caliper curves along with T_2 bin data. Track 2 shows resistivity data and MRIL-derived permeability. Track 3 displays the T_2 distributions from the short-*TE* echo trains. Track 4 includes neutron and density porosities and MRIAN answer products: volumes of capillary-bound water, free water, and hydrocarbons. The MRIAN results, resistivity data, and T_2 distributions clearly indicate a water/hydrocarbon contact at approximately X050 ft. Comparison of the MRIL porosity with the neutron and density porosities suggests that the hydrogen index of the zone above X050 ft is less than 1. The T_2 distribution in Track 3 shows that the peak values for the hydrocarbon T_2 are around 256 ms between X000 and X050 ft, thus this interval should not contain gas. Above X000 ft, however, the amplitudes of the T_2 peak at 256 ms are significantly reduced, and more signals appear at T_2 values of approximately 40 ms, which suggests the presence of gas. The permeability in Track 2 as it is derived from MRIL porosity is underestimated above X050 ft. Dual-*TW* data would allow a more accurate analysis of this reservoir.

Well Completion with MRIL: StiMRIL

StiMRIL is an interpretation program that combines the MRIL reservoir-characterization data (especially permeability, effective porosity, and total porosity) with other petrophysical measurements to optimize the design of stimulation treatments. Compared with previously available sources of information, this combination provides easier-to-obtain and more reliable answers to the following critical questions:

- Where are hydrocarbons located?

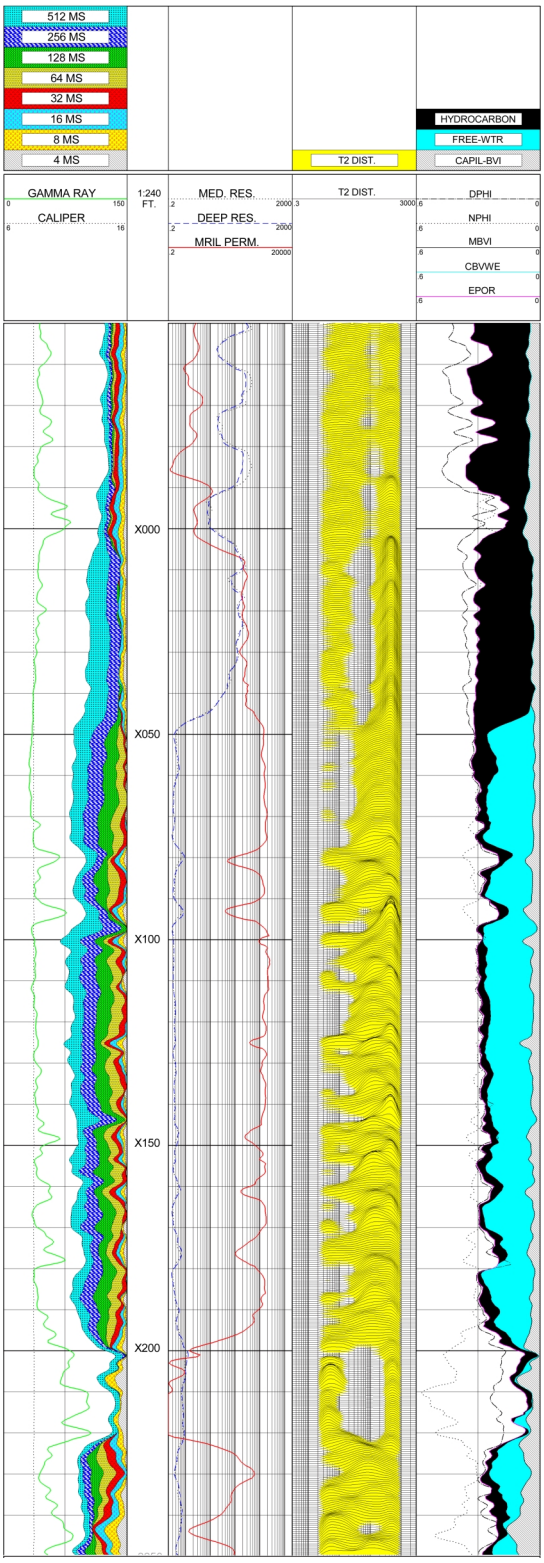

Figure 7.13—These MRIAN results were derived from dual-*TE* data gathered in a light-hydrocarbon reservoir. The porosity data above X,000 ft indicates gas, as does the T_2 data. However, between X,050 and X,000 ft, the porosity data still suggest gas, but the T_2 data give no indication of gas. Had dual-*TW* data been acquired, it could have been used to resolve this discrepancy.

- At what rate will the well produce?
- Will the zone produce water?
- What is the net present value (NPV) of the zone?

Fig. 7.14 compares a StiMRIL completion with a typical conventional completion in the Travis Peak formation of East Texas in the U.S.A. The comparison illustrates the value of MRIL data in selecting and designing completion programs. Conventional logs have generally shown little difference in the three sands represented in the figure. Consequently, in conventional completions, all three have been completed and fractured together. Production has typically been 300 Mcf/D gas with 250 B/D water. Average completion costs have been $76,000 per well.

MRIL data and other logs have also been successfully merged to improve stimulation success in Jurassic age Cotton Valley wells in East Texas and Louisiana. This play is similar to the Travis Peak. **Fig 7.15** shows a StiMRIL log from a Cotton Valley well. Track 1 contains gamma ray, caliper, bit size, and T_2 bin information. Track 2 presents *MPERM* along with the deep and medium resistivities from a high-resolution induction tool. Track 3 displays a variable-density image of the T_2 distributions generated from partially polarized data, which are associated with clay-bound water. Track 4 displays a variable-density image of the T_2 distributions generated from fully polarized data. Track 5 shows *MSWE*, non-clay water saturation from MRIAN. Track 6 displays MRIAN analysis results that include effective porosity, bound water, movable water, and hydrocarbons. Included in the depth track is a flag to show zones identified from the analysis as being hydrocarbon-bearing. The depth track also displays zonal numbering in red. In Track 5 the orange shading designated as gas represents the difference between MRIL porosity and neutron-density crossplot porosity. In this case, the hydrocarbons identified by MRIAN are also gas.

Examination of the log shows resistivity analysis identifying most of the log as having some gas saturation, but only three zones (4, 6, and 8) with acceptable permeability. MRIAN analysis shows Zone 8 to have significant free water. Because water production in this area was not the norm, this free-water indication was ignored, and all three zones were fractured. Appreciable water was produced and, accordingly, completion practices were modified for

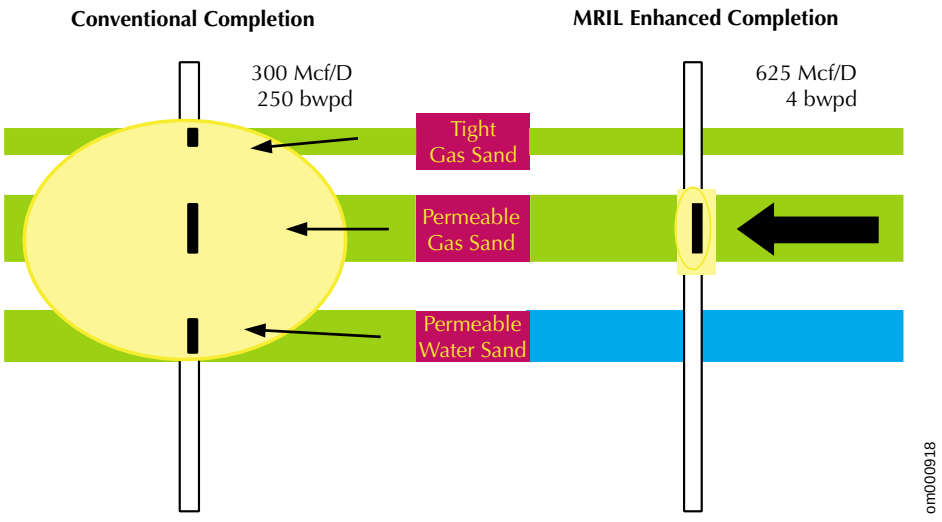

Figure 7.14—In the Travis Peak formation of east Texas in the U.S.A., a completion designed with StiMRIL data resulted in improved production and reduced completion costs compared with conventional completions. With conventional completion designs, the three depicted zones were completed and fractured together. The StiMRIL completion used special perforating guns to complete the middle zone only, and no hydraulic fracturing was used.

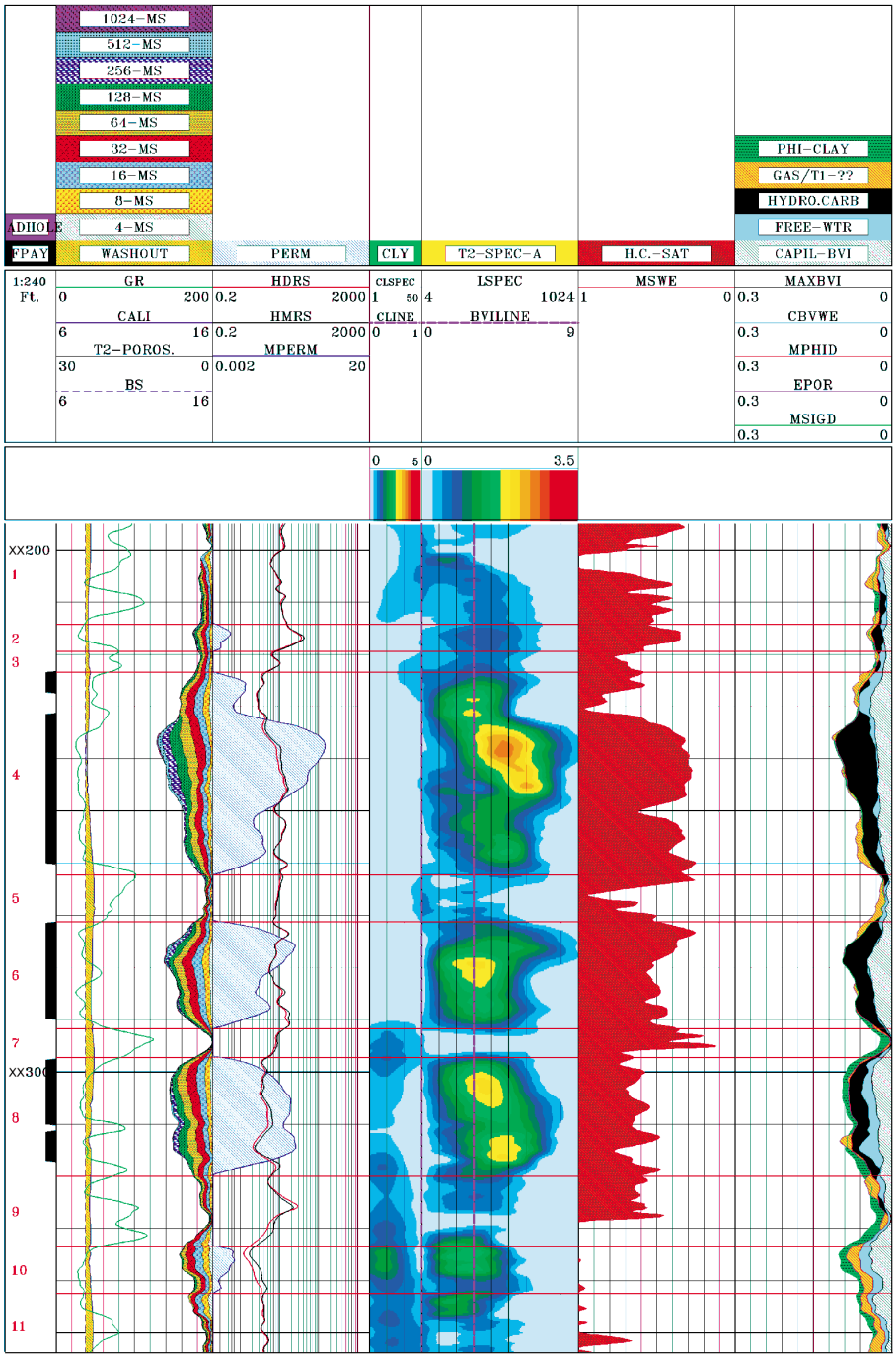

Figure 7.15—This StiMRIL standard log presentation contains MRIL data and the results of MRIAN analysis. Zones determined with StiMRIL are delineated by the red lines extending across all tracks and are numbered in the far-left track. The far-left track also contains black pay flags that resulted from StiMRIL analysis.

subsequent wells. In particular, only Zone 4 is being fractured. Zone 6 is not fractured because fractures there might extend through the thin seal separating Zone 6 and Zone 8 which contains free water. Furthermore, as estimated from permeability and thickness, Zone 6 would only flow at 17% of the rate of Zone 4.

References

1. Coates, G.R., Gardner, J.S., and Miller, D.L., 1994, Applying pulse-echo NMR to shaly sand formation evaluation, paper B, *35th Annual SPWLA Logging Symposium Transactions*, 22 p.
2. Clavier, C., Coates, G., and Dumanoir, J., 1977, The theoretical and experimental bases for the dual water model for interpretation of shaly sands, SPE 6859, 16 p.
3. Ostroff, G.M., Shorey, D.S., and Georgi, D.T., 1999, Integration of NMR and conventional log data for improved petrophysical evaluation of shaly sands, *40th Annual SPWLA Logging Symposium Transactions*, 14 p.
4. Coates, G.R., and Howard, A.D., 1992, Core data and the MRIL show a new approach to formation factor, SCA-9207, in 6th annual technical conference preprints (*33rd Annual SPWLA Logging Symposium Transactions*, v. 3): Society of Core Analysts, Society of Professional Well Log Analysts Chapter-at-Large, 14 p.
5. Coates, G., and Miller, D., 1997, Confirming Rw by reconstructing the SP using formation evaluation results employing gradient field magnetic resonance logs, paper VV, *38th Annual SPWLA Logging Symposium Transactions*, 12 p.

More NMR logging application case studies can be found in following literature:

Altunbay, M., Edwards, C.M., and Georgi, D.T., 1997, Reducing uncertainty in reservoir description with NMR-log data, SPE 38027, *1997 SPE Asia Pacific Oil and Gas Conference Proceedings*, p. 99–108.

Altunbay, M., Georgi, D., and Takezaki, H., 1997, Improving S_{wir} and permeability estimates in carbonates with hydraulic units and NMR-variable T_2-partitioning coefficients, paper I, *3rd SPWLA Well Logging Symposium of Japan Proceedings*, 9 p.

Austin, J.M., and Faulkner, T.L., 1993, Magnetic resonance imaging log evaluates low-resistivity pay, *American Oil and Gas Reporter*, v. 36, no. 8, p. 52–57.

Castelijns, C., Badry, R., Decoster, E., Hyde, C., 1999, Combining NMR and formation tester data for optimum hydrocarbon typing, permeability and producibility estimation, *40th Annual SPWLA Logging Symposium Transactions* Annual Logging Symposium, 14 p.

Chang, D., et al., 1994, Effective porosity, producible fluid and permeability in carbonates from NMR logging, paper A, *35th Annual SPWLA Logging Symposium Transactions*, 21 p. Later published in 1997 in *The Log Analyst*, v. 38, no. 2, p. 60–72.

Coates, G.R., et al., 1993, Restrictive diffusion from uniform gradient NMR well logging, SPE 26472, *1993 SPE Annual Technical Conference and Exhibition Proceedings*, v. Ω (Formation evaluation and reservoir geology), p. 575–590.

Coope, D.F., 1994, Petrophysical applications of NMR in the North Sea, paper Z, *16th SPWLA European Formation Evaluation Symposium Transactions*, 12 p. Also published

in 1994 as Petrophysical applications of NMR, *Dialog* (London Petrophysical Society Quarterly Newsletter), v. 2, no. 4, October, p. 8–10.

Corbelleri, A., et al., 1996, Application of the magnetic resonance logging in San Jorge basin (Argentina), paper VV, *37th Annual SPWLA Logging Symposium Transactions*, 12 p.

Crary, S., Pellegrin, F., and Simon, B., 1997, NMR applications in the Gulf of Mexico, paper PP, *38th Annual SPWLA Logging Symposium Transactions*, 13 p.

Crowe, B., et al., 1997, Measuring residual oil saturation in west Texas using NMR, paper JJ, *38th Annual SPWLA Logging Symposium Transactions*, 12 p.

Cunningham, A.B., and Jay, K.L., 1991, Field experience using the nuclear magnetic logging tool for quantifying microporosity and irreducible water saturation, paper EE, *32nd Annual SPWLA Logging Symposium Transactions*, 23 p.

Dodge, W.S., Shafer, J.L., and Guzman-Garcia, A.G., 1995, Core and log NMR measurements of an iron-rich glauconitic sandstone reservoir, paper O, *36th Annual SPWLA Logging Symposium Transactions*, 12 p.

Dodge, W. S., et al., 1998, A case study demonstrating how NMR logging reduces completion uncertainties in low porosity, tight gas sand reservoirs, *39th Annual SPWLA Logging Symposium Transactions*, 14 p.

Egbogah, E.O., and Amar, Z.H.B.T., 1997, Accurate initial/residual saturation determination reduces uncertainty in further development and reservoir management of the Duland field, offshore peninsular Malaysia, SPE 38024, *1997 SPE Asia Pacific Oil and Gas Conference Proceedings*, p. 79–90.

Eidesmo, T., Relling, O., and Rueslatten, H., 1996, NMR logging of mixed-wet North Sea sandstone reservoirs, paper PP, *37th Annual SPWLA Logging Symposium Transactions*, 14 p.

Flaum, C., Kleinberg, R.L., and Bedford, J., 1998, Bound water volume, permeability, and residual oil saturation from incomplete magnetic resonance logging data, UU, *39th Annual SPWLA Logging Symposium Transactions*, 11 p.

Flolo, L.H., 1998, Getting the hydrocarbon volume right—a quantitative use of NMR data in water saturation modeling, *39th Annual SPWLA Logging Symposium Transactions*.

Freeman, R., et al., 1998, Combining NMR and density logs for petrophysical analysis in gas-bearing formations, *39th Annual SPWLA Logging Symposium Transactions*.

Gibson, B-D., et al., 1995, Nuclear magnetic resonance applications in North America, paper H, *1st Annual SPWLA Well Logging Symposium of Japan Proceedings*, 14 p.

Gossenberg, et al., 1996, A new petrophysical interpretation model for clastic rocks based on NMR, epithermal neutron and electromagnetic logs, paper M, *37th Annual SPWLA Logging Symposium Transaction*, 13 p.

Gumilar, B., et al., 1996, Signal processing method for multiexponentially decaying signals and an analysis of low-contrast pay in Telisa sands packages in central Sumatra, paper IPA96-2-2-123, *25th Annual Indonesian Petroleum Association Convention Proceedings*, v. 2, p. 175–187.

Guest, R., et al., 1998, Case studies of nuclear magnetic resonance in Texas and Louisiana Gulf Coast area, *39th Annual SPWLA Logging Symposium Transactions*.

Hassoun, T.H., Zainalebedin, K., and Minh, C.C., 1997, Hydrocarbon detection in low-contrast resistivity pay zones, capillary pressure and ROS determination with NMR logging in Saudi Arabia, SPE 37770, *10th SPE Middle East Oil Show Conference Proceedings*, v. 2, p. 127–143.

Hodgkins, M.A., and Howard, J.J., 1999, Application of NMR logging to reservoir characterization of low resistivity sands in the Gulf of Mexico, *AAPG Bulletin*, v. 83, no. 1, p.114–127.

Hook, J., Basan, P., and Lowden, B., 1996, The MRIL log in a low porosity and permeability formation, paper N, *37th Annual SPWLA Logging Symposium Transactions*, 13 p.

Horkowitz, J.P., et al., 1995, Residual oil saturation measurements in carbonates with pulsed NMR logs, paper Q, *36th Annual SPWLA Logging Symposium Transaction*s, 12 p. Later published in 1997 in *The Log Analyst*, v. 38, no. 2, p. 73–83.

Howard, A., 1996, MRI logging tools locate water-free production, *American Oil and Gas Reporter*, v. 39, no. 11, October, p. 70, 72–74.

Howard, J., Williams, J., and Thorpe, D., 1997, Permeability from nuclear magnetic resonance logging in a gas-condensate field, paper XX, *38th Annual SPWLA Logging Symposium Transactions*, 13 p.

Hussein, S.M., et al., 1999, Using NMR and electrical logs for enhanced evaluation of producibility and hydrocarbon reserves in gas reservoirs with high irreducible water saturation, *40th Annual SPWLA Logging Symposium Transactions*, 9 p.

Latif, A.A., et al., 1997, Borehole nuclear magnetic resonance—experience and reservoir applications in west Kuwait carbonate reservoirs, SPE 37771, *10th SPE Middle East Oil Show Conference Proceedings*, v. 2, p. 145–154.

Logan, W.D., et al., 1997, Practical application of NMR logging in carbonate reservoirs, SPE 38740, *1997 SPE Annual Technical Conference and Exhibition Proceedings*, v. Ω (Formation evaluation and reservoir geology), p. 203–215.

Lomax, J., and Howard, A., 1994, New logging tool identifies permeability in shaly sands, *Oil and Gas Journal*, v. 92, no. 51, December 19, p. 104–108.

Looyestijn, W., 1996, Determination of oil saturation from diffusion NMR logs, paper SS, *37th Annual SPWLA Logging Symposium Transactions*, 14 p.

Looyestijn, W., Schiet, M., and Runia, J., 1994, Successful field test of nuclear magnetic resonance (NMR) logging in the Rotterdam field, paper X, *16th SPWLA European Formation Evaluation Symposium Transactions*, 11 p.

Mardon, D., et al., 1996, Characterization of light hydrocarbon-bearing reservoirs by gradient NMR well logging—a Gulf of Mexico case study, SPE 36520, *1996 SPE Annual Technical Conference and Exhibition Proceedings*, v. Ω (Formation evaluation and reservoir geology), p. 295–304. Also published in 1996 in condensed form in *Journal of Petroleum technology*, v. 48, no. 11, p. 1035–1036.

Mirotchnik, K., Allsopp, K., and Kantzas, A., 1997, Combination of NMR and ultracentrifuge techniques for effective carbonate reservoir characterization, paper SCA-9703, in 1997 international symposium proceedings: Society of Professional Well Log Analysts, Society of Core Analysts Chapter-at-Large, 10 p.

Nascimento, J.D.S., and Denicol, P.S., 1999, Anomalous NMR responses in highly permeable sandstone reservoirs: a case study, *40th Annual SPWLA Logging Symposium Transactions*.

Olesen, J.-R., et al., 1997, Evaluation of viscous oil-bearing, water flooded reservoirs, paper T, *3rd SPWLA Well Logging Symposium of Japan Proceedings*, 14 p.

Oraby, M., et al., 1997, A new NMR interpretation technique using error minimization with variable T2 cutoff, SPE 38734, *1997 SPE Annual Technical Conference and Exhibition Proceedings*, v. Ω (Formation evaluation and reservoir geology), p. 175–181.

Oraby, M.E., and Eubanks, D.L., 1997, Determination of irreducible water saturation using magnetic resonance imaging logs (MRIL)—a case study from east Texas, USA, SPE 37772, *10th SPE Middle East Oil Show Proceedings*, v. 2, p. 155–162.

Petricola, M.J.C., and Takezaki, H., 1996, Nuclear magnetic resonance logging—can it minimize well testing?, SPE 36328, *7th SPE Abu Dhabi International Petroleum Conference Proceedings*, p. 740–748.

Petricola, M.J.C., and Troussaut, X., 1999, Applications of fast NMR logging in shaly gas-bearing sands invaded by oil filtrate, *40th Annual SPWLA Logging Symposium*, 10 p.

Phen, H.A., Ajufo, A., and Curby, F.M., 1995, A hydraulic (flow) unit based model for the determination of petrophysical properties from NMR relaxation measurements, paper SCA-9514, in International SCA symposium proceedings: Society of Professional Well Log Analysts, Society of Core Analysts Chapter-at-Large, 12 p.

Prieto, M., et al., 1997, Conciliation of core data and log derived permeability from nuclear magnetic resonance and Stoneley wave in northern Monagas area, eastern Venezuela, paper WW, *38th Annual SPWLA Logging Symposium Transactions*, 14 p.

Rueslatten, et al., 1998, NMR studies of an iron-rich sandstone oil reservoir, Society of Core Analysts-9821, 10 p.

Salvignol-Bellando, A., Volokitin, Y., Slijkerman, W., Bonnie, R., 1999, The use of NMR logging for gas reservoir characterization in a north sea play with complex and variable rock properties, *40th Annual SPWLA Logging Symposium Transactions*.

Singer, J., et al., 1997, Fast NMR logging for bound fluid and permeability, paper YY, *38th Annual SPWLA Logging Symposium Transactions*, 13 p.

Slot-Petersen, C., et al., 1998, NMR formation evaluation applications in a complex low-resistivity hydrocarbon reservoir, paper TT, *39th Annual SPWLA Logging Symposium Transactions*.

Sutiyono, S., 1995, Magnetic resonance image log use in evaluation of low resistivity pay in the Attaka field, paper IPA95-2.2-056, in *24th Annual Indonesian Petroleum Association Convention Proceedings*, v. 2, Jakarta, 13 p.

Tariq, S.M., Denoo, S., and Cordes, M., 1997, Permeability estimation from modern NMR logging measurements; experiences and applications in the Rocky Mountain area, SPE 38378, *1997 SPE Rocky Mountain Regional Meeting/Geological Association Field Conference Proceedings*.

Vinegar, H., 1995, NMR log interpretation with examples, chapter 8, in Georgi, D.T., ed., Nuclear magnetic resonance logging short course notes, 36th annual SPWLA logging symposium, variously paginated.

Walsgrove, T., et al., 1997, Integration of nuclear magnetic core analysis and nuclear magnetic resonance logs—an example from the North Sea, paper UU, *38th Annual SPWLA Logging Symposium Transactions*, 12 p. A similar paper also published in 1997 as Basan, P. Lowden, B., and Stromberg, S., Developing strategies using core analysis for calibrating the NMR log, *DiaLog* (London Petrophysical Society Newsletter), v. 5, no. 6, p. 4–6.

Warrilow, I.M., et al., 1997, Nuclear magnetic resonance—a useful complement to reservoir characterization of Brunei deltaic sequences, SPE 38025, *1997 SPE Asia Pacific Oil and Gas Conference Proceedings*, p. 91–98.

White, J., and Bedford, J., 1997, Nuclear magnetic resonance applications in the North Sea, *DiaLog* (London Petrophysical Society Newsletter), v. 5, no. 6, p. 6–8.

White, J., 1997, Application of downhole magnetic resonance imaging in the North Sea, SPE 38551, 12 p.

Widjanarko, W., 1996, Integrating nuclear magnetic resonance logging data with traditional down hole petrophysical data to optimize new development wells strategies in the Bravo field offshore north west Java, paper IPA96-2-2-162, *25th Annual Indonesian Petroleum Association Convention Proceedings*, v. 2, p. 205–213.

Xiao, L.Z., 1998, *NMR Imaging Logging Principles and Applications* (in Chinese), Science Press, Beijing, 328 p.

Chapter 8

MRIL Job Planning

Previous chapters have shown that, in most reservoirs, NMR logging data offer an improved method, which can be used independently or in combination with conventional logging data, to determine reservoir properties. In some complex environments (e.g. mixed-lithology reservoirs, low-resistivity/low-contrast pay zones, low-porosity/low-permeability formations, medium-to-heavy oil reservoirs), where conventional logging tools may fail to unveil important reservoir properties, NMR may be the only technique available to assess them.

Reliable and accurate NMR measurements of these reservoir properties require careful, early job planning. Such planning is critical for the success of the logging run. Specific formation and fluid properties can be utilized to design an acquisition scheme that provides access to yet unknown reservoir characteristics and that optimizes the acquisition process and thus improves the answers derived from the data. If acquisition parameters are not selected properly, answer products may provide properties that differ significantly from the actual reservoir properties, as is demonstrated in **Fig. 8.1.**

The figure shows incremental and cumulative porosity and T_2 spectra from two sets of NMR measurements on the same core-plug. The red curves are results derived from data acquired with insufficient echoes (*NE*), insufficient polarization time (*TW*), overly long echo spacing (*TE*), and poor signal-to-noise ratio (*S/N*). In this case, the T_2 distribution is fairly broad, unimodal, and centered around 30 ms, and the cumulative porosity does not exceed 8 p.u. The blue curves are results obtained from data acquired with increased *NE*, increased *TW*, shortened *TE*, and increased echo-train stacking to improve *S/N*. In this case, the T_2 distribution is bimodal with peaks at 7 and 100 ms, and the cumulative porosity exceeds 18 p.u.

MRIL job planning can be executed in three basic steps:

1. Determine NMR fluid properties ($T_{1,\,bulk}$, $T_{2,\,bulk}$, D_0, and *HI*).
2. Assess expected NMR responses (decay spectrum, polarization, apparent porosity) over the intervals to be logged.
3. Select activation sets and determine appropriate activation parameters (*TW*, *TE*, *NE*).

All aspects of job planning involved in these steps have already been implicitly covered in previous chapters, but will be summarized in this chapter and demonstrated by examples. The first example continues over several main sections of the chapter.

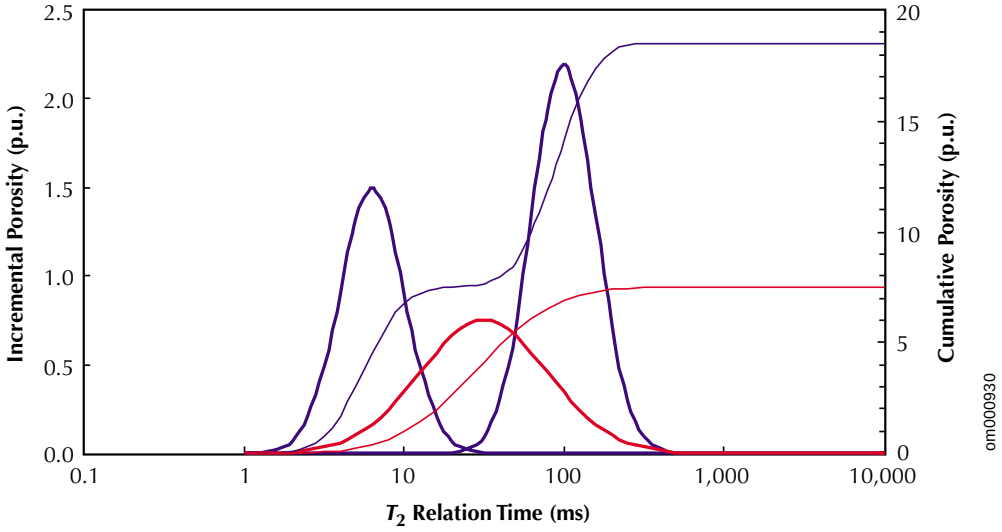

Figure 8.1—Depending on data-acquisition parameters, T_2 spectra can vary significantly. Here, the red curves represent results obtained from data acquired with inadequate acquisition parameters. The blue curves were derived from data acquired with optimized acquisition parameters.

Determining NMR Properties of Reservoir Fluids

The fluid properties that play a prominent role in NMR logging are

- bulk longitudinal relaxation time ($T_{1,B}$)
- unrestricted diffusion, characterized by the coefficient (D_0)
- hydrogen index (HI)

Values of these properties can be obtained from laboratory measurements at simulated in-situ conditions, from measurements made at ambient conditions and extrapolated to reservoir conditions, or from global correlations (available as charts or empirical equations).[1–9] The bulk longitudinal relaxation time, diffusion coefficient, and hydrogen index can be parameterized through the empirical equations listed in **Table 8.1**.

Table 8.1—NMR Fluid Properties

	Bulk Relaxation Time $T_{1,B}$, $T_{2,B}$ (s)	Diffusion Coefficient D_0(10^{-5} cm²/s)	Hydrogen Index HI
Water	$\approx 3 \frac{T}{298\ \eta}$	$\approx 1.3 \frac{T}{298\ \eta}$	≈1
Oil	$\approx 2.1 \frac{T}{298\ \eta}$	$\approx 1.3 \frac{T}{298\ \eta}$	≈1
Gas	$\approx 2.5 \times 10^{4} \frac{\rho}{T^{1.17}}$	$\approx 8.5 \times 10^{-2} \frac{T^{0.9}}{\rho}$	2.25ρ

In these equations, T is the reservoir temperature in degrees Kelvin, η is the viscosity at reservoir conditions in cp, and ρ is the in-situ gas density in g/cm^3. The gas density can be derived directly from PVT data measured in the well, can be calculated after solving the equation of state,[10] or can be read directly from the chart in **Fig. 8.2**.[1] The oil viscosity can be measured, obtained from other work in the area, or roughly estimated from tables and other information about the oil.[11]

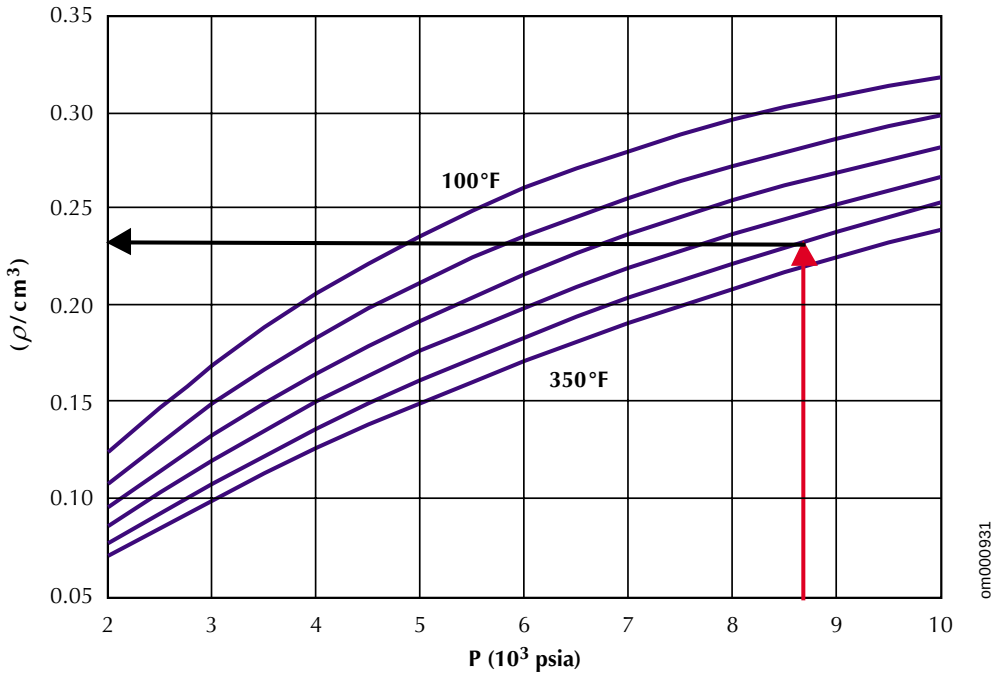

Figure 8.2—Each blue curve relates the density ρ of natural gas ($C_{1.1}H_{4.2}$) to the pressure of the gas at a specific temperature. Temperature increases from the top curve to the bottom curve in 50°F increments from 100 to 350°F. The arrows indicate ρ = 0.23 g/cm^3 at 8,700 psi and 300°F.

Example 1: OBM, Gas

Well Description

An NMR job was planned for a gas well drilled with oil-based mud (OBM). The well had reached its target depth of 20,000 ft, and maximum bottomhole temperature and pressure were 8,700 psi and 300°F, respectively.

Example 1, Step 1: Determine NMR Fluid Properties

The density of the gas at reservoir conditions is read from Fig. 8.2. In particular, the intersection of the isobar at 8,700 psi (red arrow) and the density curve for 300°F indicates a gas density of 0.23 g/cm^3 (black arrow).

The temperature is converted from degrees Fahrenheit to degrees Kelvin:

$$T(K) = \tfrac{5}{9}\left[T(F) - 32\right] + 273 = \tfrac{5}{9}(300 - 32) + 273 = 422\,K$$

The gas properties are calculated using the equations from Table 8.1:

$$T_{1,\text{gas}} = 2.5\times 10^{4}\ \frac{\rho}{T^{1.17}} = 2.5\times 10^{4}\ \frac{0.23}{422^{1.17}} = 4.9\ \ (s)$$

$$D_{0,gas} = 8.5\times 10^{-2}\ \frac{T^{0.9}}{\rho} = 8.5\times 10^{-2}\ \frac{422^{0.9}}{0.23} = 85\times 10^{-5}\ \ (cm^2/s)$$

$$HI_{gas} = 2.25\,\rho = 2.25\times 0.23 = 0.52$$

Extrapolation of the laboratory-measured OBM-filtrate properties to reservoir conditions yields

$$T_{1,mf} = 1.1\ \ (s)$$

$$D_{0,mf} = 2.5\times 10^{-5}\ \ (cm^2/s)$$

$$HI_{mf} = 1$$

For many drilling muds, the service companies can supply these numbers. Otherwise, they must be obtained from laboratory measurements.

Formation-water properties under these conditions (i.e., inside the pores) are estimated:

$$T_{1,w} < 1\ \ (s)$$

$$D_{0,w} = 1\times 10^{-5}\ \ (cm^2/s)$$

$$HI_{w} = 1$$

Assessing the Expected Decay Spectrum of Reservoir Fluids in a Formation

The T_2 spectrum for a combined water-oil-gas system in a formation is a sum of the spectra from the three fluid phases. Gas is always a non-wetting fluid[11] and decays as a single exponential with a relaxation rate (or decay constant) given by

$$\frac{1}{T_{2,g}} = \frac{1}{T_{2,g,\text{bulk}}} + \frac{D_g\ (\gamma\ G\ TE)^2}{12} \qquad (8.1)$$

where $T_{2,g}$ is the bulk T_2 for gas, D_g is the self-diffusion coefficient (which for the purposes of job planning can be assigned its unrestricted value), γ the gyromagnetic ratio, G the magnetic field gradient to which the molecule is exposed, and TE is the echo spacing used in the

CPMG-sequence. To a first approximation, G is the logging-tool gradient (neglecting the internal magnetic field gradients of the formation).

Because most reservoirs are generally considered to be water-wet, the oil relaxation follows directly from the oil bulk relaxation and diffusion effects. Most crude oils are a mixture of different alkanes, each having its own characteristic relaxation rate $(T_{2,o})_i$ given by

$$\left[\frac{1}{T_{2,o}}\right]_i = \left[\frac{1}{T_{2,o,bulk}}\right]_i + \frac{D_o(\gamma GTE)^2}{12} \qquad (8.2)$$

The oil signal is a superposition of all these individual contributions, which form a relaxation spectrum. Diffusion has more impact on the lighter alkanes (at the long-T_2 end of the relaxation spectrum) than on the heavier (more viscous) components, causing a shift to shorter T_2 values and a squeezing (narrowing) of the spectrum. The oil spectrum in a gradient field can be approximated by a unimodal distribution centered around $T_{2,o}$:

$$\frac{1}{T_{2,o}} = \frac{1}{T_{2,o,bulk}} + \frac{D_o(\gamma GTE)^2}{12} \qquad (8.3)$$

$T_{2,o,\text{bulk}}$ is calculated from the formula in Table 8.1. Note that for non-wetting fluids, T_1 and T_2 are the same in the absence of a gradient.

The part of the relaxation spectrum that comes from the formation water is composed of multiple terms, which reflect the range of pore sizes. Each individual term has a relaxation rate given by

$$\left[\frac{1}{T_{2,w}}\right]_i = \frac{1}{T_{2,w,bulk}} + \left[\rho_2 \frac{S}{V}\right]_i + \frac{D_w(\gamma GTE)^2}{12} \qquad (8.4a)$$

$$\left[\frac{1}{T_{1,w}}\right]_i = \frac{1}{T_{1,w,bulk}} + \left[\rho_1 \frac{S}{V}\right]_i \qquad (8.4b)$$

$T_{w,\text{bulk}}$ is obtained from Table 8.1, S/V is the surface-to-volume ratio for a given pore class, and ρ is the surface relaxivity. In general, ρ_1 and ρ_2 are different. Measurements of T_1 and T_2 decay spectra on a sample of 105 rocks resulted in an average T_1/T_2 of 1.65.[12] The measurements were made with zero external field gradient and TE = 0.16 ms.

Example 1, Step 2a: Assess Expected NMR Response (T_2 Distribution)

The fluid properties derived in the first step of this example are substituted into Eqs. 8.1 to 8.3 to compute the T_2 relaxation spectra shown in **Fig. 8.3**. The formation water properties are for a generic clean sandstone with a broad pore-size distribution and high permeability. In many cases only a crude idea of the rock properties is necessary for job planning. The computations are based on a magnetic field gradient of 18 gauss/cm; the echo spacings TE are indicated in the figures.

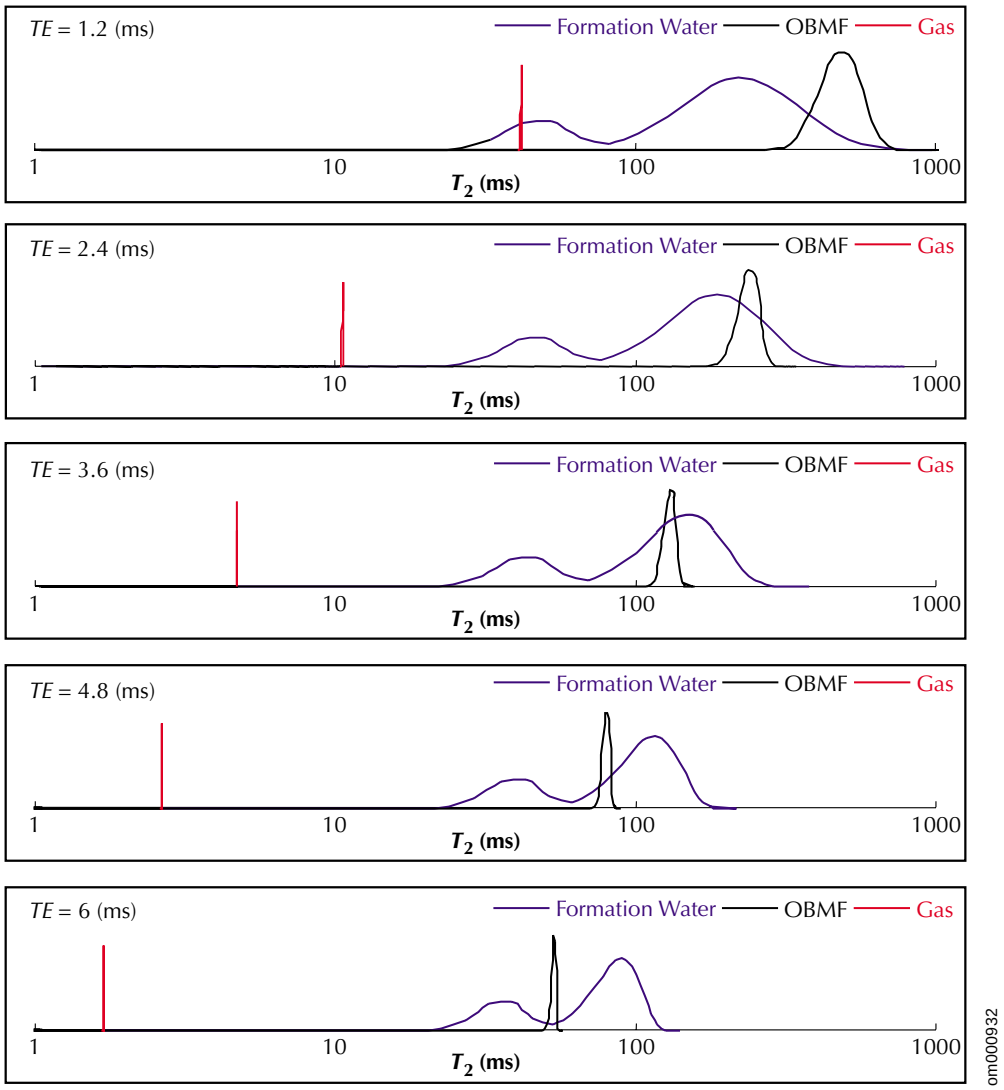

Figure 8.3—Increasing echo spacing *TE* separates fluids with different diffusivity in the T_2 domain. Notice the squeezing (narrowing) of the spectra at increased values of *TE*.

All the fluid properties overlap at the standard *TE* value of 1.2 ms. Increasing *TE* segregates the NMR signal and the individual components can be distinguished. Variation of *TE* can be used to control the appearance of the different components in the T_2 domain, provided sufficient diffusivity contrast exists. This approach forms the basis for the shifted spectrum method (SSM) for identification of fluids.

Assessing the Expected NMR Apparent Porosity of a Formation

The recorded NMR signals respond to all fluids that contain hydrogen atoms and are located inside the sensitive volume. Based on the theory presented in Chapter 3, the signal amplitude (or apparent porosity) measured at a given polarization time *TW* is the sum of the apparent porosity of water $\phi_{w,app}$, oil $\phi_{o,app}$, and gas $\phi_{g,app}$. The apparent porosity for each individual fluid is product of the total porosity ϕ, the fluid saturation *S*, the hydrogen index *HI* of the fluid,

and the fraction of the fluid's hydrogen nuclei that are polarized during the time *TW* between CPMG sequences. For gas,

$$\phi_{g,app} = \phi\, S_g\, HI_g \left(1 - e^{-TW/T_{1,g}}\right) \tag{8.5}$$

For both oil and water, the NMR response is multi-exponential, so the correction term for polarization is more complicated. Most crude oils are a mixture of different alkanes, and the recorded amplitudes reflect differences in hydrogen index and T_1 values:

$$\phi_{o,app} = \phi \sum \left[S_{o,i}\, HI_{o,i} \left(1 - e^{-TW/T_{1,o,i}}\right) \right] \tag{8.6}$$

Similarly, the recorded water-amplitudes reflect differences in T_1 values associated with different pore sizes:

$$\phi_{w,app} = HI_w \sum \left[\phi_i\, S_{w,i} \left(1 - e^{-TW/T_{1,w,i}}\right) \right] \tag{8.7}$$

In most cases though, by choosing *TW* to be 3 times the largest T_1 value associated with the oil and water, the polarization term will be close to unity. In addition, a good approximation is obtained by taking the hydrogen indices of oil and formation water to be unity, in which case the apparent porosity probed by the tool becomes

$$\phi_{app} = \phi \left[S_w + S_o + S_g\, HI_g \left(1 - e^{-TW/T_{1,g}}\right) \right] \tag{8.8}$$

Example 1, Step 2b: Assess Expected NMR Response (Apparent Porosity).

The T_1 values found in Step 1 for water, filtrate and gas are used in Eqs. 8.5 to 8.7 to compute the relative amplitude of polarization as a function of *TW*, shown in **Fig. 8.4**. The T_1 contrast of the fluids in this reservoir offers the possibility to control their contributions to

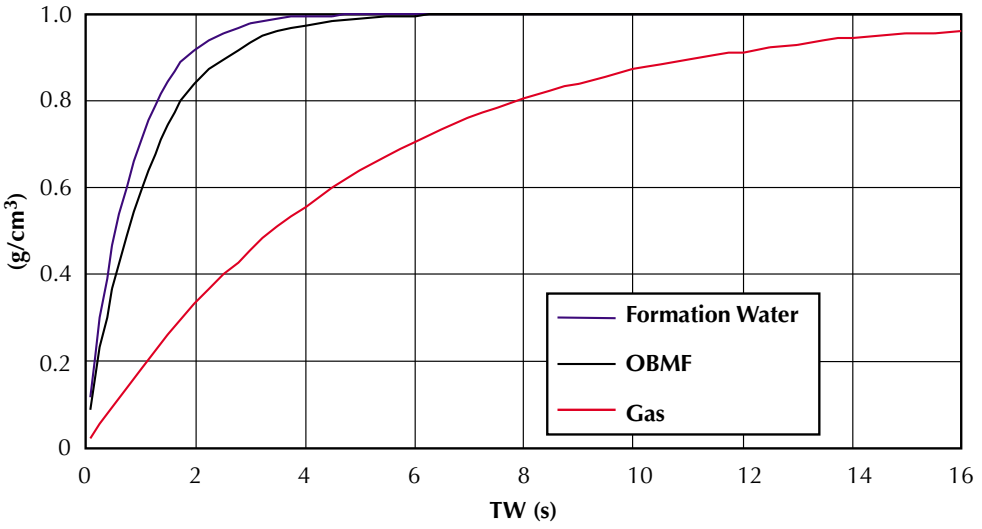

Figure 8.4—In the well of Example 1, the relative amplitude of polarization was calculated as a function of *TW* for different fluids. The following values were used in the calculations: $T_{1,gas}$ = 4.9 s, $T_{1,OBMF}$ = 1.1 s and $T_{1,water}$ < 1 s. Variation of *TW* to control the relative contributions of individual components to the total recorded signal forms the basis of the differential spectrum method (DSM), which enables hydrocarbon typing.

the recorded NMR signal by variation of the polarization time: both the water signal and the OBM-filtrate signal are almost completely (> 95 %) polarized for TW = 3 s. At this value of TW, only 45 % of the gas signal is recovered. Full polarization of the gas signal requires TW > 15 s.

Selection of the Activation Set

An early, clear definition of the logging objectives is essential in MRIL job planning and preparation. Limited objectives for porosity and permeability measurement can be met using standard activations, which allow easy and relatively fast acquisition. Extended objectives for hydrocarbon typing, however, call for advanced activations, which need to be run at reduced logging speed. Estimates of in-situ conditions are required to judge the applicability of the preferred type of activation and to optimize the acquisition parameters and enhance the value of the outcome.

Based on current understanding of NMR physics and the behavior of fluids contained in porous media at elevated pressures and temperatures, three "families" of activations have been developed to cover the full range of major logging objectives, as illustrated in **Fig. 8.5**.

Each activation type serves specific purposes and is optimized to provide data for specific analysis programs. Analysis of this data with a program associated with a different type of activation will have very limited value only and will not achieve the goals of either type.

Standard T_2 Activation

Standard T_2 activations provide data to determine porosity, permeability, and productivity (mobile fluids). (The term standard T_2 activation is sometimes used to refer to only an effective porosity measurement with TE = 1.2 ms). Earlier generations of NMR logging tools

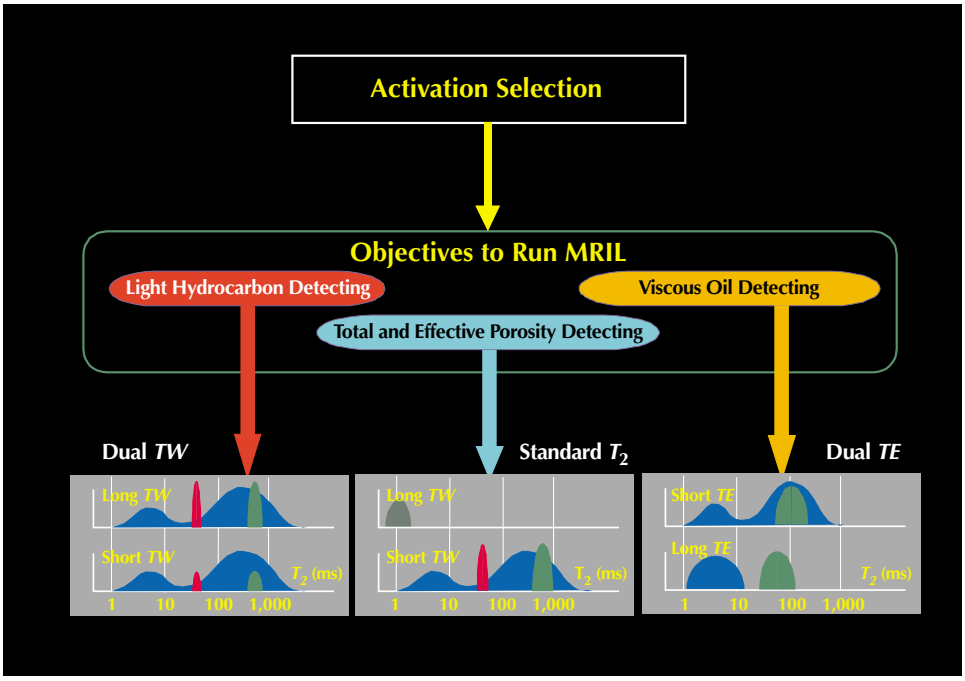

Figure 8.5—Activations are selected according to the objectives of the MRIL job.

operated at single frequencies and only allowed standard T_2 activations. Initial applications were limited to water and medium-to-light-oil zones, but were widened after realization that gas identification was possible with the tool. The standard T_2 activations are still in use with the latest generation multiple-frequency tools and are predominantly applied in situations with almost no D or T_1 contrast. In these situations, advanced, multiple activations are unable to provide extra information. The benefits of standard T_2 acquisition are increased logging speed without degradation of data quality or superior data quality when run at normal speeds.

Dual-*TW* Activation

Dual-*TW* activations provide data to determine porosity, permeability, and productivity (mobile fluids) and to perform direct hydrocarbon typing and quantification using the Differential Spectrum Method (DSM),[1] or Time Domain Analysis (TDA).[2]

Dual-*TW* activations exploit the difference in T_1 values between light hydrocarbons and water, enabling quantitative determination of these fluids. Several factors restrict logging speeds: use of a long *TW* in one acquisition channel, small signal amplitudes associated with the short *TW* values in the other channel, and the need for high-quality data to have acceptable *S/N* levels in the differential signals.

Dual-*TE* Activation

Dual-*TE* activations provide data to determine porosity, permeability, and productivity (mobile fluids,) and to perform direct hydrocarbon typing through the Shifted Spectrum Method (SSM), Diffusion Analysis (DIFAN), or the Enhanced Diffusion Method (EDM).[3]

Wide variations in the diffusivity of viscous oils, water, and light hydrocarbons are exploited in dual-*TE* activations, which aim at separating the various fluids in the T_2 domain. Initial applications were limited to gas- and light-oil reservoirs and provided fluid discrimination (typing) only. However, successful quantitative applications in all types of reservoirs have been reported recently, mainly because of enhanced interpretation methods. This activation also requires slower logging speeds to acquire high *S/N* data.

Determination of the Activation Set and Acquisition Parameters

The previous sections have discussed all the ingredients needed to design an activation. In this section, the discussion assumes that the reservoir and fluid NMR properties have been estimated, that the logging objectives are clear, and that the general type of activation (standard T_2, dual *TW*, or dual *TE*) has been chosen. Based on this information, an outline is presented to determine the optimal activation/acquisition parameters.

The pre-programmed activation that comes closest to this established ideal activation should be selected and run. If none of the available activations fits the purpose, a custom activation may need to be developed based on job planning and on duty-cycle limitations.

If some or all of the relevant formation and fluid properties are unknown, a robust acquisition program can still be designed that meets the initial objectives by using conservative estimates for the unknown parameters. The only disadvantage of this approach is that the resulting activations may require long acquisition times which could possibly have been reduced substantially had more formation and fluid information been available.

Standard T_2 Activations

The MRIL-B and MRIL-C tools were not capable of capturing the very fast, early echo decay induced by water associated with clays and very small pore systems. Hence the measured porosity values correspond to an effective porosity. Current NMR tools now capture this early decay and measure total porosity.

A standard T_2 activation is the default activation on MRIL-C/TP and MRIL-Prime tools. With this activation, a rapid, single-frequency, partial-recovery sequence is repeated 50 times and the stacked echo-data are transmitted to surface. Integration of this data with standard T_2 data yields total-porosity. The default characteristics of this rapid partial recovery sequence are TE = 0.6 ms, TW = 20 ms, and NE = 10.

The rest of the standard activation uses TE values of 1.2 ms and 0.9 ms for the for 6-in. and 4 $^7/_8$-in. sonde, respectively. The different TE values are used to compensate for the differences in the (mean) magnetic field gradient between the sondes (15.6 and 20.0 gauss/cm for large and slim sonde respectively) and to keep the product $(TE\ G)$ constant.[13] These TE selections ensure identical apparent T_2 decay times when measured with either sonde.

As shown in Fig. 8.6, full polarization requires, theoretically, infinitely long TW. For practical applications, polarization levels exceeding 95 % are used. As the following equation demonstrates, this polarization is achieved when $TW \geq 3T_1$.

$$1 - e^{-TW/T_1} \geq 0.95 \Rightarrow TW \geq 3\,T_1 \tag{8.9}$$

In gas reservoirs, this requirement may call for TW values much greater than 10 s, which puts serious restrictions on logging speed and/or depth sampling. It can be shown that with standard processing and favorable S/N levels, only relaxation rates up to about three times the measurement time ($NE\ TE$) can be resolved, leading to the condition

$$3\ NE\ TE \geq T_{2,\max} \Rightarrow NE \geq \frac{T_{2,\max}}{3\ TE} \tag{8.10}$$

Assessment of $T_{2,\max}$ for the formation water requires local knowledge. General values of T_2 for oil and gas can be extracted from the chart of **Fig. 8.7**, which was computed using the fluid parameterization presented in Table 8.1 and Eqs. 8.1 and 8.3 with a magnetic field gradient of 18 gauss/cm.

Example 1, Step 3: Determine Appropriate Activation Parameters (TW, TE, NE) for a Standard T_2 Activation.

A standard T_2 activation with TE= 1.2 ms can be selected for this job. When acquiring data with TE = 1.2 ms, the gas and OBM-filtrate signals will appear at 40 and 400 ms, respectively, in the T_2 spectrum (use $T_{1,\text{gas}}$ = 4.9 s and $T_{1,\text{mf}}$ = 1.1 s found in the first step of this example). Local knowledge gives $T_{1,\text{water}} \approx 1$ s and $T_{2,\text{water}} \approx 400$ ms.

The appropriate number of echoes must be

$$\text{NE} \geq \frac{400}{3 \times 1.2} \geq 110$$

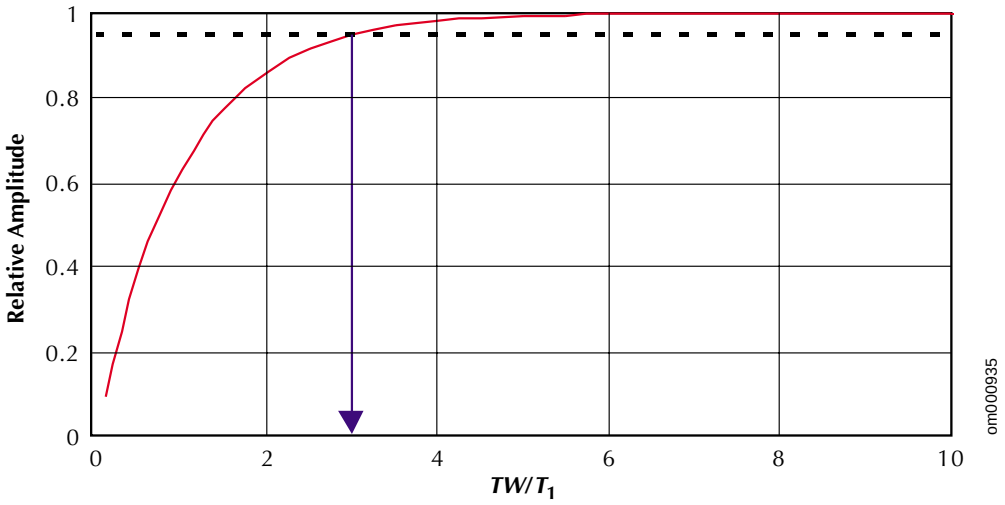

Figure 8.6—Relative amplitude of polarization is a function of TW/T_1. For practical purposes, full polarization is achieved when $TW \geq 3T_1$.

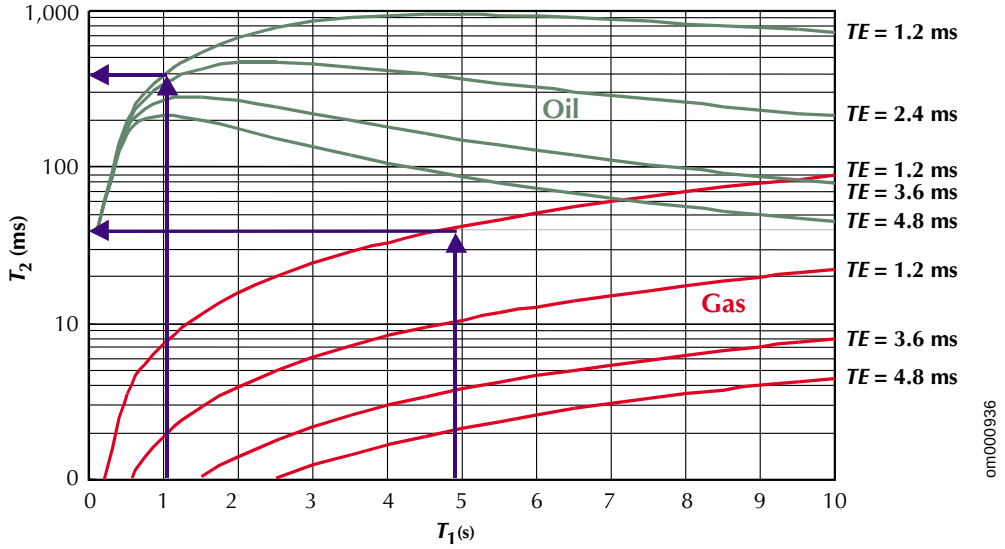

Figure 8.7—T_2 relaxation of oil and gas seen by NMR-tool with a magnetic field gradient of 18 gauss/cm as a function of the bulk T_1 relaxation time.

Determination of *TW* depends on the objectives of the logging run. If the gas signal must be recovered completely, *TW* must be greater than 3×4.9 ≈ 15 s. If only the water and OBM-filtrate signals must be recovered completely, then *TW* = 3 s is sufficient.

Dual-*TW* Activations

To run a dual-*TW* activation, TW_L, TW_S, *TE*, and *NE* must be specified.

If the water is assumed to be completely polarized, then ϕ_a is given by

$$\phi_a = \phi \{S_w + S_{hc}\ HI_{hc}(1 - e^{-TW/T_{1,hc}})\} \qquad (8.11)$$

Equation 8.12 defines constants a, b, and c

$$\begin{aligned} TW_S &= a\, T_{1,w} \\ TW_L &= b\, TW_S = a\, b\, T_{1,w} \\ T_{1,hc} &= c\, T_{1,w} \\ (a \geq 1,\ b \geq 1,\ c \geq 1) \end{aligned} \qquad (8.12)$$

Combining Eqs. 8.11 and 8.12 yields the apparent porosity measured at long- and short-wait times:

$$\begin{aligned} \phi_{a,L} &= \phi\ \{S_w + S_{hc}\ HI_{hc}(1 - e^{-a\,b/c})\} \\ \phi_{a,S} &= \phi\ \{S_w + S_{hc}\ HI_{hc}(1 - e^{-a/c})\} \end{aligned} \qquad (8.13)$$

The differential signal, $\Delta\phi$, follows directly from subtracting the short TW signal from the long TW.

To eliminate the response associated with the formation water from the differential signal, the water must be completely polarized at both short and long wait times. This condition is met when $TW_L \approx TW_S \approx 3 \times T_{1,water}$, or when $a \geq 3$. ($T_{1,water}$) is the longest T_1 associated with the pore water.)

$$\Delta\phi = \phi\ \{S_{hc}\ HI_{hc}(e^{-a/c} - e^{-a\,b/c})\} \qquad (8.14)$$

For any given value of a greater than 3, the fraction of the full hydrocarbon signal residing in the differential signal is a function of the dimensionless parameters b and c only, i.e. a function of the ratio TW_L to TW_S and the ratio $T_{1,hc}$ to $T_{1,w}$, which is the T_1 contrast between formation water and the hydrocarbon. This function is visualized in **Fig. 8.8** for a = 3.

Example 1, Step 3: Determine Appropriate Activation Parameters (TW_L, TW_S, TE, NE) for a Dual-TW Activation.

A dual-TW activation may also be selected for this example. Relevant T_1 relaxation times for this particular well are $T_{1,gas}$ = 4.9 s, $T_{1,mf}$ = 1.1 s and $T_{1,\ water} \approx$ 1 s (see Step 1 of this example), indicating a gas-water T_1 contrast c = 4.9. Entering the chart in Fig. 8.8 at this contrast indicates that the maximum fraction of the gas signal can be in the 0.5 to 0.6 range; the arrows indicate how the most favorable ratio TW_L / TW_S of 5.5 is determined. That is 5.5 results in the smallest value of TW_L which results in a fractional gas signal in the 0.5 to 0.6 range. Adequate TW values are thus

$$\begin{aligned} TW_S &= 3\ T_{1,\ water} = 3 \text{ s} \\ TW_L &= 5.5\ TW_S = 16.5 \text{ s} \end{aligned}$$

In the Step 2 of this example, the formation water signals were found to span the T_2 spectrum up to 400 ms, and the gas signal was expected to appear at 40 ms. The maximum relaxation time to be resolved is 400 ms, which requires at least 400/(1.2 x 3) = 110 echoes.

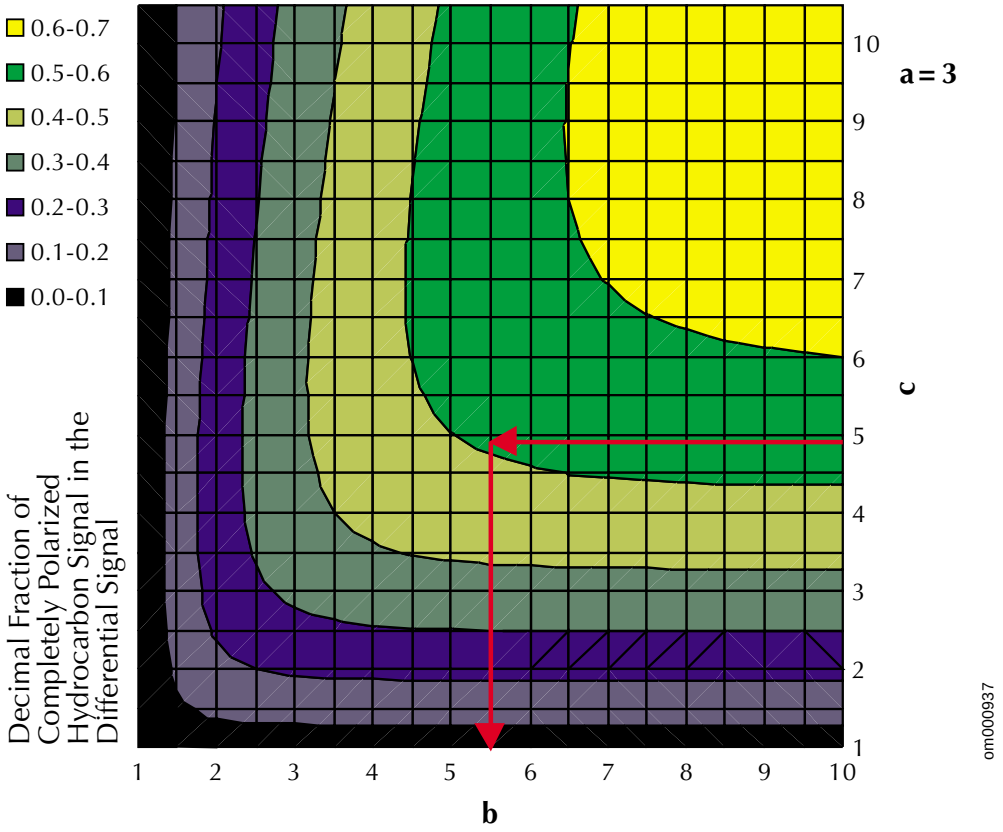

Figure 8.8—The fraction of the completely polarized hydrocarbon signal in the differential signal is a function of the long-to-short *TW* ratio (b) and of the hydrocarbon-water T_1 contrast (c). The short *TW* is three times the longest T_1 of the formation water (i.e., a = 3) to ensure at least 95% polarization of formation water.

The parameters for the dual-*TW* activation are thus

Activation 1:	TE = 1.2 ms	N = 110	TW_L = 16.5 s
Activation 2:	TE = 1.2ms	N = 110	TW_S = 3 s

This dual-*TW* activation maximizes the differential gas signal, but actual values of porosity, hydrocarbon saturation in the sensitive volume, and hydrogen index at in-situ conditions determine whether this signal is sufficiently large to be detected at all.

Average net porosity in this well is about 14 p.u., the invaded-zone gas saturation is assumed at the residual level of 30%, and the hydrogen index of gas is 0.52 (see Step 1 of this example). Substituting these values into Eq. 8.14 gives

$$\Delta\phi = 14 \times 0.3 \times 0.52 \left(e^{-3/4.9} - e^{-16.5/4.9} \right) = 2.2 \times 0.51 = 1.1 \ \ p.u.$$

This signal level is just above the detection limit for this technique and will appear at 40 ms in the differential spectrum.

The whole process can be repeated to demonstrate that this dual-*TW* activation also effectively removes the flushed zone mud-filtrate signal ($T_{1,\,obmf}$ = 1.1 s) from the differential spectrum. When the filtrate T_1 increases, the outlined approach requires minor modification

to determine the filtrate signal. The T_1 contrast between gas and OBM filtrate must be evaluated to plan suitable *TW* values. This evaluation is demonstrated in Example 2.

Example 2: OBM, Dual *TW*

Well Description

An NMR job was planned for a well with the same reservoir properties as Example 1, but with different properties of the OBM filtrate. As in Example 1, the well was a gas well, had been drilled with OBM, had reached its target depth of 20,000 ft, and had maximum bottomhole temperature and pressure of 8,700 psi and 300°F, respectively.

Step 1: Determine NMR Fluid Properties.

Gas and formation water properties are the same as the previous example. Also as in the previous example, properties of the OBM filtrate were measured in the laboratory and extrapolated to reservoir conditions. The pertinent gas, OBM filtrate, and formation-water properties determined thus far are summarized in the first three data columns of **Table 8.2**.

Table 8.2 —Example 2: NMR Fluid Properties at Reservoir Conditions

	T_1 (s)	D_0 (cm²/s)	*HI*	T_{2D} (ms)
Gas	4.9	85 x 10^{-5}	0.52	40
OBM-filtrate	2.5	2 x 10^{-5}	1	800
Formation Water	< 1	1 x 10^{-5}	1	< 400

Step 2: Assess Expected NMR Response.

The tabulated T_1 relaxation times are used in Eqs. 8.5 to 8.7 to compute the polarization as a function of *TW*, shown in **Fig. 8.9**. The graph shows that full polarization of the formation water, filtrate, and gas requires *TW* values of 3, 8, and 15 s, respectively. The T_2 values logged by an MRIL tool with a magnetic field gradient of 18 gauss/cm and an echo spacing of 1.2 ms, are determined from Fig. 8.7 and are tabulated under T_{2D} in Table 8.2.

Step 3: Determine Appropriate Activation Parameters (TW_L, TW_S, *TE*, *NE*) for a Dual-*TW* Activation.

Complete elimination of the formation-water and mud-filtrate signals from the differential spectrum requires full polarization of both signals, imposing $TW_L > TW_S > 8$ s. The critical ratio in this example is not the T_1 contrast between gas and water (i.e., $c = 4.9$), but instead the T_1 contrast between gas and OBM filtrate (i.e., $c = 2$). Entering the chart in Fig. 8.8 at this low contrast indicates that the fraction of the gas signal will not exceed the 0.2 to 0.3 range, and the most suitable wait-time ratio TW_L/TW_S is 3.5. Thus, adequate *TW* values are

$TW_S = 3\ T_{1,\,OBMF} = 8$ s

$TW_L = 3.5\ TW_S = 28$ s

Table 8.2 indicates that the longest T_2 time logged in this well is 800 ms (OBM filtrate); the number of echoes required to resolve this signal is at least 800/(1.2 x 3) = 220.

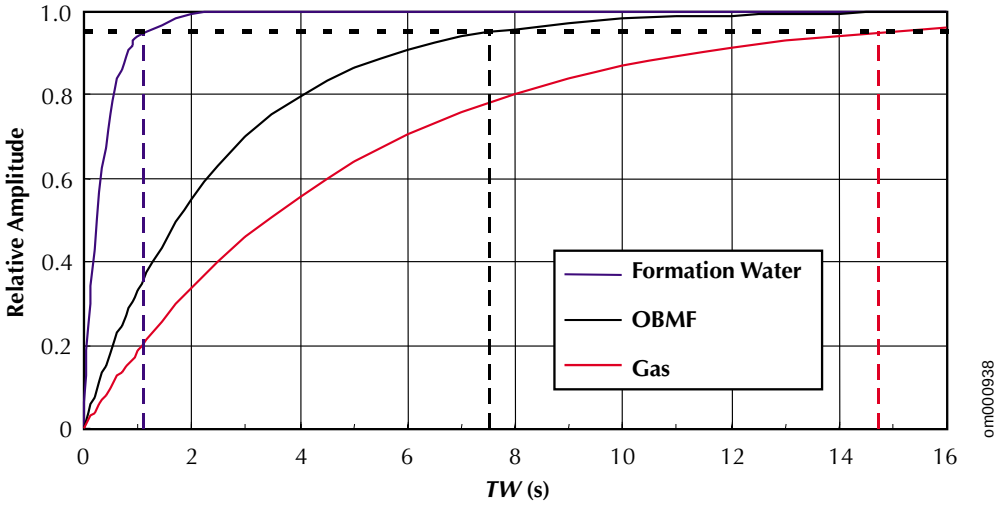

Figure 8.9—In the well of Example 2, the relative amplitude of polarization was calculated as a function of *TW* for the gas, OBM filtrate, and formation water. T_1 values from Table 8.2 were used in the calculations.

The dual-*TW* activation parameters are thus

Activation 1:	TE = 1.2 ms	N = 220	TW_L = 28 s
Activation 2:	TE = 1.2 ms	N = 220	TW_S = 8 s

The magnitude of the differential gas signal is calculated similarly to the previous example:

$$\Delta\phi = 14\times 0.3\times 0.52\left(e^{8/4.9} - e^{-28/4.9}\right) = 2.2\times 0.19 = 0.42 \quad p.u.$$

This signal is well below the detection limit, and the proposed acquisition method is not feasible. Also the very long *TW* required in this proposed acquisition is not practical: extremely low logging speeds and poor spatial resolution are immediate consequences.

Under the given conditions, an alternative approach, which eliminates the water signal and leaves a significant fraction of both gas and the OBM filtrate in the differential signal, is feasible. Entering Fig. 8.8 at the gas and water T_1 contrast of $c \cup 5$ suggests that a TW_L/TW_S ratio of 5 to 6; suitable *TW* values are 1.5 and 8 s, respectively. The modeled response in **Fig. 8.10** shows a clear separation in the T_2 domain between gas and OBM filtrate signal, facilitating independent quantification. The amplitude of the gas component is calculated as

$$\Delta\phi = 14\times 0.3\times 0.52\left(e^{-1.5/4.9} - e^{-8/4.9}\right) = 2.2\times 0.54 = 1.2 \quad p.u.$$

The amplitude of the OBM-filtrate component is calculated as

$$\Delta\phi = 14\times 0.3\left(e^{-1.5/2.5} - e^{-8/2.5}\right) = 4.2\times 0.51 = 2.1 \quad p.u.$$

The suggested dual-*TW* activation parameters are now

Activation 1:	TE = 1.2 ms	N = 220	TW_L = 8 s
Activation 2:	TE = 1.2 ms	N = 220	TW_S = 1.5 s

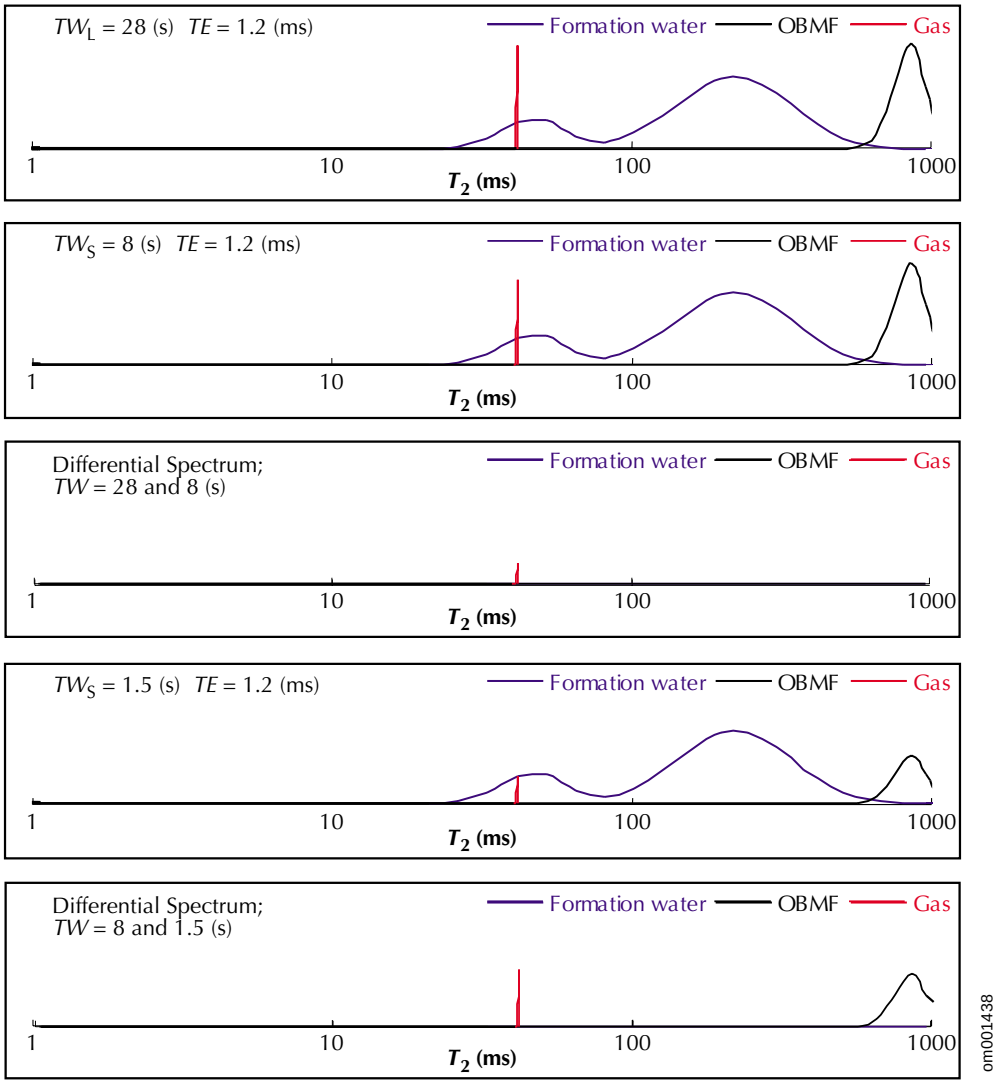

Figure 8.10—In Example 2, dual-*TW* acquisition with a TW_L/TW_S ratio of 28/8 (top three panels) eliminates the formation-water and mud-filtrate signals from the differential spectrum and maximizes the differential gas signal. However, the differential signals are small, and because of the long acquisition time, logging speeds are very slow. Alternatively, dual-*TW* acquisition with TW_L/TW_S ratio of 8/1.5 (bottom two panels) eliminates only the formation water from the differential spectrum, but the gas and OBM-filtrate signals are sufficiently separated in T_2 space to enable independent quantification.

Dual-*TE* Activations

To run a dual-*TE* activation, TE_L, TE_S, *TW*, and *NE* must be specified.

The marginal T_1 contrast between the OBM filtrate and the natural gas in Example 2 hindered differentiation of these fluids through the dual-*TW* method. However, the large separation of the gas and mud filtrate signals in the T_2 domain, a reflection of the significant diffusivity contrast in diffusivity between the two fluids, enabled quantitative determination of the fluid volumes. More generally, if the diffusivity contrast is not sufficient to establish differentiation in the spectral domain when the data have been acquired under standard conditions, then the apparent contrast can be enhanced by acquiring data at increased *TE* (see Fig. 8.3).

Example 3: WBM, Viscous Oil, Dual *TE*

Well Description

A well was to be drilled with a water-based mud system in a viscous-oil reservoir.

Step 1: Determine NMR Fluid Properties.

The relevant fluid properties are summarized in **Table 8.3**. The NMR properties of the water-based-mud filtrate are identical to those of the formation water. Note that the formation-water T_1 is shorter than its bulk value and is not single-valued but a distribution, reflecting the pore-size distribution of the rock. The T_1 value listed in the table is the logarithmic mean of this T_1 distribution.

Table 8.3—Example 3: NMR Fluid Properties at Reservoir Conditions

	T_1 (s)	D_0 (cm²/s)	*HI*	T_{2D} (ms)
Crude Oil	0.5	0.2×10^{-5}	1	486
Formation Water	< 0.8	1×10^{-5}	1	< 400

Step 2: Assess Expected NMR Response.

The tabulated T_1 relaxation times are used in Eqs. 8.5 to 8.7 to compute the polarization as a function of *TW*, shown in **Fig. 8.11**. The T_2 responses of the individual components are shown in **Fig. 8.12** (where a magnetic field gradient of 18 gauss/cm) for various values of *TE*.

Step 3: Determine Appropriate Activation Parameters (TE_L, TE_S, *TW*, and *NE*) for a Dual-*TE* Activation.

Inspection of Figs. **8.11** and **8.12** already indicates that standard T_2 logs and dual-*TW* logs will not be sufficient to differentiate fluids and to determine volumes. With a standard *TE* = 1.2 ms activation, all fluids present will have comparable T_2 relaxation times (300 to 500 ms). Variation of the *TW* will reduce the WBM-filtrate signal and the oil signal equally, eliminating both from the differential spectrum.

Eqs 8.3 and 8.4 can be used to evaluate the difference in apparent T_2 as a function of *TE* for the "free" water and oil in this well. The results, summarized in Fig. 8.12, indicate complete separation of the oil signal from the water at echo spacings in excess of 4.8 ms because of the

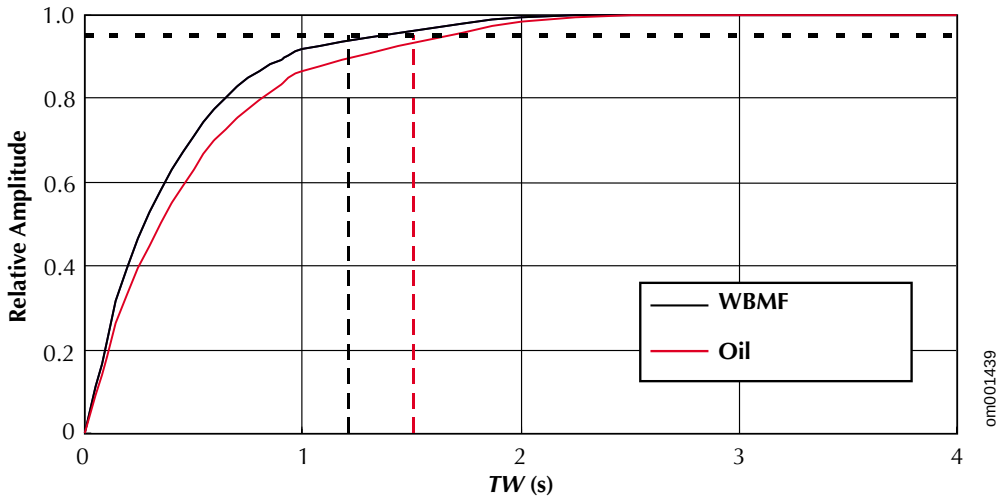

Figure 8.11—In the well of Example 3, the relative amplitude of polarization was calculated as a function of *TW* for the crude oil, water-based mud filtrate, and formation water. T_1 values from Table 8.3 were used in the calculations. The filtrate and formation water share bulk NMR properties, and thus their corresponding curves on this graph are identical.

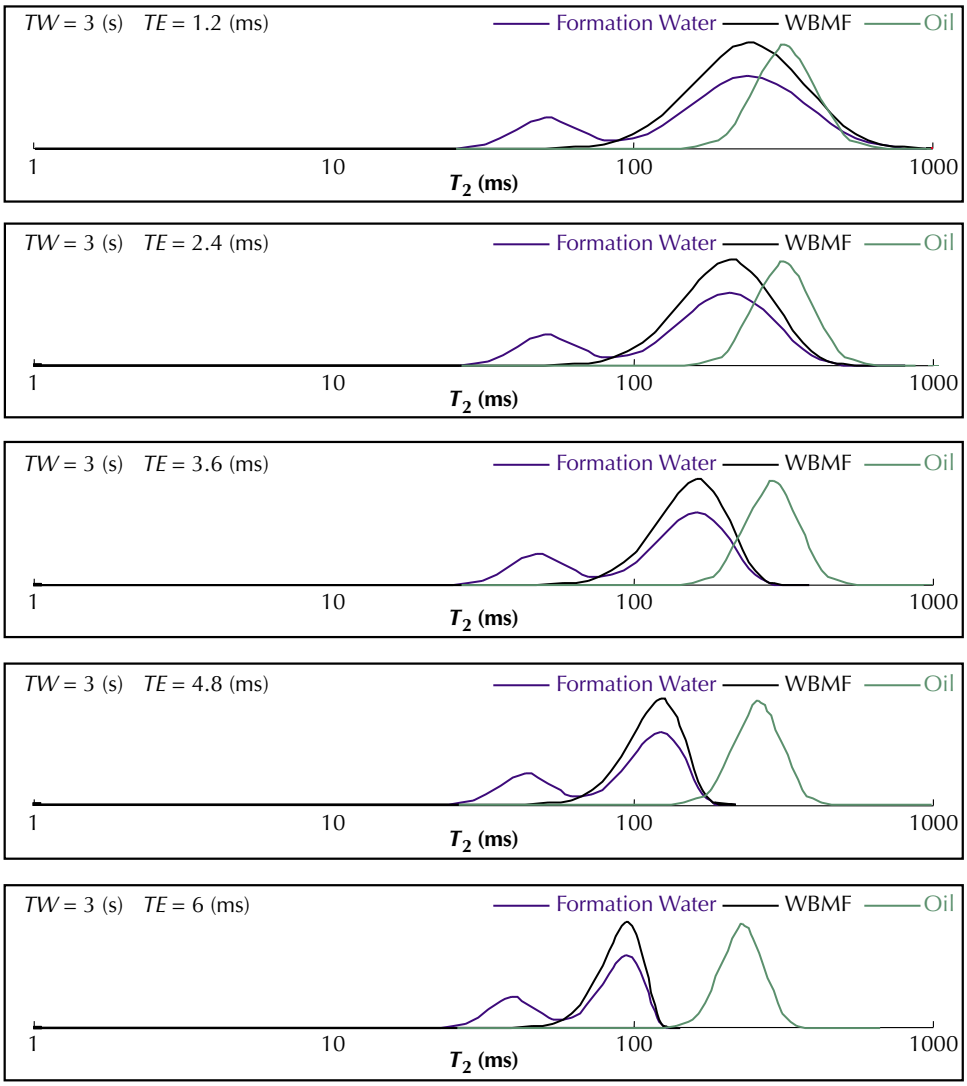

Figure 8.12—In Example 3, the T_2 responses of the formation water, oil, and water-based mud filtrate shift to lower values as *TE* increases. The apparent T_2 of oil "lags" behind the responses of the other two fluids because of the oil's lower diffusivity.

difference in diffusivity between the two fluids. The greater diffusivity of the water compared to the oil induces enhanced shortening of the apparent T_2 response at increasing echo spacing.

Analogous to the previous examples, the appropriate number of echoes to resolve even the slowest components (T_2 ~ 800 ms) with a standard echo-spacing is 800/(1.2 x 3) = 220. Increasing the spacing to 4.8 ms reduces the required number of echoes by the same factor to 220/4 = 55. The suggested dual-*TE* activation parameters are thus

Activation 1:	TE_S = 1.2 ms	*NE* = 220	*TW* = 3 s
Activation 2:	TE_L = 4.8 ms	*NE* = 55	*TW* = 3 s

To run a dual-*TW*, dual-*TE* activation set, TE_L, TE_S, TW_L, TW_S, and *N* must be specified.

Dual-*TW*/Dual-*TE* (Virgin Area Logging)

The previous paragraphs discussed in detail how to set-up the most robust and most time-efficient acquisition schemes in areas where reasonable knowledge of reservoir parameters, fluid properties and in-situ conditions exists. There is no reason, however, to restrict NMR logging, to these areas only. Inclusion of NMR logging in exploration areas should always be considered because it provides lithology-independent porosity readings, permeability estimates, producibility indications, reservoir-fluid types, and hydrocarbon saturation values. The main benefit of having *a priori* knowledge of in-situ conditions is that the acquisition can be tuned to these conditions to the better obtain the specific information required and can possibly be designed to minimize acquisition time.

The three-step approach followed in the previous examples to determine the logging specifications is equally adequate in "virgin areas," where running dual-*TW*, dual-*TE* activations may be the most appropriate course of action. A discussion of the three-step approach as applied to such activations follows.

Step 1: Determine NMR Fluid Properties.

Enter temperature and pressure at reservoir depth in Fig. 8.2 and Table 8.1 to estimate bulk relaxation times, diffusivity, and hydrogen indices for the reservoir fluids (oil, gas, water). (If temperature and pressure are unknown, assume a hydrostatic pressure gradient of 0.433 psi/ft and a temperature gradient of 0.015°F/ft.) Obtain these parameters for the mud filtrate from the supplier or estimate them as appropriate. For job planning purposes in clean sandstones, if no other information is available, the formation-water T_2 distribution can be reasonably assumed to range from approximately 1 ms up to $T_{1,bulk}/2.5$. In shaly reservoirs or in formations that contain paramagnetic impurities, these values can be reduced by a factor of 10. In carbonates, conservative estimates for the water T_2 distribution indicate that the T_2 values range from 1 ms up to $T_{1,bulk}$.

Step 2: Assess Expected NMR Response.

The bulk relaxation times found in Step 1 are subsequently used to calculate the degree of polarization as a function of *TW* to check the feasibility of dual-*TW* data acquisition and to suppress one (or more) components in the differential signal. This step will produce appropriate *TW* values.

Eqs. 8.1 through 8.4 are used to compute mean T_{2D} values for the respective fluids, i.e. the apparent relaxation times as a function of *TE* and for a magnetic field gradient of 18 gauss/cm. These results can be evaluated to check the possibility of separating fluids in the T_2 domain by increasing *TE* (shifted-spectrum approach).

Step 3: Determine Appropriate Activation Parameters (TW_L, TW_S, TE_L, TE_S, NE_L, and NE).

The most suitable polarization times for the dual-*TW*-activation with standard echo spacing (*TE* = 1.2 ms) follow directly from

$TW_S = 3\ T_{1,max}$ of formation water

$TW_L = 3\ T_{1,max}$ of hydrocarbons

The longest T_{2D} value established in Step 2 determines the appropriate amount of echoes for these activations:

$$NE = T_{2D,max}/(3\ TE)$$

To utilize diffusion contrasts, an additional set of activations should be acquired with a longer *TE* (e.g., 4.8 ms) and a corresponding number of echoes. Integrated interpretation of all data thus acquired will reveal both formation and fluid properties.

Example 4: OBM, Gas, Dual *TW, TE*

Well Description

High gas readings were observed while drilling an exploration well in an oil prospect, indicating a small gas-cap. Cuttings showed sandstone and some shale. The well, drilled with an OBM system, reached a depth of 12,000 ft, and no indications of any pressure or temperature anomalies were observed.

Step 1: Determine NMR Fluid Properties.

The temperature and pressure at reservoir depth are estimated at 12,000 x 0.015 = 180°F (355° K) and 12,000 x 0.433 = 5,196 psi, respectively. Extrapolation of the laboratory-measured mud-filtrate properties to reservoir conditions gives

$$T_{1,\,mf} = 1.5 \ \ (s)$$

$$D_{0,\,mf} = 0.92 \times 10^{-5} \ \ \left(cm^2 / s\right)$$

$$HI_{mf} = 1$$

The density of the gas at 180°F and 5,196 psi, read off Fig. 8.2 is 0.21 g/cm^3. The other gas properties are calculated using the equations listed in Table 8.1:

$$T_{1,\mathrm{gas}} = 2.5 \times 10^4 \frac{\rho}{T^{1.17}} = 2.5 \times 10^4 \frac{0.21}{355^{1.17}} = 5.4 \ \ (s)$$

$$D_{0,\,\mathrm{gas}} = 8.5 \times 10^{-2} \frac{T^{0.9}}{\rho} = 8.5 \times 10^{-2} \frac{355^{0.9}}{0.21} = 80 \times 10^{-5} \ \ \left(cm^2 / s\right)$$

$$HI_{\mathrm{gas}} = 2.25\,\rho = 2.25 \times 0.21 = 0.47$$

From experience in the area, the reservoir hydrocarbon liquid is most likely black oil with low gas/oil ratio and with viscosity about 3 cp. With this information, the equations in Table 8.1 provide the water and oil properties:

$$T_{1,\mathrm{oil}} = 3 \frac{T}{298\,\eta} = \frac{3 \times 355}{298 \times 3} = 0.84 \ \ (s)$$

$$D_{0,\,\mathrm{oil}} = 1.3 \frac{T}{298\,\eta} = \frac{3 \times 355}{298 \times 3} = 0.52 \times 10^{-5} \ \ \left(cm^2 / s\right)$$

$$T_{1,\mathrm{water}} = 3 \frac{T}{298\,\eta} = \frac{3 \times 355}{298 \times 1} = 3.6 \ \ (s)$$

$$D_{0,\text{water}} = 1.3\frac{T}{298\eta} = \frac{3\times355}{298\times1} = 1.5\times10^{-5}\ \left(cm^2/s\right)$$

$$HI_{\text{oil}} \approx HI_{\text{water}} \approx 1$$

The NMR fluid properties for this well are summarized as **Table 8.4**.

Table 8.4—Example 4: NMR Fluid Properties at Reservoir Conditions (*TE* = 1.2 ms, *G* = 18 gauss/cm)

	T_1 (s)	D_0 (cm²/s)	*HI*	T_2 (ms)
OBM Filtrate	1.5	0.92 x 10^{-5}	1	500
Gas	5.4	80 x 10^{-5}	0.47	45
Oil	0.84	0.52 x 10^{-5}	1	325
Formation Water	< 1	1.5 x 10^{-5}	1	< 400

Step 2: Assess Expected NMR Response.

The bulk relaxation times established in Step 1 are subsequently used to compute the polarization curves presented in **Fig. 8.13**. Note that surface-relaxivity and pore sizes shorten the formation water T_1 well below its bulk value, and the observed relaxation time is not single-valued but a distribution, reflecting the pore-size distribution of the rock. The T_1 value listed in the table is the logarithmic mean of this T_1 distribution.

Eqs. 8.1 through 8.4 have also been used to compute the typical T_2 responses of these fluids at various *TE* values, shown in **Fig. 8.14**.

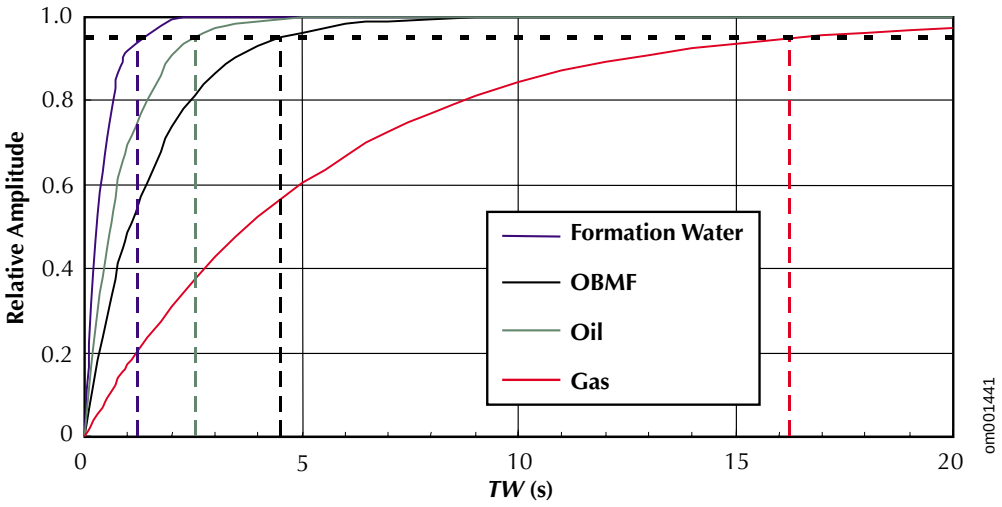

Figure 8.13—In the exploration well of Example 4, the relative amplitude of polarization was calculated as a function of *TW* for the gas, oil, formation water, and OBM filtrate. T_1 values from Table 8.4 were used in the calculations.

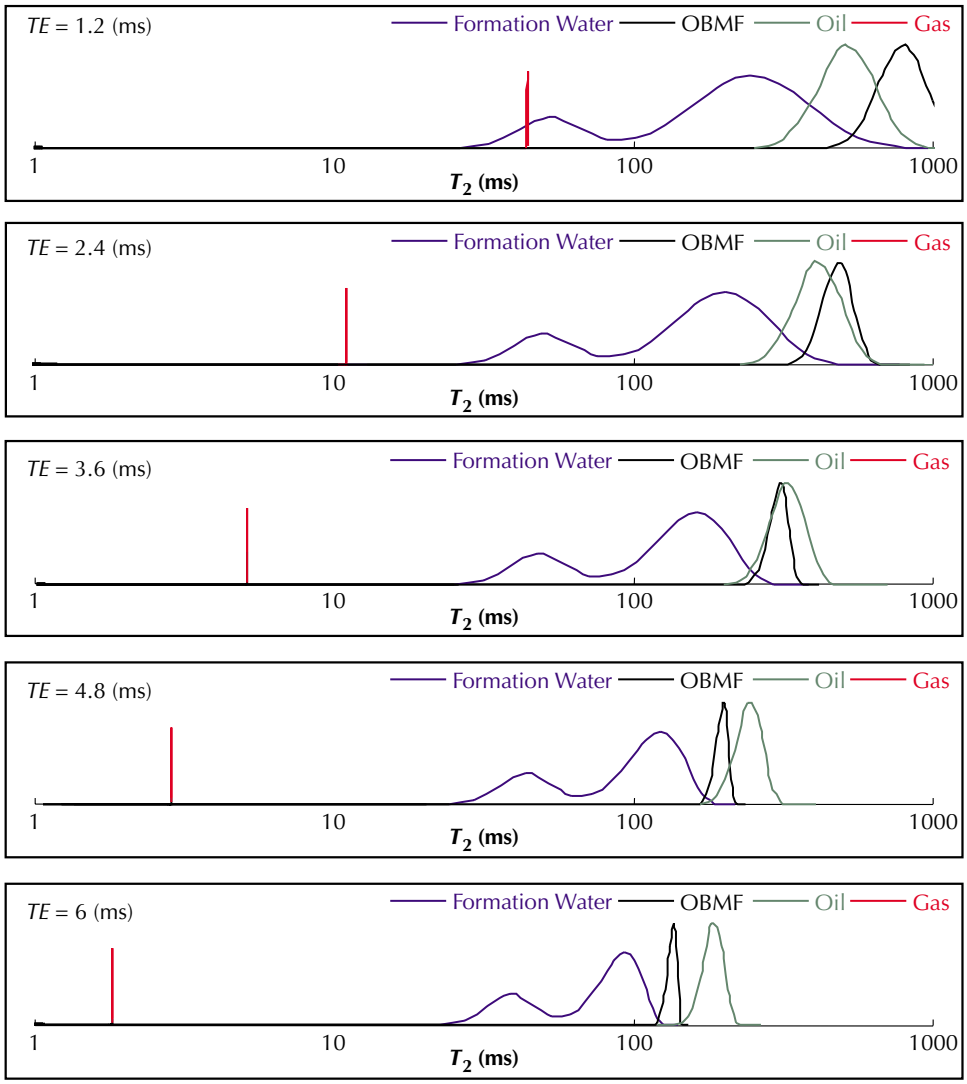

Figure 8.14—These T_2 responses at various TE values were calculated for the formation water, oil, gas, and OBM filtrate from the exploration well of Example 4.

Step 3: Determine Appropriate Activation Parameters (TW_i, TE_i, NE_i).

Inspection of the table and figures computed for the fluids in this exploration well shows that the slowest component relaxes at T_2 = a rate of some 500 ms (OBMF at TE = 1.2 ms). The appropriate number of echoes to resolve even these slow components is

$$NE = 500 / (3 \times 1.2) \approx 133$$

The big T_1 contrast between gas and all other fluids calls for differential spectrum or differential echo analysis (time domain analysis). Adequate TW values are 16 and 5 s.

The NMR properties of the native oil and the OBM filtrate are very similar. Any pair of dual-TW data will reduce both components at about equal rates. Acquiring data TE = 6 ms at TW = 5 s and TW = 1.5 s offers the possibility to eliminate the water signal from this diffusion data, which may simplify the interpretation.

The suggested activation sets for this exploration well are thus

Activation 1:	*TE* = 1.2 ms	*NE* = 300	*TW* = 16 s
Activation 2:	*TE* = 1.2 ms	*NE* = 300	*TW* = 5 s
Activation 3:	*TE* = 6 ms	*NE* = 60	*TW* = 5 s
Activation 4:	*TE* = 6 ms	*NE* = 60	*TW* = 1.5 s

Other Considerations for MRIL Job Planning

In-situ conditions must be considered when drafting the final activations because these conditions will dictate actual polarization times *TW*, echo spacing *TE*, number of echoes *NE*, logging speed, and running average number *RA*. The most critical factors are as follows:

Formation Type (Sandstone, Carbonate, Chalk, Diatomite)

In most cases, formation type has had only a minor impact on the actual acquisition, but it plays an important role in the analysis and interpretation of the data. In general, surface relaxivity ρ_2 in carbonates is weaker than in sandstones, causing slower relaxation rates. Consequently, different T_2 cut-off values must be used to discriminate between bound fluids and movable fluids (Typically, 33 ms in sandstones and 90 ms for carbonates. Note that these values are determined empirically and may not apply in some areas).

Iron-rich formations or, more generally, any formation containing paramagnetic impurities can enhance surface relaxation significantly, shifting the T_2 spectrum to very short relaxation times so that the standard cut-off values do not apply. Depending on the amount of paramagnetic material, relaxation may become too fast to be detected, and the NMR measurement will underestimate porosity.

Relatively large, isolated pores (i.e., pores that are not connected and thus hinder the free flow of fluids) are often encountered in carbonate formations. NMR logs will read correct porosity values, but the routine permeability equations are not appropriate (computed values will be higher than the actual values). Standard permeability models will usually underestimate fracture-enhanced permeability. The potential existence of larger pores and a smaller ρ_1 means that the maximum T_{1w} can be somewhat longer in carbonates than sandstones.

Wettability

In most of the discussions in this book, the rock has been assumed to be water-wet. For the case of gas and water, this is a safe assumption, but for oil and water this may not be the case. In mixed wettability, both oil and water relax by both bulk relaxation and surface interaction. Therefore, both spectra will be complex and will occur at earlier times than the bulk relaxation times. The spectra depend on the ratio of water-wet surface area to water volume and oil-wet surface area to oil volume. In this case, the interpretation of the NMR spectra is difficult and not as well understood as the water-wet case. It is almost certain that a comprehensive interpretation requires multiple *TE* activations. Multiple *TW* activations are not likely to be useful in this case.

Mud Type (Oil-Based, Water-Based)

The quality of NMR data acquired in OBM wells is generally superior to WBM data. The conductivity of oil-based mud is less, which reduces loading effects on the transmitter-receiver system. This reduced loading enables more echoes to be measured and reduces the noise levels. When the water-based mud-system is too conductive (i.e., resistivity is too low), loading effects are serious and put restrictions on the operating modes of the tool. Value may even be reached at which the tool can not be operated, as seen in **Fig. 8.15**. Depending on hole size, a fluid excluder may be necessary to operate the tool in more conductive environments.

NMR logging in OBM wells is not restricted by conductivity problems, but the OBM filtrate in the pore space produces an additional hydrocarbon signal, which complicates interpretation of the logs significantly. Careful pre-job planning is advised to reduce interference of the OBM-filtrate signal and the response from the native fluids. Most OBM base fluids have relatively long T_1 relaxation times and their diffusivity compares to water, which makes it difficult to separate them either through the shifted- or differential-spectrum approach.

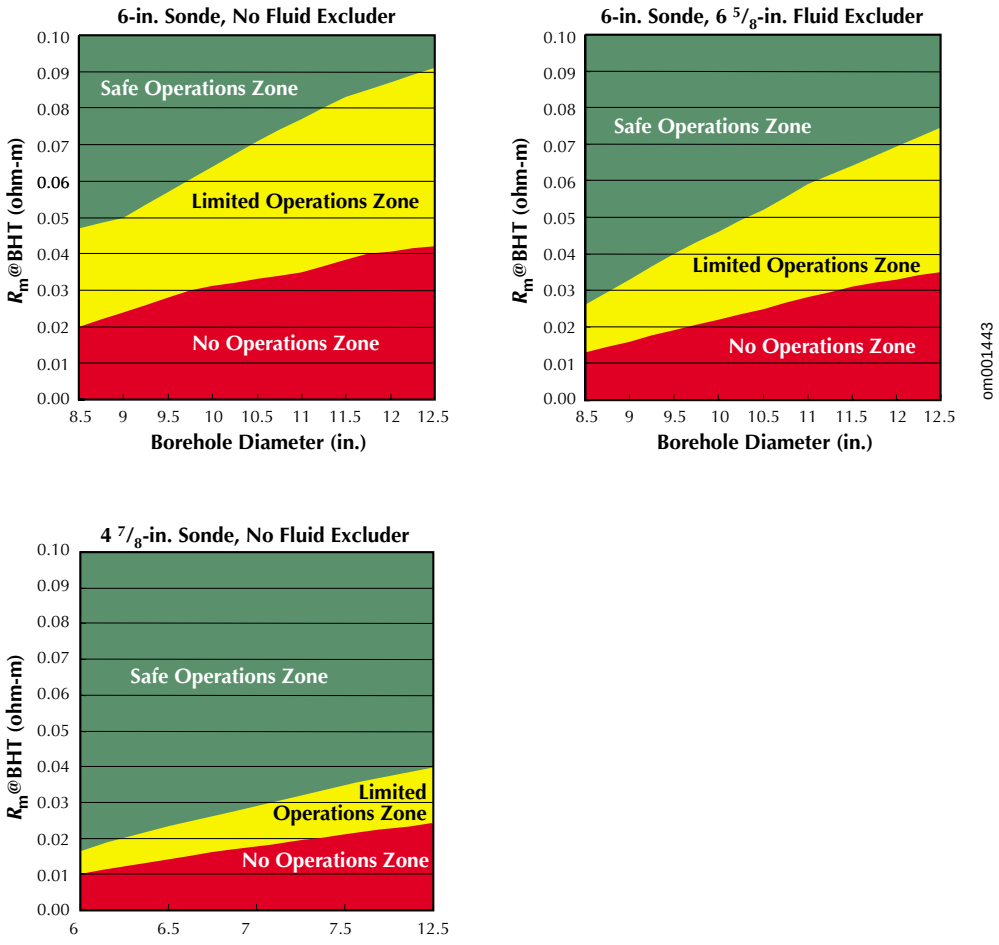

Figure 8.15—The green area indicates the minimum tolerable mud resistivity in a given borehole at which the MRIL-Prime sonde will operate within specifications. Data acquired in the "Limited Operations Zone" (yellow) may not be within the instrument's calibration range; supplying adequate power to the tool may also be problematic. Fitting the 6-in. tool with a fluid excluder expands the "Safe Operations Zone" significantly (top right).

Trade Off Logging Speed ⇔ Accuracy (*S/N*, Sampling Rate) ⇔ Type and Detail of Information

When planning the drilling of any well, the logging program must be given some attention. *S/N* is primarily controlled by borehole size and mud resistivity. As *S/N* decreases, the running average (*RA*) needed to maintain a specified error in porosity increases. The general practice is to require that the porosity have no more than one porosity unit standard deviation. The value of *RA* combined with the logging speed determines the vertical resolution. These relationships are summarized for the MRIL-Prime MAX4-activation in **Fig. 8.16.** The figure clearly indicates that mud resistivity has great impact on the maximum logging speed. The value *RA* increases exponentially when R_m falls below 0.1 ohm-m; the associated drastic decrease in logging speed is evident.

Relaxing vertical resolution in less interesting zones or over homogeneous intervals helps to speed up logging. The same holds for the NMR specific requirements: high precision and accuracy enforce slow-logging operations. For the most common activations, methods have been developed that allow higher logging speeds and only marginally compromise the outcome.

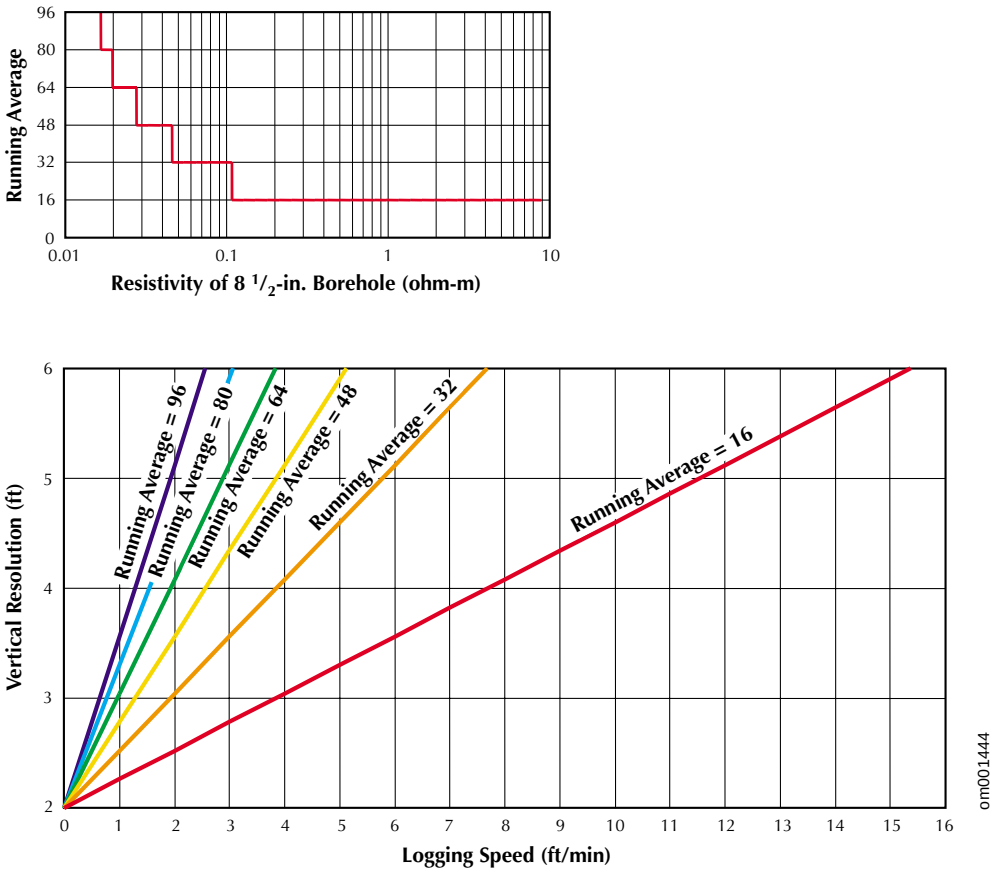

Figure 8.16— This speed-chart applies for the MAX4 MRIL-Prime activation. Entering the left chart with R_m gives the number of running averages to be used. The intercept of the corresponding trend line in the bottom graph with the desired vertical resolution indicates the logging speed.

References

1. Akkurt, R., et al., 1995, NMR logging of natural gas reservoirs, paper N, *36th Annual SPWLA Logging Symposium Transactions*, 12 p.
2. Prammer, M.G., et al., 1995, Lithology-independent gas detection by gradient-NMR logging, SPE 30562, presented at the 1995 SPE Annual Technical Conference and Exhibition, 12 p.
3. Akkurt, R., et al., 1998, Enhanced Diffusion: Expanding the range of NMR direct hydrocarbon-typing Applications, paper GG, presented at the *39th Annual SPWLA Logging Symposium*, 14 p.
4. Vinegar, H.J., 1995, Short course notes, SPWLA short course on NMR, Houston, Texas.
5. *Log Interpretation Principles/Applications*, 1987, Schlumberger Educational Services, Houston, Texas, p. 45.
6. Gerritsma, C.J., Oosting, P.H., and Trappeniers, N.J., 1971, Proton spin-lattice relaxation and self-diffusion in methanes: II. Experimental results for proton spin-lattice relaxation times, *Physica*, v. 51, p. 381–394.
7. Oosting, P.H., and Trappeniers, N.J., 1971, Proton spin-lattice relaxation and self-diffusion in methanes: IV. Self-diffusion in methanes, *Physica*, v. 51, p. 418–431.
8. Dawson, R., Khory, F., and Kobayashi, R., 1970, Self-diffusion measurements in methane by pulsed nuclear magnetic resonance: *AlChE Journal*, v. 16, no. 5, p. 725–729.
9. Zhan, Q., et al., 1998, Some exceptions to default NMR rock and fluid properties, paper FF, *39th Annual SPWLA Logging Symposium Transaction*s, 14 p.
10. Yarborough, L., and Hall, K.R., *Oil & Gas Journal*, Feb. 1974, p. 86.
11. Craig, F.F., The Reservoir Engineering Aspects of Water Flooding, SPE Monograph Volume 3 of the Henry L. Doherty series, Dallas, 1993, p. 12.
12. Kleinberg, R.L., et al., 1993, Nuclear Magnetic Resonance of Rocks: T_1 vs. T_2, SPE 26470, presented at the *1993 SPE Annual Technical Conference and Exhibition*, 11 p.
13. Prammer, M.G., et al., 1999, Theory and operation of a new, multivolume NMR logging system, paper DD, presented at the *40th Annual SPWLA Logging Symposium*, 12 p.
14. McCain Jr., W. D., 1990, Petroleum Fluids, Pennwell Books, Tulsa, Oklahoma, p. 330–331.

Chapter 9

MRIL Log Quality Control

Quality control is essential to obtaining accurate information for the MRIL log. A system of tool-integrity and log-quality indicators is used to ensure the highest level of data quality. The MRIL quality-control procedure includes calibration, verification (before-survey and after-survey), operational setup, log recording, display of quality indicators, and a final quality check. This chapter is divided into five sections: concepts and definitions needed to understand the log quality assurance discussion, calibration and verification, quality control during logging, logging quality display, and post-logging quality check.

Concepts and Definitions

Gain and Q Level

Gain indicates the amount of loading applied to the MRIL tool's transmitter circuit by borehole fluids and formation. Gain is measured in real time by using a test coil (B_1 coil) built into the tool. The test coil transmits an RF signal, which is received by the RF antenna. Gain is the ratio of the amplitude of the signal induced in the RF antenna divided by the amplitude of the signal in the test coil. A gain measurement is made as a part of each pulse sequence.

Gain is frequency-dependent. The operating frequency of a tool should be set to achieve maximum gain.

Gain measured when the tool is in the borehole includes effects caused by both the external environment and the transmitter circuit itself. External factors that affect gain are primarily the borehole fluid resistivity and, to a lesser degree, formation resistivity. Low-resistivity muds or formations produce greater signal attenuation than high-resistivity muds or formations, and thus result in lower gain. Because borehole fluid resistivity does not change drastically over typical logging intervals, changes in gain are usually the result of changes in formation resistivity or borehole size when conductive mud is used.

Gain should never be zero. Sudden changes or spikes in gain usually indicate tool problems.

MRIL activations are designed to run at a certain *Q* level: high *Q*, medium *Q*, or low *Q*. The gain value determines which *Q* level to use, as indicated in **Table 9.1**.

Table 9.1—*Q*-Level Determination

Gain	*Q* Level
>300	high *Q*
200 - 300	medium *Q*
<200	low *Q*

B_1 and B_{1mod}

B_1 is the strength of the CPMG pulse that produces proton tipping and re-phasing. As a part of every pulse sequence, B_1 is measured using the test coil. The B_1 curve should be relatively constant but should show some variation with changes in borehole and formation conductivity. B_1 will decrease across conductive washouts and conductive formations. Changes in the B_1 values should vary together with gain in the same direction following changes in total conductivity.

The value of B_1 corrected for borehole temperature is called B_{1mod}. The relation between B_{1mod} and B_1 is given by:

$$B_{1\mathrm{mod}} = B_1[1 + 0.0033(T_{magnet} - T_{calibration})] \tag{9.1}$$

where T_{magnet} is the temperature of the magnet at downhole conditions, and $T_{calibration}$ is the temperature of the magnet in the calibration tank during calibration. Both temperatures are expressed in degrees Centigrade.

To give the maximum signal value during logging, B_1 must be controlled so that B_{1mod} remains within 5% of the peak value determined during shop calibration. If B_{1mod} does not remain in this range, then the following effects occur:

- Protons will be under- or over-tipped.
- The signal-to-noise ratio for the tool and the precision of the porosity measurement will decrease.

Any sudden change or spikes on the B_{1mod} curve usually indicate tool problems and should be investigated.

Chi

Chi is a measure of the quality of fit between the calculated decay curve and the recorded echo amplitudes. Chi is one of the primary log quality indicators monitored during logging. In general, the value of Chi should be less than 2, but in certain low-*Q* situations, it may average slightly higher than 2. Sudden changes or spikes in Chi usually indicate tool problems and should be investigated, even if Chi remains below 2.

Noise Indicators: OFFSET, NOISE, RINGING, and *IENoise*

Noise for each CPMG experiment is described by four noise measures: offset (*OFFSET*), noise (*NOISE*), ringing (*RINGING*), and inter-echo noise (*IENoise*), as shown in **Fig. 9.1**.

Before the start of each CPMG experiment, *OFFSET* and *NOISE* are determined from analysis of the ambient signal. *OFFSET* is the mean of this signal, and *NOISE* is its standard deviation. The phase-alternated-pair (PAP) technique discussed in Chapters 2 and 5 is used to determine *RINGING* and *IENoise*. The summation of the PAP echoes to a first approximation contains no signal. The mean of this sum is the *RINGING* and the standard deviation of this sum is the *IENoise*. *IENoise* should be approximately equal to *NOISE*, and any significant difference between them is an indication of noise being generated internally during the transmitter pulses.

The four noise measures serve as quality indicators. They are calibrated and environment-corrected in the same way as the echoes, and therefore, they are scaled in porosity units. *NOISE* and *IENoise* are inversely proportional to gain. *RINGING* is affected by echo spacing (*TE*): *RINGING* is much stronger for short *TE* than for long *TE*. For example, the maximum *RINGING* for *TE* = 1.2 ms is approximately 40 units, while for *TE* = 0.6 ms, the maximum ringing may be 60 units. The tool operating frequency must be selected to keep *RINGING* to a minimum.

The values of these indicators should be consistently within their allowable ranges as shown in **Table 9.2**. *NOISE* and *IENoise* should not exhibit spiking.

When multi-frequency mode is used, noise features are provided for each frequency.

Low-Voltage Sensors

The MRIL quality-control procedure provides a set of low-voltage sensor data to ensure that the electronic cartridge works properly. Each low-voltage sensor should have values within the ranges shown in **Table 9.3**.

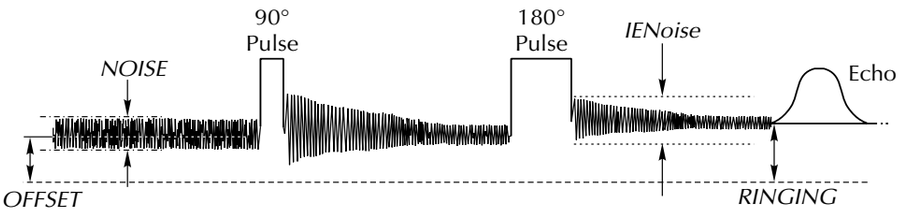

Figure 9.1—Noise features are shown here for a single CPMG experiment. *OFFSET*, *NOISE*, *RINGING*, and *IENoise* are used as quality indicators (The amplitudes of CPMG pulses and echoes are not on scale).

Table 9.2—Allowable Ranges for Noise Quality Indicators

Quality Indicator	Allowable Range
NOISE	< 10 (Low *Q*); < 8 (Medium *Q*); <5 (High *Q*)
IENoise	< 10 (Low *Q*); < 8 (Medium *Q*); <5 (High *Q*)
OFFSET	-30 to +30
RINGING	-40 to +40 (*TE* = 1.2 ms), -60 to +60 (*TE* = 0.6 ms)

Table 9.3—Low-Voltage Sensor Mnemonics and Data Ranges

Sensor Name	Real-Time-Display Mnemonic	Data Range
Ur 15 high	15VUP	19–24
+15 Analog	15V	14.8–15.2
-15 Analog	15VN	-14.8– -15.2
15 Trans	15VT	14.8–15.2
Ur 15 low	15VUM	19–24
Unreg 5 v	5VUM	9.5–12.5
+5 Analog	5VA	4.9–5.1
-5 Analog	5VAN	-4.9– -5.1
+5 Digital	5VD	4.9–5.1

High-Voltage Sensors

The MRIL surface system attempts to maintain 600 VDC on the bank of capacitors that provide the high current needed to produce CPMG pulses. Normally, the current transmitted from the surface is insufficient to keep the capacitors fully charged during an echo train, and as a result, the voltage output from the capacitors decreases during a CPMG echo train.

The MRIL tool can compensate for changes in voltage. The capacitor voltage is measured at the beginning and at the end of the pulse (echo) train, and both values are reported in real time. The voltage at the beginning of the cycle is defined as *HVmax*, and the voltage at the end of the cycle is defined as *HVmin*.

In a high-*Q* environment with 50 echoes and $TW \geq 1500$ ms, *HVmax* should be approximately the same as the voltage indicated on the voltage meter on the power-supply panel.

For standard T_2, dual-*TW*, and dual-*TE* activations, *HVmin* must remain above 400 VDC. If it does not, the tool will not be able to compensate for this reduced voltage and $\mathbf{B_1}$ will be reduced. The reduction in B_1 generally results in the porosity being underestimated, especially for the longer T_2 components.

When the total-porosity activation is used, two activation sets are run in tandem: a standard T_2 activation to measure effective porosity and a partial polarization activation to measure clay-bound water. In this case, because the partial-polarization activation immediately follows the standard T_2 activation, the reported *HVmin* is not only the voltage at the end of the CPMG for effective-porosity activation, but it is also the voltage at the beginning of the CPMG for partial-polarization activation. Thus, when logging with total-porosity activation, *HVmin* cannot be allowed to drop below 450 VDC.

Phase Correction Information: *PHER, PHNO,* and *PHCO*

The NMR signal from the antenna is fed into a phase-sensitive detector that outputs two channels of data (Channel 1 and Channel 2) 90° apart. Data from both channels can be plotted as a function of echo time, as shown in **Fig. 9.2a** for a single experiment and in **Fig.**

9.2b for eight stacked experiments**.** Data from both channels can also be crossplotted, as shown in **Fig. 9.3a** for a single experiment and in **Fig. 9.3.b** for eight stacked experiments.

The magnitude of the echo train can be calculated as

$$E_{amp}(i) = \sqrt{E^2(i) + E_y^2(i)} \tag{9.2}$$

where $E_{amp}(i)$ is the calculated amplitude for the i^{th} echo, and $E_x(i)$ and $E_y(i)$ are the amplitudes of the i^{th} echo for Channels 1 and 2, respectively. However, this calculation is affected by rectification, and all noises contribute as positive signals. Therefore, the decay curve never goes to zero but stays at some small value, which echo fitting will convert to a long T_2 component.

The magnitude of the echo train can be calculated by a different approach to remove the problem of noise rectification. This approach is designed to produce two channels of data: one channel consists primarily of the NMR signal, which is to be used for further processing, and the other channel consists primarily of noise with zero mean. In this approach, an angle φ is calculated from

$$\varphi = \tan^{-1} \frac{\sum_{i=2}^{k} E_y(i)}{\sum_{i=2}^{k} E_x(i)} \tag{9.3}$$

where i is the i^{th} echo in the echo train, and k is the number of echoes to be used for phase-angle calculation. Typically, $2 \le k \le 9$. This calculation is performed after a running average has been applied. This angle is then applied to the data from both channels as a phase-correction angle. This phase correction is equivalent to rotating the Channel 1 and Channel 2 data through an angle of φ. After rotation, one channel will contain primarily the NMR signal (whose amplitude is the real part of the echo train), and the other channel will contain primarily noise (whose amplitude is the imaginary part of the echo train), as shown in **Fig. 9.4**. The real part of the echo train is converted to a T_2 distribution.

PHER is the mean of the imaginary part of the echo train and is ideally is zero. In practice, *PHER* should be less than one for good data. *PHNO* is the standard deviation of the imaginary part of the echo train and should be comparable in size to the other noise indicators. In addition, the calculated angle for phase correction, designated as *PHCO*, can be also displayed as a quality indicator. If the measured signal is too small, then *PHCO* will show random changes with depth. If the measured signal has sufficient amplitude, then *PHCO* should remain stable with depth. For dual-*TW* or dual-*TE* logging, *PHCOA*, which is the *PHCO* for long *TW* or short *TE*, should be about the same as *PHCOB*, which is the *PHCO* for short *TW* or long *TE*.

Temperature

Three temperature indicators are reported during logging: Temp1, Temp2, and Temp3. Temp1 is the temperature of the electronics cartridge flask, Temp2 is the temperature of the transmitter module, and Temp3 is the temperature of the magnet.

Figure 9.2—After a phase-sensitive detector has separated antenna data into two channels 90° apart, the data (scaled here in porosity units) can be plotted as a function of echo time (scaled here in milliseconds). In panel **(a)**, the data in each channel are not stacked and appear to be noisy. In panel **(b)**, the data from eight experiments are stacked in each channel, which results in a significant enhancement of the signal-to-noise ratio.

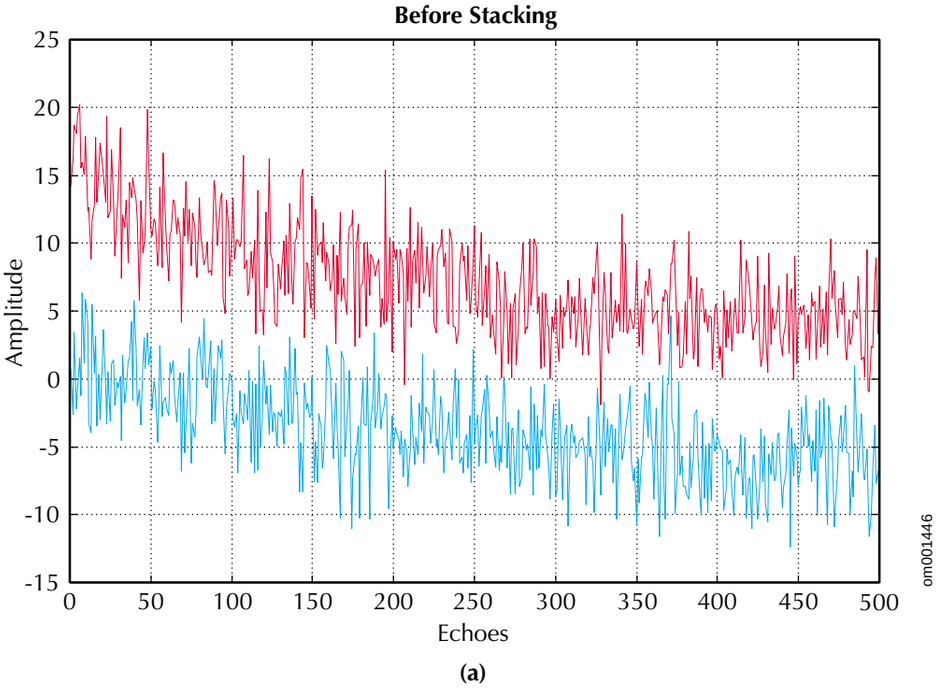

(a)

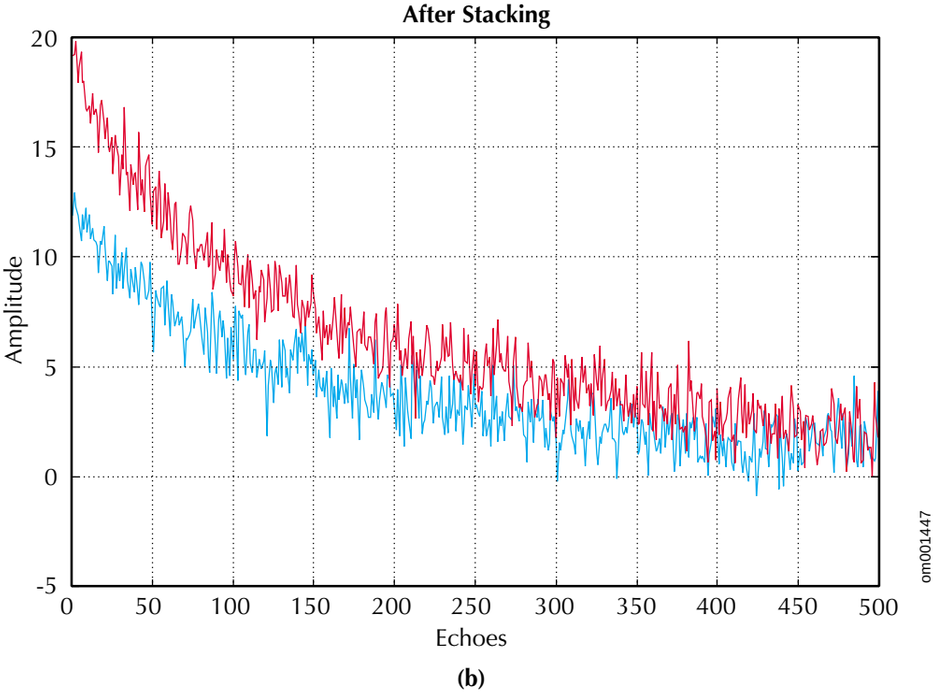

(b)

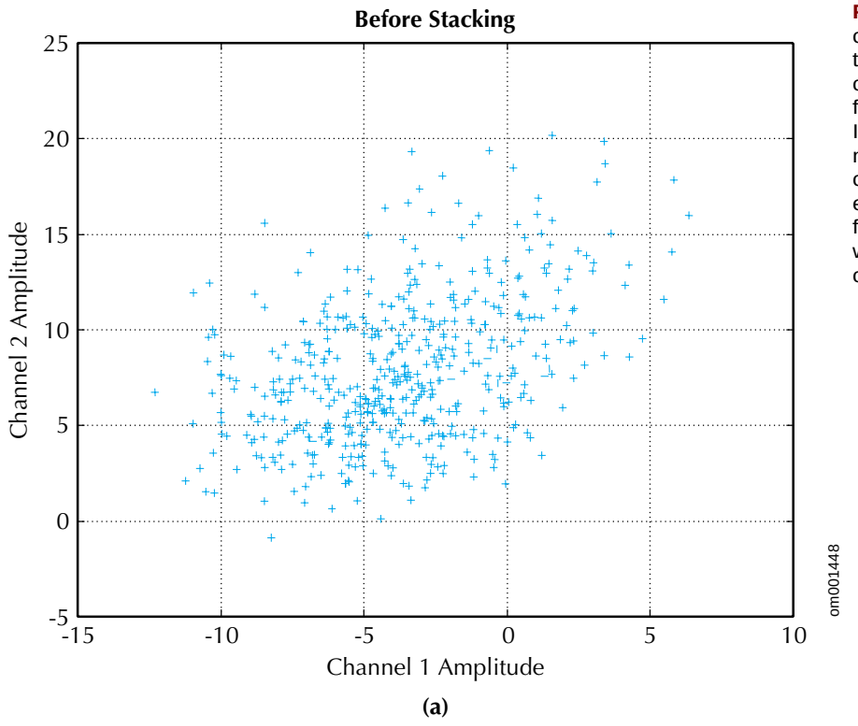

(a)

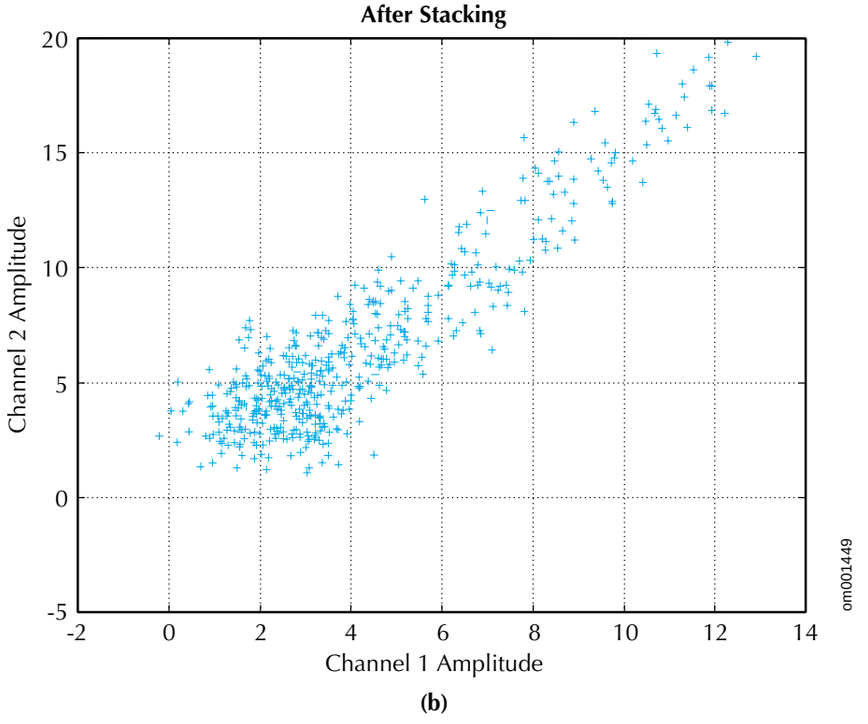

(b)

Figure 9.3—The two channels of antenna data that differ by 90° can be crossplotted as shown here for the data of Fig. 9.2. In panel **(a)**, the data were not stacked before crossplotting. In panel **(b)**, each point represents data from eight experiments that were stacked before crossplotting.

Figure 9.4—Channel 1 and Channel 2 data from the antenna can be rotated to reduce the problem of noise rectification. The base data used here are same as those used for Figs. 9.2 and 9.3. After rotation, the crossplotted data **(a)** from the two channels will cluster around a horizontal line corresponding to a Channel 2 amplitude of zero. After rotation, the amplitude of the Channel 1 data **(b)** is the real part of the echo train and is used for echo fitting. After rotation, the amplitude of the Channel 2 data is the imaginary part of the echo train.

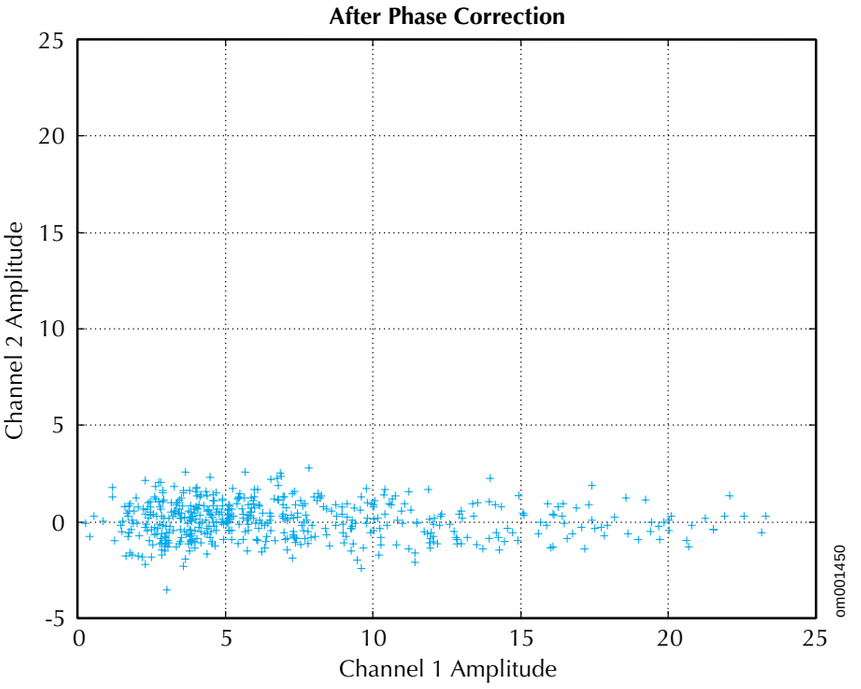

(b)

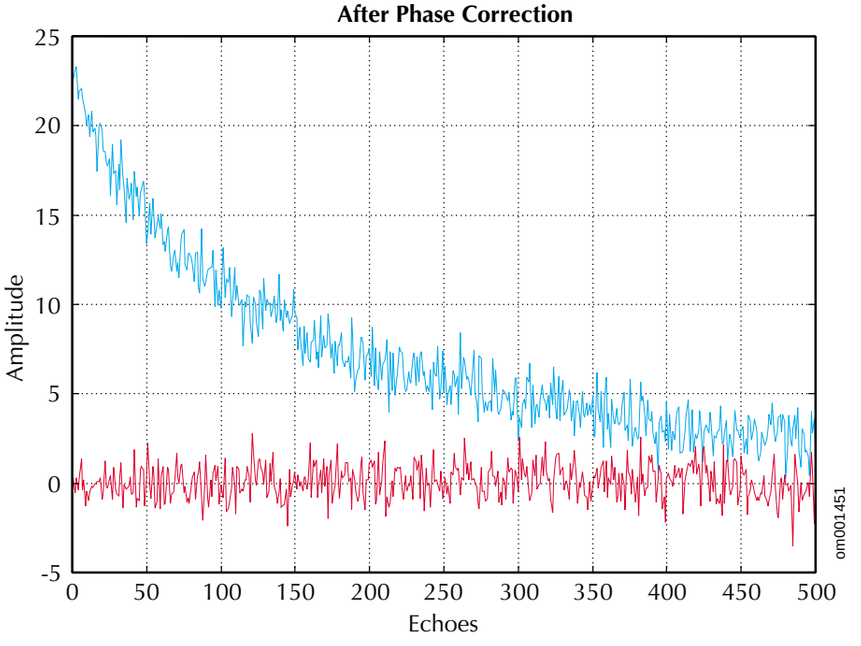

(b)

Pre-Logging Calibration and Verification

The MRIL tool is calibrated before every logging job in a calibration tank, as shown in **Fig. 9.5**. A complete calibration is not necessarily done before every logging job but is done at least monthly. The calibration procedure must be done for each activation. The calibration tank is made of fiberglass and is lined with a thin metallic coating. The tank serves as a container for the water sample and as a Faraday cage to shield out unwanted background RF signals. In its original form, the calibration tank had three chambers concentric with the axis along which the antenna is placed. To calibrate the 6-in. tool, the outer chamber is filled with water that has been doped with cupric sulfate. The cupric sulfate significantly reduces the T_1 relaxation time of water. With this setup, the sensitive volume contains 100% water, and because the water has a relatively fast relaxation time, the calibration time is short. The middle and inner chambers may be filled with waters of different salinity to simulate borehole conditions. In the calibration of the 4˚-(C) and 4 $^7/_8$-(Prime) in. tools, the middle chamber is filled with doped water, and the inner chamber may be filled with brine to simulate antenna loading. Newer versions of the calibration tank contain only one chamber, and a dummy load simulates borehole conditions.

The parameters determined during shop calibration are

- The pulse strength B_1 need to produce the maximum A_0, where A_0 is the amplitude of echo train at time zero. (Both 90° and 180° pulses have the same amplitude but different lengths.)
- The relationship between B_1 and A_0 that is required to perform a “power correction.”
- The correction to Echoes 1 and 2, resulting from the so-called stimulated echo effect.

The relationship between A_0 and porosity. (The maximum A_0 is calibrated to 100% porosity in the calibration tank.)

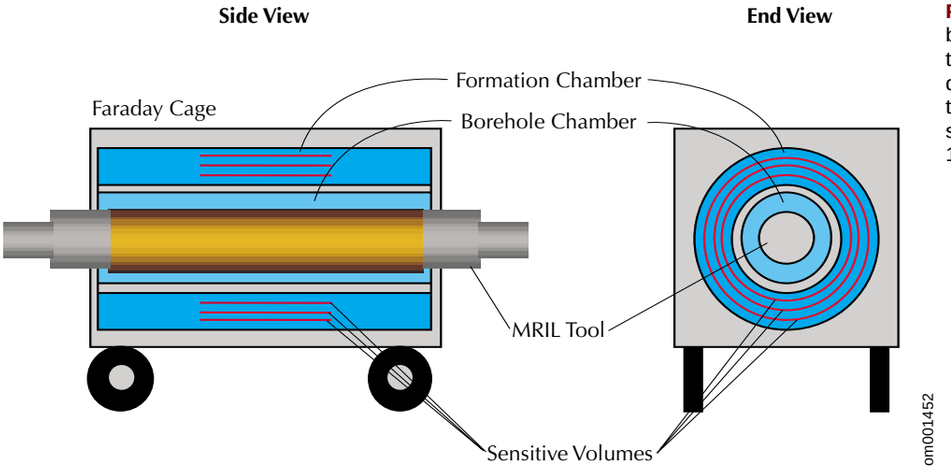

Figure 9.5—The chambers of this MRIL calibration tank are filled with doped water to simulate the borehole fluid and a sensitive volume of 100% porosity.

Calibration Procedure

The shop calibration procedure includes a frequency sweep test, a master calibration, and a tank statistical check. Only the tank statistical check must be done before every logging job.

Frequency Sweep

A frequency sweep is performed to find a frequency at which the highest gain occurs. During a frequency sweep, software is used to change the transmitter frequency over a fairly wide range in the test coil while simultaneously measuring gain at the RF antenna. As the frequency graph in **Fig. 9.6** illustrates, a frequency can be found at which the maximum gain occurs. The transmitter is then set to operate at this frequency.

A frequency sweep is essential for proper operation of the tool. The operating frequency affects the tool's transmitter and receiver circuits in two ways. First, if the transmitter and receiver circuits are not tuned to the same frequency and power transmission is not efficient, then the tool may overheat and become inoperable. Second, the efficiency of the receiver circuit decreases sharply outside a very narrow frequency band centered on the resonant frequency of the antenna. Consequently, if an incorrect operating frequency is selected, echo amplitudes are artificially reduced and the signal-to-noise ratio decreases. Likewise, if the tool is calibrated at an incorrect frequency, subsequent logs will contain incorrect data.

Master Calibration

The master calibration determines the amplitude of the CPMG pulses as well as the relations for power and stimulated-echo corrections[1]. The amplitudes E_1 and E_2 of Echo 1 and Echo 2, respectively, are recorded, and the amplitude A_0 of the echo train at time 0 is calculated by using the exponential decay fit curve determined from Echo 3 to last echo. Then three multipliers A_{0mul}, E_{1mul}, and E_{2mul} are calculated and displayed with the B_1 amplitude, as shown in **Fig. 9.7**. The A_{0mul} is the factor necessary to normalize the decay curve so that it reads 100% porosity in the water tank. The E_{1mul} and E_{2mul} are the correction factors needed to remove the stimulated echo effect. A_{0mul} and E_{1mul} are functions of B_1. These multipliers are defined by

$$A_{0\mathrm{mul}} = \frac{A_0}{100}$$
$$E_{1\mathrm{mul}} = \frac{E_{1\mathrm{fit}}}{E_1} \qquad (9.4)$$
$$E_{2\,\mathrm{mul}} = \frac{E_{2\mathrm{fit}}}{E_2}$$

where E_{1fit} and E_{2fit} are the values for Echo 1 and Echo 2 calculated from the fitting curve determined from Echo 3 to last echo.

The amplitude needed for CPMG pulses to produce 90° tipping and 180° rephasing is determined at maximum A_0. The power-correction relation is found with the regression of B_1 and A_{0mul} (red curve). The relation for the stimulated-echo correction for Echo 1 is found with the regression of B_1 and E_{1mul} (green curve). The stimulated echo correction for Echo 2 is normally a constant (black asterisks).

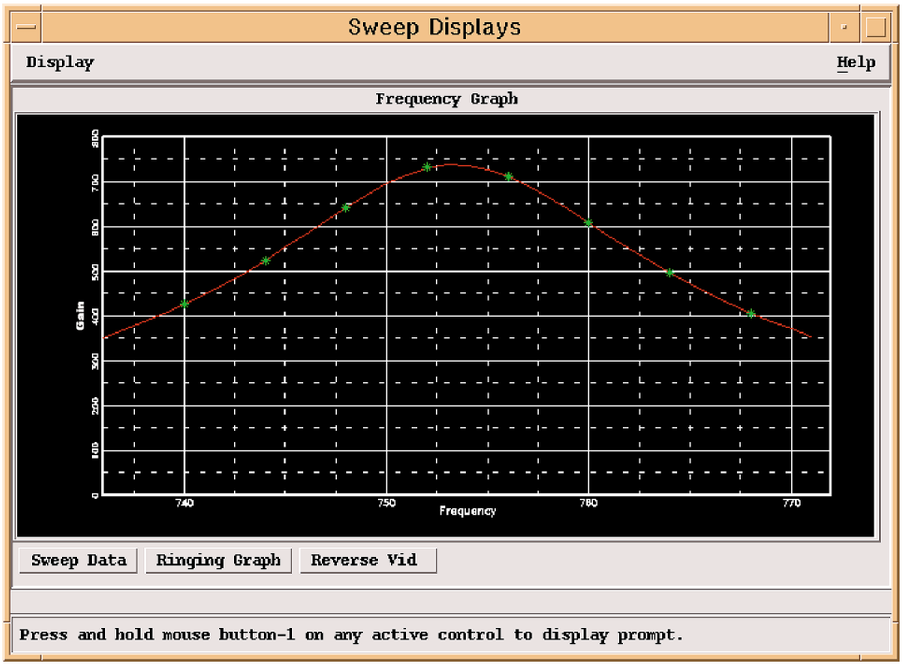

om001627

Figure 9.6—This frequency sweep reveals an operating frequency at which maximum gain is achieved.

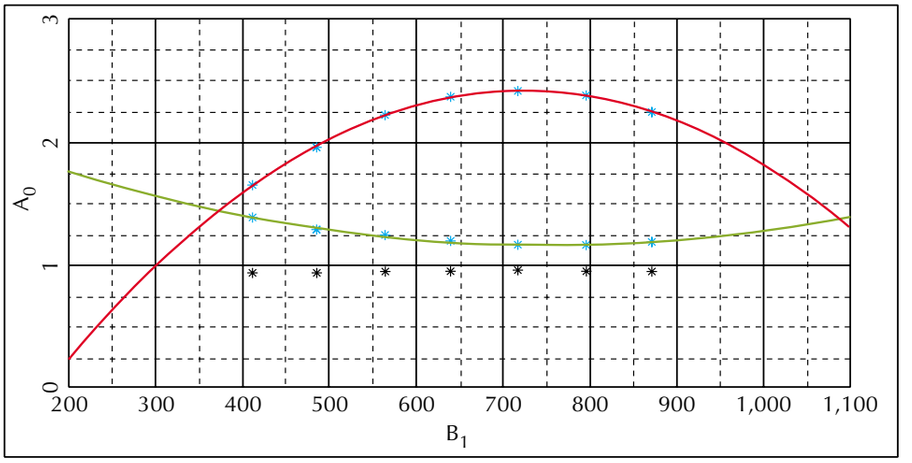

om001450

Figure 9.7—Master-calibration display: the amplitude for CPMG pulses to produce 90° tipping and 180° re-phase is determined at maximum A_0. The power correction relation is found with the regression of B_1 and A_{0mul} (red curve). The stimulated echo correction relation for Echo 1 is found with the regression of B_1 and E_{1mul} (green curve). The stimulated echo correction for Echo 2 is a constant (black stars).

The B_1 corrections for A_0 and E_1 are fit to a second-order polynomial of the form

$$A_{0mul} = A_{0-A} B_1^{\,2} + A_{0-B} B_1 + A_{0-C}$$
$$E_{1mul} = E_{1-A} B_1^{\,2} + E_{1-B} B_1 + E_{1-C} \qquad (9.5)$$

to determine $A_{0\text{-}A}$, $A_{0\text{-}B}$, $A_{0\text{-}C}$, $B_{1\text{-}A}$, $B_{1\text{-}B}$, and $B_{1\text{-}C}$. Then, corrections for a range of B_1 values can be calculated.

The calibrated MRIL porosity is given by

$$\phi_{\mathrm{MRIL}} = \frac{A_0}{A_{0\,\mathrm{mul}}} \tag{9.6}$$

All the multiplier factors and relations are also reported with the master calibration report (**Table 9.4**). T2R in the table is calculated with a single-exponential decay fit to the measured echo train because the calibration tank is filled with water. The value of B_1 is adjusted by changes to a software parameter called global amplitude, as shown in the left column of Table 9.4. For the C-type tool, the global amplitude for a 6-in. sonde has values ranging from 70 to 135, and the global amplitude for a $4\,^1/_2$-in. sonde can be between 40 and 80.

Table 9.4—Master Calibration Report

MRIL Shop Calibration Summary

Performed: 20-Oct-1997 10:47
Serial Number: C093B124 Model: MRIL-C

Activation: 12DFHQCAL

Amp	AO	T2R	Gain	E1Mu1	E2Mu1	AOMu1	B1
75	187.3	158.1	622.9	1.36	0.97	1.87	474.4
85	216.3	160.6	622.8	1.27	0.97	2.16	564.3
95	234.3	164.1	622.7	1.22	0.96	2.34	652.6
105	242.4	165.3	622.4	1.19	0.97	2.42	740.7
115	238.8	164.9	623.0	1.20	0.98	2.39	827.0
125	223.8	164.1	622.9	1.21	0.98	2.24	920.3

A_{0_A}: -6.86007E-06 A_{0_B}: 0.010392 A_{0_C}: -1.51424
E_{1_A}: 1.71249E-06 E_{1_B}: -0.00270606 E_{1_C}: 225627
$E_{2\ \mathrm{Multiplier}}$: 0.971747 $A_{0\ \mathrm{Chi}}$: 1.3111E-05 $E_{1\ \mathrm{Chi}}$: 1.9125E-05

Tank Statistical Check

The tank statistical check verifies tool response in a 100% porosity water tank. It is done before every logging run for each combination of *TE*, frequency, and expected *Q* level. Different *TW* and the number of echoes do not require additional calibrations. The check is performed with the tool inside the calibration tank and with the values determined during the frequency sweep and master calibration. **Fig. 9.8** is an example of a report for a tank statistical check. The mean of the porosity measured in the tank should be within 2% of 100 p.u.

Following the logging job, a final validation of tool response is obtained by checking the tool in the tank after the tool has been returned to the shop. To check long-term consistency of tool response, a comparison of current calibration data with historical calibration data is always recommended.

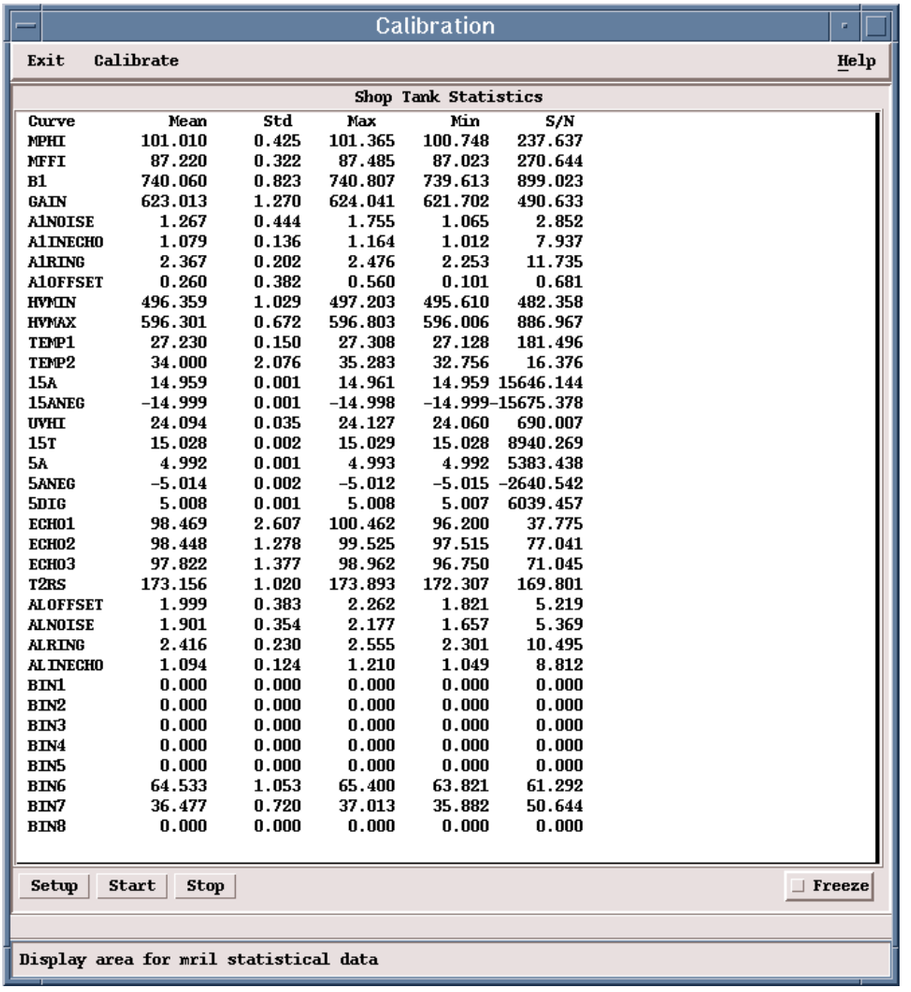

Figure 9.8—On the report of a tank statistical check, the measured porosity *MPHI* should be within 2% of 100 p.u. All of the quality indicators, such as noise features and voltage-sensor data, should fall within their allowable ranges.

Results of the calibration and of the tank statistical check are included on the logs and should be checked against their reference values.

To prepare for an MRIL job, the logging tool is calibrated for each of the basic activations and for the expected downhole environment.

Electronics Verification

After shop calibration, a primary verification that tool electronics are functioning properly is performed. In this verification, a field verifier is connected to the tool's electronics to check the response of several internal tool parameters. **Table 9.5** displays the verification parameters and their allowable ranges. The allowable standard deviations for all the noise features should be checked with Table 9.5 and are used as a go/no-go template. Because the

Table 9.5—MRIL Field Verification Ranges and Tolerances

Sensor Name	Normal Range	Allowable Tolerance	Standard Deviation
B1	450–750	±25	7.5
A1NOISE	<12	±2	2.0
A1NECH	<12	±2	2.0
A1RING	-30–30	±2	
A1OFFSET	-30–30	±2	
GAIN	250–350	±15	7.5
TEMP1	AMBIENT		
TEMP2	AMBIENT		
HVmin	530–590	±10	2.5
HVmax	570–610	±10	2.5
15VUP	19–24		0.005
15V	14.8–15.2		0.005
15VN	-14.8– -15.2		0.005
15VT	14.8–15.2		0.005
15VUM	19–24		0.005
5VUM	9.5–12.5		0.005
5VA	4.9–5.1		0.005
5VAN	-4.9– -5.1		0.005
5VD	4.9–5.1		0.005

verification is only a check of tool electronics, a successful verification alone does not necessarily ensure correct logging responses. However, if the check fails, the tool should not be run in the well.

Verifier measurements are repeated at the wellsite before and after logging to yield before-survey and after-survey verification values. These two sets of values should be compared with each other, and the before-survey values should also be compared with the primary-verification values.

In a single verification, *A1RING* and *A1OFFSET*, which are *RINGING* and *OFFSET* respectively for Frequency 1 in multi-frequency mode, should be approximately equal. A difference of more than 5 units indicates a problem in either the verifier or the tool electronics. *A1NOISE* and *A1IENoise*, which are the *NOISE* and *IENoise* respectively for Frequency 1 in multi-frequency mode, are dependent on *GAIN* and will vary from system to system. Their values should be consistent within each system, and any changes greater than 2 from the primary verification value to the before-survey value, or from the before-survey value to after-survey value, may indicate a tool problem.

Table 9.6 is an example of a shop verification report, which shows the measured values of $\mathbf{B}_1$, *GAIN*, *NOISE*, *IENoise*, *RINGING*, *OFFSET*, *HVmin*, *HVmax*, and temperature of the transmitter and cartridge, their expected ranges, standard deviations, and allowable deviations.

Table 9.6—Example of Shop Verification Report Along with Allowed Ranges

MRIL Shop Check Summary

Performed: 22-Jun-1998 10:32
Serial Number: C179B011 Model: MRIL-C

Statistical Check with Dummy Load Performed: 29-Jun-1998 10:32
Activation: cblkbox Experiment Range: 50-150
Field Verifier # c107

	Shop	Expected Range	Std. Dev.	Allowable Dev
B1	301.436	450 - 750	0.534	7.5
GAIN	342.010	250 - 350	1.700	7.5
A1NOISE	2.704	<12	0.646	2.0
A1INECHO	2.530	<12	0.381	2.0
A1RING	5.106	-30 - 30	0.505	2.0
A1OFFSET	2.310	-30 - 30	0.967	2.0
HVMIN	586.445	530 - 590	0.000	2.5
HVMAX	602.381	570 - 610	0.000	2.5
Cart Temp	32.486	-Ambient	0.142	
Tran Temp	33.047	-Ambient	0.261	

Quality Control During Logging

Operating Frequency

The MRIL operating frequency is the center frequency of the B_1 field. Before logging, just as before calibration, a frequency sweep is performed downhole. The transmitter is then set to operate at the frequency at which the maximum gain was found during the frequency sweep.

MRIL-C tools may be set to operate with two frequencies in dual-frequency mode, both of which must be selected from one of two frequency ranges: standard frequency (700 to 750 kHz) and low frequency (600 to 650 kHz). The MRIL-Prime tool is set to operate at nine frequencies: for example, at 760, 686, 674, 656, 644, 626, 614, 596, and 584 kHz. Changing a tool's operating-frequency range requires significant hardware modifications that must be performed at the shop.

Logging Speed and Running Average

MRIL logging speed is affected by many factors. Speed charts, which determine the logging speed, are based on

- gain
- activation
- polarization time
- tool type (C or Prime)
- tool size
- desired vertical resolution
- operating frequency

Information from the speed chart is essential to selecting the correct (minimum) running average based on tool gain. **Fig. 9.9** shows examples of speed charts for the MRIL-C tool. A different speed chart is designed for each desired vertical resolution, with high-resolution and standard-resolution charts being shown in Fig. 9.9.

Fig. 9.10 shows of how to use the speed chart in Fig. 9.9. In this example, tool gain is assumed to be 470, a high-resolution run is desired, and *TW* is 3000 ms. Beginning at 470 on the horizontal axis (Dual Frequency Gain), a line is projected vertically until the red Running Average curve is reached. At this point, a value of 8 is read on the right-side Running Average scale. When the vertical projection line is continued upward, the green dotted

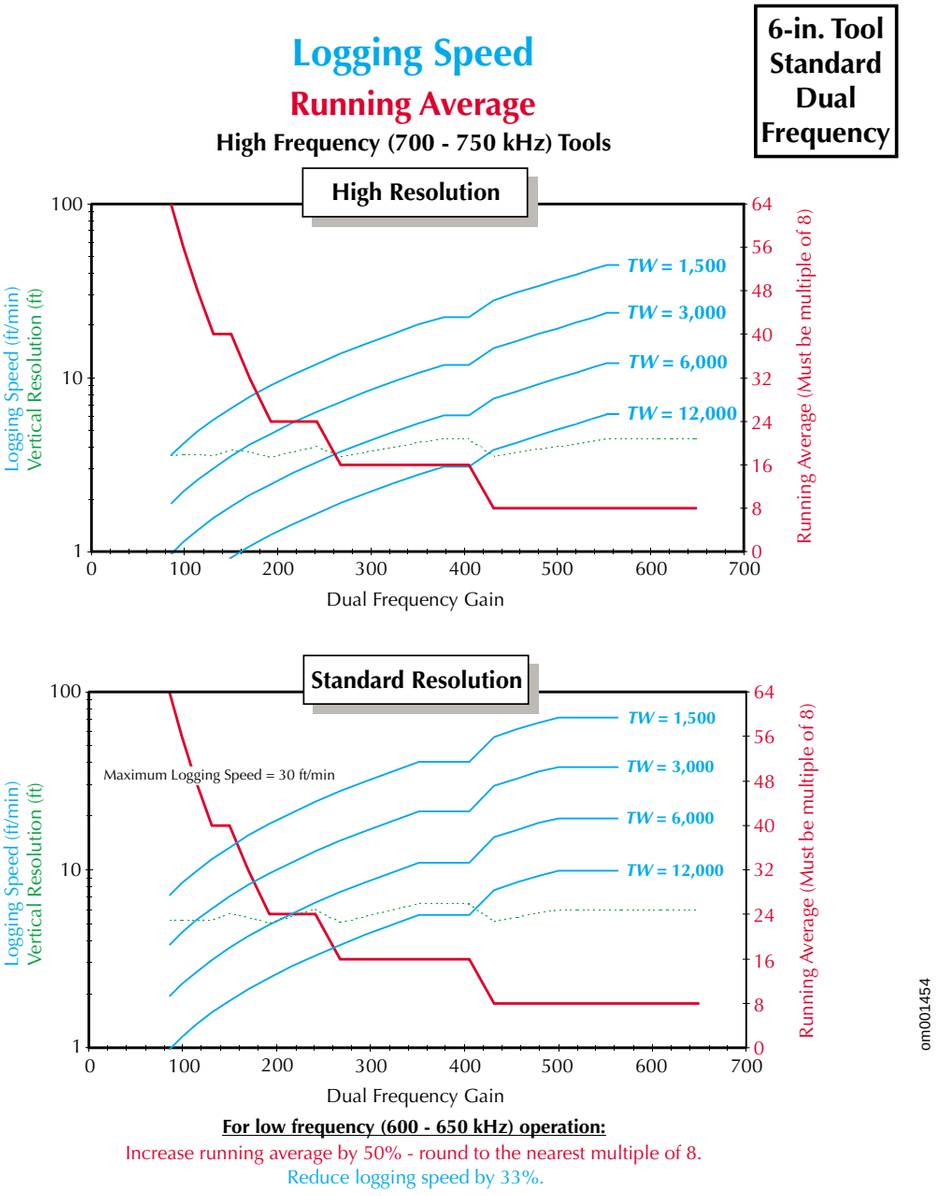

Figure 9.9—This speed chart is designed for use with a 6-in. MRIL-C tool operating in dual-frequency mode at high frequency, i.e., 700 to 750 kHz. The upper section of the chart is used when acquiring a high-resolution log. (A high-resolution log is one having vertical resolution of approximately 4 ft for any gain). The lower section is used for standard-resolution logs. (A standard-resolution log is one having a resolution of approximately 6 ft for any gain.) Speed charts such as the one shown are available for 6-in. and 4 ½-in. tools; for single-, dual-, and triple-frequency modes; and for standard-T_2, dual-*TW*, dual-*TE*, and total-porosity activations.

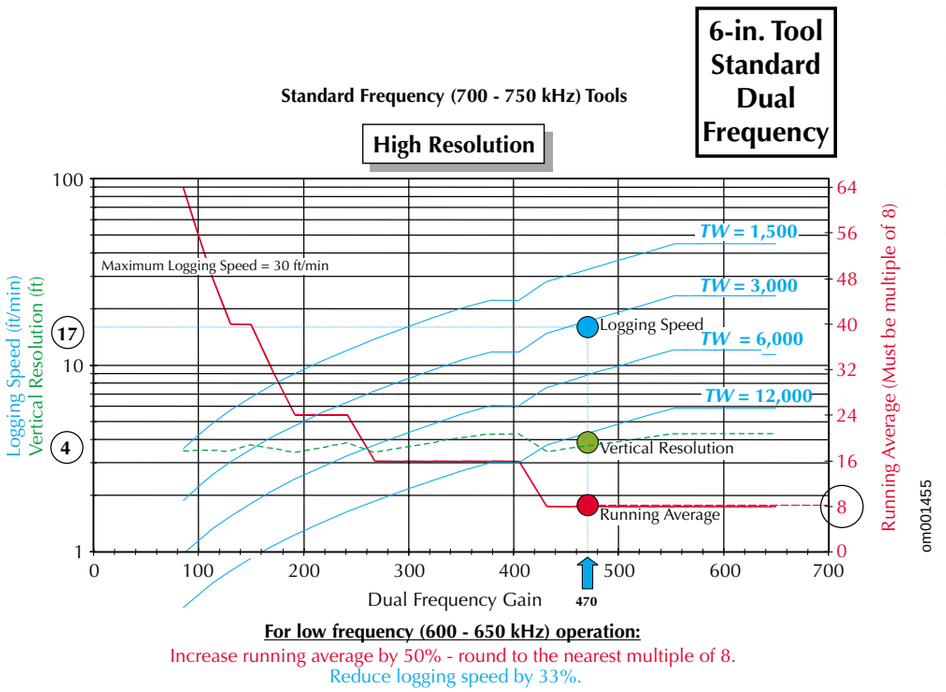

Figure 9.10—This speed chart shows that if tool gain is 470, *TW* is 3000 ms, and a high-resolution run is desired, then a logging speed of 17 ft/min and a running average of 8 must be used. As the chart indicates, a 4-ft vertical resolution is achieved in this case.

Vertical Resolution curve is reached. At this point, a value of 4 is read on the left-side Vertical Resolution scale. When the vertical projection line is once again continued upward, the blue *TW*=3000 Logging Speed curve is reached. At this point, a value of 17 is reached on the left-side Logging Speed scale. A note at the bottom of the chart explains how to adjust the logging speed and running average values obtained from the chart when the low-frequency mode is used.

B_1 Adjustment for Downhole Conditions

A very important adjustment that is required during logging setup is B_1. B_1 is the strength of the CPMG pulses that produce proton 90° tipping and 180° rephasing. The value of B_1 must be corrected for borehole temperature. B_1 must be adjusted and controlled so that $B_{1\text{mod}}$ remains within 5% of the B_1 peak value determined during shop calibration.

Quality Monitoring During Data Acquisition

The MRIL main window on the monitor of the Halliburton Excell-2000 surface acquistion system displays most of the quality indicators in real time during CPMG echo-train acqusition (**Fig. 9.11**). The window includes three columns of parameter values, a raw echo-train graph, and graphs of T_2 distributions and bins. The top section of the first column gives the basic parameters that describe the acquisition, such as tool serial number, activation name, operating frequency, strength of CPMG pulses (in global amplitude), *TW*, number of echoes, and running average. The bottom section of the first column has basic correction factors, such as power correction, gain correction, temperature correction, and Echo 1 and 2 corrections.

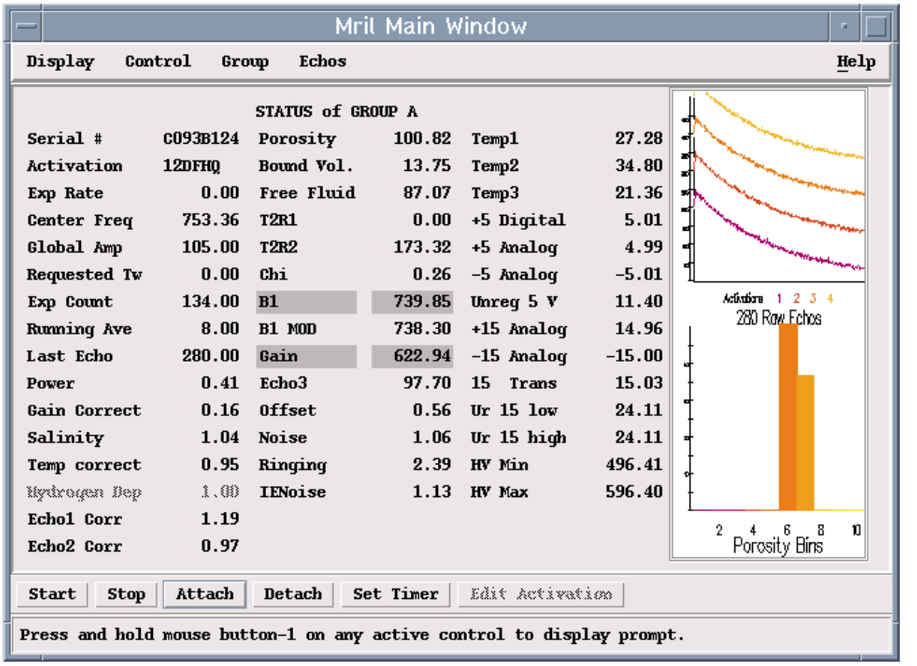

om001629

Figure 9.11—The MRIL main window displays most of the quality indicators so that the log quality can be monitored during CPMG echo-train acquisition. Values shown in this figure are from an echo-train acquisition in a 100-p.u. water calibration tank.

The top section of the second column displays the measured porosity (*MPHI*), calculated *BVI*, and *FFI* based on a defaut $T_{2cutoff}$, (which is 33 ms for sandstone and 92 ms for carbonates). The bottom section of the second column has the primary quality-control indicators, such as Chi, gain, B_1, B_{1mod}, and noise features (*OFFSET*, *RINGING*, *NOISE*, and *IENoise*).

The third column displays auxiliary sensors, such as temperatures (Temp1, Temp2, and Temp3) from electronic cartridge, transmitter, and magnet, respectively, and all the electronics voltage-sensor data. When the value of any quality indicator is outside its allowable range, this window will automatically show a red flash under its name and warn the field engineer.

Log-Quality Display

All of the quality indicators are recorded in the raw data file and are available for playback whenever needed. MRIL log quality can be displayed in different ways and formats, one of which is shown in **Fig. 9.12**. Track 1 includes gamma ray (*GR*), cable speed (*CS*), and tension (*TENS*). Track 2 contains gains for two groups of echo trains described in the next paragraph (*GAINA* and *GAINB*), amplitudes of the corresponding CPMG pulses (*B1A* and *B1B*), and amplitudes of corresponding CPMG pulses corrected for temperature (*B1MODA* and *B1MODB*). Track 3 includes all the voltage sensor data. Track 4 shows the temperatures of the transmitter (*TXTA*), electronic cartridge (*ECTA*), and antenna (*ANTA*). Track 4 also shows phase-correction parameters, such as the phase angles (*PHCOA* and *PHCOB*), the means of the imaginary parts of the echo trains (*PHERA* and *PHERB*), standard deviations of the imaginary parts of the echo trains (*PHNOA* and *PHNOB*). Track 5 includes *NOISE* and *IENoise* for Groups A and B and Frequencies 1 and 2 (*N1A*, *N1B*, *N2A*, *N2B*, *IEN1A*, *IEN1B*, *IEN2A*, and *IEN2B*, where for example, *N1A* is *NOISE* for Group A and Frequency 1). Track 6 includes *OFFSET* and *RINGING* for Groups A and B and Frequencies 1 and 2. Track 7 includes Chi for Group A and B, *MPHI* from Groups A and B, and *BVI* from Group A.

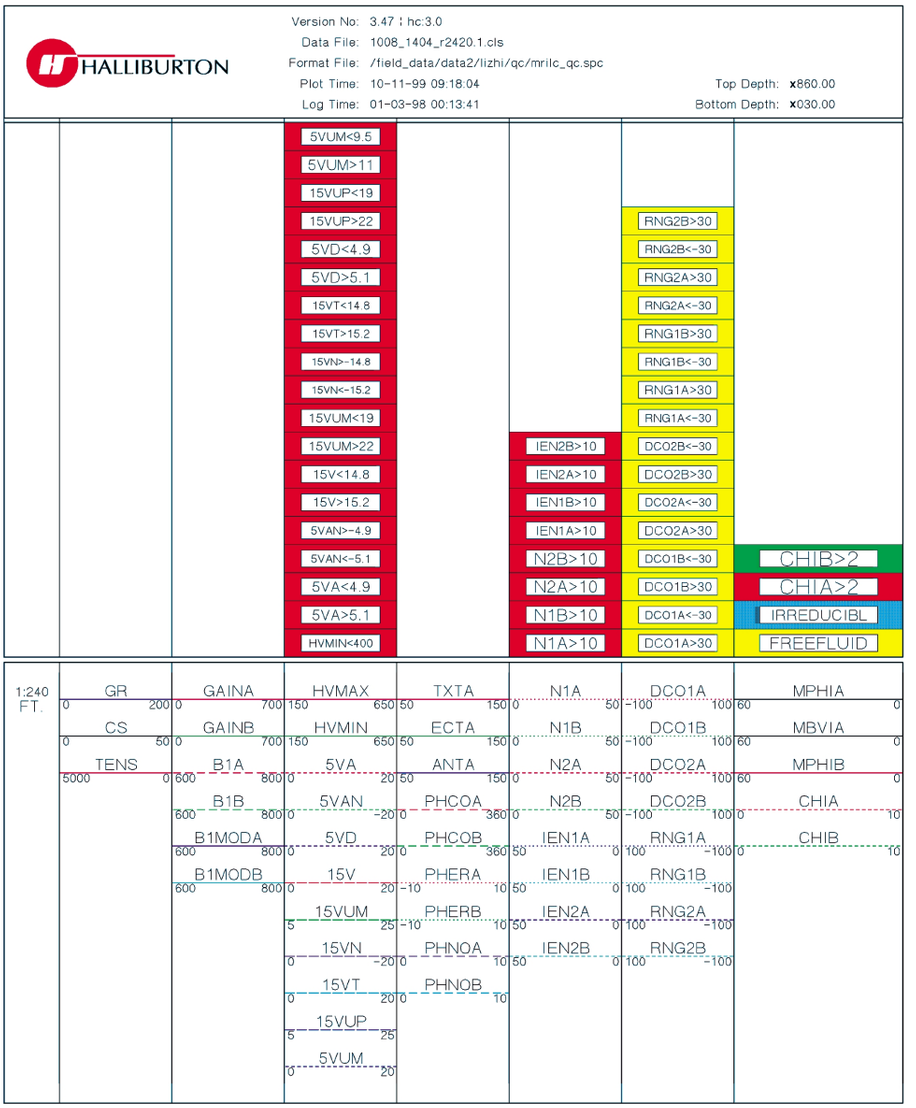

Figure 9.12—The MRIL log quality display includes *GAIN*, *B1*, *B1MOD*, voltage-sensor data, echo-train phase characters, noise features, Chi, and measured *MPHI* and *BVI*, for different group and different frequencies. If the value of any indicator is outside its allowable range, the indicator will be shaded by certain color.

The display Fig. 9.12 can be used for different activations such as C/TP, dual *TW* and dual *TE*. When a C/TP activation is used, Group A represents echo trains acquired with fully polarized *TW* and 1.2-ms *TE*, while Group B represents echo trains acquired with partially polarized *TW* and 0.6-ms *TE*. When dual-*TW* activation is used, group A comprises the long-*TW* echo trains, and Group B comprises the short-*TW* echo trains. When dual-*TE* activation is used, Group A contains the short-*TE* echo trains, and group B contains the long-*TE* echo trains.

All the quality indicators should be checked according to the principles and criteria discussed in previous sections. Indicators, such as the voltage-sensor data, noise features, and Chi, have certain shading if their values are outside of their allowable ranges. In addition, it is important to pay close attention to the difference in the value of the same indicator from different groups. Normally their values should be very similar.

Fig. 9.13 is an example of log quality display for dual-*TW* logging. Checking the log, no abnormal shading is present for voltage-sensor data, noise features, and Chi. All the indicators for Groups A and B at Frequencies 1 and 2, are within their allowable ranges. The phase-correction parameters—*PHCOA*, *PHCOB*, *PHERA*, *PHERB*, *PHNOA*, and *PHNOB*—are small and stable. B_1 and B_{1mod} vary with the *GAIN* changes. B_{1mod} should be further checked against the shop calibration report and must be within 5% of the peak value of the CPMG pulse found during calibration. Cable speed is about 6 ft/min. This speed and running average should be checked with speed chart according to gain, *TW*, and vertical resolution. Track 7 indicates that a T_1 contrast exists between fluids in the logged formation because *MPHIA* is significantly greater than *MPHIB*.

Raw echo data and T_2 distributions can also be displayed at the well site for quick look and quality check, as shown in **Fig. 9.14**. Group data from dual-*TW* logging are displayed for the same well and same interval as shown in Fig. 9.13. The tension data is plotted in the depth track. Tracks 1 and 2 show the bin data for Group A and B, respectively. Tracks 3 and 5 include echo trains from Groups A and B, respectively. Tracks 4 and 6 are T_2 distributions for Groups A and B, respectively. Tracks 7 and 8 are Chi, gain, *MPHI*, and *MBVI* for Group A and B, respectively. The echo trains can clarify some of noise problems, such as high Chi.

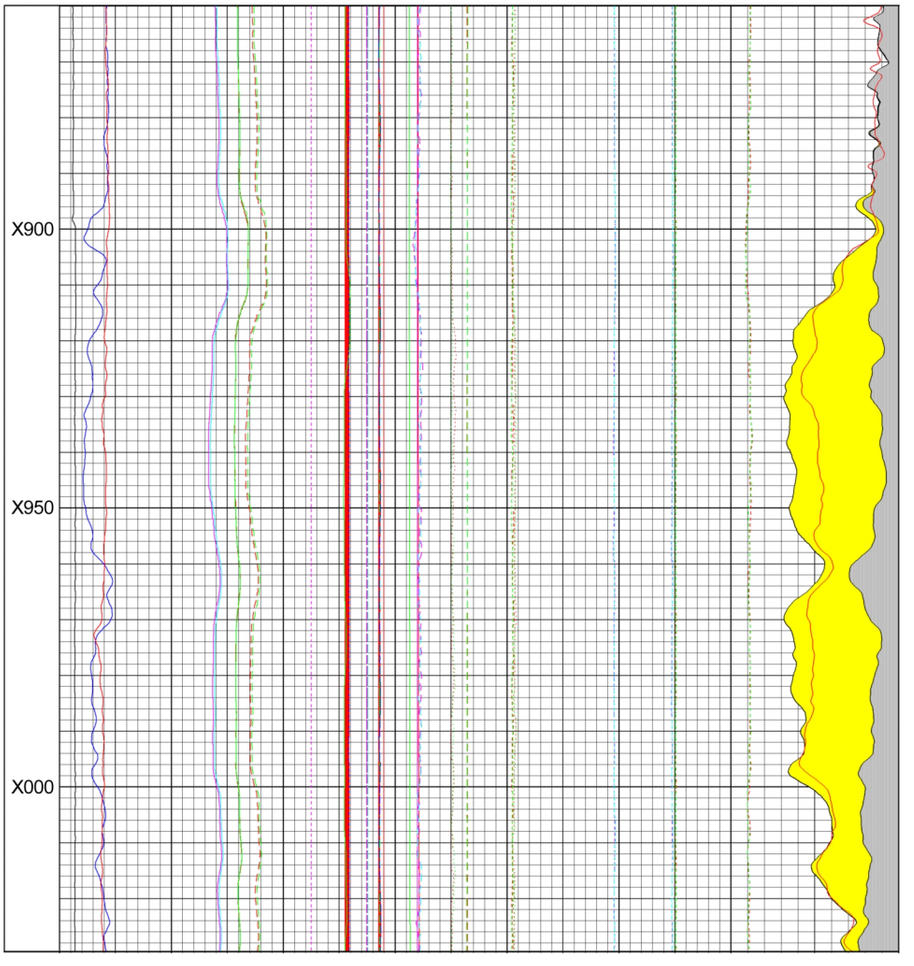

Figure 9.13—This example of a log-quality display for dual-*TW* logging shows no abnormal shading for voltage-sensor data, noise features, and Chi. All the indicators for Group A and B and Frequencies 1 and 2 are within their allowable ranges. B_1 and B_{1mod} vary with the *GAIN* changes. *MPHIA*, in Track 7, is greater than *MPHIB*, which means that a T_1 contrast exists between fluids in the logged formation. The log quality can be completely verified if B_{1mod} is checked with the B_1 found at calibration and if the logging speed is verified with the speed chart and measured gain.

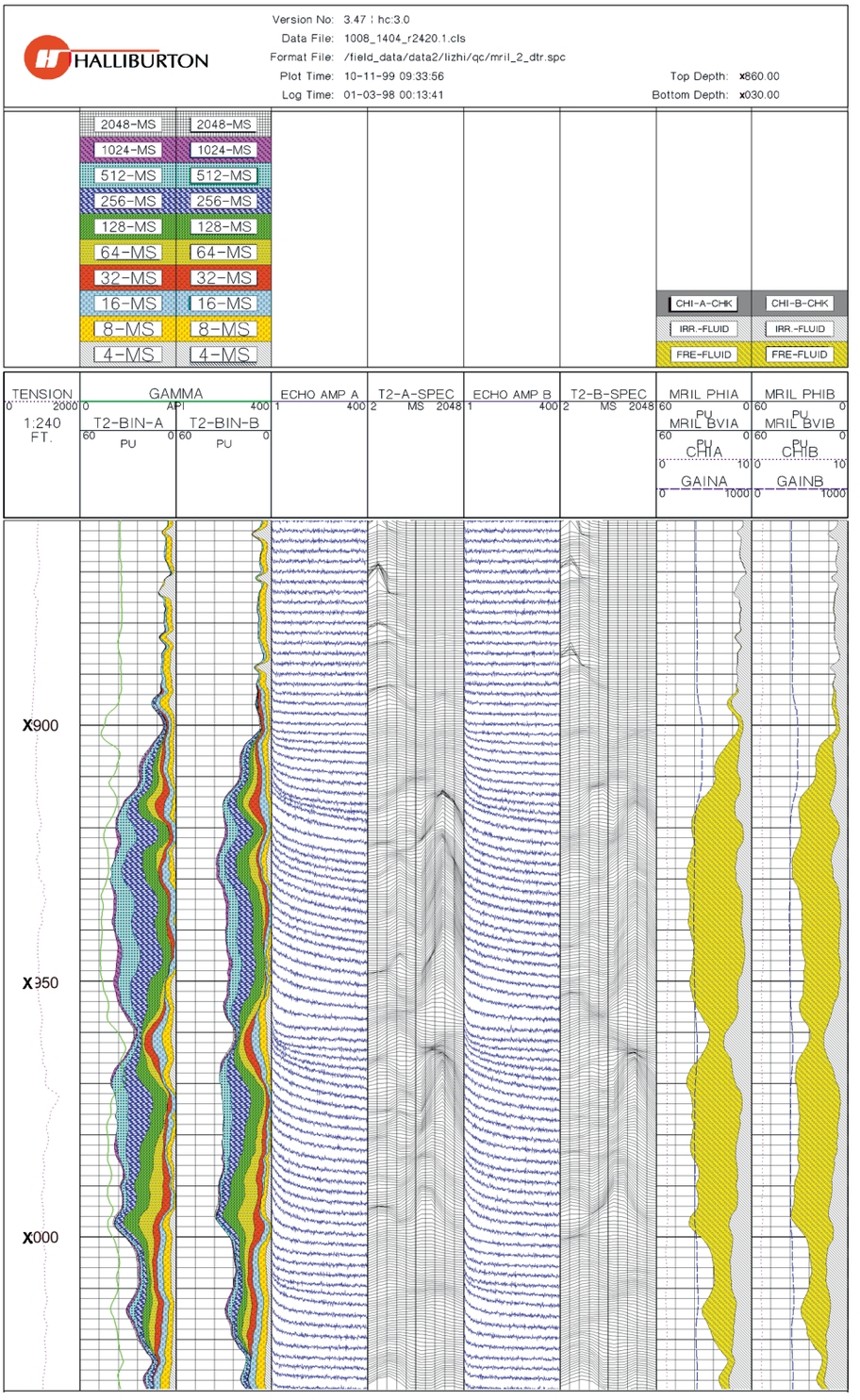

Figure 9.14—This group data, which displays the dual-*TW* logging for the same well and same interval as shown in Fig. 9.10 is available at well site for both quick-look and quality check. The tension data is plotted in the depth track. Tracks 1 and 2 show the bin data for Groups A and B, respectively. Tracks 3 and 5 include echo trains from Groups A and B, respectively. Tracks 4 and 6 are T_2 distributions for Groups A and B, respectively. Tracks 7 and 8 are Chi, *GAIN*, *MPHI*, and *MBVI* for Groups A and B, respectively. Some of the noise problems, such as high Chi, can be clarified by displaying the echo trains.

Post-Logging Quality Check

The MRIL responses should be checked against other logs when other logs are available. Two equations are essential for understanding MRIL tool responses and their relationships to petrophysical parameters:

$$MPHI = \phi_e HI[1 - e^{-(\frac{TW}{T_1})}] \quad (9.7)$$

$$MSIG = MPHI + MCBW \quad (9.8)$$

where

$MPHI$	=	effective porosity measured by the MRIL tool
ϕ_e	=	effective porosity of the formation
HI	=	hydrogen index of the fluid in the effective porosity system
TW	=	polarization time used during logging
T_1	=	longitudinal relaxation time of the fluid in the effective porosity system
$MSIG$	=	total porosity measured by MRIL total-porosity logging
$MCBW$	=	clay-bound water measured by the MRIL tool with TE = 0.6 ms and partial-polarization activation

MPHI may not equal effective porosity because of the effects of both hydrogen index and long T_1 components. The MRIL-Prime measurement process usually eliminates the porosity underestimation that results from the T_1 effects. The measurements are still affected by *HI*.

MPHI Relation to *MSIG* on Total-Porosity Logs

MRIL effective porosity (*MPHI*) is always less than MRIL total porosity (*MSIG*), except in very clean formations. In the latter case, clay-bound-water porosity (*CBW*) is zero; thus, *MPHI* equals *MSIG*. In general, $MPHI \leq MSIG$.

MPHI TW_S Relation to *MPHI* TW_L on Dual-TW Logs

Porosity measured with a short polarization time ($MPHI_{TW_S}$) is usually underestimated and thus will be less than porosity measured with a longer polarization time ($MPHI_{TW_L}$). Such is the case even if TW_L is not long enough for full polarization. This underestimation is especially prevalent in hydrocarbon-bearing zones. So, in general, $MPHI_{TW_S} \leq MPHI_{TW_L}$.

MPHI TE_S Relation to *MPHI* TE_L on Dual-TE Logs

Because of diffusion effects, a T_2 distribution obtained with a long *TE* will appear to be shifted to the left of a distribution obtained with a shorter *TE*. Because some of the T_2 components may be shifted out of the very early bins, some porosity in the early bins will not be recorded with a long *TE*. Therefore, in general, $MPHI\ TE_L \leq MPHI\ TE_S$.

Agreement between *MPHI* and Neutron-Density Crossplot Porosity

In clean, water-filled formations, *MPHI* should be approximately equal *XPHI*, the neutron-density crossplot porosity. In clean gas zones, *MPHI* values obtained from stationary measurements should be near neutron porosity values calculated with the correct matrix. In shaly sands, *MPHI* should approximately equal density porosity calculated with the correct grain density.

Knowledge of the mud type is essential in analyzing the response of an MRIL tool. Because of the tool's relatively shallow depth of investigation, the tool investigates primarily the flushed zone.

Effects of Hydrogen Index and Polarization Time on *MPHI*

MPHI may not equal effective porosity because of the effects of both hydrogen index and long T_1 components. The MRIL Prime measurement process usually eliminates the porosity underestimation that results from the T_1 effects. The measurements are still affected by *HI*. In clean gas zones, *MPHI* values obtained from stationary measurements should be near neutron porosity values calculated with the correct matrix.

Reference

1. Goelman, G., and Prammer, M.G., 1995, The CMPG pulse sequence in strong magnetic field gradients with applications to oil-well logging: *Journal of Magnetic Resonance*, Series A, v. 113, p. 11-18.

Glossary

A

Activation
Programmed command sequences that control how MRIL tools polarize formations and measure NMR properties of those formations. Activations may contain single or multiple CPMG sequences.

Activation, Dual-*TE*
An activation that enables the acquisition of two CPMG echo trains at different echo spacings (*TE*) but at identical re-polarization times (*TW*). Data acquired with dual-*TE* activations are used for hydrocarbon identification. The hydrocarbon identification technique takes advantage of the different diffusivities of the different reservoir fluids. Because the MRIL tool produces a magnetic field gradient, the T_2 of each fluid has a component that depends on its diffusivity and on the *TE* used in the NMR measurements. Increases in *TE* will shift the T_2 spectrum toward smaller T_2 values, and the shift will be different for each fluid type. Separation in T_2 space follows from the diffusion relaxation term $T_{2\text{diffusion}}$

$$\frac{D(\gamma G TE)^2}{12}$$

This activation has been successfully used in detecting and quantifying medium-viscosity oils.

Activation, Dual-*TW*
An activation that enables the acquisition of two CPMG echo trains at different wait times (*TW*) and identical echo spacings (*TE*). Data acquired with dual-*TW* activations are used to improve detection of gas and light oils. This detection is based on the fact that the T_1 of gas and light oils is much larger than the T_1 of water in a formation. Polarization p is proportional to *TW*, i.e.,

$$p \propto 1 - e^{-TW/T_1}$$

The smaller *TW* is chosen such that the NMR signal from the formation water is completely polarized, but the oil and/or gas signals are not. The longer *TW* is chosen so that most of the hydrocarbon signals are also polarized. The signal left after the subtraction of the two echo trains or the two resulting T_2 distributions contains only signal from the hydrocarbon. This method can be used to quantify oil and gas volumes.

Activation, Standard-T_2

An activation that enables the acquisition of a CPMG echo train with a *TW* with which formation fluids can be fully polarized, and with a *TE* with which the diffusion effects on T_2 can be eliminated. Typical values for this activation are *TE* = 1.2 ms, 3 s ≤ *TW* ≤ 6 s, and NE = 300. This activation is mainly used for determining "effective" porosity and permeability.

Activation, Total-Porosity

An activation that enables the acquisition of two CPMG echo trains with different echo spacings (*TE*) and different wait times (*TW*). One echo train is acquired with *TE* = 0.6 ms and *TW* = 20 ms (only partial polarization is achieved) and is used for quantifying the small pores, which are at least in part associated with clay-bound water. The other echo train is acquired with *TE* = 0.9 or 1.2 ms and with a *TW* that is sufficiently long so that full polarization is achieved. This echo train is used to determine effective porosity, and the summation of the two porosities (clay-bound and effective) provides total porosity information. The combination of *TE* and *TW* used to acquire the latter echo train constitutes a standard T_2 activation.

B

$\mathbf{B_0}$ Static magnetic field generated by the NMR tool. It may also be designated as $\mathbf{B_z}$. The symbols B_0 and B_z are use when referring to the scalar value of the field.

$\mathbf{B_1}$ Oscillating magnetic field generated by a radio-frequency (RF) resonant circuit. This field is applied in the plane perpendicular to $\mathbf{B_0}$ and is used to flip the magnetization by 90° and 180°. B_1 refers to the magnitude of the field.

Bound Water

A somewhat loosely defined term that can refer either to water that is not producible or water that is not displaceable by hydrocarbons. Bound water consists of both capillary-bound water and clay-bound water.

Bulk Volume Irreducible (*BVI*)

The fractional part of formation volume occupied by immobile, capillary-bound water.

Bulk Volume Irreducible, Cutoff (*CBVI*)

BVI is estimated by summing the MRIL T_2 distribution up to the time $T_{2cutoff}$.

Bulk Volume Irreducible, Spectral (*SBVI*)

BVI obtained by the MRIL spectral method. This *BVI* estimate is determined from a model that assigns a percent of the porosity in each spectral bin to bound water. Various models are available for use with this method.

Bulk Volume Movable (*BVM*)

The fractional part of formation volume occupied by movable fluids, also referred to as free fluid index (*FFI*). It can be water, oil, gas, or a combination.

Bulk Volume Water (*BVW*)

The fractional part of formation volume occupied by water. BVW is the product of water saturation and total porosity.

BVI See *Bulk Volume Irreducible*.

BVM See *Bulk Volume Movable*.

BVW See *Bulk Volume Water*.

B_z see **B_0**

C

Carr-Purcell-Meiboom-Gill Pulse Sequence (CPMG)

A pulse sequence used to measure T_2 relaxation time. The sequence begins with a 90° pulse followed by a series of 180° pulses. The first two pulses are separated by a time period τ, whereas the remaining pulses are spaced 2τ apart. Echoes occur halfway between 180° pulses at times 2τ, 4τ, ... , where 2τ equals *TE*, the echo spacing. Decay data is collected at these echo times. This pulse sequence compensates for the effects of magnetic field inhomogeneity and gradients in the limit of no diffusion, and reduces the accumulation of effects of imperfections in the 180° pulses as well.

CBVI See *Bulk Volume Irreducible, Cutoff*.

CBW See *Clay-Bound Water*.

Clay-Bound Water (*CBW*)

Immobile structurally bound water on the surface of clay minerals. Clay surfaces are electrically charged due to ionic substitutions in the clay structure, which allow them to hold substantial amounts of ionically bound water. This water is referred to as water of adsorption or surficially bound water. Clay-bound water also includes water of capillary condensation in the micropores in clay aggregates. *CBW* is a function both of the surface area of the clay and the charge density on its surface. Clay consists of extremely fine particles, so it has a very high surface area. *CBW* contributes to the electrical conductivity of the sand but not its hydraulic conductivity. Clay-bound water cannot be displaced by hydrocarbons and will not flow. It has very short T_1 and T_2 times.

CMR™ Tool*

The Schlumberger Combinable Magnetic Resonance logging tool was introduced in 1995. The CMR tool is a pad device with a sensitive volume that extends about 1 in. in front of the pad face. This very shallow depth of investigation makes the tool very sensitive to invasion, mud cake, and borehole rugosity.

The 6-in. long CMR antenna is placed on the center of a 12-in.long magnet. This arrangement provides 3 in. of magnet length to polarize protons before they are measured.

The sensitive volume of the CMR tool is a 1-in. diameter, 6-in. long cylinder. The CMR tool operates in single-frequency mode.

CPMG See *Carr-Purcell-Meiboom-Gill Pulse Sequence*.

**Trademark of Schlumberger Technology Corporation*

D

D See *Diffusion Constant*.

DIFAN See *Diffusion Analysis*.

Differential Spectrum Method (DSM)
An interpretation method based on dual-*TW* measurements. DSM relies on the T_1 contrast between water and light hydrocarbon to type and quantify light hydrocarbons. The differential spectrum is the difference between the two T_2 distributions (spectra) obtained from dual-*TW* measurements with identical *TE*. DSM interpretation is performed in the T_2 domain.

Diffusion
Process by which molecules or other particles intermingle and migrate because of their random thermal motion.

Diffusion Analysis (DIFAN)
An interpretation method based on dual-*TE* measurements. DIFAN relies on the diffusion contrasts between water and medium-viscosity oil to type and quantify oils. The data for DIFAN are acquired through dual-*TE* logging with a single, long polarization time.

Diffusion Constant (*D*)
Also known as diffusivity. *D* is the mean square displacement of molecules observed during a period. *D* varies with fluid type and temperature. For gas, *D* also varies with density and is therefore pressure dependent. *D* can be measured by NMR techniques, in particular by acquiring several CPMG echo trains with different echo spacings in a gradient magnetic field.

Diffusion Limit, Fast
The case where protons carried across a pore by diffusion to the surface layer relax at the surface layer at a rate limited by the relaxers at the surface and not by the rate at which the protons arrive at the surface. The diffusion process happens much faster than that of the fluid protons relaxing in a pore. Thus, the magnetization in the pore remains uniform, and a single T_1 or T_2 can be used to describe the magnetization polarization or decay for an individual pore. This assumption is the basis of the conversion of T_1 and T_2 distributions to pore-size distributions.

Diffusion Limit, Slow
The case where protons carried across a pore by diffusion to the surface layer relax at the surface layer at a rate limited not by the relaxers at the surface but by the rate at which the protons arrive at the surface. Thus, diffusion does not homogenize the magnetization in the pore space. Multiple exponential decays then are needed to characterize the relaxation process within a single pore.

Diffusion Relaxation
A relaxation mechanism caused by molecular diffusion in a gradient field during a CPMG measurement. Molecular diffusion during a CPMG or other spin echo pulse sequence causes signal attenuation and a decrease in the apparent T_2. This attenuation can be quantified and the fluid diffusion coefficient measured if a known magnetic field gradient is applied during the pulse sequence. Diffusion only affects the T_2 measurement, not the T_1 measurement.

Diffusion, Restricted

Effect of geometrical confinement of pore walls on molecular diffusive displacement. NMR diffusion measurements estimate the diffusion constant from the attenuation caused by molecular motion over a very precise time interval. If the time interval (*TE* in the CPMG sequence) is large enough, molecules will encounter the pore wall or other barrier and become "restricted." The apparent diffusion constant will then decrease.

DSM See *Differential Spectrum Method*.

E

Echo Spacing (*TE*)

In a CPMG sequence, the time between 180° pulses. This time is identical to the time between adjacent echoes.

EDM See *Enhanced Diffusion Method*.

Enhanced Diffusion Method (EDM)

An interpretation method based on diffusion contrasts between different fluids. Enhancement of the diffusion effect during echo-data acquisition allows water and oil to be separated on a T_2 distribution generated from data acquired with a selected long *TE*. For typing medium-viscosity oils, EDM uses CPMG measurements acquired through standard T_2 logging with a long *TE*. For quantifying fluids, EDM needs data acquired through dual-*TW* logging with a long *TE* or through dual-*TE* logging with a long *TW*.

F

FFI See *Free Fluid Index*.

FID See *Free Induction Decay*.

Free Fluid Index (*FFI*)

The fractional part of formation volume occupied by fluids that are free to flow. A distinction must be made between fluids that can be displaced by capillary forces, and fluids that will be produced at a given saturation. In MRIL logging, *FFI* is the *BVM* estimate obtained by summing the T_2 distribution over T_2 values greater than or equal to $T_{2cutoff}$.

Free Induction Decay (FID)

The FID is the transient NMR signal resulting from the stimulation of the nuclei at the Larmor frequency, usually after a single RF pulse. The characteristic time constant for a FID signal decay is called T_2^*. T_2^* is always significantly shorter than T_2.

G

G The strength of the gradient magnetic field seen by the NMR measurement.

Gain Represents the relative voltage gain of the system: both the antenna gain and electronics gain. Because the electronics gain is quite stable, the gain is sensitive to antenna loading, *Q*. At the beginning of each pulse sequence, a measured low-level signal is sent from a test antenna (known as the B1 loop) to the main antenna, and the received signal is processed just as echoes would be processed. The received signal is then measured and compared to the original input signal. This provides the gain. The gain is used to compensate for signal losses due to *Q* loading effects of the borehole and due to system drift.

Gauss Unit of magnetic field strength. 10,000 gauss = 1 tesla. The earth's magnetic field strength is approximately 0.5 gauss.

Gradient
Amount and direction of the rate of change in space of some quantity, such as magnetic field strength.

Gradient Magnetic Field
A magnetic field whose strength varies with position. The MRIL tool generates a gradient magnetic field that varies in the radial direction. Within the small sensitive volume of the MRIL tool, this gradient can be regarded as linear and is usually expressed in gauss/cm or Hz/mm.

Gyromagnetic Ratio (γ)
Ratio of the magnetic moment to the angular momentum of a particle. A measure of the strength of the nuclear magnetism. It is a constant for a given type of nucleus. For the proton, $\gamma = 42.58$ MHz/Tesla.

H, I

Hydrogen Index (*HI*)
The ratio of the number of hydrogen atoms per unit volume of a material to the number hydrogen atoms per unit volume of pure water at equal temperature and pressure. The *HI* of gas is a function of temperature and pressure.

HI See *Hydrogen Index*.

Inversion Recovery
A pulse sequence employed to measure T_1 relaxation time. The sequence is "180° - t_i 90° -Acquisition - *TW*," where $i = 1 \ldots N$. The first 180° pulse inverts the magnetization 180° relative to the static magnetic field. After a specific wait time (t_i , the inversion time), a 90° pulse rotates the magnetization into the transverse plane, and the degree of recovery of the initial magnetization is measured. After a wait time *TW* to return to full polarization, the sequence is repeated. To produce sufficient data for measurement of T_1, this sequence must be repeated many times with different t_i and thus is very time-consuming.

L

Larmor Equation

$f = \gamma B_0 / 2\pi$. This equation states that the frequency of precession, f, of the nuclear magnetic moment in a magnetic field is proportional to the strength of the magnetic field, $\mathbf{B}_0$, and the gyromagnetic ratio, γ.

Larmor Frequency

The frequency at which the nuclear spins precess about the static magnetic field, or the frequency at which magnetic resonance can be excited. This frequency is determined from the Larmor equation.

M

M Net magnetization vector. See *Magnetization*.

$\mathbf{M}_0$ Equilibrium value of the net magnetization vector directed along the static magnetic field.

Magnetization, Longitudinal ($\mathbf{M}_z$)

Component of the net magnetization vector along the static magnetic field $\mathbf{B}_0$ (or $\mathbf{B}_z$).

Magnetic Moment

A measure of the magnetic properties of an object or particle (the proton for example) that causes the object or particle to align with the static magnetic field.

Magnetic Resonance (MR)

Magnetic resonance describes a group of phenomena more general than NMR. It also includes nuclear quadruple resonance (NQR) and electron paramagnetic resonance (EPR). Because the term nuclear is often related with radioactivity, the term MR is used to avoid this connotation. (NMR means nuclear magnetic resonance, i.e., the term *nuclear* refers to the magnetic resonance of an atomic nucleus.)

Magnetic Resonance Image Logging (MRIL)

The name for the specific NMR logging tool developed by NUMAR Corporation in the mid-1980s. The MRIL tool uses a permanent gradient magnetic field and an orthogonal RF magnetic field (for generating CPMG pulse sequences) to select concentric cylindrical shell volumes for NMR measurements.

Magnetic Resonance Imaging (MRI)

Refers to imaging with NMR techniques. Most MRI machines use a pulsed gradient magnetic field that permits one to localize the NMR signals in space. MRI is used on core samples and in core flooding or flow mechanism studies.

Magnetic Susceptibility (χ)

The measure of the ability of a substance to become magnetized. Differences in magnetic susceptibility of the pore fluids and the matrix cause internal field gradients.

Magnetization (M)

A macroscopic vector quantity resulting from the alignment of the nuclear magnetic moment with the static magnetic field. This vector projected into the plane

perpendicular to the static magnetic field is known as the transverse magnetization. It is this quantity that is observed by NMR.

MAP A software program developed by NUMAR for inverting echo-train data to a T_2 distribution. The inversion algorithm used in MAP is based on singular-value decomposition (SVD).

MCBW *CBW* estimate obtained by summing the T_2 distribution obtained from partially polarized CPMG echo trains acquired with a TE = 0.6 ms and TW = 20 ms.

MPERM

Permeability estimate obtained from MRIL measurements. Many formulas are in use for determining permeability from NMR measurements. The two most commonly used are the Coates equation and the Schlumberger-Doll Research (SDR) equation. According to the Coates equation,

$$k = \left(\frac{\phi}{C}\right)^4 \left(\frac{FFI}{BVI}\right)^2$$

where C is an empirically determined constant.

According to the SDR equation,

$$k = a\phi^4 T_{2gm}^2$$

where $T_{2gm}$is the geometric mean of the T_2 distribution, a is constant, and ϕ is porosity.

MPHI The porosity estimate obtained by summing the T_2 distribution over T_2 values greater than or equal to 4 ms and less than or equal to the highest T_2 value in the distribution, e.g., 1024 ms. *MPHI* is often referred to as the *effective porosity*.

MR See *Magnetic Resonance*.

MRI See *Magnetic Resonance Imaging*.

MRIAN

See *MRIL Analysis*.

MRIL See *Magnetic Resonance Imaging Logging.*

MRIL Analysis (MRIAN)

An interpretation method that incorporates deep resistivity data, MRIL standard T_2 logging measurements, and the dual water model. MRIAN determines water-filled porosity in the virgin zone, which can be compared with the flushed-zone results provided by MRIL stand-alone analysis techniques, such as TDA, EDM, and DIFAN.

MRIL B_0 Radial Dependence

The static magnetic field $\mathbf{B_0}$ of the MRIL tool is a gradient field, whose strength B_0 decreases as the distance from the tool axis increases. The radial dependence is $B_0 \propto r^{-2}$, where r is the distance from the axis of the tool.

MRIL B_0 Temperature Dependence

The static magnetic field $\mathbf{B}_0$ of the MRIL tool is generated by a permanent magnet. The temperature dependence of the strength of $\mathbf{B}_0$ arises from the fact that the magnetization of the permanent magnet is temperature dependent. The mean field approximation gives T^{-1} temperature dependence in the temperature regime, typical of borehole conditions, where T is the absolute temperature.

MRIL B_1 Temperature Correction

The $\mathbf{B}_1$ 90° pulse is determined during the MRIL shop calibration done at room temperature. Because of the difference between room temperature and downhole temperature, the energy of the B_1 pulse needed for 90° tipping downhole will be different from the energy determined at the shop; therefore, a temperature correction for $\mathbf{B}_1$ is needed.

MRIL Borehole Washout Effect

An MRIL log will show the effect of serious borehole washouts when the sensitive volume intersects the borehole. An increase in *MPHI* and *BVI* will be seen in the log response. The MRIL tool responds to water-based mud as bound formation fluid because of the large quantity of dispersed clays and the associated water of hydration. Oil-based mud exhibits short relaxation times because of the large quantities of emulsifiers used to control water.

Washouts may be affecting an MRIL log if

- A comparison of caliper measurements with the depth of investigation for the appropriate downhole temperature indicates that the borehole is intersecting the sensitive volume of the tool.
- An abnormally large *BVI* is observed.
- An increase in *MPHI* corresponds to an increase in the caliper and *MBVI* = *MPHI*.

MRIL-C Tool

NUMAR's second-generation MRIL tool introduced in 1994. This tool is capable of performing multiple experiments simultaneously (e.g., the MRIL-C has dual-frequency capability, and the MRIL-C^+ has triple-frequency capability). The MRIL-C/TP tool, which was introduced by NUMAR in 1996, provides an estimate of total porosity as well as effective porosity. The C/TP tool is able to measure total porosity because the tool can use a reduced *TE* (0.6 ms). Furthermore, because the tool experiences reduced ringing, the first echo contains valuable information.

Because MRIL-C tools operate in either dual- or triple-frequency mode, successive measurements at different frequencies can follow one another more quickly. Each MRIL frequency excites a signal from a different physical locations and thus it is not necessary to wait for repolarization to occur in one location before making a measurement in another location. Alternating between frequencies allows more measurements to be made in a given time, thus permitting logging speed to be increased without reducing *S/N*, or permitting *S/N* to be increased without reducing logging speed.

MRIL Depth of Investigation

The depth at which the MRIL tool provides information about. Because the Larmor frequency is a function of B_0 and B_0 is radially dependent, the Larmor frequency is

also radially dependent and thus defines the depth of investigation of the MRIL tool. Furthermore, because B_0 is also temperature-dependent, it follows that the Larmor frequency and thus the depth of investigation are also temperature-dependent when a fixed $\mathbf{B}_1$ frequency is used, which is always the case. As the temperature of the magnet increases, B_0 decreases, and the depth of investigation decreases accordingly (e.g., a depth of investigation of about 16 in. at 25ºC decreases to about 14 in. at 150ºC). The variation of depth of investigation with temperature for MRIL tools is discussed and displayed in NUMAR literature and charts.

MRIL-Prime Tool

NUMAR's latest generation of MRIL tool introduced in 1998. This tool is capable of performing multiple experiments at up to nine frequencies. By alternating between nine frequencies, measurements can be made at a much higher rate. The MRIL-Prime provides measurements of clay-bound water, effective porosity, capillary-bound water, and hydrocarbon typing in just one pass. Besides saving time, acquiring all the data in one pass eliminates depth-shift errors.

The MRIL-Prime tool has additional pre-polarization magnets placed above and below the antenna that allow for full polarization of the fluids. This pre-polarization design can provide 12 s of polarization at logging speeds as high as 24 ft/min. Furthermore, the capability of the tool to fully polarize fluids at high logging speeds and obtain a full T_2 distribution without any corrections makes the logging results much less sensitive to certain job-design parameters. Planning logging jobs for earlier tools required some knowledge of the time needed to polarize fluids. The MRIL-Prime tool can simply handle the longest polarization times without reducing logging speed. Thus, this tool can be run much like standard triple-combo tools—just run the tool to the bottom of the hole and log up without special passes in the hole and without having to subsequently assemble data from different passes. This is why the MRIL-Prime tool is the first NMR device that can realistically be considered a "primary formation evaluation" logging tool.

MRIL Sensitive-Volume Thickness

The thickness of the zone for which the MRIL tool provides information. The thickness of the sensitive volume for the MRIL tool is approximately 1 mm and is a function of the gradient strength of the $\mathbf{B}_0$ field and the frequency band of the $\mathbf{B}_1$ field.

MSIG Porosity estimate obtained by combining data from dual-*TE* logging with *TE* = 0.6 and 1.2 ms. *MSIG* should agree well with total porosity measured on cores. *MSIG* = *MCBW* + *MPHI*.

Mud Doping

The practice of adding magnetite to the drilling mud. With the now obsolete NML tool, doping was essential to kill the borehole signal. However, doping the mud with a paramagnetic substance to change the NMR properties of invading mud filtrate may still be desirable. For instance, if the invaded zone is flushed with paramagnetic ions, then the bulk relaxation time of the brine is shortened, and water signals are killed. Thus, only oil signals remain, and residual oil saturation can be determined through NMR measurements. $MnCl_2$, has recently been shown to be a cost-effective doping agent for this application.

$\mathbf{M}_x$ See *Transverse Magnetization*.

$\mathbf{M}_z$ See *Longitudinal Magnetization*.

N

N E Number of echoes in a CPMG echo train.

NML™ Tool*

The Nuclear Magnetic Logging tool, an obsolete NMR logging tool that utilized the earth's magnetic field. The NML tool measured the precession of hydrogen protons in the earth's magnetic field after the alignment of protons with a superimposed magnetic field. The sensitive volume of the NML was not a thin cylindrical shell, but a full cylinder centered around the tool; therefore, the measurement contained borehole signals. Operation of the NML required special doping of the borehole fluids to eliminate the signal from the protons in the borehole.

NMR See *Nuclear Magnetic Resonance*.

Nuclear Magnetic Resonance (NMR)

NMR, as a physical phenomenon, is the absorption or emission of electromagnetic energy by nuclei in a static magnetic field, after excitation by a stable RF magnetic field. NMR, as an investigative tool, is a method that uses the NMR phenomenon to observe the static and dynamic aspects of nuclear magnetism. The method requires a static magnetic field to orient nuclear magnetic moments, and an orthogonal oscillating field (at RF frequencies) to excite the nuclear magnetic moments. The frequency of the oscillating field must satisfy the Larmor resonance condition.

NMR can be used to detect molecular structures and probe molecular interactions. It is a major chemical spectroscopic technique with many applications, including probing properties of fluids in porous media.

Despite the term *nuclear*, NMR does not involve radioactivity.

P

PAP See *Phase Alternate Pairs*.

Paramagnetic Materials

Materials with a small but positive magnetic susceptibility. The addition of a small amount of paramagnetic material to a substance may greatly reduce the relaxation times of the substance. Most paramagnetic substances possess an unpaired electron and include atoms or ions of transition elements (e.g., manganese and vanadium) or rare earth elements. Oxygen (O_2) is also paramagnetic and contributes to the relaxation of water. Paramagnetic substances are used as contrast agents in medical MR imaging and to dope the borehole fluids in some applications of NMR logging. Copper sulfate ($CuSO_4$) is used to dope the water in a calibration tank to reduce water relaxation times, thereby significantly reducing MRIL calibration time.

Permeability, Absolute

A measure of the ability of a rock to conduct a fluid or gas through its interconnected pores when the pores are 100% saturated with that fluid. Measured in darcies or millidarcies (md).

Permeability, Effective

The capability of a rock to conduct a fluid in the presence of another fluid, immiscible with the first, is called its effective permeability to that fluid. Effective

**Trademark of Schlumberger Technology Corporation.*

permeability not only depends on the permeability of the rock itself, but also on the relative amounts of the different fluids in the pores.

Permeability, Relative

The ratio between the effective permeability to a given fluid at a partial saturation and the permeability at 100% saturation. Relative permeability is the ratio of the amount of a specific fluid that will flow at a given saturation, in the presence of other fluids, to the amount that would flow at a saturation of 100%, other factors remaining the same.

Phase Alternate Pairs (PAP)

A method of acquiring two echo trains that are 180° out of phase. The change in echo-train phase is accomplished by changing the phase of the initial 90° pulse in the CPMG sequence by 180°. The effect of this change is to reverse the sign of the echo data. In processing, the two echo trains are subtracted to eliminate the effects of ringing and baseline offset.

Polarization Time (*TW*)

See *Wait Time*.

Pore-Size Distribution (From T_2 Distribution)

A rock generally consists of a large number of pores of different sizes. Neglecting interpore fluid exchange, relaxation in a rock saturated with a single-phase fluid can be viewed as relaxation of a collection of isolated pores of different sizes. The relaxation distribution is a superposition of the relaxation rates of the individual pores. In the fast diffusion limit, the T_2 of a fluid in a single pore is determined by

$$\frac{1}{T_2} = \rho_2 \frac{S}{V} + \frac{1}{T_{2B}}$$

Where T_{2B} is the bulk fluid relaxation rate. For smaller pores as found in most sandstones, $\frac{1}{T_{2B}} << \rho_2 \frac{S}{V}$ and can be ignored.

When two or three fluid phases are present, however, the non-wetting phases occupy the larger pores while the wetting phase occupies the smaller pores because of the capillary effect. In addition, the relaxation rate of non-wetting fluids is smaller than that of wetting fluids because the T_2 of non-wetting fluid does not include the surface term. Both the capillary and surface effect result in shorter T_2 for wetting-phase fluids compared to the T_2 for the same fluid types in bulk. Much less change is expected for the non-wetting fluid T_2. Thus, different fluid phases can be identified by carefully analyzing the T_2 distribution or by using relaxation-weighting techniques (such as dual *TW* and dual *TE*) for multiphase saturation cases.

Porosity, Effective

A somewhat arbitrary term sometimes used to refer to the fractional part of formation volume occupied by connected porosity and excluding the volume of water associated with clay. In NMR logging, the term has usually been associated with porosity that decays with T_2 greater than 4 ms.

Effective porosity often refers to the interconnected pore volume occupied by movable fluids, excluding isolated pores and pore volume occupied by adsorbed water. Effective porosity contains fluid that may be immovable at a given saturation or capillary pressure. For shaly sands, effective porosity is the fractional volume of a formation occupied by only fluids that are not clay bound and whose hydrogen indexes are 1.

Porosity, Total

The total pore volume occupied by fluids in a rock. Includes isolated non-connected pores and volume occupied by adsorbed, immobile fluids. For a shaly sand formation, total porosity is the fractional part of formation volume occupied by both clay-bound and non-clay-bound fluids.

Precession

The motion of the axis of a spinning body so as to trace out a cone. It is caused by the application of a torque tending to change the direction of the rotation axis. The precession of the proton spin axis about the $\mathbf{B}_0$ field axis occurs at the Larmor frequency.

Proton

A positively charged elementary particle that provides the charge in an atomic nucleus. A hydrogen nucleus contains one proton. The symbol ^{1}H is used to designate the hydrogen nucleus.

Proton Density

The concentration of mobile hydrogen atoms per unit volume. NMR data can be corrected for hydrogen density changes by dividing the apparent NMR porosity by the appropriate hydrogen index.

Pulse, Hard

A term used to describe a high-power, short-duration RF pulse used in NMR pulse sequences. In contrast, soft pulses are usually low-power, long-duration RF pulses. Hard pulses are usually rectangular shaped in the time domain and excite wide frequency bands often extending beyond the desired resonance frequency. Hard pulses generally make good use of available RF power but exhibit poor frequency selectivity. Because of the narrower pulse widths, hard pulses are more suitable for pulse sequences that require short echo spacing (*TE*). See *Pulse Shaping* for frequency selectivity.

Pulse Shaping

The amplitude, shape, and width of RF pulses define the frequency selectivity of an NMR measurement (see also *Hard Pulse* and *Soft Pulse*). Soft pulses are shaped to improve their frequency selectivity as well as other parameters. How shaping brings about these improvements can be easily understood by taking the Fourier transform of RF pulses. A hard pulse is rectangular in shape and excites a wide range of frequencies far from the main lobe. Thus, the frequency selectivity of a hard pulse is poor. A soft pulse has a greater spread in the time domain, but excites a narrow, uniform range of frequencies. Thus, the frequency selectivity of a soft pulse is good.

Pulse, Soft

Low-power, long-duration RF pulses used in NMR measurements. Soft pulses in time domain are rectangular pulses in frequency domain. In medical MRI applications, a soft 90° pulse typically has a width of a few milliseconds. Although soft pulses need not conform to a particular shape, they usually have crafted pulse

envelopes, e.g., truncated Sinc pulses (bell-shaped envelopes), to improve frequency selectivity. See *Pulse Shaping* for frequency selectivity.

Pulse, 90°

An RF pulse designed to rotate the net magnetization vector 90° from its initial direction in the rotating frame of reference. If the spins are initially aligned with the static magnetic field, this pulse produces transverse magnetization and free induction decay (FID).

Pulse, 180°

An RF pulse designed to rotate the net magnetization vector 180° in the rotating frame of reference. Ideally, the amplitude of a 180° pulse multiplied by its duration is twice the amplitude of a 90° pulse multiplied by its duration. Each 180° pulse in the CPMG sequence creates an echo.

R

Radio Frequency (RF)

Electromagnetic radiation at a frequency in the same general range as that used for radio transmissions.The Larmor frequency for ^{1}H is typically in this range. For an MRIL tool, the Larmor frequency is in the range of 580 to 750 KHz.

Regularization

The process which is used to stabilize the inversion from the measured NMR echo decay to the T_2 spectra. There are many methods in use, of which MAP is one. They all result in a smoothed spectra, which varies depending on the method and amount of regularization. The need to use regularization means that there is no unique NMR spectra or pore distribution. In most cases, the major features of the spectra are independent of the method of regularization.

Relaxation Time

A time constant associated with the return of nuclear spins to their equilibrium positions after excitation. Several relaxation times are defined in NMR measurements. Each is related to different molecular interaction mechanisms. The most frequently measured relaxation times are T_1 and T_2. For bulk water, T_1 and T_2 are approximately 3 s. The relaxation times of water in rocks are much smaller and are generally less than 300 ms.

Relaxation Time, Bulk Fluid

The relaxation produced by interaction of the fluid with itself. For most cases of interest T_1 and T_2 are equal. For gas, however, because the diffusivity of gas is much higher than that of liquids, the apparent T_2 of gas measured by CPMG technique in a gradient magnetic field can be much smaller than T_1.

Relaxation Time, Longitudinal (T_1)

Longitudinal, or spin-lattice, relaxation time. This time constant characterizes the alignment of spins with the external static magnetic field.

Relaxation Time, Transverse (T_2)

Transverse, or spin-spin, relaxation time. This time constant characterizes the loss of phase coherence that occurs among spins oriented at an angle to the main magnetic field and that is due to interactions between spins. T_2 never exceeds T_1. Both T_2 and

T_1 have been successfully related to petrophysical properties of interest, such as pore size, surface-to-volume ratio, formation permeability, and capillary pressure.

Residual Oil
Oil remaining in the reservoir rock after the flushing or invasion process, or at the end of a specific recovery process or escape process.

Resonance
Vibration in a mechanical or electrical system caused by a periodic stimulus, with the stimulus having a frequency at or close to a natural frequency of the system.

RF See *Radio Frequency*.

Ringing
The oscillatory response of a magnet to the application of high-energy RF pulses. When the MRIL RF antenna is energized with high-energy RF pulses, the MRIL magnet resonates or "rings." The MRIL magnet acts like a piezoelectric crystal, generating an acoustic oscillating voltage that interferes with the formation signal. Ringing is frequency-dependent, and each magnet has a different ringing window (typically 20 to 40 kHz wide) where the ringing effect is smaller than at other frequencies. The ideal operating frequency is one that is located in the middle of a broad ringing window.

Rotating Frame of Reference
A frame of reference, which rotates around the axis of the static magnetic field ($\mathbf{B}_0$) at a frequency equal to that of the applied RF magnetic field ($\mathbf{B}_1$).

Running Average
This represents the total number of individual experiments (i.e., complete echo trains) needed to produce a high signal-to-noise. Because the PAPs technique is used during a CPMG measurement, the Running Averaging is at least two.

S

SBVI See *Spectral Bulk Volume Irreducible*.

Shifted Spectrum Method (SSM)
An interpretation method based on dual-*TE* measurements with identical *TW*. The SSM relies on the diffusivity contrast between fluids with different diffusivity to type viscous hydrocarbons. The shifted spectrum refers to the observation of the T_2 distribution shifted to smaller T_2 values when *TE* is increased. Gases have much higher diffusivity than oil or water, and are more sensitive to the echo spacing (*TE*) changes. Heavy oils have very low diffusivity, and are least sensitive to *TE* changes. The SSM is performed in the T_2 domain and uses the difference in the shift between fluids of different diffusivity to identify fluids.

Signal Averaging
A method of improving signal-to-noise ratio by averaging echo trains.

Signal-to-Noise Ratio (*S/N*)
The ratio of signal amplitude to noise amplitude. *Signal* refers to the desired part of a detected signal; *noise* refers to the remainder of the detected signal and includes random noise. *S/N* is a measure of data quality. The *S/N* of NMR measurements can

be improved by averaging several echo trains, by sampling larger volumes, or by increasing the strength of the $\mathbf{B}_0$ magnetic field. If the noise is random (statistical) noise only, then averaging n measurements improves S/N by $n^{1/2}$.

S/N See *Signal-to-Noise Ratio*.

Spin Intrinsic angular momentum of an elementary particle or system of particles, such as a nucleus. Spin is responsible for the magnetic moment of the particle or system.

Spin Echo

After spins are excited by an RF pulse, the spins experience FID because of $\mathbf{B}_0$ inhomogeneities. Spin isochromats, which are groups of spins precessing at exactly the same Larmor frequency, lose phase coherence during FID. However, during this decay, the isochromats do not experience many spin-spin interactions and still retain phase memory. If a second pulse (180º) is applied at time τ after the first RF pulse, the spin isochromats will re-phase in the same amount of time τ. A macroscopic signal (the spin echo) then occurs at precisely $TE = 2\tau$. Even if the second pulse is not a 180º pulse, a spin echo can still be observed, but this echo will be of smaller amplitude. A third pulse will repeat the process.

Stimulated Echo

The echo formed after magnetization evolves first in the x-y plane, then in the z direction, and again in the x-y plane. A stimulated echo is observed after a three-pulse sequence. Because of $\mathbf{B}_1$ inhomogeneities, stimulated echoes occur during CPMG sequences used on logging tools at the same times as regular echoes and must be compensated for through calibration.

Surface Relaxivity (ρ)

A measure of the capability of a surface to cause protons to relax, i.e., lose orientation or phase coherence. This quantity depends on the strength of fluid-matrix interactions. It also varies with the wettability of the rock surface. Surface relaxation strength ρ falls in the range of approximately 0.003 to 0.03 cm/s for clastics. ρ is smaller for carbonates.

T

T_1 See *Longitudinal Relaxation Time*.

T_2 See *Transverse Relaxation Time*.

T_2* Time constant characterizing the loss of phase coherence that occurs among spins oriented at an angle to the main magnetic field and that is due to a combination of magnetic field inhomogeneity and magnetic interaction. T_2* is always much shorter than T_2. In the limit of no diffusion, loss of coherence produced by field inhomogeneity can be reversed by the application of 180º pulses, which results in the formation of spin echoes.

$T_{2cutoff}$ A value of T_2 that is empirically related to the capillary properties of the wetting fluid in a rock. It is used to differentiate different pore sizes and quantify the amount of bound water. Typically, porosity associated with T_2 values less than approximately 33 milliseconds ($T_{2cutoff}$ = 33 ms) are summed to obtain *BVI* for

clastics and, similarly, $T_{2cutoff}$ of approximately 90 ms for carbonates. Note that these values are empirical and may be rock-specific.

T_{2S} Time constant that describes the contribution of surface relaxivity to the transverse relaxation time of fluid in a rock. When a single wetting fluid fills the pores, T_{2S} dominates the relaxation process. Thus, T_2 is proportional to $(S/V)^{-1}$ of a pore, where S/V is the surface-to-volume ratio. If a spherical pore is assumed, T_2 is proportional to the pore radius.

TDA See *Time Domain Analysis*.

TE See *Echo Spacing*.

Time Domain Analysis (TDA)

An alternate method to the differential spectrum method for processing dual-*TW* echo trains. The interpretation is performed in the time domain rather than in the T_2 domain. The key features of the TDA are subtraction of the two echo trains from one another, and the processing of the echo differences in the time domain using predicted or measured oil, gas, and water relaxation times and hydrogen-index values.

In the DSM, the dual-*TW* echo trains are first inverted into T_2 spectra and subtracted from one another. The interpretation is done in T_2 spectrum domain. The effect of T_2 spectrum broadening because of noise and regularization smears the partial porosities into adjacent bins, and the subtracted spectrum may contain negative amplitudes that are obviously incorrect. The TDA method has fewer problems with the noise-induced T_2 spectrum broadening, and because fewer free parameters need to be determined, the solution is more stable. However, subtracting echoes reduces *S/N*.

Transverse Magnetization (M_x)

Component of the net magnetization vector at right angles to the static magnetic field.

TW See *Wait Time*.

V, W

Viscosity

Resistance of a fluid to flow. Viscosity is due to internal friction caused by molecular cohesion in the fluid. The diffusion constant *D* is inversely proportional to viscosity.

Wait Time (*TW*)

The time between the last CPMG 180° pulse and the first CPMG pulse of the next experiment at the same frequency. This time is the time during which magnetic polarization or T_1 recovery takes place. It is also known as *polarization time*.

Water-Wet

A solid surface is water-wet when the adhesive attraction of water molecules for the solid substance is greater than the attraction between water molecules, i.e., adhesive force > cohesive force. The angle of contact of a water droplet on a water-wet solid surface will be less than 90° (measured inside the water phase). A mobile non-wetting oil phase would advance over the adhesive layer of water. Only water has a surface relaxation mechanism in a water-wet formation.

Wettability

The capability of a solid surface to be wetted when in contact with a liquid. A liquid wets a solid surface when the surface tension of the liquid is reduced so that the liquid spreads over the surface. Only the wetting fluid in a rock pore has a surface relaxation mechanism. Therefore, wettability affects the NMR properties of fluids in reservoir rocks.

Nomenclature

γ See *Gyromagnetic Ratio*.

ρ See *Surface Relaxivity*.

χ See *Magnetic Susceptibility.*

η See *Viscosity*

ϕ *Porosity*

References

Glossary of Magnetic Resonance Imaging Terms, in Bushong, S.C., *Magnetic Resonance Imaging, Physical and Biological Principles*, Second Edition, Mosby, 1996.

Glossary of Terms and Expressions Used in Well Logging, Second Edition, SPWLA, Houston, 1984.

NMR Terminology Glossary, Western Atlas, 1996.

Index

D

E

F

G

H

I

J

L

M

N

O

P

Q

R

S

T

U

V

W

Z

H02308